A Sub-ppb Measurement of the Mass of Cesium for a New Determination of the Fine-Structure Constant

by

Michael Patrick Bradley
B.Sc. (Honours) University of New Brunswick (1992)

Submitted to the Department of Physics
in partial fulfillment of the requirements for the degree of

Doctor of Philosophy

at the

MASSACHUSETTS INSTITUTE OF TECHNOLOGY

February 2000

Author ______________________________
Department of Physics
Jauary 28, 2000

Certified by ______________________________
David E. Pritchard
Professor of Physics
Thesis Supervisor

Accepted by ______________________________
Thomas J. Greytak
Associate Department Head for Education

A Sub-ppb Measurement of the Mass of Cesium for a New Determination of the Fine-Structure Constant

by

Michael Patrick Bradley
B.Sc. (Honours) University of New Brunswick (1992)

Submitted to the Department of Physics
on Jauary 28, 2000, in partial fulfillment of the
requirements for the degree of
Doctor of Philosophy

Abstract

This thesis describes recent single-ion Penning trap mass spectrometry measurements of the mass of atomic Cesium with a relative uncertainty of 2×10^{-10}. This measurement reduces the uncertainty on the mass of Cesium by a factor of 100, and removes this uncertainty as a limitation on the accuracy of a determination of the fine-structure constant alpha via a Cesium photon recoil experiment. Removal of this limit should ultimately allow this value of alpha to have a relative accuracy ~ 1 ppb, which would be comparable to or even better than the most accurate measurement of alpha currently available. This value of alpha will help shed light on the current ~ 50 ppb discrepancies between values of alpha measured via different routes.

In addition to the mass measurement of Cesium, this thesis also describes related mass measurements of atomic Rubidium and Sodium which reduce the uncertainties on these masses by factors ~ 100, with a view to possible future photon recoil measurements using these species.

The measurements were taken using a new Penning trap mass spectrometer constructed by the author and his colleagues. This new spectrometer followed the general design principles of previous MIT ICR Lab Penning trap mass spectrometers, and incorporated a DC SQUID as an ion detector for the first time.

This thesis concludes with a discussion of a passive two-coil system designed for shielding magnetic field gradients. These may prove to be the key enabling technology for a future double Penning trap mass spectrometer.

Thesis Supervisor: David E. Pritchard
Title: Professor of Physics

To my parents, my dear wife Rachel,
and my sisters Arlyn and Megan,
for their constant enouragement and support over the years.

Give your heart to the trade you have learnt, and draw refreshment from it.

— Marcus Aurelius, *Meditations*

Contents

List of Figures

Chapter 1

Introduction

1.1 Single-Ion Penning Trap Mass Spectrometry at MIT

Mass spectrometry is the science of measuring atomic and molecular masses. Mass is one of the three fundamental quantities in physics (the others are length and time) and mass is one of the most basic properties of any atomic species. Measurements of relative atomic masses were among the earliest efforts in quantitative physical chemistry.

Atomic and molecular ions have been used to make accurate atomic mass measurements since the early part of this century. Until the advent of ion trap mass spectrometers of the type described in this thesis came into use, the highest relative precision which could be achieved was about 1 part in 10^8 in magnetic spectrometers. This limitation was due primarily to beam space charge effects and the difficulty of maintaining a constant magnetic field over an extended region.

Single particle trapping techniques (pioneered by Hans Dehmelt and Robert Van Dyck at the University of Washington in Seattle) remove both of these obstacles: space charge effects by the use single ions and spatial magnetic field variations by the use of a trap to confine the ion to a small region of uniform field.

MIT's effort in this field was begun in 1983 by Prof. David E. Pritchard. Since that time the MIT group has developed a variety of novel techniques for atomic mass measurement and has used these to measure 12 atomic masses in addition to the neutron. Except for the mass of H [VFZ98] the MIT values are the most accurate ever reported [DNB94]. The accuracies on these masses is generally $\sim$ 0.1 ppb., making them typically 100 times more accurate than previously measured values. Our accuracies are somewhat lower for our measurements of the heavy alkali metal atoms Cs and Rb, due we believe in part to their lower cyclotron frequencies, higher charge states used, and greater difficulty to cleanly trap them. Our ability to load a wide variety of masses into our trap has enabled us to base all our atomic mass determinations on 2 different measurement routes, which has provided a stringent check on the systematic errors which are the bane of metrologists everywhere, giving us high confidence in our results.

I have had the good fortune to be preceded in this work by 6 talented students whose theses [FLA87], [WEI88], [COR90], [BOY92], [NAT93], [DIF94] provide excellent background for for this work. It has been a privilege to build on their groundbreaking efforts.

1.2 Motivating Applications

1.2.1 Introduction

Einstein's mass-energy relation $E = mc^2$ means that mass spectrometry can be used to probe energy levels and thus the structure of nuclei. Since this structure is governed by the fundamental dynamics of the constituent particles involved, mass spectrometry can tell us much about fundamental physics.

It is is useful to consider the energy scales which can be probed with the 0.1 ppb accuracy possible with our state-of-the-art single ion Penning trap mass spectrometer. Nucleons have mass equivalent energies $mc^2 \approx 1000$ MeV, so mass measurements of a typical atom containing $\sim$ 10 nucleons with precision $\sim 10^{-10}$ will have an energy resolution $\sim$ 1 eV. Thus mass spectrometry at this level can probe nuclear binding energies with high precision, and is even sensitive to chemical binding energies.

The goal of the MIT ICR Lab's mass spectrometry program has always been to make atomic mass measurements which can be applied to various problems in fundamental physics and metrology. After a brief disucussion of atomic mass units, I discuss some of the most important applications of our mass measurements. The MIT ICR lab has already completed mass measurements for an atomic kilogram standard (Section 1.2.3), recalibration of the X-ray wavelength standard (Section 1.2.5), and a photon-recoil determination of the fine-structure constant α (the subject of this thesis). Future applications include a test of Einstein's mass-energy relation $E = mc^2$ (Section 1.2.4) and measurement of the available energy in the β-decay of ^{3}H to contribute to the effort to determine the rest mass of the neutrino (Section 1.2.7). (Note that the following material regarding applications is complementary to that in Chapter 5, Section 5.5.)

1.2.2 Mass Units

Atomic masses are measured in atomic mass units. The atomic mass unit u is defined by the statement:

One ^{12}C atom at rest in the ground state has a mass of exactly 12 u

Throughout this thesis I will use lowercase m to denote masses measured in SI units (kg) and uppercase M to denote masses measured in atomic mass units.

The SI unit of "quantity of substance" is the mole. One mole of any atomic or molecular material is M grams where M is the atomic mass of an individual atom or molecule of the substance expressed in u. This statement defines a quantity of substance- the number of atoms or molecules in one mole. This quantity is called the Avogadro constant and is determined experimentally:

$$N_A = 6.022\,136\,7\,(36) \times 10^{23}\,\mathrm{mol}^{-1} \tag{1.1}$$

If m is the mass in kg of a single atom and M is the mass in grams of one mole of atoms, then we have the result:

$$m = \frac{M}{10^3 N_A} \tag{1.2}$$

1.2.3 Kilogram standard

As part of a program to redefine the kilogram in terms of an operational standard based on a nearly perfect silicon crystal, DiFilippo et al. measured the mass of ^{28}Si with an uncertainty of 7×10^{-11} [DNB94]. This was a factor of 350 improvement in the uncertainty of its previously measured mass.

1.2.4 Neutron capture for $N_A h$ and tests of relativity

The energy available for radiation by gamma rays after neutron capture by a nucleus $^A\mathrm{X}_Z$ is

$$\Delta E = \Delta m c^2 \tag{1.3}$$

where

$$\Delta m = m(^A\mathrm{X}_Z) + m(^1\mathrm{n}_0) - m(^{A+1}\mathrm{X}_Z) \tag{1.4}$$

is the mass difference between the reactant and product nuclei in SI units. The equivalent energy Δmc^2 is $\sim$ 8 MeV for typical nuclei with $10 < A < 50$. Thus mass spectrometry at the 0.1 ppb level can determine Δm to $\approx 10^{-7}$.

Another measure of this energy difference is

$$\Delta E = \frac{hc}{\lambda'_{eff}} \tag{1.5}$$

where λ'_{eff} is the effective wavelength of the radiated gamma rays (allowing for the emission of multiple gamma rays and correcting for recoil shifts). Thus we have

$$\Delta mc^2 = \frac{hc}{\lambda'_{eff}} \Rightarrow \Delta m \lambda'_{eff} = \frac{h}{c} \quad . \tag{1.6}$$

Accurate measurements of the mass difference Δm will be in atomic mass units u and must be converted to SI using Eq. 1.2. Therefore

$$\Delta M \lambda'_{eff} = \frac{10^3 N_A h}{c} \quad . \tag{1.7}$$

Thus precision measurements of ΔM and λ'_{eff} at the 10^{-7} level can determine the *Molar Planck constant* $N_A h$ to $\sim 10^{-7}$.

Neutron-capture measurements of $N_A h$ have two significant metrological applications. The first is a test of the basic assumption of special relativity that the "mechanical" speed of light c_m (the limiting velocity of a massive particle) and the "electromagnetic" speed of light c_{em} (the speed of propagation of electromagnetic waves) are equal. Rewriting Eq. 1.7 using $\Delta E = \Delta m c_m^2 = h c_{em}/\lambda$ we get:

$$\Delta M \lambda'_{eff} = \frac{10^3 N_A h c_{em}}{c_m^2} \quad . \tag{1.8}$$

This can be combined with a relationship between $N_A h$ and the fine-structure constant α (Eq. 4.14) to give the following relationship between $N_A h/c_{em}$ and an "electromagnetic" measurement of α based on the Quantum Hall Effect:

$$\frac{N_A h}{c_{em}} = \frac{\alpha_{QHE}^2}{2R_\infty}(\frac{M_e}{M_p})(\frac{M_p}{10^3}) \quad . \tag{1.9}$$

From this we get

$$(\frac{c_{em}}{c_m})^2 = \Delta M \lambda'_{eff}(\frac{2R_\infty}{\alpha_{QHE}^2})(\frac{M_p}{M_e})(\frac{1}{M_p}) \quad . \tag{1.10}$$

It is anticipated that gamma-ray spectrometry with a flat-crystal spectrometer will allow measurements of λ'_{eff} with uncertainty 5×10^{-7} for the neutron capture reaction [KES95]:

$$^{32}\mathrm{S} + ^1\mathrm{n}_0 \rightarrow ^{33}\mathrm{S} + \gamma\text{-rays} \tag{1.11}$$

and the MIT ICR lab should be able to measure ΔM with uncertainty 5×10^{-7} (assuming mass measurement accuracy of 10^{-10}). All the other quantities in Eq. 1.10

are known to much higher accuracy: R_∞ to 0.008 ppb [SJD99], [UHG97], α_{QHE} to 24 ppb [JEL97], M_p/M_e to 2 ppb [FVS95], and M_p to better than 1 ppb [DNB94], [VFZ98], so the equality of c_{em}/c_m could be tested to 5×10^{-7} via this method. Although this is many orders of magnitude less precise than the $\sim 10^{-22}$ tests of relativity based on measurements of the anisotropy of the speed of light, it has the advantage of not relying on any assumption of a preferred reference frame.

The other metrological application of a neutron capture measurement of $N_A h$ is to contribute to a new determination of the fine-structure constant α. This is described in Section 4.3.5.

1.2.5 Recalibration of X-ray standard

The MIT ICR lab measured the mass differences ^{14}N + ^{2}H - ^{15}N - ^{1}H and ^{12}C + ^{2}H - ^{13}C - ^{1}H with uncertainties 1×10^{-7} and 4×10^{-7} respectively [DNB94] in anticipation of accurate neutron-capture gamma ray measurements in order to measure $N_A h$ and test relativity. Unfortunately the gamma-spectroscopy proved to be less accurate than anticipated [KES95]. However, the measurements still bore fruit because the MIT measurement of the mass difference ^{14}N + ^{2}H - ^{15}N - ^{1}H [DNB94] along with accurate gamma-ray measurements of the deuteron binding energy [GRE86] corrected an 8000 ppb error in the wavelength of the ^{14}N neutron-capture gamma rays, which are widely used by gamma-ray spectroscopists as calibration lines.

1.2.6 Fine-Structure Constant via Neutral-Particle Interferometry

The subject of this thesis is a measurement of M(^{133}Cs) and other alkali metals with the goal of contributing to measurements of $N_A h$ and therefore α. A photon-recoil/mass spectrometry route to α is potentially capable of a $\sim$ 50-fold higher accuracy than the neutron capture method.

1.2.7 Neutrino mass

One of the most significant questions in fundamental physics has been that of the rest mass of the neutrino. A non-zero mass would have significant implications for the standard model. Neutrino spectroscopists study this problem by counting the number of electrons as a function of emitted energy in the beta decay of ^{3}H:

$$^3\text{H} \rightarrow ^3\text{He} + e^- + \bar{\nu}_e \tag{1.12}$$

Beta decay has a continuous spectrum because the available energy (18 keV for ^{3}H) is divided between the electron, the antineutrino, and the recoiling nucleus in the three-body process. Any difference between the limiting energy of the electron and the available energy must be due to the rest mass of the anti-neutrino. Single ion mass spectrometry can help by providing beta-decay spectroscopists with an accurate value of total mass-equivalent decay energy available.

To help with a determination of the neutrino rest mass to sub-eV accuracy we would need to measure the total mass energy available in the decay (18 keV) to < 1 eV precision.

By measuring the masses of ^{3}He and ^{3}H to 3.3×10^{-10} and 5.1×10^{-10} respectively, Van Dyck et al. were able to determine [VFS93a]

$$\Delta mc^2(^3\text{H} -^3\text{He}) = 18\,590.1\,(1.7)\ eV. \tag{1.13}$$

The MIT ICR lab has plans to increase mass measurement accuracy to 10^{-11} and beyond, which would then allow a determination of this mass difference to ~ 0.1 eV. This would be an accuracy well beyond what the beta-spectroscopy currently requires, and would not present any limitation on the final accuracy of the measurements.

1.3 Background/History

Mass spectrometry with charged particles began with J.J. Thomson's measurement of m_e/e in 1897. Over the intervening century the mass-to-charge ratio, has remained the basic quantity of interest, but the methods have changed considerably. The original method of measuring m/e by measuring the radius of curvature of a beam of known velocity travelling perpendicular to a magnetic field has been superseded in accuracy by direct measurements of the cyclotron frequency. With the advent of single-ion Penning trap measurements in the 1980s, sub-ppb accuracy was achieved for the first time. With the improved accuracy now possible over a wide range of masses, Penning trap mass measurements are finding wide applicability in metrology and fundamental physics, as befits measurements of such a fundamental quantity.

Construction of the MIT ICR mass spectrometer began in 1983, and ions were first detected in 1986 [FLA87]. By 1988 single ions were being trapped [WEI88]. 1989 saw the first high-accuracy mass spectrometry results, a 0.4 ppb measurement of the $M(\mathrm{CO}^+/M(\mathrm{N}_2^+)$ mass ratio [CWB89], [COR90]. In 1992 a number of apparatus improvements lead to a 0.1 ppb measurement of the same mass ratio, a factor of four improvement in accuracy [BOY92]. In 1992-93 the apparatus was used to measure a number of mass ratios leading to an atomic mass table containing masses for H, D, the neutron, ^{12}C, ^{13}C, ^{14}N, ^{15}N, ^{16}O, Ne, Ar with accuracies $\sim$ 0.1 ppb [NAT93], [DIF94], [DNB94].

There followed a period of work on two-ion methods for mass spectrometry. Though these showed some promise, various complications prevented them from being used for a successful mass measurement. During this work the apparatus developed an unsealable leak in the vacuum can. As a result, a new apparatus was constructed which incorporated for the first time a DC SQUID detector. This apparatus was first cooled down in September 1996, but unfortunately it required a year and a half to get it working to the point of trapping and detecting single ions once again due to difficulties with feedback and noise pickup in the DC SQUID detector. Finally it was used to make mass measurements on alkali metals Cs, Rb, and Na during the fall of 1998 [BPR99].

1.4 Survey of state of Penning trap mass spectrometry

Several groups in the U.S. and Europe are involved in high-precision Penning trap mass spectrometry for various goals. Their work is briefly reviewed below.

1.4.1 University of Washington

At the University of Washington Hans Dehmelt pioneered the trapping of single charged particles for precision measurements [WED73] and Robert Van Dyck began a program of single-ion mass spectrometry. In the area of mass spectrometry Schwinberg, Dehmelt, and Van Dyck measured the electron/positron mass ratio m_{e^-}/m_{e^+} to 130 ppb [SDV81], and Van Dyck's group has measured the masses of ^{1}H, ^{2}H, ^{3}H, ^{3}He, ^{4}He, ^{14}N, and ^{16}O [VFS93a], [VFS93b], [VFS93c] with uncertainties ~ 0.3 ppb, as well as the proton-electron mass ratio m_p/m_{e^-} to 2 ppb [FVS95]. Recently they have installed a self-shielding solenoid of the type designed by Gabrielse and Tan [GAT88] with a shielding factor of 180, as well as an active shielding system with a shielding factor of ~ 100, giving a net shielding factor $\sim 10^4$. Using this new system they have measured the mass of the proton with an uncertainty of 1.4×10^{-10} [VFZ98]

1.4.2 Harvard

Gabrielse's group working at Harvard and CERN have recently published a measurement of the proton/anti-proton mass-to-charge ratio with uncertainty 9×10^{-11}. This was achieved by alternately measuring the cyclotron frequencies of an H^- ion and an anti-proton confined simultaneously in the same Penning trap [GKH99]. This is the most stringent test of the mass equivalence of matter and antimatter, which is a consequence of CPT symmetry.

1.4.3 JILA

Dunn's group at JILA (Joint Institute for Laboratory Astrophysics, Boulder, Colorado) operated a Penning trap fed by a sophisticated ion loader. They used this device to measure the mass ratios $^6Li^+/^{12}C^{++}$ and $^6Li^+/D_3^+$ resulting in a measurement of M[^{6}Li] with an uncertainty of 2.7 ppb. This measurement removes uncertainty due to mass from the experimental search for parity-violating weak neutral current interactions in the ^{6}Li nucleus. They also made a 1.1 ppb measurement of the $D_2^+/^4He^+$ mass ratio [HJD99]. Unfortunately the JILA apparatus has since been de-comissioned and disassembled.

1.4.4 SMILETRAP

A Swedish-German collaboration operates a time-of-flight Penning trap mass spectrometer (Stockholm-Mainz Ion LEvitation Trap) fed by the CRYSIS ion storage ring in Stockholm. This allows great versatility in loading a wide variety of highly charged ions into the trap. Currently the use of uncooled ions limits the accuracy to ~ 1 ppb, but there are plans to switch to a cooled system. The SMILETRAP group has measured the masses of a number of species (^{16}O, ^{40}Ar, ^{28}Si, ^{86}Kr, ^{2}H, ^{1}H, ^{3}He, ^{4}He) with accuracies ~ 1 ppb [BOR97]. Recently they measured M[^{133}Cs] with uncertainty 1.8 ppb [CFB99].

1.5 Overview of Thesis

This thesis contains reports on measurements of the masses of ^{133}Cs [1], ^{85,87}Rb and ^{23}Na [2], mass measurements undertaken with the goal of improving the accuracy of the fundamental constants $N_A h$ and α.

- Chapter 1: Discusses the motivation for and applications of high-precision mass spectrometry. Briefly outlines the history of Penning-trap mass spectrometry in gen-

---

[1] Measured by M. Bradley

[2] Measured by J. Thompson and S. Rainville

eral and of the MIT apparatus in particular, and surveys the current state of the field.

- Chapter 2: The basic theory behind single-ion Penning-trap mass-spectrometry is introduced. I then discuss the specific techniques used by the MIT ICR lab.
- Chapter 3: In this chapter I discuss the new apparatus which was built for the measurements described in this thesis.
- Chapter 4: The current state of metrology of the fine-structure constant α is reviewed, and the contribution of mass spectrometry to a new determination of the fine-structure constant based on atom interferometry is introduced. The bulk of the chapter is then devoted to a discussion of the ICR's labs recent measurements of the masses of Cs, Rb, and Na for the purposes of contributing to a new determination of α. The final section of this chapter is a paper published in Physical Review Letters, "Penning Trap Measurements of the Masses of ^{133}Cs, ^{87,85}Rb and ^{23}Na with Uncertainties $\leq$ 0.2 ppb" [BPR99] which describes these measurements.
- Chapter 5: This chapter is a first draft of a paper entitled "Single-Ion Cyclotron Resonance Mass Spectrometry at MIT", which the ICR lab ultimately plans to submit to the journal "Reviews of Modern Physics". This paper contains a discussion of the lab's standard techniques and practices, as well as a discussion of the analysis of all the data ever taken by the ICR lab.
- Chapter 6: This chapter discusses a proposed method for shielding an experimental region from the effect of an applied magnetic field gradient. The final section in the chapter is a preliminary draft of a paper which will be submitted for publication.

Chapter 2

Penning Trap Theory and Experimental Techniques

In this chapter I discuss the dynamics of an ion in a Penning trap and the theory underlying the use of trapped ions for precision measurements. The theory of a charged particle in a Penning trap is well understood and has been discussed by many authors. Perhaps the most generally useful review is that by Brown and Gabrielse [BRG86]. Most of the detailed theory for the MIT ICR experiment has been discussed by Robert Weisskoff in his excellent thesis [WEI88]. This chapter is heavily based on these two works. It duplicates to a large extent the related material in the paper draft in Chapter 5, but goes into more detail, since it is intended to serve as a reference for future students and postdocs.

2.1 The Ideal Penning Trap: Theoretical Principles

2.1.1 Introduction

The basic idea underlying Ion Cyclotron Resonance (ICR) mass spectrometry is to exploit the fact that an ion of mass m and charge q in a magnetic field B orbits the field axis at a cyclotron frequency given by (SI units)

$$\omega_c = \frac{qB}{m}. \tag{2.1}$$

To take advantage of the high precision to which frequencies can be measured using RF techniques, it is necessary to confine and observe the ion being measured for as long as possible since frequency measurement uncertainty $\Delta f \propto 1/T$ where T is the measurement time. A magnetic field alone is not sufficient to confine ions; since the Lorentz force it exerts is perpendicular to the field direction ions are not confined along the axis of the field.

2.1.2 Ion Confinement

To confine ions axially we use a Penning trap, a configuration of electrodes invented by the Dutch physicist F.M. Penning in the 1930's to increase the path length of electrons in an ionization pressure gauge [PEN36]. The basic Penning trap configuration is three electrodes, an annular ring and two endcaps (see Fig. 2-1). Positive ions are confined by making the ring negative with respect to both endcaps; then the electric field lines run from the endcaps towards the ring. In the absence of the magnetic field the radial electric field would eject positive ions from the trap; however the magnetic field prevents this, with the Lorentz force providing the necessary radial confinement.

The dynamics of an ion confined in a Penning trap are well understood (for a thorough review see [BRG86]) and are briefly outlined below.

An ideal Penning trap consists of a uniform axial magnetic field $\vec{B} = B\hat{z}$ and a quadrupole electrostatic field generated by the electrodes:

$$\Phi(\rho, z) = \frac{V}{2}\left(\frac{z^2 - \frac{1}{2}\rho^2}{d^2}\right) \tag{2.2}$$

where the "trap voltage" V is the potential of the ring with respect to the endcaps ($V < 0$ to confine positive ions), $d^2 \equiv z_0^2/2 + \rho_0^2/4$ and z_0 and ρ_0 are the trap half-height and radius defined in Fig. 2-1. The electrodes of our Penning traps are hyperboloids of revolution, which are the equipotentials of Laplace's equation for this quadrupolar field. In an ideal Penning trap the electrodes extend to infinity along

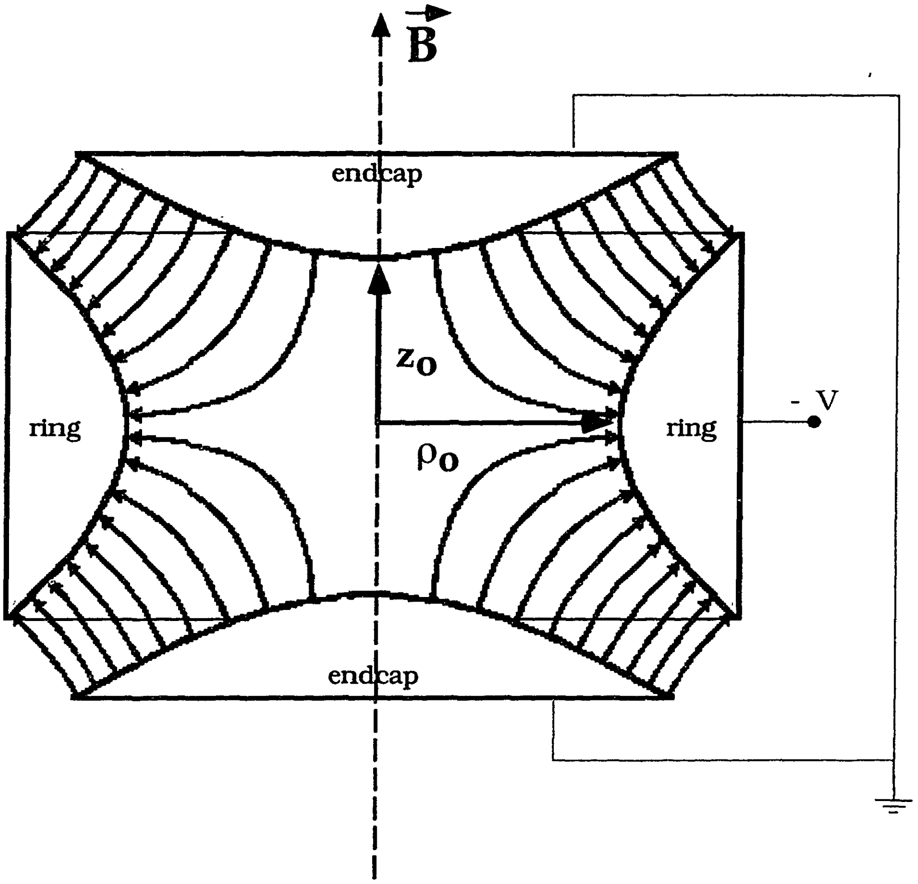

Figure 2-1: Cross-section of Penning trap electrodes. In the three-dimensional article the electrodes are cylindrically symmetric about the z-axis. To confine ions the endcaps are grounded and the ring is made negative. The electrodes are precisely machined to be hyperbolas of revolution, which are the equipotentials of Laplace's equation for a quadratic potential.

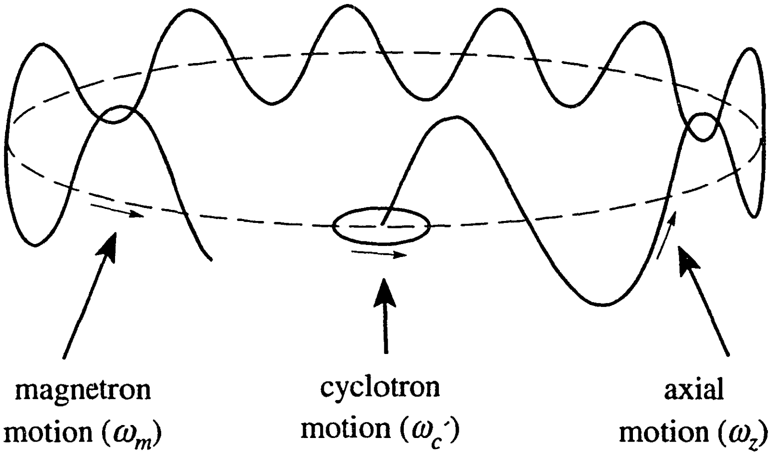

Figure 2-2: The three normal modes of motion of an ion in a Penning trap (adapted from [BRG86]). We adjust $\omega_z/2\pi = 160$ kHz for detection. For precision measurements we operate in the regime where $\omega_c' >> \omega_z >> \omega_m$. For example, Cs^{+++} has $\omega_c'/2\pi = 3$ MHz, $\omega_z/2\pi = 160$ kHz, $\omega_m/2\pi = 4$ kHz.

the equipotentials to generate a pure quadrupole field. In a real trap the electrodes must be truncated, which introduces a non-quadrupolar component to the field. This can be compensated for using extra "guard ring" electrodes (this is discussed further below).

2.1.3 Normal Modes

In the ideal Penning trap an ion of mass m and charge q has three normal modes of motion [BRG86]. These are the trap cyclotron, axial, and magnetron modes (depicted in Fig. 2-2); they have normal mode frequencies ω_c', ω_z, and ω_m given by the following expressions.

$$\omega_z = \sqrt{\frac{qV}{md^2}} \tag{2.3}$$

$$\omega_c' = \frac{1}{2}[\omega_c + \sqrt{\omega_c^2 - 2\omega_z^2}] \tag{2.4}$$

$$\omega_m = \frac{1}{2}[\omega_c - \sqrt{\omega_c^2 - 2\omega_z^2}] \tag{2.5}$$

The axial mode is a simple harmonic oscillation along the z axis of the trap in the electrostatic potential well. The trap cyclotron mode is reduced in frequency relative to the free-space cyclotron frequency by the repulsive radial electric field. The magnetron mode is an $\vec{E} \times \vec{B}$ drift motion due to the perpendicular radial electric field and axial magnetic field. It is worth noting that an approximate expression for the magnetron frequency can be derived by balancing the Lorentz and electrostatic forces as follows:

$$F_B = q\vec{v} \times \vec{B} = qr\omega_m B \tag{2.6}$$

$$F_E = -q\vec{\nabla}(\Phi) = -q\frac{\partial}{\partial\rho}[\frac{V}{2}\frac{z^2 - \frac{1}{2}\rho^2}{d^2}] = \frac{qV\rho}{2d^2} \tag{2.7}$$

$$F_E - F_B = ma \approx 0 \quad \text{(since the magnetron motion is slow)} \tag{2.8}$$

$$\omega_m = (\frac{1}{qB})\frac{qV}{md^2} = \frac{\omega_z^2}{2\omega_c} \tag{2.9}$$

This approximate form can also be derived from 2.5.

It is easy to see from Eqs. 2.4 and 2.5 that the result:

$$\omega_c' + \omega_m = \omega_c \tag{2.10}$$

is true in an ideal Penning trap, however it does not hold in the presence of trap imperfections or tilts of the trap axis with respect to the magnetic field. In general the equations 2.3, 2.4, 2.5 hold when the z-axes of the trap and the $\vec{B}$ field are aligned. Misalignment or ellipticity of the trap electrodes will modify the frequencies. However the following extremely useful result has been proved [BRG86] to hold true for any degree of trap tilt or ellipticity:

$$\omega_c^2 = \omega_c'^2 + \omega_z^2 + \omega_m^2 \tag{2.11}$$

Table 2.1: Required measurement precision for the mode frequencies to allow a cyclotron frequency measurement with a precision $\sim 10^{-10}$.

Mode	Typical Frequency	Req'd Relative Precision	Req'd Absolute Precision
ω_c'	3 MHz	10^{-10}	0.0003 Hz
ω_z	160 kHz	4×10^{-8}	0.006 Hz
ω_m	4 kHz	10^{-4}	0.4 Hz

We use this equation to recover ω_c (our measure of the inertial mass of the ion) from the measured mode frequencies. In our trap we detect the axial motion with a narrowband detector (discussed later in this thesis) at 160 kHz. We therefore adjust the trapping voltage V so that $\omega_z/2\pi = 160$ kHz to bring the trapped ions into resonance. This requires that we set $V = md^2\omega_z^2/q = (0.3 \text{ Volt } e/u) \times m/q$. In our 8.5 Tesla magnetic field an ion with $m = 1$ u and $q = e$ has a cyclotron frequency of $\omega_c/2\pi = 131$ MHz. Thus a typical atomic or molecular ion with $m/q \approx 40$ u/e has $\omega_c/2\pi \approx 3$ MHz, and a magnetron frequency $\omega_m \approx 4$ kHz, and we have the hierarchy of mode frequencies

$$\omega_c' >> \omega_z >> \omega_m \tag{2.12}$$

necessary for precision measurements. This hierarchy of mode frequencies 2.12 has the consequence that ω_z and ω_m do not need to be measured to as high precision as ω_c'. See Table 2.1.

From the invariance relation Eq. 2.11 it is easy to derive the result that

$$\frac{\Delta\omega_c}{\omega_c} = \left(\frac{\omega_z}{\omega_c}\right)^2 \left(\frac{\Delta\omega_z}{\omega_z}\right) \tag{2.13}$$

Clearly (and especially for heavy ions with low ω_c) axial frequency fluctuations (due for example to instability and fluctuations in our trap voltage source) can be a significant source of uncertainty in the measured free-space cyclotron frequency ω_c. More generally, any electric field variations at the location of the ion being measured (such variations may be caused by the Coulomb field of contaminant ions, etc.) can cause significant variations in the measured ω_c if they shift ω_c' and ω_z.

2.2 Measurement Techniques

2.2.1 Introduction

We measure mass to accuracies of parts in 10^{10} by making relative mass ratio measurements via cyclotron frequency ratio measurements. By linking our mass ratios directly and indirectly to ^{12}C we obtain absolute atomic masses, since ^{12}C is the reference for the atomic mass system, defined to have a mass of exactly 12 u, where u is the atomic mass unit.

The following sections describe the methods we use to trap, isolate, cool and detect single ions, and then measure their cyclotron frequencies.

2.2.2 Making and Trapping Ions

We make ions by ionizing neutral atoms within the volume of the trap with an electron beam emitted from a field emission point mounted below the trap. By adjusting the beam current ($\sim$20 nA) and the amount of gas injected we can make a cloud containing a small number of (< 5) ions. (As shown in Appendix A, we can determine the number of ions in the trap by measuring the linewidth of the detected axial signal.)

The Coulomb field of a contaminant ion of charge q a distance r from the ion of interest will cause cyclotron frequency shifts of the order of:

$$\delta\omega_c' = \frac{1}{4\pi\epsilon_0}\frac{q}{r^3}\frac{1}{B} \tag{2.14}$$

This gives a fractional frequency shift $\Delta\omega_c'/\omega_c' \sim 10^{-9}$ for $r \sim 1$ mm. Thus we are unable to make precision measurements unless we have just one ion in the trap, so we need to rid the trap of contaminant ions without expelling the ion of interest. This is particularly necessary when we make large molecular ions like $C_5H_6^+$, since they can fragment in many different ways when ionized, and when we multiply ionize atoms to make ions like Cs^{+++}, since we will inevitably make large clouds of lower-charge-state ions. We expel unwanted ions from the trap by exciting their axial motions with either broadband noise excitation (for the case of unknown contaminant ions) or narrowband RF when we know the mass of the likely contaminants [BOY92]. The contaminant ions are thereby driven to large axial amplitudes. The ion of interest is cooled continually as described below, and so does not have a large axial amplitude. We then move the center of the ion cloud toward the lower endcap of the trap by applying an offset voltage to the endcaps. The contaminant ions in large orbits strike the lower encap, where they are neutralized and presumably stick. The desired ion has a small axial amplitude because it is continually damped and so it remains in the trap.

2.2.3 Tuning the Trap

We use guard ring electrodes mounted where the hyperbolic surfaces of the trap asymptote together to trim the electrostatic field and "tune" the trap for for a maximally harmonic axial resonance, necessary for precision measurements. The prescription for optimal tuning in the absence of charge patches is to set $V_{GR} = V_R/2$. We typically see deviations from this $\sim 10 - 30$ mV, which we ascribe to charge patches. We tune the trap by driving a trapped ion with a cw drive and sweeping through its resonance. If the trap is harmonic we see a symmetric Lorentzian profile for both sweep directions. If the trap is mistuned the lineshape becomes asymmetric and eventually hysteretic. We are easily able to discern changes in the lineshape for guard ring mistunings of as little as 0.1 mV.

2.2.4 Axial Detection

We detect the ion's axial motion using a DC SQUID (Superconducting Quantum Interference Device) coupled to the ion via a high-Q resonant transformer (Fig. 2-3). The detection system has a threefold purpose: it serves to detect, damp, and cool the ion's motion.

We use the image currents to detect the axial motion of the ion. (Although the

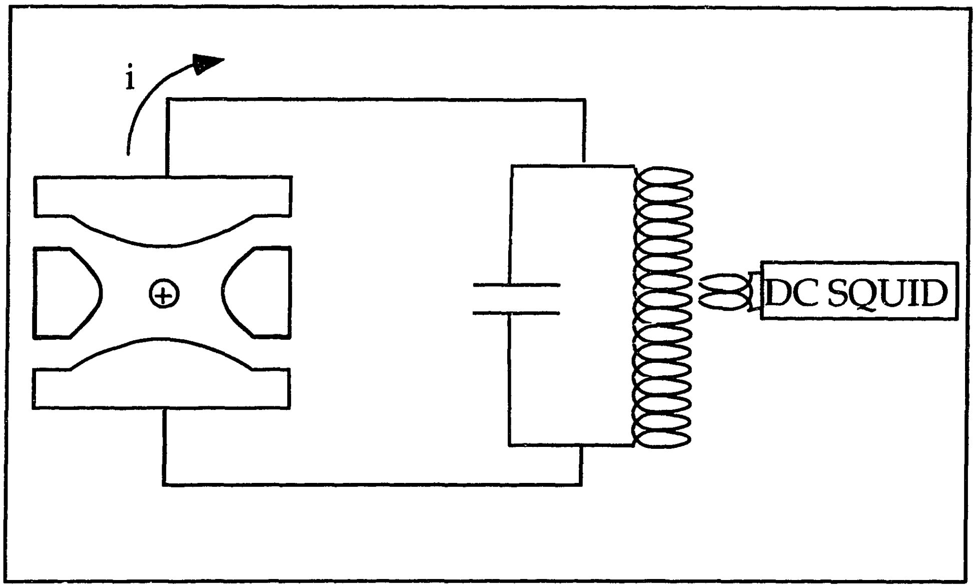

Figure 2-3: Schematic of ion detector system.

cyclotron mode can be detected this way, we choose to detect only the axial motion to avoid the inevitable damping and frequency shifts associated with detection.)

Image currents (Eq. 2.48) in the trap electrodes generate a current $I = Qi_{image}$ in the detector coil. We detect this current with a DC SQUID (Superconducting Quantum Interference Device) inductively coupled to the detector coil (see Fig. 2-4). A SQUID is a loop of superconductor broken by 1 (RF) or 2 (DC) tunnel junctions. SQUIDS rely on the Josephson effects, which are consequences of the phase-coherence of the Cooper-pair wavefunction around the loop. In a simple closed superconducting loop the QM phase around the loop must be multiple of 2π. Since the phase is related to the vector potential $\vec{A}$ this results in the quantization of the magnetic flux through the loop in units of 2×10^{-15} Wb, called the flux quantum or fluxon. This is an extremely small unit, and a SQUID's periodic response to flux changes of this size is the basis of its use as an amplifier. SQUIDs are basically magnetic field sensors, but they can also be configured as curent detectors by running current through a pickup loop coupled via mutual inductance to the SQUID loop.

Energy sensitvities are of the order of 10^{-30} J/Hz for DC SQUIDS. DC SQUIDs are extremely broadband devices with a usable bandwidth running from 1 Hz to 1 THz. (Thus the name "DC" is a misnomer.) We take advantage of this wide bandwidth

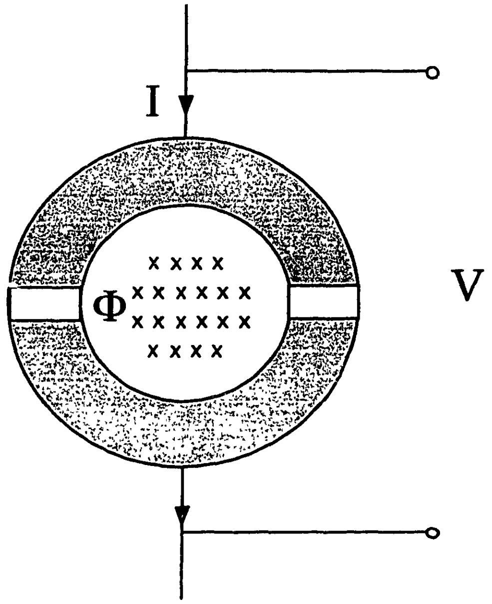

Figure 2-4: DC SQUID Schematic. The flux Φ through the SQUID loop is quantized in units of $h/2e = 2 \times 10^{-15}$ Wb.

by using relatively low axial frequency, which helps to reduce the influence of axial frequency perturbations on our cyclotron frequency measurements.

2.2.5 Measuring Cyclotron Frequency

With a single ion in a well-tuned harmonic trap we can make precision cyclotron frequency measurements. Unlike the axial motion, we do not directly detect the cyclotron motion; instead we use the mode coupling method outlined below.

In the usual Penning trap quadrupole field the cyclotron, axial and magnetron modes are orthogonal and uncoupled. We can excite (i.e. drive to a finite amplitude) any of these modes by applying an RF dipole field which is resonant (or nearly resonant) with the desired mode frequency. To excite the axial mode we apply an RF voltage at $\omega_{RF} \approx \omega_z$ across the trap endcaps; to excite either the cyclotron or magnetron mode we apply an RF voltage with $\omega \approx \omega_c'$ or ω_m across the upper guard ring electrode, which is split into two halves to allow a field to be applied horizontally across the trap. (Recall from Section 2.2.3 that the other use of the guard ring electrodes is to tune the trap.) Thus we have both spatial and frequency selectivity

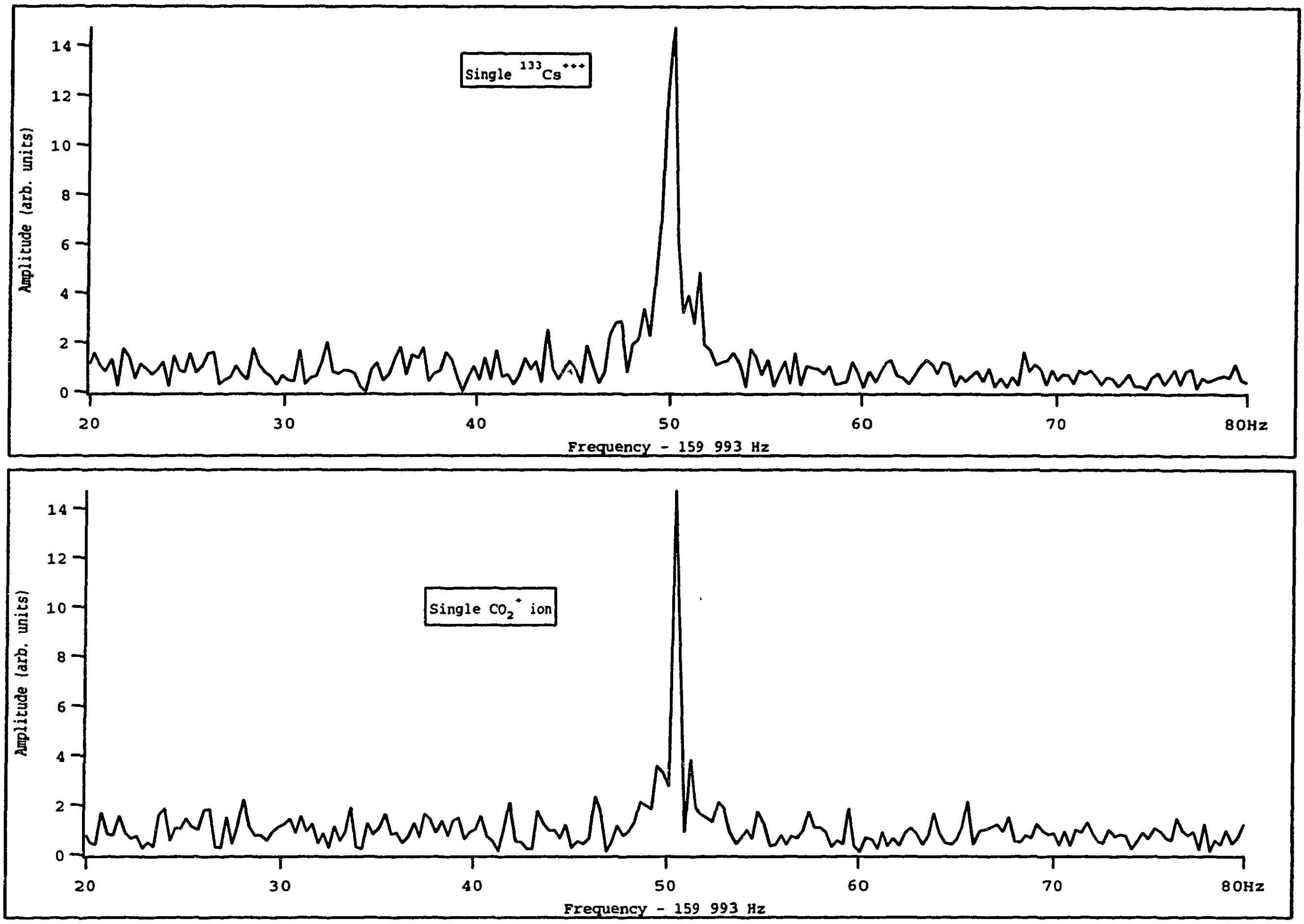

Figure 2-5: Axial signals of detected single Cs^{+++} and CO_2^+ ions. The width of the CO_2^+ is 1/3 of the width of the Cs^{+++} signal because of the q^2/m scaling of the ion damping rate (Eq. 2.63). The scaling of the linewidth with $q^2/m \propto N$ provides a way to determine the number of ions of known m and q in the trap.

distinguishing the modes. Additional fields can induce coupling between the modes. To measure the cyclotron mode amplitude and phase (normally undetected) we couple it to the detected axial mode. We apply an RF quadrupole field at frequency ω_{cpl} to couple the modes. In the presence of a coupling field at frequency ω_{cpl} the cyclotron and axial mode amplitudes are governed by the equation [CWP90]:

$$\begin{pmatrix} \dot{Z} \\ \dot{C} \end{pmatrix} = \begin{pmatrix} 0 & \frac{\Omega^*}{2} e^{-i\delta t} \\ -\frac{\Omega}{2} e^{i\delta t} & 0 \end{pmatrix} \begin{pmatrix} Z \\ C \end{pmatrix} \tag{2.15}$$

where $\delta = \omega_{cpl} - (\omega_c' - \omega_z)$ is the detuning of the applied drive from the mode coupling resonance frequency $(\omega_c' - \omega_z)$ and $\Omega \equiv ie\epsilon_p / 2m\sqrt{\omega_z \omega_c'}$ (where ϵ_p is the magnitude of the coupling field gradient) expresses the strength of the coupling in frequency units. Z and C are the classical actions $S \equiv \oint \vec{p} \cdot d\vec{q}$ of the modes. These are the same equations of motion as those obtained from the Schrodinger equation for the coupling of two quantum states by an oscillating field. The solution of this problem with the initial conditions $C(t = 0) = C_0$, $Z(t = 0) = 0$ is an oscillation of the amplitudes $Z(t)$ and $C(t)$ [RAM57]:

$$Z = \frac{|\Omega|}{\sqrt{|\Omega|^2 + \delta^2}} sin(\frac{1}{2}\sqrt{|\Omega|^2 + \delta^2 t}) \tag{2.16}$$

$C(t)$ being given by the condition that $|Z(t)|^2 + |C(t)|^2 = C_0^2$.

Thus we have a continual oscillation of amplitudes between the modes at a frequency $|\Omega| = 1/2\sqrt{|\Omega|^2 + \delta^2}$. When $\delta = 0$ (the "on-resonance" case) there is complete transfer of mode amplitudes at the *Rabi frequency* $|\Omega|$.

We use the Rabi oscillation between the coupled cyclotron and axial modes to detect or "read out" the amplitude and phase of the otherwise undetected cyclotron mode. By choosing $\delta = 0$ and a pulse duration $\Delta t = 1/2(2\pi/\Omega)$ we completely and *phase-coherently* transfer the cyclotron mode amplitude and phase to the axial mode where we detect it.

Practical use of this technique requires that we know $\omega_c'/2\pi$ to within ≈ 1 Hz and Ω to within $\approx 1\%$. Both ω_c' and $|\Omega|$ can be measured with the necessary accuracy

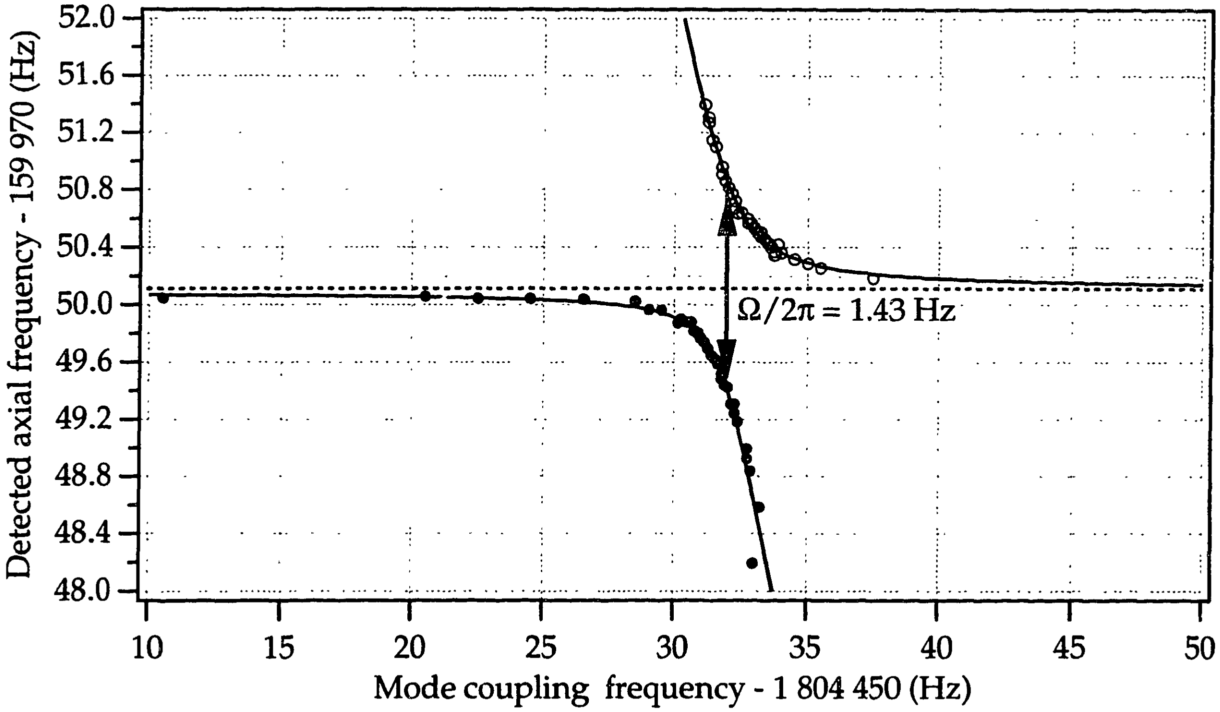

Figure 2-6: Cs^{++} avoided crossing. The solid and open circles are the axial frequencies of the coupled modes, plotted as a function of frequency ω_{cpl} of the applied coupling field. The solid lines are fits to the lineshape given by Eq. 2.17. The observed "mode splitting" $|\Omega| = 1.43$ Hz (obtained using a nominal drive of 1.5 Vpp) shows that we need to use a π-pulse time of 350 msec. The name "avoided crossing" comes from the formal similarity between the variation of mode frequencies and the variation of coupled quantum mechanical levels as a function of the coupling.

by mapping the variation of the frequencies of the axial components of the coupled modes when ω_{cpl} is varied. Solution of the normal modes of the Rabi problem in the presence of arbitrary detuning gives two modes with frequencies [CWP90]

$$\epsilon = -\delta/2 \pm \frac{1}{2}\sqrt{\delta^2 + |\Omega|^2} \tag{2.17}$$

Due to the presence of the coupling field, each mode is a combination of axial and cyclotron motion. When $\delta = 0$ the peaks are split by an amount equal to Ω. Thus finding the $\delta = 0$ point of the avoided crossing provides a measurement of Ω as well as $(\omega_c' - \omega_z)$.

Our measurements of $\omega_c' - \omega_z$ and ω_z from the "avoided crossing" method are accurate to $2\pi \times 0.05$ Hz, which would give measurements of ω_c' accurate to $\sim$ 10 ppb, clearly not sufficient for our purposes. To make high-precision measurements of $\omega_c'/2\pi$ with uncertainities we need to measure for longer times. We make precision measurements of ω_c' by using the above mode coupling method to measure the evolved trap cyclotron phase $\phi_c'(t)$ as a function of time t. We refer to this technique as the "Pulse-and-Phase" (PNP) method [CWP90]. The time derivative of $\phi_c'(t)$ is ω_c'. We measure the phase at time t by using a π-pulse to phase-coherently couple the trap cyclotron mode to the axial mode. A PNP sequence consists of the following three steps: start with an ion with its cyclotron motion cooled and drive the ion to a finite radius with an RF dipole electric field at frequency ω_c'; then let the ion evolve freely for time T; finally couple the ion's cyclotron motion to the axial mode for detection using a π-pulse. (Fig. 2-7) The dipole drive oscillator at ω_c' and the quadrupole coupling oscillator at $\omega_\pi \approx \omega_c' - \omega_z$ are obtained from signal generators locked to the same ovenized quartz crystal reference oscillator, as is the mixer at $\omega_z/2\pi - 50$ Hz which is used to mix the axial signal down to 50 Hz for data acquisition by our Macintosh IIci computer which is equipped with an MIO-16 data acqusiiton board. The action of the coupling π-pulse can be regarded as a mixer which mixes the cyclotron phase information from the trap cyclotron frequency ω_c' down to the axial frequency ω_z by exploiting the Rabi coupling of the center of mass modes of the ion. In a sense what we are really doing is tracking the evolution of the free-space trap cyclotron phase at frequency ω_c' with respect to the phase of the coupling drive plus the axial mixdown oscillator, evolving at a total rate of $\omega \equiv \omega_\pi + \omega_{mix}$, plus a constant offset phase due to the pi pulse (which will never be perfectly resonant). Of course, the constant offset phase is added on to all our cyclotron phase measurements, and so does not affect the determination of the trap cyclotron phase evolution frequency.

The ultimate precision of a PNP phase measurement is set by the phase measurement uncertainty and the evolution time T. For example, our typical phase measurement uncertainty of 10° and an evolution time $T = 50$ sec will give an uncertainty $10°/360° \times 3 \times 10^6 \times 50 = 1.9 \times 10^{-10}$ for a Cs^{+++} ion with $\omega/2\pi = 3$ MHz. Thus by going to longer phase evolution times we can increase the precision of the measurement indefinitely, in the absence of long-term frequency drift. The use of

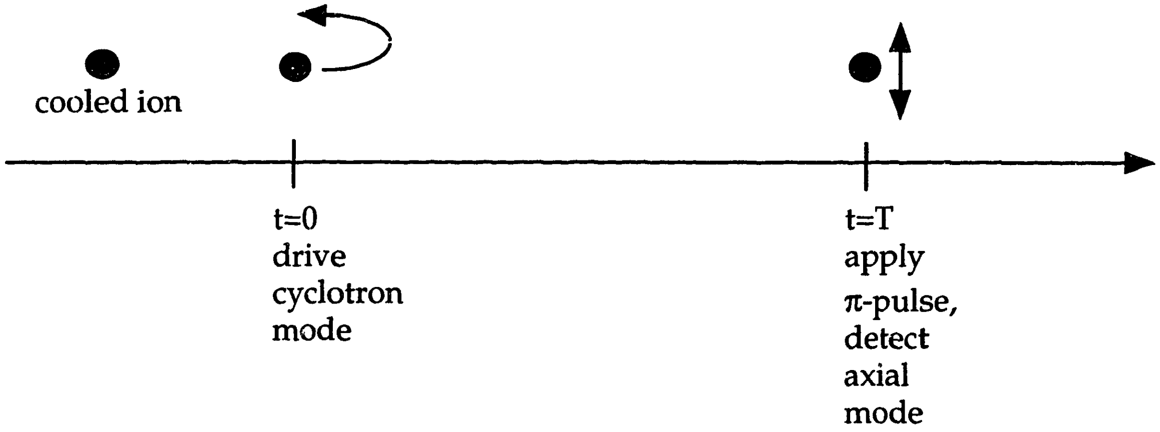

Figure 2-7: Pulse and Phase (PNP) sequence schematic

PNP method is complicated somewhat by the fact that phases can only be measured modulo 2π. This requires the use of intermediate-time points to track the phase evolution. More fundamentally, the precision of the measurement is limited by the maximum time T over which the phase drifts by $< 2\pi$. Our measured magnetic field drifts of ~ 1 ppb/h limit us to maximum phase evolution times $T \sim$ minutes. Fig. 2-8 shows the results of a fit to PNP data taken on a $C_5H_6^+$ ion.

The PNP measurement gives us a set of axial frequencies ω_z and trap cyclotron frequencies ω_c'. We use the invariance relationship 5.6 to reconstruct the true free-space cyclotron frequency ω_c from the measured ω_c' and ω_z. During a precision measurement, we do not measure the magnetron frequency ω_m accurately. Instead we use the measured ω_c' and ω_z in the formula [BRG86]

$$\omega_m = (\omega_z^2/2\omega_c')(1 + 9/4\sin^2\theta) \tag{2.18}$$

to obtain ω_m. The angle $\theta \approx 0.16°$ is the tilt of the trap with respect to the magnetic field axis. We obtain it by careful magnetron frequency measurements during the day.

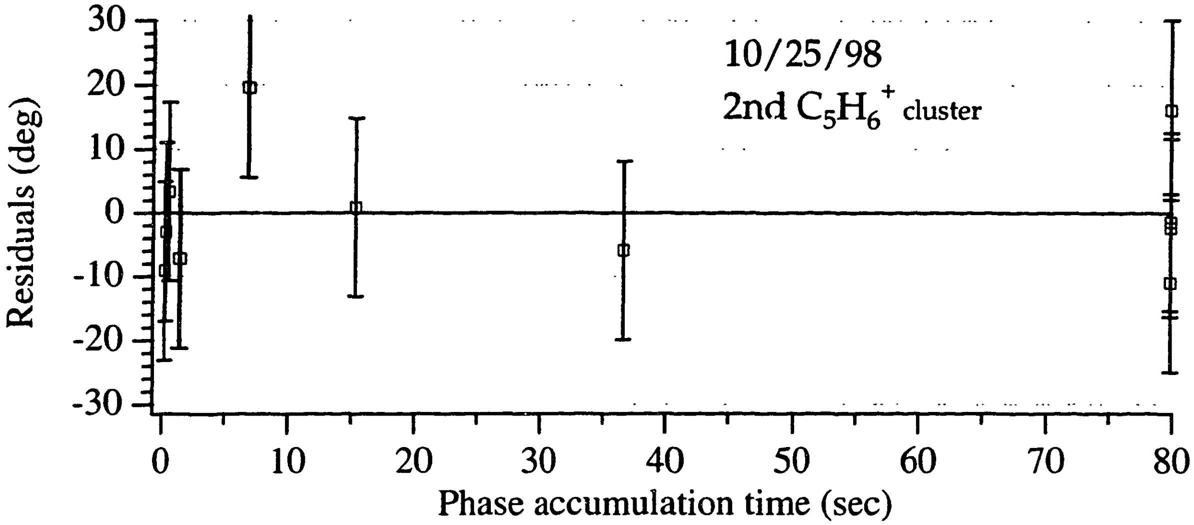

Figure 2-8: Results of a PNP measurement on a single $C_5H_6^+$ ion. Shown are the residuals from a fit to trap cyclotron phases $\phi_c'(t)$ measured using the PNP method with phase evolution times T = 0.250, 0.314, 0.585, 1.421, 6.914, 15.321, 36.613, 79.828, 79.828, 79.828, 79.828 sec. The short evolution times were chosen to ensure unambiguous "phase-unwrapping" so that a cycle is not missed when the frequency is determined. The long-time points with T = 79.828 sec give the high-precision measurements of ω_c'. We distribute the long-time phase measurements so that one comes at the beginning, one at the end, and the rest in the middle of the PNP sequence.

2.3 Deviations from the Ideal Penning Trap: Implications for Precision Measurement

2.3.1 Introduction

In the preceding sections I have outlined the basic physics behind our measurements. This is sufficient for a qualitative understanding of our method, but as with any precision experiment, the devil is truly in the details, the details being the host of small effects and imperfections which can systematically shift the measured frequencies away from their desired values. We use a combination of theory and measurement to combat these shifts either by measuring them, calculating them accurately and subtracting them from the measured results, or demonstarting that they are small enough to neglect. This section list discusses these effects in turn. All have been discussed previously but until our current measurements on multiply charged heavy ions the image charge and frequency pulling effects have been negligiblein our measurements.

2.3.2 Radius-Dependent Frequency Shifts: Field Imperfections and Relativity

The electric and magnetic fields in a real Penning trap experiment differ from those of the ideal Penning trap for various reasons. We can quantify the nonuniformities in our B field by the power series expansion:

$$\vec{B}(\rho, z) = B_0\hat{z} + B_1(z\hat{z} - \rho\hat{\rho}) + B_2\left[(\rho^2 - z^2/2)\hat{z} - z\rho\hat{\rho}\right] + \ldots \tag{2.19}$$

Superconducting magnets are typically "shimmed" using additional trim coils to reduce the magnitude of the inhomogeneities B_1, B_2, etc. Our magnet was last shimmed by Oxford Instruments engineer John Davidson in March 1993 using a 16 mm × 16 mm NMR probe. His measurement of an inhomogeneously broadened linewidth of 2.55 Hz with a center frequency of 55 MHz implied a final shimmed field inhomogeneity of < 50 ppb over a 1 cm^3 volume. However placing our trap made of diamagnetic copper in this field introduces inhomogeneities estimated to be ~ 5 ppm over this same volume [FLA87]. Thus we need to re-shim the field with an ion in the trap. Our most recent ion shimming procedure (August 1998) yielded final field inhomogeneities $B_1 = -134$ mG/cm$\rightarrow B_1/B_0 = -1.6 \times 10^{-6}$ cm^{-1} and $B_2 = -83.6$ mG/cm$^2 \rightarrow B_2/B_0 = 1 \times 10^{-6}$ cm^{-2}.

Just as the magnetic field is not perfectly uniform, the trap electrostatic field will never be a pure quadrupole. We can describe it by an expansion in Legendre polynomials [WEI88]:

$$\Phi(\vec{r}) = -\frac{V}{2} \sum_{l=0,2,4...}^{\infty} C_l r^l P_l(\cos\theta) + K \tag{2.20}$$

where the C_l are dimensionless and K is an unobservable arbitrary constant. The $l = 2$ term with $C_2 = 1$ gives the trap potential of Eq. 2.2. The higher-order electrostatic field imperfections arise from the truncation of the electrodes of the ideal Penning trap, imperfections in machining the hyperbolodial surfaces of the trap, and charge patches on the trap surface which displace and distort the equipotentials.

Calculations [GAB84] for our trap geometry give

$$D_4 \equiv V_R \frac{\partial C_4}{V_{GR}} = 0.11 \tag{2.21}$$

Measurements using swept drives give $D_4 = 0.076(4)$ [WEI88], while pulsed measurements of chirped ringdowns give $D_4 = 0.09(2)$ [COR90]. These two measurements agree with one another and the theoretical calculation if we allow for the uncertainty in absolute orbit size.

Using the result for our trap that

$$\Delta C_4 = 0.1 \Delta V_{GR}/V_R \tag{2.22}$$

we see that we can tune $C_4 < 10^{-5}$ by this method, for $V_R = 10$V.

For the moment we ignore any terms with odd reflection symmetry about the (ρ, θ) plane. Later we will see that charge patches on the endcap electrodes can give rise to such terms in the potentials, and displace ions from the geometrical center of the trap.

The relevance of these magnetostatic inhomogeneities and electrostatic imperfections is that they result in radius-dependent frequency shifts of the modes of the Penning trap, which can be conveniently summarized in matrix form [COR90], [BRG86].

$$\begin{pmatrix} \delta\omega_c'/\omega_c' \\ \delta\omega_z/\omega_z \\ \delta\omega_m/\omega_m \end{pmatrix} = D \begin{pmatrix} \rho_c^2 \\ a_z^2 \\ \rho_m^2 \end{pmatrix} \tag{2.23}$$

where $D =$

$$\begin{bmatrix} -\frac{1}{2}\frac{B_2}{B_0} - \frac{\omega_c'^2}{2c^2} + \frac{3\omega_m C_4}{2\omega_c' d^2} & \frac{1}{2}\frac{B_2}{B_0} - \frac{3\omega_m C_4}{\omega_c' d^2} & -\frac{1}{2}\frac{B_2}{B_0} - \frac{3\omega_m C_4}{\omega_c' d^2} \\ \frac{\omega_c'}{4\omega_m}\frac{B_2}{B_0} - \frac{\omega_c'^2}{4c^2} - \frac{3C_4}{d^2} & \frac{3C_4}{4d^2} & \frac{1}{2}\frac{B_2}{B_0} - \frac{3C_4}{2d^2} \\ \frac{\omega_c'}{2\omega_m}\frac{B_2}{B_0} - \frac{\omega_c'^2}{2c^2} - \frac{3C_4}{d^2} & -\frac{1}{2}\frac{B_2}{B_0} + \frac{3C_4}{d^2} & \frac{1}{2}\frac{B_2}{B_0} - \frac{3C_4}{2d^2} \end{bmatrix}$$

(2.24)

We use the frequency shifts to measure the leading-order B_2 and C_4 field imperfections and reduce them as much as possible. We measure B_2 by measuring the "bottle shift" of the axial frequency (the cyclotron-radius dependent axial frequency shift). For a light ion this is the dominant cyclotron radius-dependent axial frequency shift. By adjusting the current in the shim coils of our magenet we can reduce the measured magnetic field inhomogeneity. Fig. 2-9 show the result of our most recent magnet shim with a C^+ ion. After shimming we had $B_2 = -83.6$ mG/cm^2.

2.3.3 Frequency Pulling

The correct axial frequency ω_z to be used in Eq. 2.11 is the value due to the quadrupole trapping potential, the radial component of which is responsible for the magnetron mode and the "downshifting" of the trap cyclotron frequency. The addi-

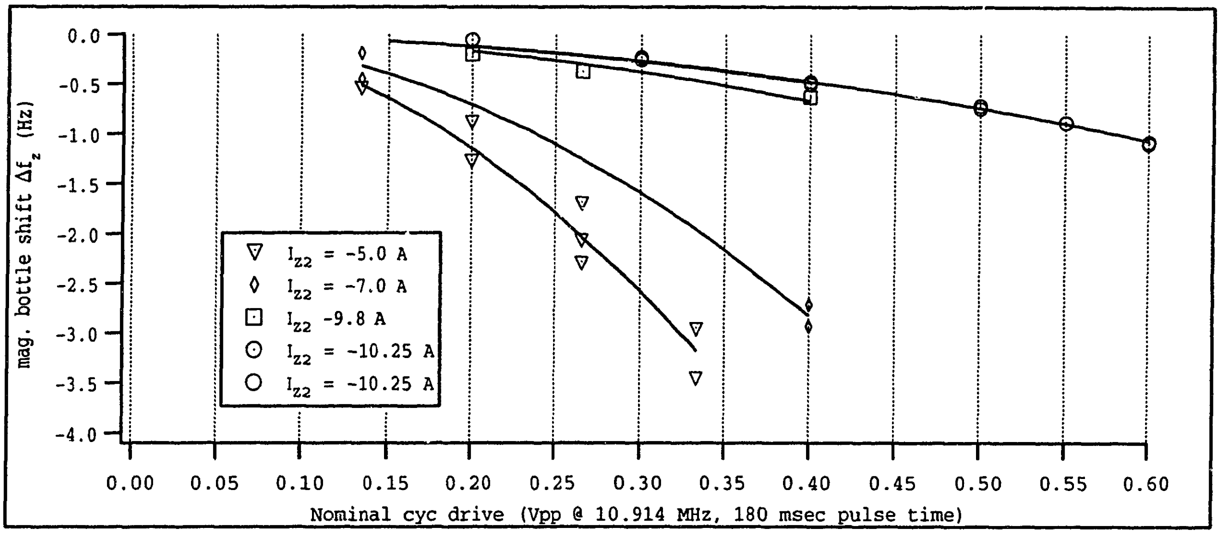

Shim results (C^+ ion, linear cyc drives)
(8/20/98 and 2/16/99)

I_{z2} = -5.0 A Δf_z = -28.59 +/- 1.14 Hz/V_{pp}^2
I_{z2} = -7.0 A Δf_z = -17.65 +/- 0.61 Hz/V_{pp}^2
I_{z2} = -9.8 A Δf_z = -4.20 +/- 0.35 Hz/V_{pp}^2
I_{z2} = -10.25 A Δf_z = -3.03 +/- 0.44 Hz/V_{pp}^2
I_{z2} = -10.25 A Δf_z = -2.96 +/- 0.43 Hz/V_{pp}^2

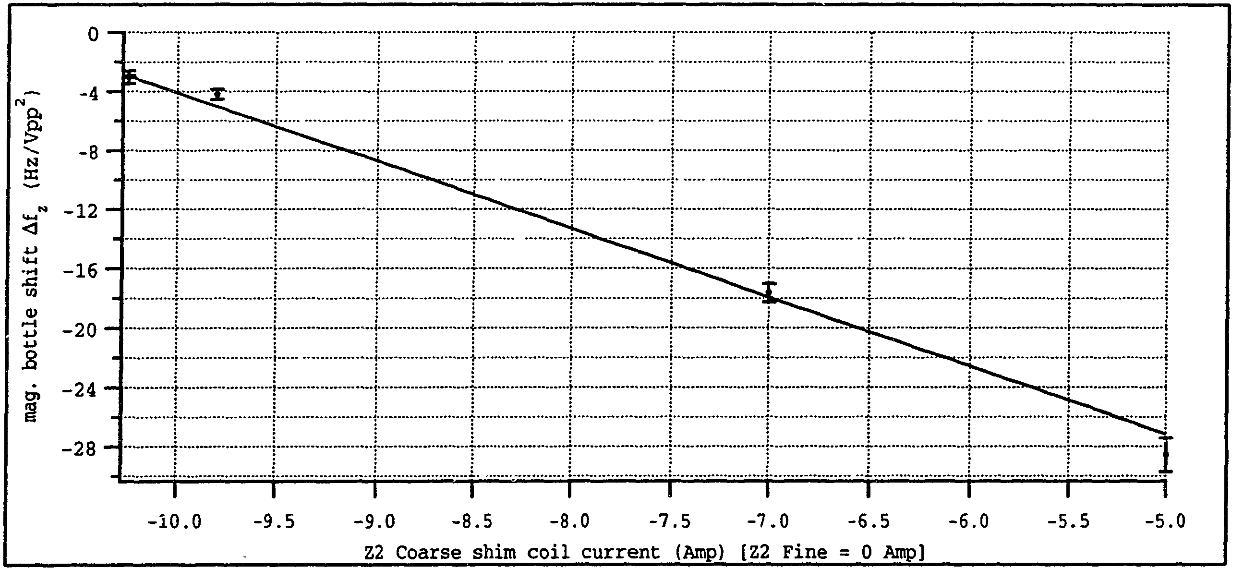

Fit: $\Delta f_z = (-50.3 - 4.62 \times I_{z2C})$ Hz/Vpp^2
compare -4.62 (Hz/V_{pp}^2)A^{-1}
with Oxford shim coil strength = 0.153 G/cm^2 to get:
ρ_{cal} = 416 +/- 12 µm for C^+, 1 V_{pp} x 180 msec drive

Figure 2-9: B_2 shimming results.

tional shift in ω_z due to the ion's interaction with the tuned circuit of the detector must be subtracted from the measured ω_z before use in Eq. 2.11 or the value of ω_c obtained will be incorrect.

We show in Appendix A (following Weisskoff [WEI88]) that the ion's axial frequency ω_z is "pulled" by its coupling to the detector coil parallel resonant circuit. This results in the following measured axial frequency ω_z^{meas}:

$$\omega_z^{meas} = \omega_z^0 + \frac{1}{4}\gamma_0\gamma_z \frac{(\omega_z - \omega_0)}{(\omega_z - \omega_0)^2 + (\gamma_0/2)^2} \tag{2.25}$$

where ω_z^0 is the axial frequency which would be measured in the absence of frequency pulling. See Fig. 2-10 for an experimental measurement of this effect.

For ions nearly in resonance with the coil ($\omega_z \approx \omega_0$) we have the approximate result:

$$\Delta\omega_z = \omega_z^{meas} - \omega_z^0 \approx (\gamma_z/\gamma_0)(\omega_z - \omega_0) \tag{2.26}$$

near resonance, where ω_0 and $\gamma_0/2\pi$ are the detector circuit resonance frequency and FWHM. For the heavy multiply-charged ions Cs^{++}, Cs^{+++} and Rb^{++} and the coil $Q \approx 50000$ used in 1998-99 the axial frequency shift due to pulling is large ($\gamma_z/\gamma_0 = 0.12$ for Cs^{+++}) and caused significant relative shifts in the low cyclotron frequencies.

2.3.4 Image Charge Shifts

In the presence of conducting boundaries a charged particle experiences an electric field

$$\vec{E}_{TOT} = -\vec{\nabla} V_{trap} + \vec{E}' \tag{2.27}$$

where V_{trap} is the electric potential due to the potentials of the various conducting surfaces, and $\vec{E}'$ is the electric field produced by the effective image charges which enforce the boundary condition that the electric field be everywhere perpendicular

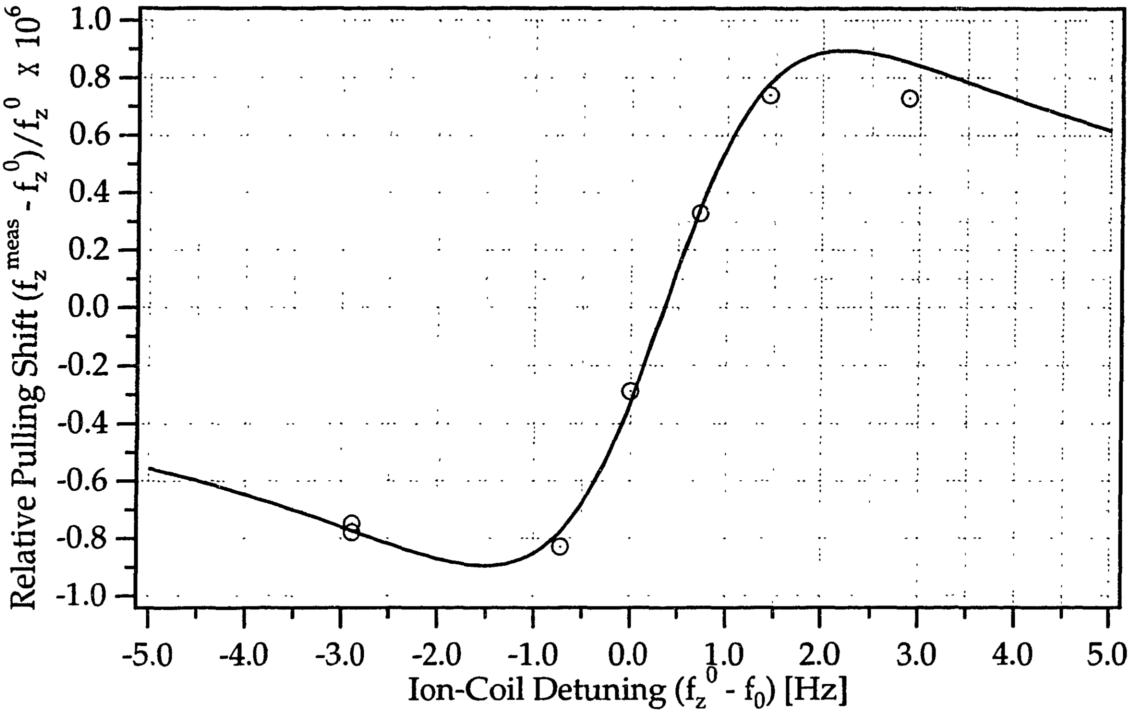

Figure 2-10: Experimental Measurement of Frequency Pulling

to the boundaries. Hence an ion in a trap feels a force due to its image charges in addition to the force due to the quadrupole field of the trap. This force attracts the ion toward the walls of the trap; thus it is an anti-trapping field. This additional image-charge field modifies the trap frequencies and must be taken into account to obtain the correct value of ω_c.

When the ion is displaced from the trap center (as is the case when we make measurements of the cyclotron frequency with an ion at finite cyclotron radius ρ) and the displacement is small in comparison with the characteristic trap dimension d, the image charge field may be treated to good approximation as a dipole field with terms:

$$\vec{E}'(\rho', z') \approx E'_\rho \frac{\rho'}{d}\hat{\rho} + E'_z \frac{z'}{d}\hat{z} \tag{2.28}$$

where (ρ', z') are the coordinates of the ion. For a spherical conducting boundary $E'_\rho = E'_z$, whereas for a general cylindrically symmetrical set of conducting boundaries $E'_\rho \neq E'_z$. Substitution of these additional terms into the trapping potential, and solution of the equations of motion gives the following modified trap frequencies (terms of order $(\omega_z/\omega_c')^2(\Delta_{\rho,z}/\omega_c')$ have been ignored):

$$\omega_z^2 = \omega_{z0}^2 - \Delta_z \tag{2.29}$$

$$\omega_m = \omega_{m0} + \frac{\Delta_\rho}{\omega_c'} \tag{2.30}$$

$$\omega_c' = \omega_{c0}' - \frac{\Delta_\rho}{\omega_c'} \tag{2.31}$$

where $\Delta_{\rho,z} \equiv qE'_{\rho,z}/md$. This modifies the invariance relationship (Eq. 5.6) to the following:

$$\omega_c^2 = \omega_{c0}'^2 + \omega_{z0}^2 + \omega_{m0}^2 + 2\Delta\rho + \Delta z \tag{2.32}$$

In analyzing the our cyclotron frequency data we use the invariance relationship with the measured frequencies and then subtract the quantity $\Delta\rho + 1/2\Delta z$ from the value of ω_c to compensate for the image charge effect.

It therefore remains to calculate the electric fields $E_{\rho,z}$. We have approached this problem in two different ways. Fred Palmer arrived at an approximate result for E_ρ' using a numerical relaxation technique to solve Laplace's equation for a charge displaced from the origin in the presence of the conducting trap electrodes. The image field is obtained from the numerical solution to the total field as follows:

$$\vec{E}' = -\vec{\nabla} V_{tot} - \frac{q}{|\vec{r} - \vec{r}'|^2} \tag{2.33}$$

This method is implemented by representing the trap and internal volume as a mesh of points and constraining the potential on the electrodes to be zero, and the potential on the mesh point containing the fixed charge to be $q/(h/2)$ where h is the mesh size, and then repeatedly setting each mesh point's potential to be the average of the potentials of the neighboring points (this is the finite-difference implementation of Laplace's equation) until convergence. The method makes the approximation that the potential on the surface of the charge's mesh point is simply the Coulomb potential due to that charge and neglects the image charge contribution, but this is reasonable in the case where the displacement of the ion charge from the origin is small compared with the trap dimension.

A different method for calculating the image charge shift was developed and implemented by James V. Porto. The following summary of the calculations is a condensation of notes prepared by Dr. Porto for future publication. The method relies on the observation that the image charge field can be obtained from the constraint that the net field due to the ion charge and the image charge must be zero on the conducting boundary. Thus if

$$G(\vec{r},\vec{r'}) = \frac{1}{|\vec{r}-\vec{r'}|} + F(\vec{r},\vec{r'}) \tag{2.34}$$

is the Green's function for the charge surrounded by the conducting boundary, we wish to find $F(\vec{r},\vec{r'})$, the term due to the image charge. Now we know that on the conducting boundary $G(\vec{r},\vec{r'}) = 0$. In practice we can enforce this condition numerically by demanding that

$$\int |G(\vec{r},\vec{r'})|^2 d\vec{\Omega} = 0 \tag{2.35}$$

where the integral extends over the conducting boundaries. Although at first this might appear to be a weaker condition, in fact it is not since $|G(\vec{r},\vec{r'})|^2$ is always ≥ 0, so it does not permit the oscillation of $G(\vec{r},\vec{r'})$ about the desired value of 0.

We can take advantage of the cylindrical symmetry of the trap and use the well-known result expressing the $1/r$ potential in terms of Legendre polynomials to write for G

$$G = \sum_{l=0}^{\infty} \sum_{m=0}^{l} 2^t \left[\frac{r'^l}{r^{l+1}} \frac{(l-m)!}{(l+m)!} P_l^m(\cos\theta') + r^l B_l^m(\vec{r'}) \right] P_l^m(cos\theta) cos(m\phi) \tag{2.36}$$

without loss of generality.

We can show that that each m term can be considered separately, and thus we need to solve

$$\int \left| \sum_{l=m}^{N} \left[2^t \frac{(l-m)!}{(l+m)!} \frac{r'^l}{r^{l+1}} P_l^m(cos\theta') + B_l^m(\vec{r'}) r^l \right] P_l^m(cos\theta) \right|^2 d\Omega \qquad (2.37)$$

The integral can be minimized by setting the derivatives with respect to the $B_k^m(\vec{r'})$ equal to 0, resulting in the set of $N-m$ linear equations

$$C_{kl} B_l(\vec{r'}) + D_{kl} r'^l P_l^m(cos\theta') = 0 \qquad (2.38)$$

where we have

$$C_{kl} = \int_S r^{l+k} P_l^m(cos\theta) P_k^m(cos\theta) d\Omega \qquad (2.39)$$

and

$$D_{kl} = 2^t \frac{(l-m)!}{(l+m)!} \int_S r^{k-l-1} P_l^m(cos\theta) P_k^m(cos\theta) d\Omega \qquad (2.40)$$

Thus by evaluating the integrals numerically on the conducting boundaries, and then solving the linear equations, we can determine the coefficients B_{lk}.

James Porto's calculation of the image charge shift using this Green's function/matrix inversion method gave values of 60.0 μHz/e and 33.1 μHz/e for the contributions of the radial and axial components of the image charge field, respectively. This is in reasonable agreement with Fred Palmer's relaxation method calculation of the image charge shift due to the radial component of the field, for which he computed a value of 57.8 μHz/e. These values are also consistent with the values measured and calculated for Van Dyck's trap, and as well as a simple spherical model of the trap [VMF89]. In Penning trap mass spectrometry experiments in which $\omega_c = \omega_c' + \omega_m$ is measured directly (most notably the time-of-flight mass spectrometers used in Stockholm and Mainz) the effect of the image charge shift cancels. In our experiment we need to correct our measured values of ω_c' for the image charge shift. The value of these corrections for our Cs, Rb, and Na measurements are given in Chapter 4, Section 4.10. The maximum relative shift caused by the image charge effect is 6×10^{-11}, for

Cs^{+++} and Cs^{++} Because the image charge frequency shift is an absolute frequency shift which depends only on the charge and not on the mass, the image charge effect only causes a differential frequency shift when ions of two different charge states are compared. Thus it was not an effect which was important for previous measurements in our apparatus, where we typically compared ions with equal charge states. (We did make measurements using Ar^{++}, for which the image charge shift is 4×10^{-11}).

2.3.5 Equilibrium Position Shifts

Charge patches on the trap electrodes will distort and displace the trap equipotentials; thus the equilibrium position of an ion in areal trap will not be at the geometrical center [WEI88]. In the presence of magnetic field inhomogeneities Eq. 5.8 different equilibrium positions will result in different cyclotron frequencies; thus the differing equilibrium positions are a potential source of systematic error [BOY92] [NAT93].

Displacements of the trap center will be due to electrostatic potential terms with odd symmetry. These terms are given by [WEI88]:

$$\Phi(\vec{r}) = -\frac{V_{LEC}}{2} \sum_{l=1,3,5...}^{\infty} C_l \left(\frac{r}{z_0}\right)^l P_l(\cos\theta) + K \tag{2.41}$$

where V_{LEC} is the electric potential on the lower endcap (the upper endcap is grounded). A potential on the lower endcap causes an ion to feel a force along the z axis [WEI88]:

$$\frac{qV_{LEC}}{2z_0}\left(C_1 - \frac{3}{2}C_3\frac{\rho^2}{z_0^2} + 3C_3\frac{z^2}{z_0^2}\dots\right) \tag{2.42}$$

which both displaces the ion axially and shifts ω_z quadratically. Fig. 2-11 shows a measurement of this quadratic frequency shift, which we interpret as evidence for an axially antisymmetric field component due to electrode charge patches. (We measured this V_{LEC} offset before and after a month of measurements on Cs^{+++} ions, and found it had changed by only 10%.)

By displacing the ion along the z-axis as above and measuring the resultant shift in the cyclotron frequency we were able to measure the B_1 component of the magnetic

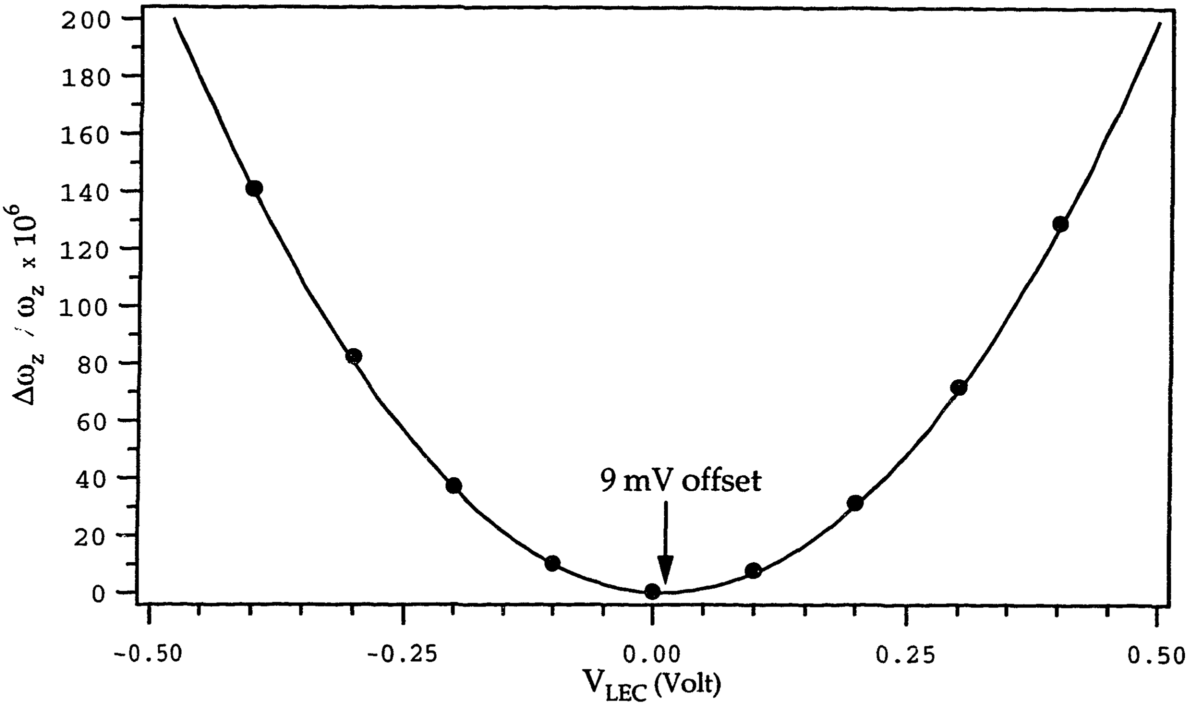

Figure 2-11: Experimental measurement of antisymmetric axial patch offset using a single trapped $C_2D_6^+$ ion. $V_R = -11.4547$ Volt. The parabola is offset by 9 mV because of the presence of a charge patch. From the curvature of the parabola we calculate $B_1B_3 = 0.219(1)$.

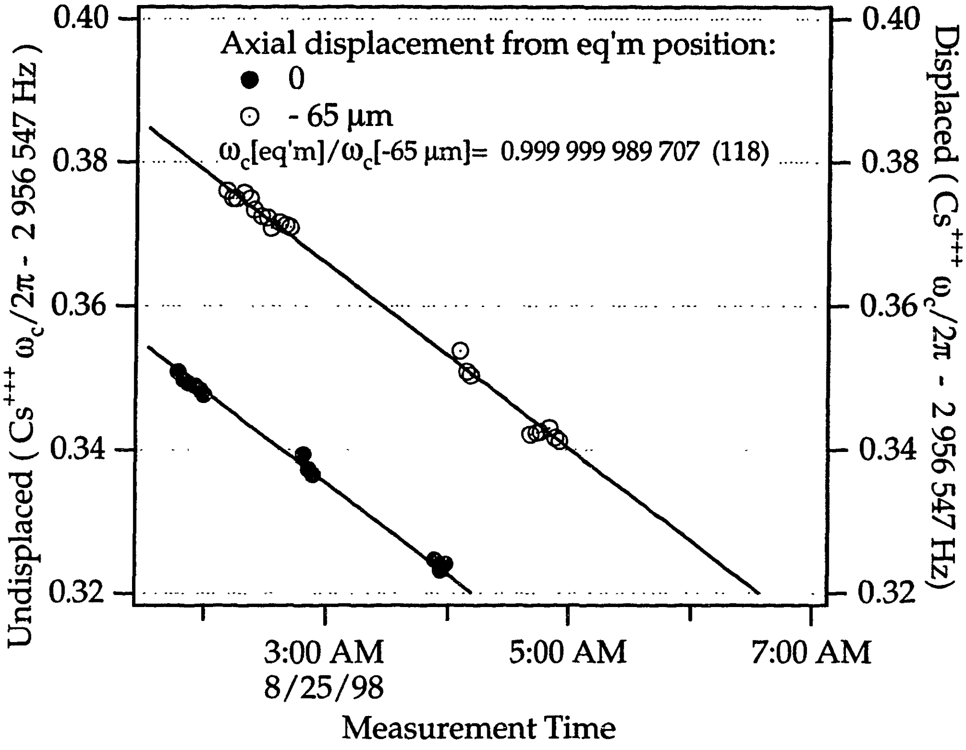

Figure 2-12: Measurement of linear magnetic field gradient B_1 using a Cs^{+++} ion. By measuring the cyclotron frequency shift due to an axial displacement of the ion, we measured $B_1 = -134(2)$ mG/cm.

field to be $B_1 = -134.0(1.5)$ mG/cm. (Fig. 2-12) In Chapter 4 Section 4.10 we use our values for B_1 and Δ to correct for the systematic frequency shifts caused by this effect.

2.3.6 Trap Tilt

Tilt of the trap axis with respect to the magnetic field axis by angle θ_m results in a modification of the trap magnetron frequency:

$$\omega_m = \frac{\omega_z^2}{2\omega_c'}\left(1 + \frac{9}{4}sin^2\theta_m\right) \tag{2.43}$$

We have measured the angle θ_m to be $\approx 0.16°$ by making careful magnetron measurements during the day It is interesting to note that the 3/16"= 0.48 cm clearance between the outer wall of our trap can and the magnet bore and the 175 cm length of our insert allows a maximum angle of arcsin(0.48/1.75) = 0.16°. Thus it appears that our trap can is butting up against one wall of the cryogenic bore, perhaps not an ideal situiation. (The likelihood of this possibility was pointed out by James Thompson)

2.4 Appendix A: Detecting, Damping and Cooling the Axial Motion

The process of ionization by an electron beam leaves ions with residual motional energy which must be damped away before a measurement. Furthermore, we need the ability to detect the tiny ($\sim 10^{-14} A$) currents induced in the trap endcaps by the ion motion. Our detector (Fig. 2-3), which consists of a DC SQUID coupled to the ion via a high-Q superconducting parallel resonant transformer (all at 4 K) accomplishes this.

Detection and damping are intimately related in the sense that any detector must extract some energy from the system to make a measurement on it. One might imagine detecting the ion's motion by the radiation from it as an accelerated charge. This radiation rate can be derived from the Poynting vector $\vec{S} = \vec{E} \times \vec{B}$ for the fields $\vec{E}$ and $\vec{B}$ derived from the Liénard-Wiechert potentials. For the case of a charge moving at velocities $<< c$ this radiation rate is given by (SI units) [PAP62]

$$\frac{dU}{dt} = -\frac{q^2 \ddot{\rho}^2}{6\pi\epsilon_0 c^3} \tag{2.44}$$

This gives a damping time τ

$$\tau = 3\pi\epsilon_0 \frac{mc^3}{q^2\omega^2} \tag{2.45}$$

For an ion with $m = 40$ u and $q = 1$ e, $\omega_c/2\pi \approx 3$ MHz and $\tau \sim 10^{13}\ sec \sim 500 \times 10^3$ years. Clearly the radiation rate is too low for practical damping or detection of the ion's motion.

We can rewrite Eq. 2.45 as

$$\gamma = \frac{1}{\tau} = \frac{1}{m}\left(\frac{e}{z_0}\right)^2 \frac{4\pi}{3}\sqrt{\frac{\mu_0}{\epsilon_0}}\left(\frac{z_0}{\lambda}\right)^2 \tag{2.46}$$

where $\sqrt{\mu_0/\epsilon_0} = 377\Omega$ is the "impedance of free space" [PAP62]. This form for $\gamma = 1/\tau$ indicates that the radiation rate is so low because the effective resistance presented by the environment $R_{eff} = \sqrt{\mu_0/\epsilon_0}(z_0/\lambda)^2 \approx 40\ \mu\Omega$ is tiny. In practice the radiation rate will be even lower than predicted by Eq. 2.46 because the conducting walls of the trap form a cavity with dimension $\sim$ 1 cm which does not support modes of the long wavelength ($\lambda = (3 \times 10^8$ m/s)/(3×10^6 Hz) = 100 m radiation from the ion's motion.

In order to damp the ion's motion and extract energy for detection in reasonable time, we need to increase the impedance it sees in the near field environment. Since the ion is nearly monochromatic in frequency this can be acheived quite effectively using a parallel resonant tuned circuit. Such a circuit with a high Q can present a very large impedance on resonance. By raising the impedance approx 15 orders of magnitude to $\sim$ 100 MΩ we reduce the axial damping rates to experimentally reasonable times $\sim$ 1 sec.

We damp and detect the ion's motion via the *net imbalance* of image charge which it induces on the upper and lower endcaps [WEI88]:

$$q_{image} = qC_1\left(\frac{z}{2z_0}\right) \tag{2.47}$$

where z is the ion's axial displacement from the center of the trap and $C_1 \approx 0.8$ [GAB84] is a factor expressing the fact that some of the field lines from the ion charge terminate on the ring electrode, rather than on either endcap. If the endcaps were planes extending to infinity and there were no ring electrode then C_1 would be 1 and moving the ion from $z = -z_0$ to $z = +z_0$ would cause a net change $\Delta q_{image} = q$, as we would expect.

The consequence of Eq. 2.47 is that an ion moving with axial amplitude a_z in our trap induces tiny image currents in the endcap electrodes:

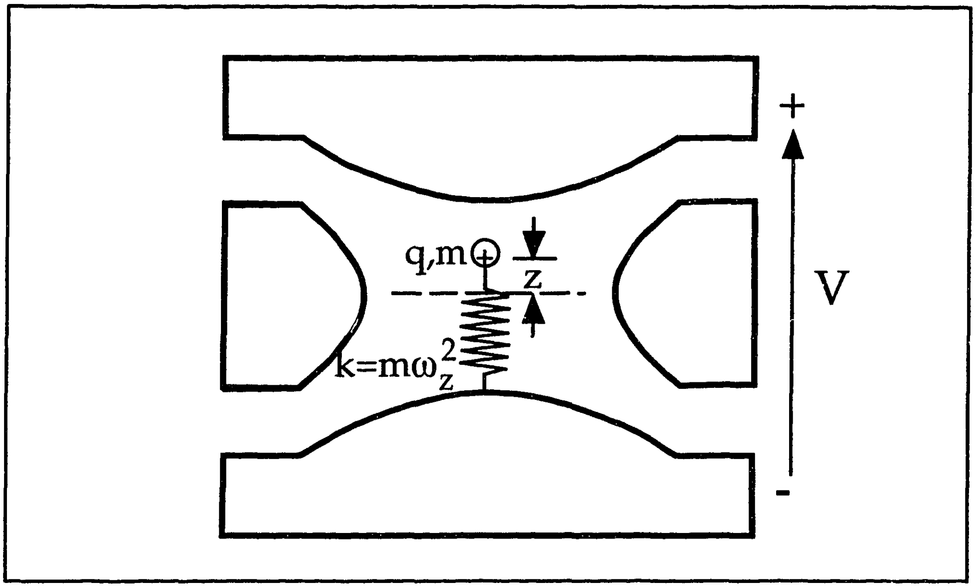

Figure 2-13: Mechanical model of ion axial oscillation

$$i_{image} = qC_1 \left(\frac{\dot{z}}{2z_0}\right) \approx qC_1 \frac{\omega_z a_z}{2z_0} \sim 10^{-14}\text{A for } a_z \approx 0.1z_0 \tag{2.48}$$

In order to understand the detection it is extremely useful to model the ion's motion by an equivalent electrical circuit. This allows us to use the circuit-theory concept of impedance to understand the ion-detector coupling.

The differential equation for the axial motion of the trapped ion (Fig. 2-13) is

$$\ddot{z} + \omega_z^2 z = \frac{F_{ext}}{m} = \frac{qC_1 V}{2z_0 m} \tag{2.49}$$

where F_{ext} is the force due to the electric field from the antisymmetric voltage V across the trap. Following [WID75] we propose the series lc circuit model of Fig. 2-14 for which $V = V_l + V_c$ gives:

$$l\frac{d^2 i}{dt^2} + \frac{1}{c} i = \dot{V} \tag{2.50}$$

If we differentiate Eq. 2.49 with respect to t and substitute $\dot{z}$ from the time derivative of Eq. 2.47, we get

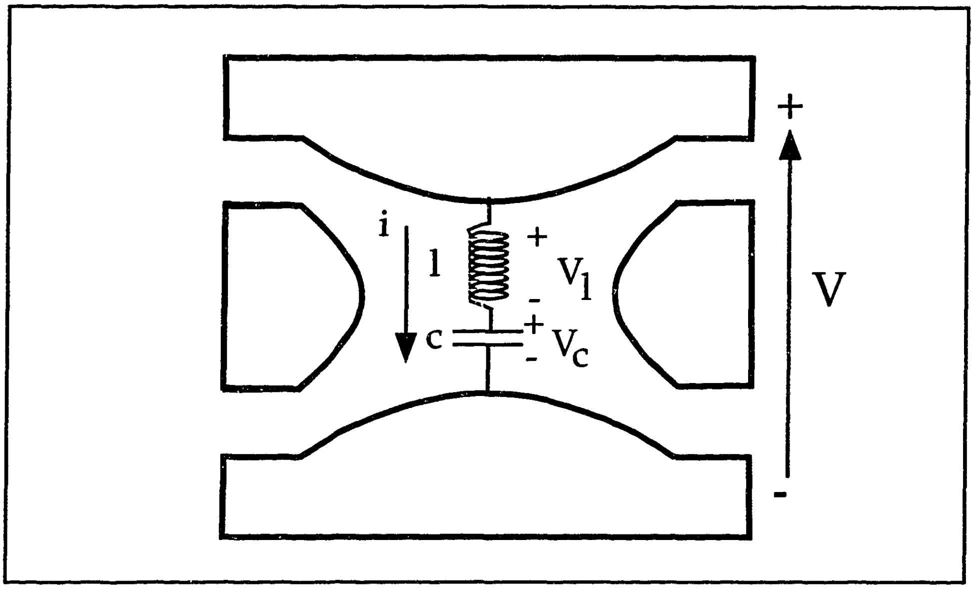

Figure 2-14: Electrical equivalent model of ion axial oscillation

$$m\left(\frac{2z_0}{qC_1}\right)^2\frac{d^2i}{dt^2}+\left(\frac{2z_0}{qC_1}\right)^2 m\omega_z^2 i=\dot{V} \tag{2.51}$$

Matching coeffcients in Eq. 2.51 with Eq. 2.50 gives us the expressions for the equivalent electrical circuit elements needed to model the ion axial motion:

$$l=\frac{m}{q^2}\left(\frac{2z_0}{C_1}\right)^2 \qquad \text{and} \qquad c=\frac{1}{l\omega_z^2} \tag{2.52}$$

For $m = 40$ u, $q = 1$ e, $l \sim 6 \times 10^8$ H and $c \sim 1.7 \times 10^{-15}$ F. Note that because the radiative damping level is negligible, there is no intrinsic damping term in the differential equation for the ion's axial motion; damping will be solely a consequence of coupling to the detector.

Modelling the detector tuned circuit as another electrical oscillator and writing the differential equation for the coupling gives:

$$\frac{d^4z}{dt^4}+\frac{1}{\tau}\frac{d^3z}{dt^3}+(\omega_0^2+\omega_z^2+\omega_l^2)\frac{d^2z}{dt^2}+\frac{\omega_z^2}{\tau}\frac{dz}{dt}+\omega_0^2\omega_z^2 z=0 \tag{2.53}$$

(where $\omega_l^2 \equiv 1/lC$). This fourth-order differential equation is complicated and gives little physical insight. Fortunately, we can successfully model important features of

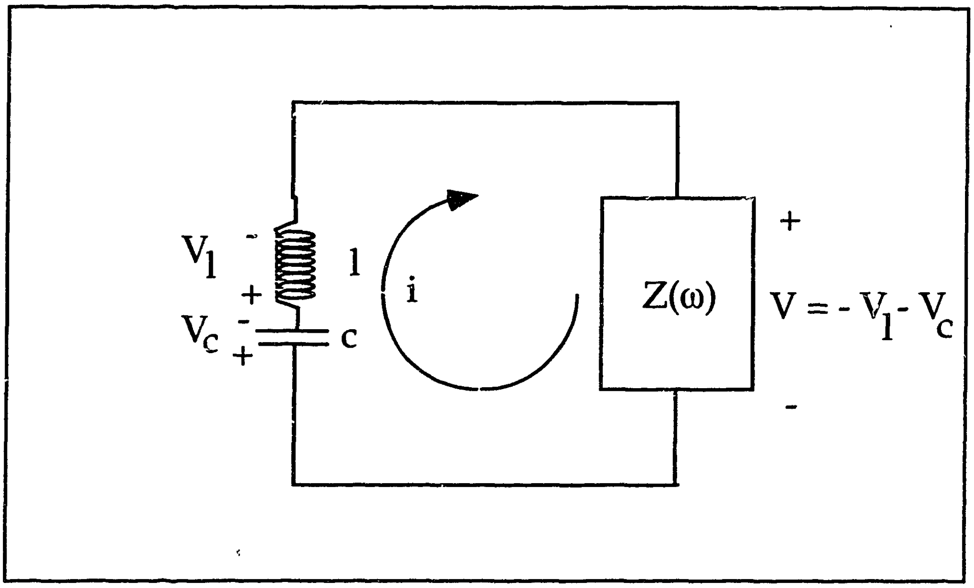

Figure 2-15: Coupling of ion and detector modeled using circuit theory.

the ion-detector coupling by modelling the detector as a complex impedance $Z(\omega)$. This approach was first suggested by James Thomspon. Figs. 2-15 and 2-16 illustrate this approach. Note that the parallel resistance $R \equiv Q\omega_0 L$ in the tuned circuit model for the detector is a fictitious resistance which models the lumped effect of all the loss mechanisms in the coil which give rise to its Q [NGU98]. Use of this model gives an expression for the damping rate of the ion's axial motion as well as a frequency shift due to the ion-detector coupling.

We write Kirchoff's voltage law $V = -V_l - V_c$ for the circuit of Fig. 2-15 we obtain the following equation:

$$\frac{d^2i}{dt^2} + \frac{Z}{l}\frac{di}{dt} + \frac{1}{lc}i = 0 \qquad (2.54)$$

We use the Ansatz $i = I_0 e^{j\tilde{\omega}t}$ to solve the equation; note that $\tilde{\omega}$ may be complex. (We neglect the $e^{-j\tilde{\omega}t}$ solution because it gives the wrong sign for reactive impedances.) From this we obtain the characteristic equation:

$$\tilde{\omega}^2 - \frac{jz}{l}\tilde{\omega} - \frac{1}{lc} = 0 \qquad (2.55)$$

which has the solution

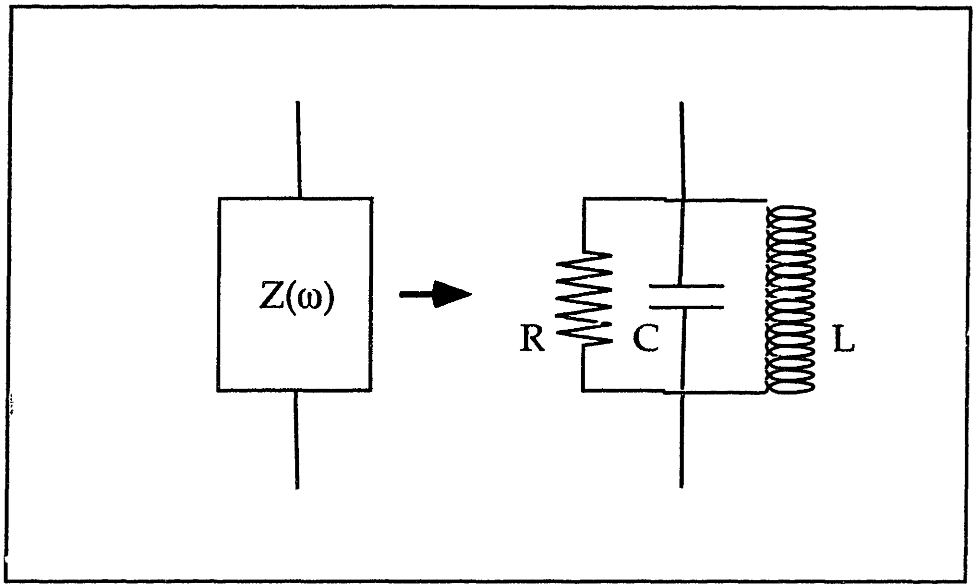

Figure 2-16: Impedance of front-end of detector circuit. Note that $R \equiv Q\omega_0 L$ is not a real circuit element; rather, it is a fictitious resistance which mimics the effect of all the various loss mechanisms which result in the coil's observed Q.

$$\tilde{\omega} = \frac{jZ}{2l} \pm \omega_z^0 \sqrt{1 - \frac{Z^2}{4(\omega_z^0)^2 l^2}} \tag{2.56}$$

where $(\omega_z^0)^2 \equiv 1/lc$ is the unperturbed axial frequency.

Consideration of orders of magnitude allows us to drop the $Z^2/4(\omega_z^0)^2 l^2$ term in our case because the detector impedance has its maximum value $Q\omega_0 L \approx 10^8\ \Omega$ at $\omega = \omega_0$.

$$\frac{Z^2}{4(\omega_z^0 l^2)^2} \sim \left[\frac{Q\omega_0 L}{\omega_z^0 l}\right]^2 = \left[\frac{10^5 \times 10^{-2}\mathrm{H}}{10^8\mathrm{H}}\right]^2 = 10^{-10} \tag{2.57}$$

Thus we get the approximate characteristic equation:

$$\tilde{\omega} = \pm\omega_z^0 + \frac{jZ}{2l} \tag{2.58}$$

Insertion of the correct form for $Z(\omega)$ will allow us to derive the ion damping rate as a function of detuning, as well as the frequency pulling effect. The parallel resonant cirucit front-end of the detector (Fig. 2-16 has impedance

$$Z = (j\omega L)\frac{1}{(1-\omega^2 LC) + j(\frac{\omega L}{R})} \tag{2.59}$$

Making the standard narrow-resonance approximation and rationalizing gives us

$$Z = (j\omega_0 L)\left(\frac{\omega_0}{2}\right)\frac{(-\Delta\omega) - j(\gamma_0/2)}{(\Delta\omega)^2 + (\gamma_0/2)^2} \tag{2.60}$$

Insert into 2.58

$$\tilde{\omega} = \pm\omega_z^0 - \left(\frac{\omega_0^2 L}{4l}\right)\frac{(-\Delta\omega) - j(\gamma_0/2)}{(\Delta\omega)^2 + (\gamma_0/2)^2} \tag{2.61}$$

Using the fact that $\gamma_0\gamma_z = (\omega_0/Q)(Q\omega_0 L/l) = \omega_0^2 L/l$ gives us

$$\tilde{\omega} = \pm\omega_z^0 + \frac{\gamma_0\gamma_z}{4}\frac{\Delta\omega}{(\Delta\omega)^2 + (\gamma_0/2)^2} + j\left(\frac{\gamma_z}{2}\right)\frac{(\gamma_0/2)^2}{(\Delta\omega)^2 + (\gamma_0/2)^2} \tag{2.62}$$

These are the same results obtained by Weisskoff using the more complicated and less transparent admittance method.

The flow of the image current through the real part of the detector impedance creats a back-emf which damps the ion's motion, giving it an on-resonance linewidth:

$$\gamma_z = \frac{Q\omega_0 L}{m}\left(\frac{qC_1}{2z_0}\right)^2 \tag{2.63}$$

For N ions in the trap, the center of mass motion is the same as for an ion of charge Nq and mass Nm. Thus the damped linewidth is proportional to $(Nq)^2/Nm \propto N$. This scaling of the linwidth gives us a way to count the number of ions in the trap.

As the ion is detuned away from the detector resonance, the damping time increases and there is also a frequency shift due to the ion coil interaction (discussed later).

Note that we only cool the axial motion directly. Cooling of the other modes by sideband coupling is discussed below.

Note the Johnson noise voltage across the detector tank circuit due to its finite (i.e. non-zero temperature) are $< V_n^2 >= 4k_\beta TR \times BW = 4k_\beta TQ\omega_0 L\gamma_z$, and that this fluctuating voltage excites the ion to a mean-square amplitude such that its final energy is $1/2m\omega_z^2 A_z^2 = k_\beta T$. Thus after any initial excitation dies away, the ion comes to equilibrium at the temperature of the coil. This is a particular example of the general fluctuation/dissipation theorem which states that any dissipative (i.e incoherent) process has associated with it random fluctuations.

2.5 Appendix B: Cyclotron Radius Calibration

Our measurements require the use of a finite non-zero cyclotron radius at which phase is accumulated, to ensure a reasonable signal-to-noise ratio for axial signal detection and readout after the π-pulse. This means that the cyclotron frequency we measure will always be shifted with respect to its free-space unperturbed value by the shifts in Eq. 2.23. Thus it is important to have a calibration of the cyclotron radius used in order to be able to calculate the size of cyclotron frequency shifts involved.

Our calibration is based on the results of measurements of the frequency shifts experienced by a C^+ ion as a function of cyclotron radius. By measuring these frequency shifts we were able to convert between our known cyclotron drive voltage and the cyclotron orbit size.

We drive the cyclotron motion of the ions with a resonant RF electric dipole field. The driven ion's cyclotron radius grows linearly with time at a rate which depends only on the strength of the driving electric field and not on the mass or charge of the ion. We can see why this is so by using the following simple argument. The impulse given to the ion is:

$$F\Delta t = m\Delta v = m\Delta(\rho_c\omega_c) \Rightarrow \Delta\rho_c = \frac{qE_d\Delta t}{m\omega_c}. \tag{2.64}$$

Integrating this from $t' = 0$ to $t' = t$ we get:

$$\rho_c = \frac{qE_d\Delta t}{m\omega_c}. \tag{2.65}$$

Thus we have the result:

$$\dot{\rho_c} \approx \frac{1}{2}\frac{qE_d}{m\omega_c'} \approx \left(\frac{qE}{m}\right)\left(\frac{1}{mqB}\right) = \frac{E_d}{B} \tag{2.66}$$

We have shown that the final radius achived by an ion driven by an RF electric field E_d resonant with its cyclotron frequency was proportional to the prodcuct of the electric field strength E_d and the pulse time t, and was independent of the mass, charge , or cyclotron frequency. Hence we know that ρ_c is linear in the drive field × pulse-time product, and that we can, for example, halve or double the radius by correspondingly adjusting $E_d t_d$. Generally speaking this allows us to adjust radii relative to one another. Ideally, however, we wish to know the cyclotron radius in units of metres. We term this an "absolute" calibration.

When we apply an RF drive voltage V_1 at frequency ω to the coaxial line leading down to our trap electrodes the ion feels an electric field V_2/d' where d' is a characteristic dimension fixed by our trap geometry, and $V_2 = T(\omega)V_1$ where $T(\omega)$ is the total transfer function of the electronics linking the drive port and the trap. Consequently the cyclotron radius achieved by a driven ion is given by the formula

$$\rho_c^B = \left(T(\omega_c)V_d t_d\right)\rho_{cal}^A \tag{2.67}$$

where ρ_c^B is radius of the driven ion B, V_d and t_d are the amplitude and duration of the applied RF voltage pulse in some convenient units (we choose V_{pp} and msec), $T(\omega)$ is the transfer function of the RF electronics between the drive oscillator and the trap, and ρ_{cal}^A is a calibrated radius measured for ion A by the means described below.

Note that $T(\omega_c)$ is normalized so that $T(\omega_A) = 1$. The only frequency depedence in this formula is in the transfer function. If a transfer function could be designed which was completely flat as a function of frequency, all ion species would be driven to the same radius by the same drive pulse, regardless of mass or charge.

A measurement of the relativistic shift

$$\left(\frac{\Delta\omega_c}{\omega_c}\right)_{rel} = -\frac{\omega_c'^2}{2c^2}\rho_c^2 \tag{2.68}$$

can be used to calibrate ρ_{cal} directly, since the only quantities involved are the measurable frequencies $\Delta\omega_c$, ω_c, and the known speed of light c. Thus it is immediately possible to convert a measured relativistic shift $(\Delta\omega_c/\omega_c)_{rel}$ to a corresponding radius ρ_c, so the calibration link between the drive pulse voltage-time product can be made.

Effective use of this measurement requires that it be made with a light ion, so that the relativistic shift will dominate the B_2 and C_4 shifts. For a light ion like $^{12}\mathrm{C}^+$ the C_4 shift is negligible, but the B_2 shift may be important. Fortunately the B_2 axial bottle shift of ω_z is

$$\frac{\omega_z}{\omega_z} = \frac{\omega_c'}{4\omega_m}\frac{B_2}{B_0}\rho_c^2 \tag{2.69}$$

provides a calibration-independent way to measure the effect of B_2 so that it may be subtracted from the measured radius-dependent cyclotron frequency shift to yield the part of that shift which is due to relativity.

By measuring both the B_2 bottle axial shift for $^{12}\mathrm{C}^+$ and the relativistic shift for a $^{12}\mathrm{C}^+$ ion we were able to arrive at the following radius calibration: $1 V_{pp} \times 1$ msec $\rightarrow$ $\rho_c = 5$ μm for $^{12}\mathrm{C}^+$ $(\omega_c/2\pi = 10.914$ MHz).

Chapter 3

New Spectrometer

3.1 Overview

In 1996 I designed and assembled the current MIT ICR apparatus (Fig. 3-1) with the assistance my postdoctoral colleague Dr. Fred Palmer, the MIT LNS shop led by Peter Morley, Steve the LNS welder, and two undergraduate assistants Mark Huang and Roland Nguyen. It is in principle a straightforward apparatus consisting primarily of a copper vacuum can containing the Penning trap, and is based on previous MIT lab apparatus designs [FLA87], [BOY92]. The vacuum can hangs in the bore of an 8.5 Tesla Oxford Instruments superconducting magnet. The entire apparatus is cooled by a liquid helium bath to 4 K. This serves the dual purpose of cooling the walls of the apparatus for effective cryopumping, and cooling our superconducting detector.

Running from the room-temperature end of the apparatus down to the vacuum can is a nonmagnetic stainless steel tube down which neutral atoms are injected for ion making. Within the trap they are ionized by an electron beam from a cryogenic tungsten field emission tip (custom manufactured by FEI Incorporated).

Running down along the inside diameter of the bore of the stainless steel tube is a 4-tube wiring harness through which are strung the the wires and coaxial cables which carry voltages and RF to the trap.

Our DC SQUID/superconducting coil ion detector is mounted in a niobium box approximately 1 m above the vacuum can. The ion current signal to be detected runs from the trap up to the detector though a cryogenic high-vacuum feedthrough and a rigid triaxial cable up to the detector box.

The following sections discuss different aspects of the apparatus in more detail.

3.2 Vacuum Seal

Making phase-coherent measurements on a single ion requires an extremely good vacuum. Our ability to trap a multiply-charged ion for hours indicates a very low probability of charge-exchange collisions and a pressure $< 10^{-14}$ Torr. We achieve such high vacuum because of the excellent cryopumping provided by our apparatus walls at 4 K. (This effective cryopumping can be a source of problems as well; once we accidentally dumped a large volume of CO_2 gas into the apparatus, where it promptly froze as dry ice on our field emission tip, rendering it useless as an electron gun and necessitating a warm-up of the entire apparatus.)

The trap and cryoelectronics stages are accessed by removing the copper vacuum can from the bottom of the apparatus. This can is sealed to the rest of the apparatus using a low-melting solder. The original choice of solder was indium (m.p. 157 °C), but we also experimented with Woods metal (a 50% Bi/ 27% Pb/ 13% Sn/ 10%Cd alloy, m.p. 70 °C). Although this is extensively used in cryogenic applications we were unhappy with its sealing properties and concerned by its propensity by to crystallize, which we feared would lead to voids and small leaks. We eventually turned to a more expensive and higher-melting temperature 52% In 48% Sn eutectic mixture (m.p. 118 °C), which has been completely reliable. During our various leak-sealing efforts we tried an Ivory-soap (TM) glycerol mix as a temporary leak seal; previous workers had used Kurt J. Lesker leak sealant. Although these do work as final kluges to seal tiny leaks, my experience was that they gunk up the joint and make soldering harder next time, so it is better to avoid them if possible.

Before cooling the apparatus down to 4 K we first pump it down to a pressure of $\leq 1 \times 10^{-6}$ Torr at 300 K. We used to bake out the vacuum can while pumping but we don't do this anymore because zinc outgasses readily from the brass screws

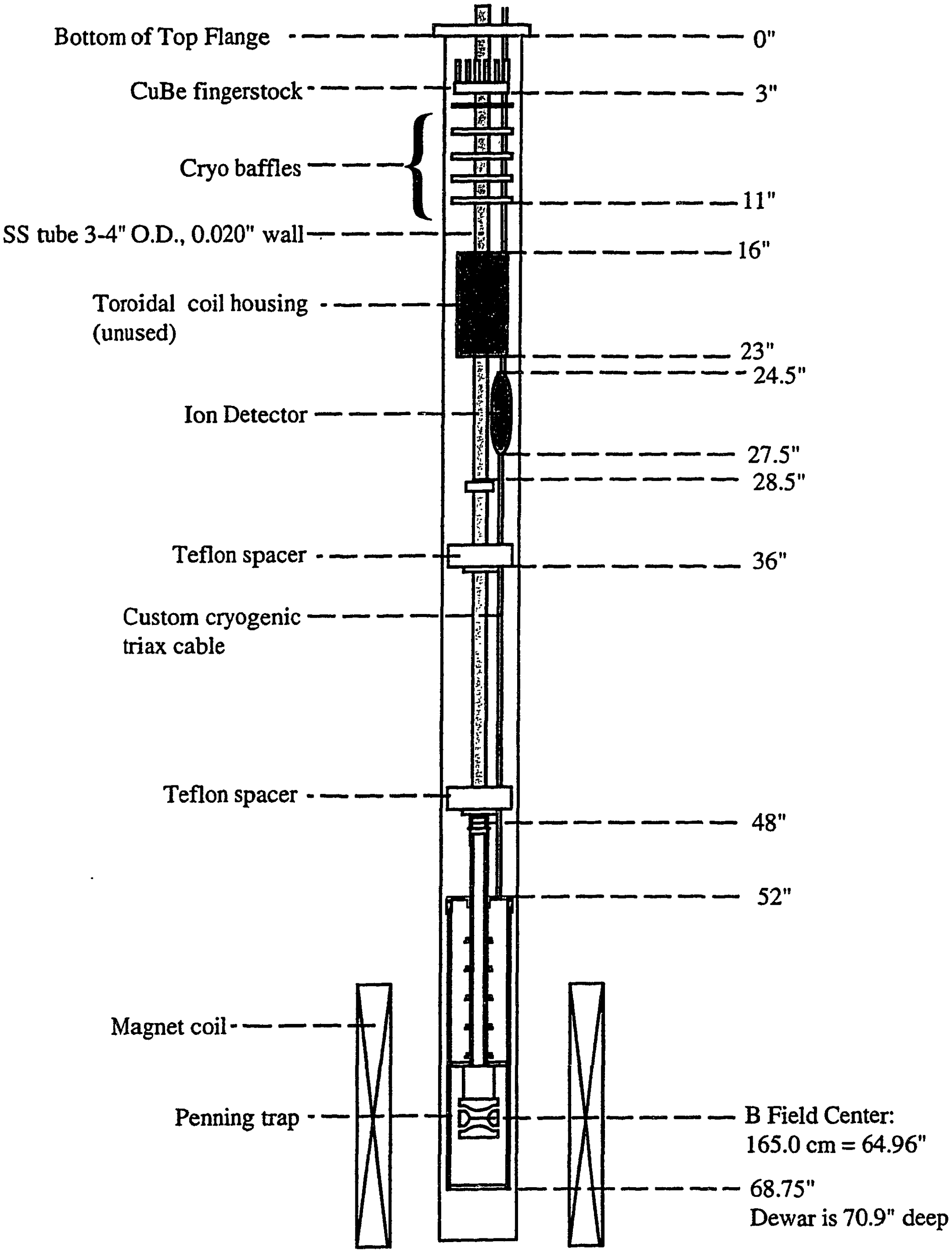

Figure 3-1: Schematic Drawing of Apparatus

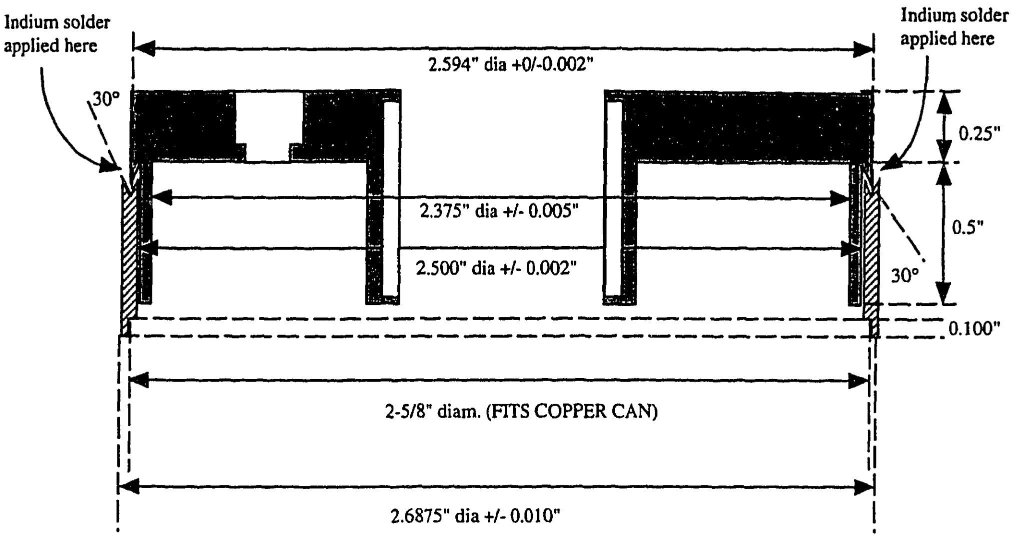

Figure 3-2: New brass tongue-in-groove indium solder joint.

used to fasten our cryoelectronics stages (even at temperatures as low as 50 °C) and we feared that the plating of zinc on our trap electrode surfaces might contribute to charge patches which would compromise the harmonicity of our trap.

Of course we cannot tolerate even a small leak in the portion of the apparatus which is immersed in liquid helium. Helium does not cryo-pump at 4 K, so a leak in the seals between the copper can and main tube will cause disaster. We experienced such a disaster with our old apparatus when the soft-soldered SQUID vacuum feedthrough was accidentally melted one day; all subsequent (and acrobatic) attempts to re-solder it were unsuccessful. Furthermore, the main can seal had by that time been soldered and unsoldered many times and was in pretty rough shape. After 3 months of unsuccessful re-sealing attempts (a lengthy process since we had to seal at 300 K, pump down, leak check, then cool to 4 K and leak check again) we decided to rebuild the apparatus. In the re-designed apparatus we replaced the original simple Cu-Cu butt seal with a more sophisticated tongue-in-groove seal (Fig. 3-2) made of harder brass which has worked like a charm and is capable of many more cycles. We also eliminated the original problem, the soft-solder seal on the SQUID vacuum feedthrough. Vacuum sealing has worked reliably ever since.

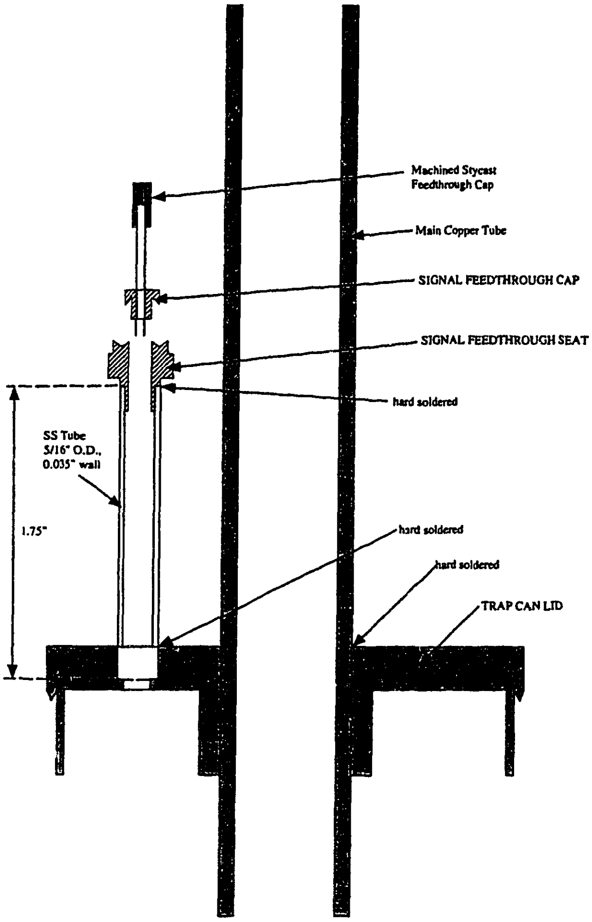

Figure 3-3: Cryogenic vacuum signal feedthrough assembly with bored Stycast epoxy feedthrough.

3.3 Vacuum Feedthrough

The ion axial signal from the trap runs up a short length of twisted pair and then passes through a vacuum feedthrough and runs up a triaxial line to the coil and DC SQUID which are housed in a niobium box about 1 m above the trap can. The vacuum feedthrough is made of Stycast epoxy preformed into a cyclinder and bored with two holes for the leads to run through (see Fig. 3-3). It is then sealed in place with more Stycast to make the vacuum seal. We have found this to be much more reliable than our old method of simple running wires through a glob of stycast. This feedthrough design was contributed by James V. Porto.

Table 3.1: Heat Conduction Budget for ICR Apparatus.

Item	Heat Load (W)
Main Stainless Steel tube (0.02" wall × 0.75" O.D.	0.053 W
6 32 AWG phosphor-bronze wires	0.001 W
3 stainless-steel coax cables	0.002 W
Total heat conduction:	0.056 W

3.3.1 Cryogenic Design

A low helium boiloff rate is always desirable in a cryogenic apparatus. Financially, minimizing the use of liquid helium ($\sim$ \$5/L at the time of this writing) makes sense. From a more fundamental point of view, a low boiloff rate means a low rate of thermal expansion of the apparatus, resulting in low rate of change of the magnetic field at the trap center due to its motion in field gradients.

We fill our apparatus with 4 L of liquid helium every 48 h (a boiloff rate of 0.083 L/h). The heat conduction budget of Table 3.1 shows that the main heat load is thermal conduction down the main stainless steel tube of the apparatus. (1 W boils 1.38 L of liquid helium per hour, so 0.056 W boils off 0.078 L/h).

3.4 Cryo-Electronics

Fig. 3-4 is a schematic of the low-temperature filter electronics used to filter the DC voltages and RF drive lines running to the trap.

A problem with the previous apparatus was that the cyclotron drive transformer had a sharp ($Q \approx 30$) resonance in its transfer function, which could lead to significant imbalances in drive voltage for ions with different cyclotron frequencies. It was originally thought that this was a cable resonance but in fact it was simply an LC parallel resonance in the transformer. In the new apparatus we spoiled the Q of this resonance by placing a metal-film resistor in parallel with the transformer. See Fig. 3-5. Knowledge of this transfer function is important for our cyclotron radius calibrations.

When we first assembled the new insert we tried using simple capacitive voltage dividers couple the RF drives to the trap. The advantage of these was their frequency-independent transfer function. However, during our attempts to debug stray pickup and oscillation problems with the DC SQUID we removed the capacitive dividers, thinking that they might be sources of stray capacitive coupling. We returned to using transformer coupling, which has worked very well.

3.5 Alkali Metal Loader and Detector

In order to make mass measurements on alkali metals we needed a way to load them into our trap. We needed only a relatively small amount of material but we had to be able to gate the source on and off quickly, and the source had to be as contaminant-free as possible. We found that SAES Getters brand Alkali Metal Dispensers (suggested to us by Chris Ekstrom) satisfied our requirements nicely. They are 1 cm long × 1 mm wide nichrome boats stuffed with an alkali metal chromate, for example $CsCrO_4$, and a special proprietary getter material and they are designed for the release of well-controlled amounts of contaminant-free alkali metal surfaces for the industrial production of photocathodes. We mounted the SAES getter source above the insert,

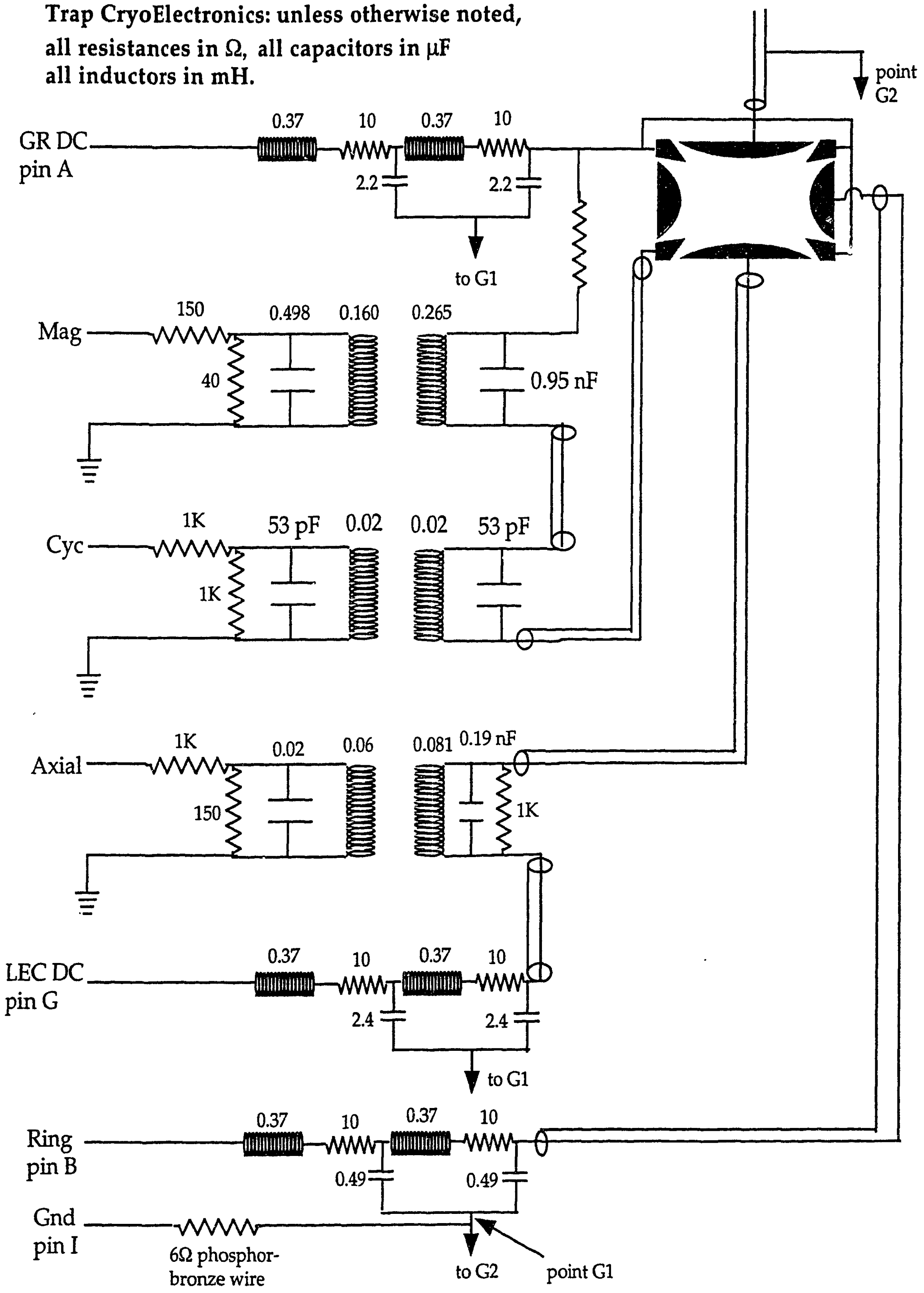

Figure 3-4: Schematic of cryogenic electronics

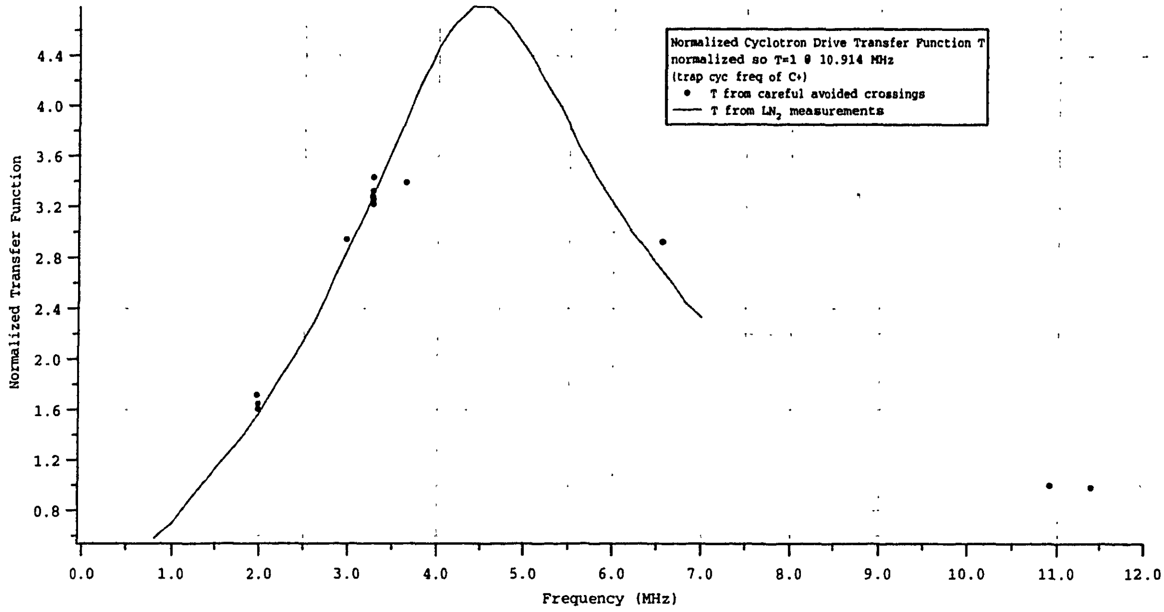

Figure 3-5: Transfer function of cyclotron drive circuit

with a gate valve between the alkali loader and the insert vacuum. We detected the emission of of alkalis with a hot wire detector scheme (discussed further below). A 30 sec pulse of 7 A through the Cs filament released enough Cs to make 1000's of Cs^{+} ions, 100's of Cs^{++} ions, and 10's of Cs^{+++} ions when 10 nA of field emission current were used.

We used a hot-wire detector, in which an alkali metal is ionized by giving up a loosely-bound valence electron to a heated wire to monitor alkali emission from the source. The ion is then accelerated toward a collection plate, generating a current which can be measured. Fig. 3-6 is a schematic of our hot wire circuit and Fig. 3-7 shows a sample output of the hot wire detector. Fig. 3-8 shows our first detection of single Cs^{+++} ions.

3.6 DC SQUID

Although the DC SQUID has proved to be a robust and effective ion detector, getting it to detect single ions at first proved to be a difficult task. SQUIDS are extremely sensitive devices, and can easily be overwhelmed by noise to the point of complete

Hot-wire Detector Circuit

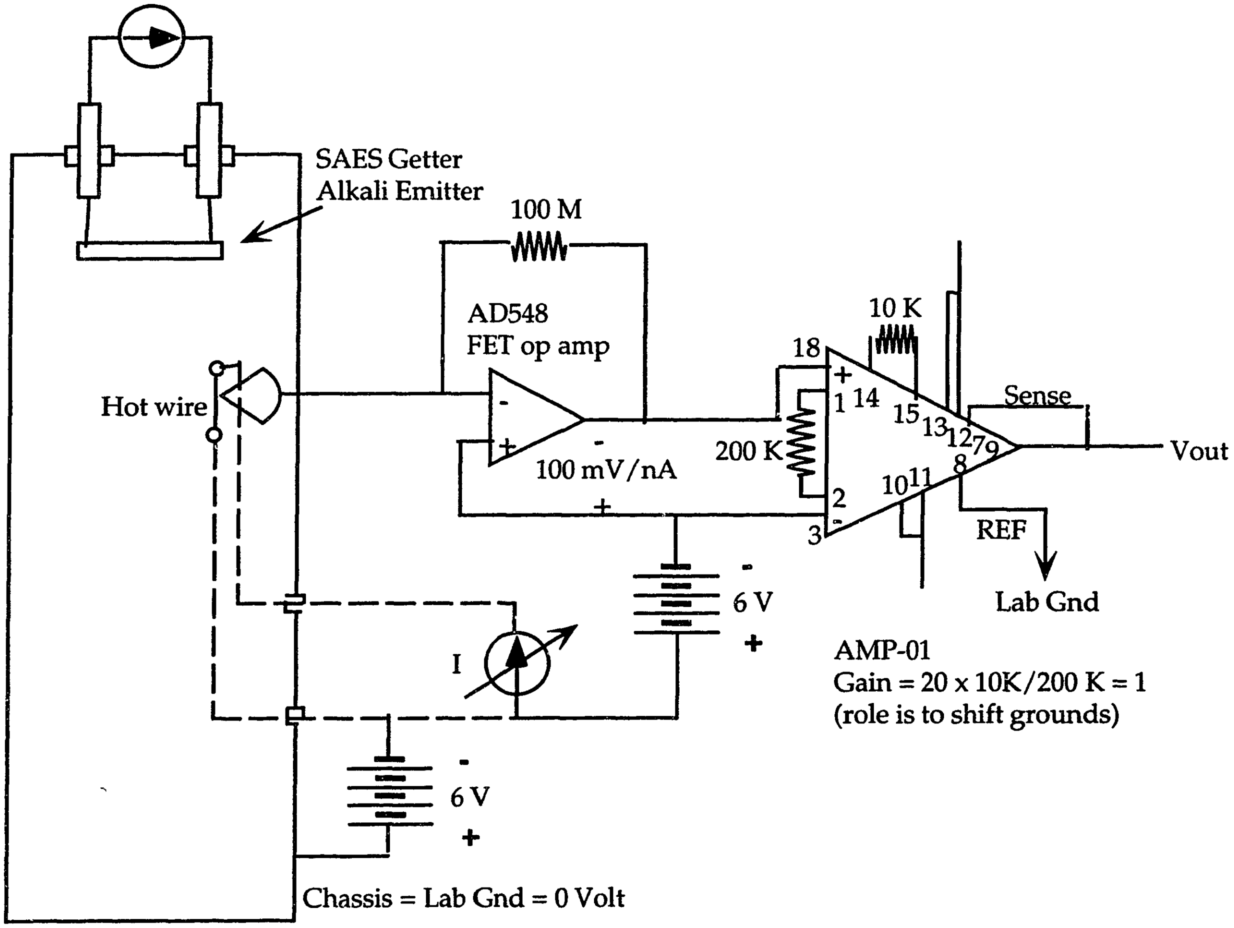

Figure 3-6: Hot Wire Detector Circuit

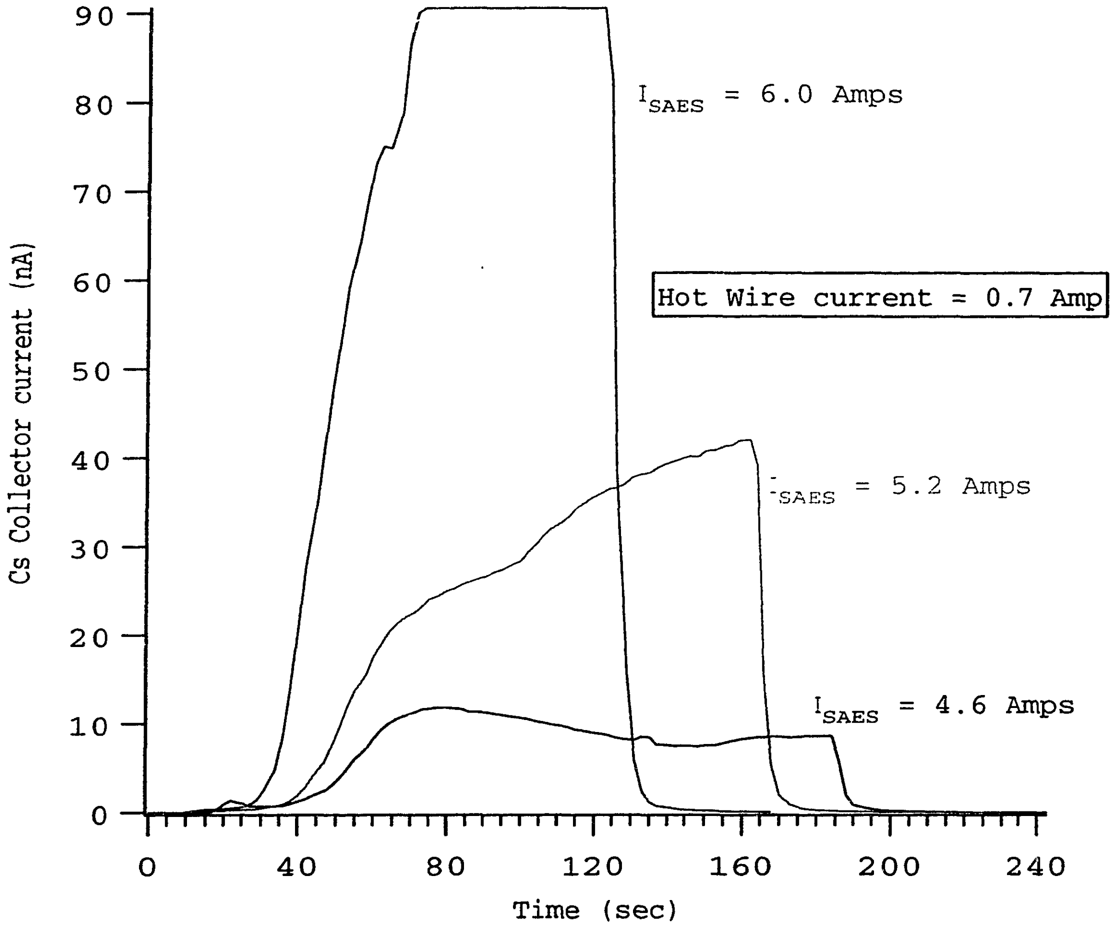

Figure 3-7: Hot Wire Detector Calibration

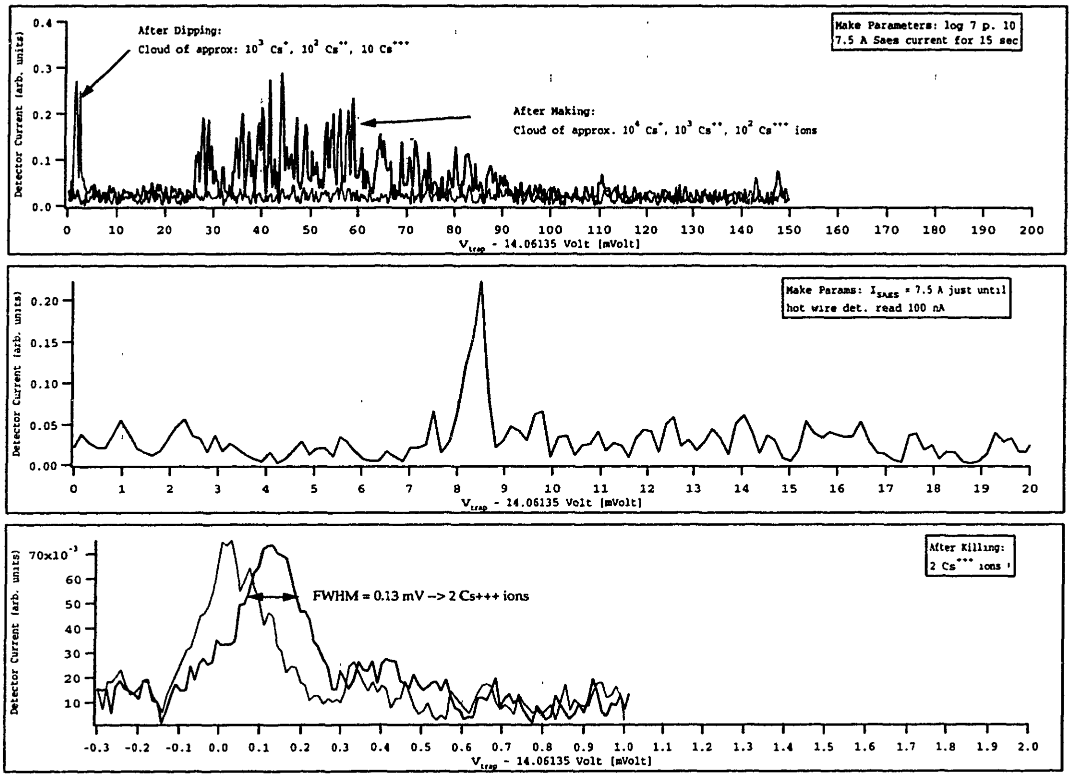

Figure 3-8: The above graphs show our first experimental isolation of 2 Cs^{+++} ions in the trap. The top graph shows the signal from a large cloud of $\sim 10^4$ Cs ions spread over a wide frequency range (or equivalently, trap voltage). After the cloud is "dipped" toward the lower trap endcap using an electrostatic offset potential, $\sim 90\%$ of the ions struck the endcap and were neutralized, resulting in a much smaller cloud spread over a narrower frequency (voltage) range. The second graph shows the result of starting with an empty trap and making a fresh cloud of Cs ions with a much smaller dose of neutral Cs. After "killing" this cloud, i.e. driving it with RF at 92 kHz and 131 kHz to drive out the Cs^{+} and Cs^{++} ions respectively, what remained were 2 Cs^{+++} ions at $\omega_z = 160$ kHz.

non-functionality. Such situations are extremely difficult to debug because there is only very limited diagnostic information available when the primary detector isn't working. This section describes various problems which afflicted the detector and their cures.

The SQUID will not operate in the high magnetic field near the trap, so it is necessary to shield it. We do so by mounting the detector about 1 m above the trap, where the field is $\sim$ 100 G. This is still too large a field for the SQUID to function, and so we need to null it, which we accomplish using a set of external bucking (see Fig. 3-9). The current in these external coils would not be stable enough to permit low-noise operation of the SQUID and therefore we surround the SQUID with a superconducting shield (a Niobium box wrapped with two layers of lead foil). We then null the field above the critical temperature, cool the apparatus down to below the critical temperature, and reduce the current in the bucking coils to zero. Persistent supercurrents are thus induced in the superconducting box walls to maintain the low-field region inside the detector box indefinitely. In the past there was much lore about the number of lead bags to use. It was found through trial and error that two separately lead foil enclosures insulated from one another by teflon sheet were needed to properly shield the SQUID. It was never clear whether this was a manifestation of a strange kind of flux transformer behavior or a consequence of the floppy nature of the lead foil resulting in impefect shielding.

Experimentally we found a short circuit between the bucking coils and the insert body, through which μA ground currents flowed. Therefore we disconnected the bucking coils from their power supply during our measurements to eliminate any noise pickup due to this source.

We also experimented with a large toroidal coil mounted around the main tube of the insert. It was hoped that this would make possible a larger inductance and a higher Q. In practice we found it impossible to shield adequately and abandoned the attempt. The toroidal shield case mounted permanently on the main tube is a permanent relic of this effort.

When we first began using the DC SQUID we were plagued by a confusing noise

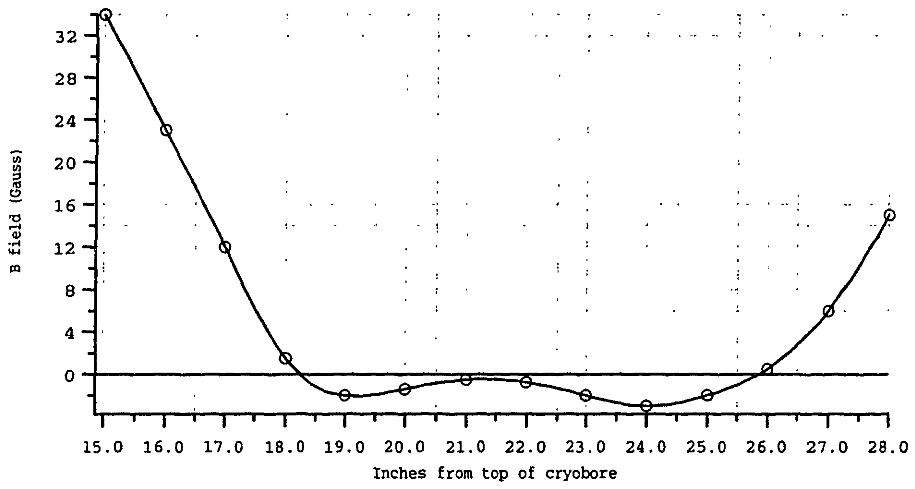

Figure 3-9: Bucker field at location of DC SQUID

problem. We found that the observed noise dependend on the ion's axial frequency ω_z relative to the frequency of the detector ω_0. For $(\omega_z - \omega_0) > 0$ we observed much greater noise in both CW and pulsed modes. As the ions were moved from low to high ω_z across the coil profile, a clear noise peak always appeared. Apparently, unanticipated feedback and pickup distorted the ion lineshapes and made ion counting and trap tuning impossible. By careful experimentation with many (!) grounding and shielding configurations we were we finally able to eliminate these problems and observe clean ion signals. Below I list the different experimental problems we faced, and the solutions we developed. We feel that replacing the current pickup line by a triax cable (c) and adding room temperature filter capacitors (d) were the critical fixes which eliminated stray pickup and made low-noise operation of the DC SQUID possible.

a. Elimination of ground loops The basic configuration of the apparatus is a pair of tubes (the main bore and the tube housing the SQUID cable) running from the 4 K vacuum can up to the room-temperature end of the apparatus. We found it necessary to ensure no electrical contact between these tubes other than their common connection at the vacuum can to eliminate ground loops.

b. Breaking contact to gas handler We discovered that the gas handling manifold was a significant sink for DC ground currents as well as a significant source of noise

pickup. We solved this problem by installing a high-vacuum electrically insulating ceramic break in the stainless steel line running from the gas handler to the apparatus.
c. Use of triaxial detector cable Formerly we used a shielded twisted pair cable to connect the trap upper endcap to the detector coil. This worked well when we used an RF SQUID in our detector. However we found that there was a large capacitive coupling between the signal lead and grounded shield surrounding the twisted pair, which we believe was the cause of many of our problems with the DC SQUID. Noise currents flowing in the apparatus chassis could easily swamp the SQUID and prevent its correct operation, or, more insidiously, cause unwanted feedback resulting in spurious oscillations. We therefore switched from shielded twisted pair to a triaxial cable with a central signal line, a coaxial return line, and finally an outer ground sheath which reduced the capacitance between the inner signal line and the outer chassis by an order of magnitude.
d. Room temperature filter capacitors We installed extra 10 μF filter capacitors to ground at the room temperature end of the insert. This additional filtering has the advantage that any noise currents so filtered have return paths which do not run through the 4K chassis of the insert near the SQUID. It is difficult to eliminate capacitive coupling between the chassis and the signal wires, so return noise currents near 160 kHz flowing back to ground through the chassis could be picked up by the SQUID, even though they had been successfully filtered by the 4K electronics. (See Fig. 3-10)

After completing all the above modifications we found that the spurious noise pickup which had been plaguing us had disappeared. Since that time the DC SQUID detector has proven to be a reliable low-noise detector.

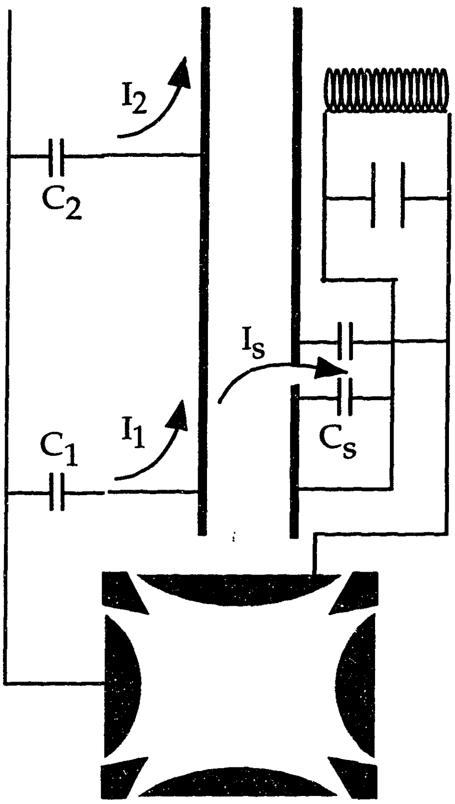

Figure 3-10: Stray pickup of ground return currents in detector system.

Chapter 4

Mass Measurements of Cs, Rb, and Na for α

4.1 Introduction

In this chapter I discuss our measurements of the neutral atomic masses of the stable alkali metal atoms ^{133}Cs, ^{85,87}Rb, and ^{23}Na. [1] The ultimate purpose of these measurements (particularly the measurement of the mass of ^{133}Cs) was to contribute to a new determination of the fine-structure constant α by combining photon recoil, mass spectrometry (see Section 4.3.5), and optical frequency metrology. I begin this chapter with a review of α (Section 4.2), and a survey of various measurements of α (Section 4.3). I then discuss the specfic measurements we made (Section 4.4, and the experimental challenges posed by these measurements (Section 4.5). I then summarize the experimental and analysis steps required to obtain high-precision measurements of the cyclotron frequencies of these ions from measurements of the evolved cyclotron phase (Section 4.6). The methods used here have been described previously, so I merely present them in outline form.

Next I discuss the data analysis methods we used to extract cyclotron frequency

---

[1] The author was the primary operator for the measurements of $M[^{133}\text{Cs}]$, with the assistance of James Thompson and Simon Rainville. James Thompson and Simon Rainville were the primary operators for the measurements of $M[^{87,85}\text{Rb}]$ and $M[^{23}\text{Na}]$. All of us collaborated in the data analysis.

ratios from the measured cyclotron frequencies. The most striking result of these analyses is that for Cs and Rb the measured cyclotron frequency ratios are distributed with uncertainties which are much greater than predicted, and much greater than has been seen in the past (for Cs and Rb we see relative uncertainties > 0.3 ppb, compared with relative uncertainties ~ 0.1 ppb seen in the past). Sections 4.8 is devoted to attempts to explain this uncertainty. First I discuss whether the error might be attributable to errors in the analysis by comparing the variation in results from different analysis methods with the observed uncertainty. Ultimately we concluded that variations due to analysis techniques are too small to be the source of the observed scatter in the frequency ratios. Next I address the various physical effects (introduced in Chapter 2) which can cause frequency variations. Again we found that none of these effects could explain the observed scatter.

Once we concluded that we could not ascribe the excess scatter in our results to either analysis errors or to known physical effects, we decided to quote for each measured cyclotron frequency ratio an average value with an uncertainty reflective of the excess scatter in the data (Section 4.9). We then corrected the measured frequency ratios for systematic frequency shifts (Section 4.10), and computed neutral mass ratios and differences by correcting for the missing electron masses and binding energies (Section 4.11). These mass difference equations constitute an overdetermined set of linear equations which we solve to arrive at final values for the neutral atomic masses (Section 4.12). From the overdetermined set of ratios, we were able to determine each mass in two different ways, which enabled us to verify the absence of systematics > 0.2 ppb. Finally, in Section 4.13 we use our new result for the atomic mass of Cs along with preliminary photon recoil results to obtain a value of α. The results presented here were published in *Physical Review Letters* [BPR99]. I have included this paper as Section 4.15.

Note that Sections 4.6, 4.7, 4.10, 4.11 and 4.12 describe standard procedures and methods of our laboratory. These have been described before in detail [COR90], [BOY92], [NAT93], [DIF94], and they are also presented in the paper "Single-Ion Cyclotron Resonance Mass Spectrometry at MIT", which we plan to submit to the journal *Reviews of Modern Physics*, and a draft of which is included as an appendix to Chapter 4. The discussion of this material in this chapter is intended to complement the discussion in both papers, giving more detail than was possible in either and complementing their discussion.

4.2 The Fine-Structure Constant α

The fine-structure constant ($\alpha \equiv e^2/\hbar c$) [2] $\approx 1/137$ first appeared in Sommerfeld's extension of Bohr's model to explain the observed fine structure of the spectral lines. As quantum theory and atomic physics developed in parallel it became clear that α was a fundamental scale parameter for atomic properties. For example it is easy to show that the characteristic wavelength scale for atomic optical radiation ($1/\pi R_\infty$), the characteristic size of atoms (the Bohr radius a_0) the Compton wavelength of the electron ($h/m_e c$), and the classical electron radius $r_c = e^2/m_e c^2$ are related by successive powers of the fine-structure constant [3]:

$$\frac{1}{\pi R_\infty} : a_0 : \frac{h}{m_e c} : \frac{e^2}{m_e c^2} = 1 : \alpha : \alpha^2 : \alpha^3 \tag{4.1}$$

Note that the size of the atomic nucleus does not enter into the above quantities, since nuclear radii ($\sim 10^{-15}$ m) are much smaller than any atomic length scale and nuclear dynamics are governed by the strong force rather than by electromagnetic forces.

In the early years of Quantum Electrodynamics (QED) it was recognized that α was the basic coupling constant for the interaction of the unit charge and light, and that all the interesting quantities in atomic physics (magnetic moments, scattering cross sections, etc.) could be written as perturbation expansions in powers of α. The mathematical issue of the ultimate convergence of these perturbation series was and still is a subtle one, but the high accuracy which has been achieved in comparison of

---

[2] cgs units. In SI units we have $\alpha \equiv \mu_0 c e^2/2h$ where $\mu_0 = 4\pi \times 10^{-7}$ N/A^2 is an exactly defined quantity

[3] I learned this scaling relation from Prof. D.E. Pritchard. I am unsure of the original reference

various QED calculations with experiment is remarkable.

α appears in many contexts in physics and arises in diverse physical systems because of its role as the dimensionless coupling constant describing the interaction of electrons and positrons with the electromagnetic field. This has resulted in numerous experimental routes to measuring α. Comparison of these measurements enables us to test the underlying assumption that all these diverse systems are ultimately governed by the same theory, namely renormalizable QED.

Measurements of α may be divided into two classes. The first class consists of those measurements which are essentially direct measurements of the constituent quantities e and h (note that c = 299 752 458 m/s exactly) in experimentally measurable combinations which can be themselves combined to give α. The second class consists of those measurements which require the use of complicated QED calculations to extract a value for α from measured quantities.

4.3 Survey of Precision Measurements of α

4.3.1 Introduction

Table 4.1 and Fig. 4-1 summarize the current status of the four most precise experimental routes to α. These different measurements are briefly discussed below, in approximate order of increasing precision.

4.3.2 AC Josephson Effect

The AC Josephson effect is the oscillation of frequency ν observed when a voltage V is applied across a Josephson junction. Theory predicts that ν and V are related by [JOS62]

$$\nu = (\frac{2e}{h})V \tag{4.2}$$

This relationship has been shown to be independent of the materials used to fabricate the Josephson junction to a level of 2 parts in 10^{16} [TJL83]. Thus measurements of

Table 4.1: Tabulated Values of α, with absolute uncertainties given in parentheses. The references to the measurements are given in the text.

CODATA 1986: The value from the 1986 least-squares adjustment of the fundamental constants (45 ppb).

acJ: AC Josephson effect (56 ppb).

q Hall: quantum Hall effect (24 ppb). Measured in 1989 and 1997, with 42 ppb discrepancy.

(g-2): anomalous magnetic moment of e^-, e^+ (4 ppb). In 1995 the value of α was shifted down by 55 ppb due to the correction of a calculation error [KIN95].

h/mn: neutron interferometry (35 ppb).

ICR: The mass spectrometry/photon recoil route to h/m_{Cs} and α (the subject of this thesis).

Method	α^{-1}	Error (ppb)
1986 CODATA	137.035 989 50 (610)	44.5
1989 acJ	137.035 977 00 (770)	56.2
1989 q Hall	137.035 997 90 (320)	23.4
old (g-2)	137.035 991 90 (57)	4.2
1995 (g-2)	137.035 999 44 (57)	4.2
1997 q Hall	137.036 003 70 (330)	24.1
1997 (g-2)	137.035 999 93 (520)	3.8
1998 h/mn	137.036 010 62 (503)	36.7
2000 ICR	137.035 992 20 (400)	29.2

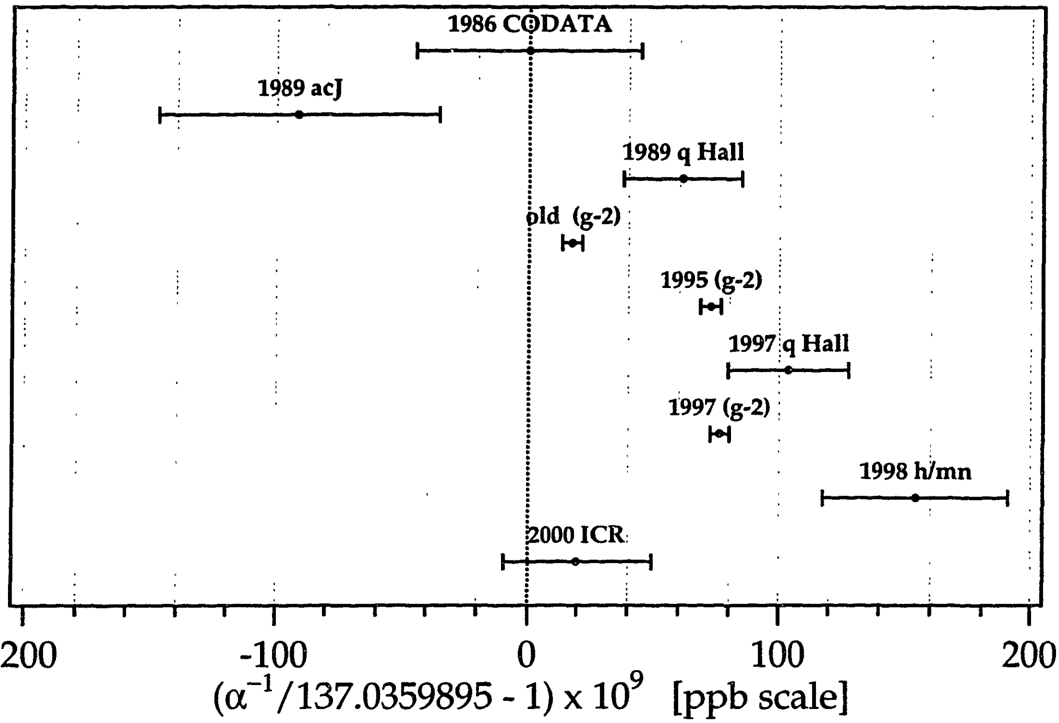

Figure 4-1: Precision Measurements of the Fine-Structure Constant. The relative uncertainties are given in parentheses. The most recent measurements are at the bottom of the graph. The references to the measurements are given in the text.
CODATA 1986: The value from the 1986 least-squares adjustment of the fundamental constants (45 ppb).
acJ: AC Josephson effect (56 ppb).
q Hall: quantum Hall effect (24 ppb). Measured in 1989 and 1997, with 42 ppb discrepancy.
(g-2): anomalous magnetic moment of e^-, e^+ (4 ppb). In 1995 the value of α was shifted down by 55 ppb due to the correction of a calculation error [KIN95].
h/mn: neutron interferometry (35 ppb).
ICR: The mass spectrometry/photon recoil route to h/m_{Cs} and α (the subject of this thesis).

the AC Josephson effect provide a way to measure e/h to high precision.

The highest-precision route relating $2e/h$ to α is

$$\alpha^2 = (\frac{4R_\infty \gamma_p'}{c})(\frac{\mu_B}{\mu_p'})(\frac{h}{2e}) \tag{4.3}$$

where R_∞ is the infinite-nuclear-mass Rydberg constant, γ_p' is the proton gyromagnetic ratio (the prime refers to the fact that γ_p' is measured using nuclear magnetic resonance on an H_2O sample), μ_p' is the proton magnetic moment, and $\mu_B = e\hbar/2m_e c$ is the Bohr magneton.

R_∞ is known to 0.008 ppb [UHG97], γ_p' is known to 110 ppb [1], (μ_p'/μ_B) is known to 10 ppb [COT86], and $(2e/h)$ is known to 30 ppb. Thus the overall uncertainty on α via this route is limited by γ_p' to 56 ppb.

4.3.3 Quantum Hall Effect

For any effectively two-dimensional electron gas system in a magnetic field and cooled to cryogenic temperatures, the Hall resistance $R_H = V_T/I$ (where V_T is the voltage generated across the sample transverse to the direction in which current I flows) is quantized:

$$R_H = \frac{h}{e^2 n} \qquad n = 1, 2, 3 \ldots \tag{4.4}$$

Measurement of R_H by comparison to a standardized Ohm (based on a calculable capacitor) can provide a high precision measurement of $h/e^2 \approx 25\ 813\ \Omega$; this is essentially a direct measurement of α. Two measurements of α by this route have been made by the same group at NIST. Both measurements have 24 ppb precision, but the values differ by 42 ppb. It is felt that the 1997 measurement is the correct value [CAG89], [JEL97], [TAY99].

4.3.4 Electron & Positron Anomalous Magnetic Moment

The spin magnetic moment of the electron μ_e may be written as $\mu_e = g(1/2)\mu_B$ where $\mu_B = e\hbar/2mc$ is the Bohr magneton, 1/2 is the electron spin in units of $\hbar$ and g is the electron "g-factor". Simple classical models of the electron predict $g = 1$. However in the 1920's Goudsmit and Uhlenbeck showed that $g = 2$ was needed to explain the observed structure of spectral lines. One of the most remarkable sucesses of theoretical physics was Dirac's discovery of his relativistically correct wave equation, which predicted that $g = 2$ exactly.

Nonetheless, careful measurements revealed that in fact g was not exactly equal to 2. Explaining the so-called "anomaly" $a_e \equiv (g-2)/2 \approx 0.001\ldots$ became a new challenge for theorists to puzzle over.

The development of Quantum Electrodynamics (QED) provided an explanation for the non-zero anomaly a_e. Schwinger was the first to calculate a correction to $g = 2$. Using an abstract formulation of QED he was able to derive the result that $a_e = \alpha/2\pi$ [SCH51], a result correct to first order in α.

Feynman's diagrammatic approach to QED can be used to calculate the anomaly and gives an intuitive picture of the physics behind the result. Fig. 4-2 shows the Feynman diagram for a Dirac electron interacting with an external classical Coulomb potential, and ignoring the possibility of the electron emitting or reabsorbing virtual photons. From this diagram we obtain the result that $g = 2$ exactly. Fig. 4-3 shows the lowest-order (first order in α) QED modification to the interaction. Now the electron can emit and reabsorb one virtual photon of wavevector $\vec{k}$. This results in a "one-loop vertex correction" to the interaction of the electron and the external field and gives the result that $a_e = \alpha/2\pi$.

The electron anomaly a_e can be measured to high precision by comparing the electron spin-flip frequency $\omega_s = g\mu_B B/\hbar$ to the cyclotron frequency $\omega_c = eB/mc$ (cgs units). Simple algebra gives $\omega_s = (g/2)\omega_c$ so that $a_e = (g/2) - 1 = (\omega_s/\omega_c) - 1 = (\omega_s - \omega_c)/\omega_c$. Using an electron confined in a Penning trap, $(\omega_s - \omega_c)$ can be measured directly. Hans Dehmelt and co-workers at the University of Washington pioneered

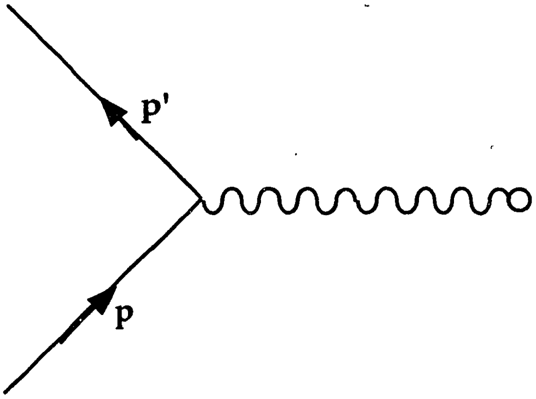

Figure 4-2: Feynman diagram for a Dirac electron the the presence of (or scattering off) an external Coulomb potential ([KAK93], p. 138). The first-order QED modification to this diagram is shown in Fig. 4-3.

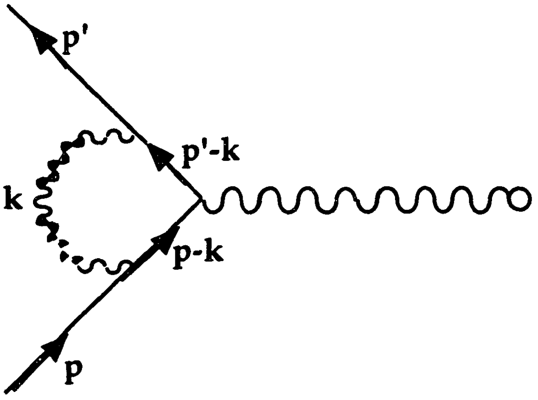

Figure 4-3: "One-loop vertex correction" modification to Fig. 4-2, showing the emission and reabsorption of a virtual photon of wavevector $\vec{k}$ during the interaction with the external field. Calculation of this diagram gives $a_e = \alpha/2\pi$ ([KAK93], p. 189)

the trapping of single electrons for the measurement of $(g-2)$. The most precise results from the UW group (for electrons and positrons) are [VSD87]:

$$a_{e^-} = 1\ 159\ 652\ 188.4\ (4.3) \times 10^{-12} \quad \text{electron anomaly} \tag{4.5}$$

$$a_{e^+} = 1\ 159\ 652\ 187.9\ (4.3) \times 10^{-12} \quad \text{positron anomaly} \tag{4.6}$$

The equality of the measured electron and positron g-factors within experimental uncertainties is a strong test of matter-antimatter symmetry.

Complementary to these high-precision measurements of a_e are high-order QED calculations of a_e. These calculations have been contributed to by a number of authors since Schwinger and Feynman. The dean of this field is Tochiro Kinoshita of Cornell University. Using the VEGAS Monte-Carlo integration routines [KIN95], [KIN96], [KIN97] running on a supercomputer he has calculated QED corrections up to and including fourth-order in α. The QED contribution to a_e is

$$A_1 = A_1^{(2)}(\alpha/\pi) + A_1^{(4)}(\alpha/\pi)^2 + A_1^{(6)}(\alpha/\pi)^3 + A_1^{(8)}(\alpha/\pi)^4 + A_1^{(10)}(\alpha/\pi)^5 + \ldots \tag{4.7}$$

This is the dominant contribution to the total expression:

$$a_e = A_1 + A_2(m_e/m_p) + A_2(m_e/m_\tau) + A_3(m_e/m_\mu, m_e/m_\tau) \tag{4.8}$$

A_2 and A_3 are small mass-dependent QCD terms. The current best values for the QED terms are [KIN97]:

$$\begin{aligned}
A_1^{(2)} &= \ 0.5 \quad \text{exact} \\
A_1^{(4)} &= -0.328\ 478\ 965\ldots \quad \text{purely analytic} \\
A_1^{(6)} &= \ 1.181\ 259\ (40) \quad \text{numerical} \\
A_1^{(6)} &= \ 1.181\ 241\ 456\ldots \quad \text{analytic} \\
A_1^{(8)} &= -1.409\ 2\ (384) \quad \text{numerical} \\
A_1^{(10)} &= \ \text{unknown}
\end{aligned} \tag{4.9}$$

As discussed above, $A_1^{(2)} = 0.5$ is an exact analytic result. $A_1^{(4)}$ has contributions from 7 Feynman diagrams, all obtained analytically. $A_1^{(6)}$ has contributions from 72 Feynamn diagrams. Until recently this term was calculated as a hybrid of analytical results for 57 diagrams and numerical results for 15 diagrams. More precise numerical work by Kinoshita [KIN95] led to the discovery of an error in one of the analytical integrals which has since been corrected. In addtion, the remaining diagrams have also since been calculated analytically [LAP95], [LAR96], giving a result which agrees well with the precise numerical result. This illustrates the importance of both analytical and numerical results for such complex calculations; both are necessary if we are to have confidence in the final results. $A_1^{(8)}$ is the current challenge. It consists of 891 Feynman diagrams which can be reduced to 86 integrals using the Ward-Takahashi identity. Each integrand has about 20000 terms. Thus the computations are extensive. A point-by-point cancellation of singularities is used to renormalize the integrals and make them integrable [KIN97].

An extremely precise value of α can be obtained from the average of the experimental measurements of a_{e^-} and a_{e^+} and the QED calculations described above. This value is:

$$\alpha = 137.035\ 999\ 93\ (52) \tag{4.10}$$

This value has a precision of 3.8 ppb and is the most precise available by a factor of 5. It can be seen from Fig. 4-1 that the $(g-2)/\text{QED}$ measurement is in reasonable agreement with the 1997 Quantum Hall effect measurement, and disagrees with the

1998 h/m_n measurement. The interest in the photon-recoil method for measuring α (see Section 4.3.5) stems from the fact that it is an independent method with an accuracy which is potentially comparable to that of the $(g-2)$/QED measurement, and thus it may help to shed light on the apparent discrepancy in the measured values of α.

It is worth noting that Kinoshita has pointed out that our complete lack of knowledge of $A_1^{(10)}$ will prevent determinations of α below 10^{-13} via the $(g-2)$/QED method. This represents an ultimate theoretical limit to the $(g-2)$/QED route to α.

4.3.5 h/m: Neutron Interferometry and Photon Recoil

Consideration of $\alpha \equiv e^2/\hbar c$ and the infinite-nuclear-mass Rydberg constant $R_\infty \equiv (2\pi^2 m_e e^4)/(h^3 c) \approx 1.09 \times 10^5$ cm^{-1} (cgs units) makes it easy to see that

$$\alpha^2 = \frac{2R_\infty}{c}\frac{h}{m_e} \tag{4.11}$$

Since R_∞ is known with an accuracy of 0.008 ppb [UHG97], and c is a defined constant, this provides a route to α of potentially sub-ppb precision.

To exploit the route to α of Eq. 5.32 it is necessary to measure h/m_e to high precision. High-precision mass spectrometry frees the experimenter from the need to measure h/m_e directly because accurate mass ratios can be used to link a measurement of h/m_X for an arbitrary mass m_X to h/m_e:

$$\frac{h}{m_e} = \left(\frac{h}{m_X}\right)\left(\frac{m_X}{m_p}\right)\left(\frac{m_p}{m_e}\right) \tag{4.12}$$

(m_p/m_e) has been measured by Van Dyck et al. to a precision of 2 ppb [FVS95] and the MIT ICR lab is capable of measuring m_X/m_p to precisions ~ 0.1 ppb. Thus the door is open for ppb-level determinations of α via this route.

By equating the classical ($p = mv$) and quantum ($p = h/\lambda_{dB}$) expressions for particle momentum we see that measurements of the deBroglie wavelength λ_{dB} and the velocity v of a particle provides a way to measure h/m_X. Moreover, in combination with measurements of the atomic mass M_X (in atomic mass units u) we see that we obtain the same Molar Planck constant $N_A h$ obtained in Chapter 1 (obtained there by equating classical and quantum expressions for energy). Thus measurements of λ_{dB}, v, and M_X can be used to obtain $N_A h$:

$$\lambda_{dB} v = \frac{h}{m_X} = \frac{10^3 N_A h}{M_X} \tag{4.13}$$

Rewriting Eq. 5.32 in terms of $N_A h$ gives us the same result for α obtained in Chapter 1:

$$\alpha^2 = \frac{2R_\infty}{c}\frac{10^3}{M_p}\frac{m_p}{m_e}(N_A h) \tag{4.14}$$

Thus measurements of λ_{dB}, v, and M_X can provide a (nearly) QED-independent measurement of α, like the AC Josephson and Quantum Hall effect methods. It is true that QED calculations of the $2P_{1/2}$, $2P_{3/2}$ and 8D Lamb shifts are needed to allow R_∞ to be obtained from measurements of the 1S-2S and 2S-8D transitions in hydrogen [UHG97], but these corrections are small and do not need to be known to high accuracy (the largest calculational uncertainty contribution to R_∞ is 0.00026 ppb due to the 8D Lamb shift). Thus even in the event that QED is flawed or approximate, this method for measuring α is robust and reliable. If a ppb-level measurement of α can be made by this method QED could be tested for the first time at the ppb-level allowed by the QED/(g-2) measurement.

Kruger et al. have used neutron interferometry to precisely measure λ_{dB} and v for a beam of neutrons, resulting in a measurement of h/m_n with a precision of 73 ppb [KRU98]. Combining this with a precise measurement of M_n (from Penning trap measurements of $M[^2\mathrm{H}]$, $M[^1\mathrm{H}]$ and γ-ray measurements of the nuclear binding energy of ^{2}H [DNB94], [VFS93a], [GRE86]) results in a value of α with a precision of 37 ppb (see Fig. 4-1). This measurement illustrated the promise of the method but was not precise enough to test QED at the 10^{-9} level.

The group of Prof. S. Chu at Stanford University is using photon recoil in Cs to measure h/m_{Cs} for α. The process of resonant photon recoil by an atom provides another way to measure h/m. After a photon absorption/emission process an atom recoils with a velocity $v_r = h/m\lambda$ where λ is the wavelength of the photon (which is equal to λ_{dB} of the recoiling atom). The resultant Doppler shift $\Delta\omega = (4\pi^2\hbar)/(m\lambda^2)$ of the atomic absorption and emission frequencies with respect to the laboratory frame provides a way to measure h/m in terms of the wavelength λ (which has been accurately measured in another experiment done in Garching, Germany [URH99]).

The photon recoil frequency shift is measured using the Ramsey method in which the atom is initially put into a superposition of ground and excited states by a $\pi/2$ pulse of applied radiation. A second $\pi/2$ pulse applied a time T later transfers maximum population into the excited state for detection if the frequency is equal to the internal atomic transition frequency. By varying the frequency of the applied radiation one can map out population transfer "fringes" which can be used to determine the atomic resonance frequency to high precision. Ramsey interferometry in the optical regime is complicated by the very photon recoil effect introduced above. The momentum kick given to the "excited" portion of the superposition state causes the wavepacket for the superposition state to separate, meaning that a second $\pi/2$ pulse alone cannot create Ramsey fringes because the parts of the superposition state to be interfered no longer spatially overlap.

As shown in Fig. 4-4 this problem of photon-recoil induced separation of the wavepacket can be solved using two additional $\pi/2$ pulses (at B and C) between the initial and final $\pi/2$ pulses (at A and D). These extra $\frac{\pi}{2}$ pulses "flip" the superpostion state and add in extra recoil kicks resulting in two distinct paths where the two halves of a coherent superposition overlap. The final $\pi/2$ pulse can then recombine the spatially overlapped portions of the superposition state. The frequencies of the central Ramsey fringes for the two paths will differ by 2 photon recoil kicks. Still higher precision can be achieved by adding additional π pulses between the middle $\pi/2$ pulses at B and C. These serve to add additional recoil kicks and spread the center frequencies of the two paths further apart, allowing higher precision.

Initial experiments at Stanford using this interferometer configuration in a Cs atomic fountain achieved a precision of 100 ppb in 2 h of integration time. However it was found that the value of h/m_{Cs} so measured was 850 ppb smaller than the accepted value. This led to a search for systematic effects and a rebuilding of the apparatus. The resultant precision is now 22 ppb for 4 h of run time [YOU97], but currently systematics limit the accuracy to 55 ppb. However it is expected that a ppb-level measurement is possible. It is in anticipation of this result that the sub-ppb measurement of $M(^{133}\mathrm{Cs})$ described in this thesis was undertaken.

4.4 Mass Measurements Chosen

The goal of the alkali metal measurements described in this chapter was to measure the atomic masses of the stable atomic species ^{133}Cs, ^{85,87}Rb, and ^{23}Na, in order to contribute high-precision atomic masses for the project of determining the fine-structure constant α via the photon-recoil/mass spectrometry route discussed in Section 4.3.5. ^{133}Cs was of particular interest because of the atom interferometer experiment to measure h/m_{Cs} currently ongoing at Stanford University [WYC93], [YOU97]. Similar efforts to measure h/m for Na and Rb are not yet in progress, but are feasible. It is anticipated that future efforts to measure h/m for Na and Rb may exploit Bose condensation techniques to allow high-resolution atom interferometry [DEP99].

For this series of measurements we measured the ratios of the cyclotron frequencies of Cs^{+++}, Cs^{++}, Rb^{++}, Na^{+}, and Na^{++} ions with respect to a reference ion, each of whose masses were known very accurately from our previous work. We used two different reference ions for each alkali atom to provide a check on systematic errors, since the measurements involving different comparison species involved different charge states and different cyclotron frequencies. Table 4.2 lists the series of mass ratio measurements we made to determine the masses of ^{133}Cs, ^{85,87}Rb, and ^{23}Na.

I was primarily responsible for the runs involving Cs, with the assistance of James Thompson and Simon Rainville. James Thompson and Simon Rainville performed the runs involving Rb and Na, using the method and apparatus I had developed with previous collaborators for the Cs runs. All of us were involved in the analysis of these data, along with Prof. David E. Pritchard and Dr. James V. Porto.

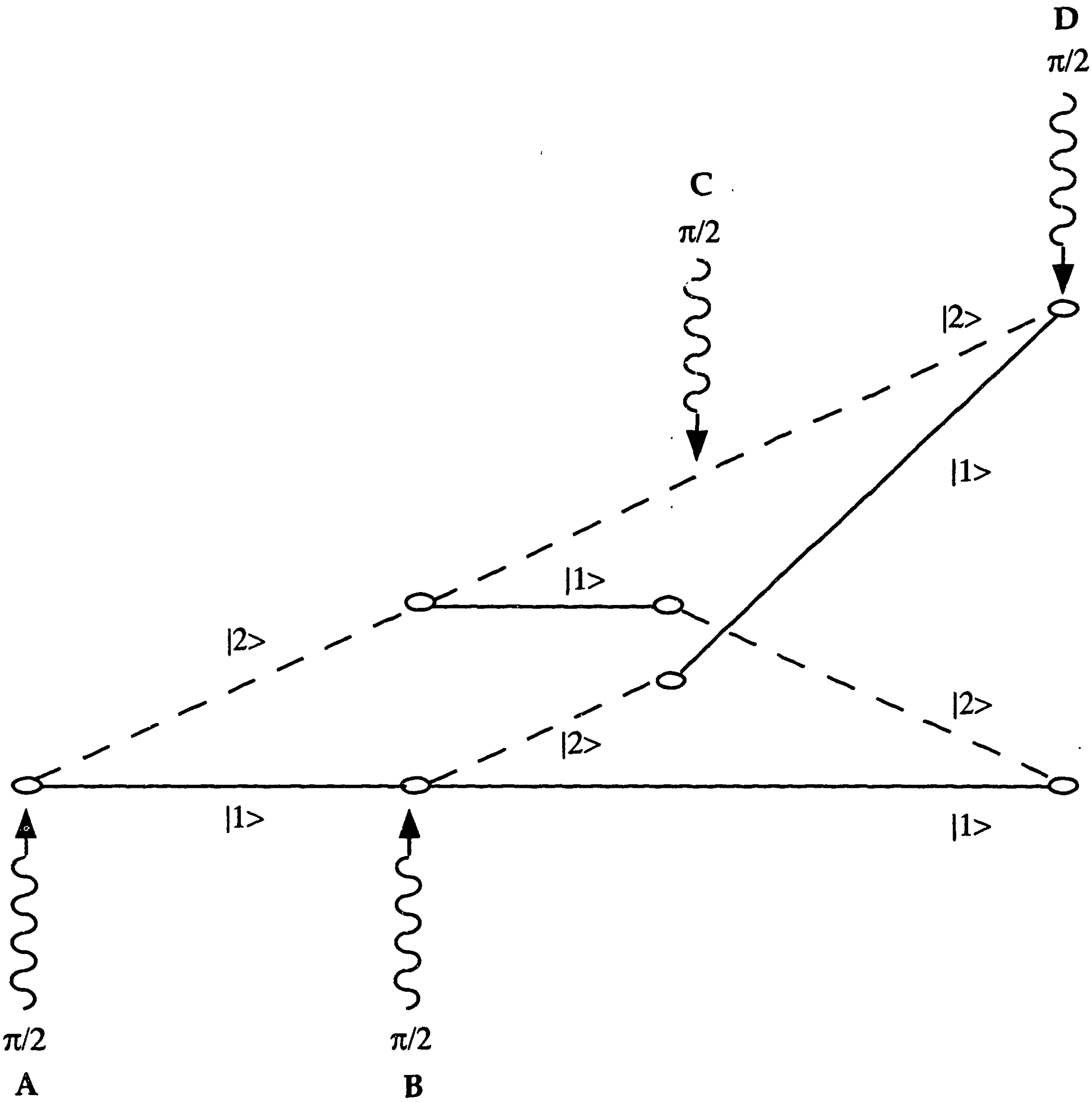

Figure 4-4: Schematic of the Stanford Cs beam Ramsey interferometer (from [YOU97]). The $\pi/2$ pulse at A begins the Ramsey process by putting the atom into a superposition of the upper state $|2>$ and the lower state $|1>$. The photon absorption by $|2>$ results in a spatial separation of the paths followed by the two components of the superposition state. Thus the $\pi/2$ pulse at D alone is not sufficient to coherently recombine the superposition into state $|2>$. The two additional $\pi/2$ pulses at B and C solve this problem by creating two more paths which spatially overlap at D with the correct phase, allowing interference. Additional π-pulses may be added between B and C to spread the Ramsey fringes at D further apart for higher precision. The additional paths created by B and C which do not contribute to the interference at D are not shown.

Table 4.2: Ion cyclotron frequency ratios measured to determine the masses of the alkali metals ^{133}Cs, ^{85,87}Rb, and ^{23}Na. Along with each ratio is listed the mean cyclotron frequency and the number of measurement runs. I also tried measuring the ratio $\mathrm{Cs}^{++++}/\mathrm{O}_2^+$, but it was essentially impossible to isolate a single Cs^{++++}. I hypothesize that this was due to the fact that $\omega_z(Cs^+) = \omega_z(Cs^{++++})/2$, so that in the process of driving large clouds ($\sim 10^3$ ions) of contaminant Cs^+ ions (with $\omega_z/2\pi = 80$ kHz) from the trap we would drive them into large anharmonic orbits, resulting in significant motion at the second harmonic 160 kHz. I suspect that this would excite the small cloud of Cs^{++++} ions and usually drive them out of the trap.

A/B	$\bar{\omega}_c/2\pi$ (MHz)	Runs
$^{133}\mathrm{Cs}^{+++}/\mathrm{CO}_2^+$	2.968	7[4]
$^{133}\mathrm{Cs}^{++}/\mathrm{C}_5\mathrm{H}_6^+$	1.977	4
$^{87}\mathrm{Rb}^{++}/\mathrm{C}_3\mathrm{H}_8^+$	2.994	2
$^{87}\mathrm{Rb}^{++}/\mathrm{C}_3\mathrm{H}_7^+$	3.028	3
$^{85}\mathrm{Rb}^{++}/\mathrm{C}_3\mathrm{H}_7^+$	3.064	2
$^{85}\mathrm{Rb}^{++}/\mathrm{C}_3\mathrm{H}_6^+$	3.100	2
$^{23}\mathrm{Na}^{+}/\mathrm{C}_2^+$	5.578	2
$^{23}\mathrm{Na}^{++}/\mathrm{C}^+$	11.155	2

4.5 Mass Spectrometry Challenges of Multiply-Charged Ions

The alkali metal mass measurements of Table 4.2 presented new experimental challenges for our group. Until these measurements we had never loaded into our trap any species which was not gaseous at room temperature. Fortunately the high vapor pressure of the alkali metals at low temperatures makes it relatively easy to evaporate a gas from the solid phase. Because of our requirements for low contamination and small gas loads we chose to use SAES alkali metal dispensers [5], designed as low-contamination alkali metal dispensers for photocathode production. These are electrically heated nichrome filaments which enclose alkali metal chromates $\mathrm{M_2CrO_4}$ and a ZrAl alloy which serves as a reducing agent to liberate free alkali atoms when the filament is heated, and as a getter to absorb other gases produced during the reduction reaction.

---

[5] SAES Getters/USA Inc. 1122 E. Cheyenne Mtn. Blvd., Colorado Springs, CO 80906

^{133}Cs and ^{85,87}Rb are significantly heavier than the heaviest atom (^{40}Ar) we had measured before. The precision of our cyclotron frequency measurements can be lower for heavy ions with low ω_c because the contribution to the overall uncertainty due to uncertainty in the axial frequency increases quadratically as ω_z^2/ω_c^2 [BRG86]. Thus we prefer to multiply ionize these heavy atoms to increase ω_c for mass measurements. Another, technical, reason for using multiply ionized Cs and Rb was that the maximum output of our precision trap voltage source is $\sim$ 21 Volt, which sets a practical upper limit of $m/q \approx 70$ u/e on the m/q of ions which can be brought into resonance with our 160 kHz axial frequency detector.

Our use of multiply-charged ions significantly increased the time which had to be spent clearing contaminant ions from the trap. Alkali metal ionization cross sections typically decrease by a factor of $\sim$ 3 for each successive charge state [HFH82], resulting in large clouds of lower charge state ions when multiply-charged ions are made. Furthermore the hydrocarbons C_5H_6 and C_3H_x used as comparison species break apart under electron-beam bombardment, resulting in many unwanted fragment ions. The overall effect of these factors was to increase the ion-making time to $\sim$ 20 minutes from the $\sim$ 5 minutes required for previous measurements.

Multiply-charged ions are also subject to larger frequency shifts due to frequency pulling and the image charge effect, and the binding energy corrections required to convert ion masses to neutral masses are larger and hence contribute more to the final uncertainty.

It is also worth noting that the mass numbers A of ^{133}Cs, ^{85,87}Rb and ^{23}Na are odd numbers and $A = 133, 85, 23$ are prime, so it was not possible when comparing multiply charged alkalis to singly charged molecular ions to work with true mass doublets (ions with nearly equal m/q) because of the non-integral values of m/q. Note that ^{87}Rb^{++} has $m/q = 29$ u/e; this is an exception which we did not exploit.

4.6 Measurement Procedure and Initial Analysis: from ϕ_c to ω_c

The measurement procedure we used was essentially the same procedure which has been used extensively in the past and is described thoroughly in several theses and publications [FLA87], [WEI88], [COR90], [BOY92], [NAT93], [DIF94]. I briefly review it here, highlighting the areas of particular concern for our work with multiply charged Cs, Rb, and Na ions.

During the day the ambient magnetic field in our laboratory fluctuates with rms amplitude 1 mG ($\sim 10^{-8} B_0$)) and periods ~ 0.1 sec due to the nearby subway. These relatively large and rapid fluctuations severely reduce the time over which a PNP or SOF measurement can be extended without loss of a cycle (2π), and hence they limit the precision which can be achieved in a PNP measurement. Therefore we take data in the early morning between the hours of $\sim$ 1 a.m. and 5:30 a.m when the subway is not running. We measure a single mass ratio on any particular night, so the date is a suitable index for the runs

The hours before a run begins are occupied in preparation. We initially focus on loading single ions of each species into the trap, adjusting the parameters of the RF drive and trap dipping ion expulsion procedure until we are able to load single ions of each species as regularly and quickly as possible. The longer ion making time for the multiply-charged alkali ions and the fragmentable comparison ions limited the overall accuracy which could be achieved in one night's run.

For each ion we then adjusted the electric field strength of the RF coupling drive at $(\omega_c' - \omega_z)$ which we use to couple the trap cyclotron and axial modes for PNP measurements. We adjusted the strength of this RF field to obtain a measured "avoided crossing" splitting $|\Omega| \approx 2$ Hz, which corresponds to a "π-pulse" duration of $\Delta t = 250$ ms. Choosing $2\pi/\omega_0 = 50\mu\mathrm{s} < \Delta t < 2\pi/\gamma_z \approx 1$ s is a convenient duration time since it prevents the detector from being impulsively excited, but it is short compared to the ion's damping time.

We then "tune" the trap, i.e. we adjust the value of the leading order electrostatic anharmonicity C_4 to be as small as possible, by measuring the lineshape of a continously driven single ion, and adjusting the voltage on the guard ring electrodes until the line profile is as symmetric as possible. We can typically discern line profile changes for guard ring less than 1 mV. This corresponds to a resolution $\Delta C_4 = 0.1 \Delta V_{GR}/V_R = (0.1)(1 \times 10^{-3}\mathrm{V}/10\mathrm{V}) \sim 10^{-5}$ for a typical trap voltage $V_R \sim 10$ Volt.

Having practiced making single ions, adjusted the coupling drives to give 250 msec π-pulse times, adjusted the cyclotron RF drive voltages to give cyclotron radii which correspond to axial amplitudes after the π-pulse which are as large as possible for good signal-to-noise, but aren't chirped due to anharmonicities, and finally tuned the trap, we are ready to make precise cyclotron frequency measurements. Our last step before making the measurements is to shut down the freight elevator in our building, since in going from floor to floor it changes the ambient field by ~ 1 mG.

The actual cyclotron frequency measurement process for each ion is a series of PNP experiments with different delay times. The PNPs with short delay times are used to help "unwrap" the evolving phase. Our typical series of PNP sequences includes 3 or 4 which have delay times ~ 50 s. These give cyclotron frequency resolution $\sim 10^{-10}$ with our typical phase measurement error $\sim 10^{\circ}$ (this is limited by the signal to noise ratio of our detector). Thus each series of PNP measurements gives a "cluster" of 3-4 long-time measurements of the cyclotron phase ϕ_c which we convert into measurements of the trap cyclotron frequency ω_c'.

After we have made a cluster of cyclotron phase measurements on one ion (an entire series of PNP runs requires about 10 min altogether, including the overhead time of the computer which controls our RF pulses and data acquisition), we need to expel it from the trap and load in a single ion of the other species. We then make a cluster of PNP measurements on that ion. We continue cyclotron frequency measurements on alternate ion species throughout the night. Except for the relative calm during a PNP series, where we merely need to watch that the ion doesn't accidentally get expelled from the trap (an occasional occurence probably caused by a collsion with a background contaminant ion), most of the night is spent trying to make and isolate single ions as quickly as possible.

The first step in our data analysis procedure is to extract the free-space cyclotron frequency ω_c from our numerous measurements of the evolved phase ϕ'_c of the trap cyclotron mode of each ion. We start by obtaining the trap cyclotron frequency ω'_c. Once we have "unwrapped" the phase, (i.e determined the total phase to within 2π) of the long-time PNPs by using the phases of the intermediate data points to bootstrap our way up to long phase evolution times, we can immediately compute the trap cyclotron frequency from the formula (see Section 2.2.5)

$$\omega'_c = \frac{\phi'_c + \phi_{unwrap}}{T} + (\omega'_c - \omega_z) + \omega_{mix} \tag{4.15}$$

where the measured phase ϕ'_c has the offset phase ϕ_{unwrap} (determined from the phase unwrapping) added in. Because of the mixdown chain for our axial frequencies, the measured value of ϕ'_c evolves at 50 Hz. Now we need to go from the trap cyclotron frequency ω'_c to the free-space cyclotron frequency ω_c, because the trap cyclotron frequency is systematically lowered by the trap radial electric field and is not a measure of the ion's inertial mass.

We obtain the free-space cyclotron frequency using the invariance theorem from Chapter 3. The free space cyclotron frequency is simply the quadrature sum of the three mode frequencies ω'_c, ω_z, and ω_m. We obtain measurements of both ω'_c and ω_z directly from the PNP phase measurements and we use

$$\omega_c = \sqrt{\omega'^2_c + \bar{\omega_z}^2 + \left[\left(\frac{\bar{\omega_z}^2}{2\omega'_c}\right)\left(1 + \frac{9}{4} sin^2\theta\right)\right]^2} \tag{4.16}$$

For the multiply-charged ions and high-Q ($Q = 5\times10^4$, wound for us by R. Nguyen for his senior thesis project) detector coil used for these measurements the shift in the axial frequency due to the coupling to the detector ("frequency pulling") was significant. During these measurements we measured ω_0 with uncertainty $\sim$ 20 mHz before each alkali metal ion in a PNP sequence. (The process of measuring the detector resonance frequency ω_0 required about 5 min, so over the course of one night with 10 ion switches measuring ω_0 would use up almost 1 h of the 4 h measurement

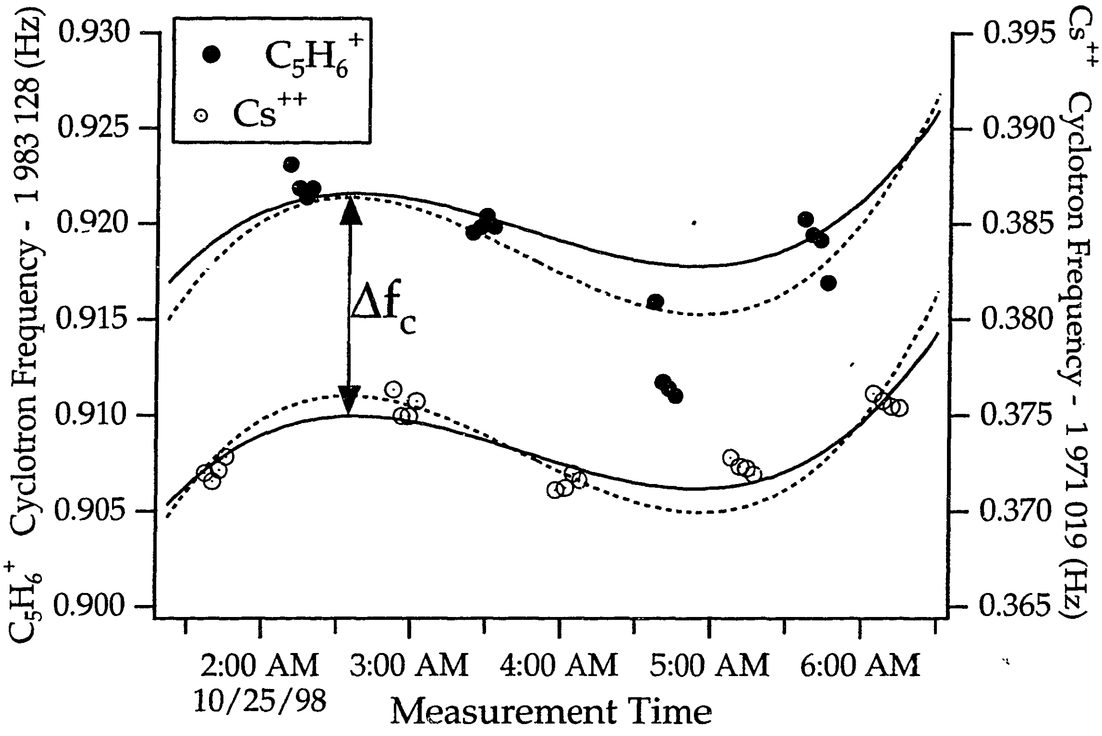

Figure 4-5: $Cs^{++}/C_5H_6^+$ data for 10/25/98. Third-order fits are shown. The solid line is a robust fit, the dashed line a least-squares fit to the data. It can be seen that the least-squares fit is excessively pulled by the $C_5H_6^+$ outlier cluster.

window. To reduce the time spent measuring ω_0 we therefore measured ω_0 only before each alkali metal ion PNP.) We then used the measured values of $(\bar{\omega}_z - \omega_0)$ and the detector Q to correct the final free-space cyclotron frequency for the effect of the pulling using the formula

$$\omega_c^{corr} = \omega_c^{meas} - \left(\frac{\omega_z^2}{2\omega_c}\right)\left(\frac{q^2Q^2}{m}\right)\left(\frac{C_1^2L}{4z_0^2}\right)(\bar{\omega}_z - \omega_0) \tag{4.17}$$

where the quantities in Eq. 4.17 were introduced in Chapter 2. After this analysis procedure we are left with a series of measured values of the free space cyclotron frequency for each ion at successive times. These measurements come in distinct clusters separated by the ion making time ~ 15 min. From these measurements it is our task to extract the best value of the measured cyclotron frequency ratio.

4.7 Determining a Frequency Ratio

The least-squares and robust fitting methods used by our group to extract mass ratios from cyclotron frequency data have been thoroughly discussed in previous references [NAT93], [DIF94]. Moreover, they are summarized in Section 5.3.1, where we also discuss two newer cluster-based methods, cluster-based least-squares fits (developed by Fred Palmer) and piecewise linear fits. For completeness, I give here Table 4.3 which lists for each of the alkali metal ratios the number of clusters, the fit order chosen, and the fit order suggested by the F-test. Table 4.4 gives the results of robust fitting. In Section 4.7.1 I discuss more completely the method of piecewise linear fitting in order to expand on and complement the discussion of Section 5.3.1.

The most striking conclusion from our data analysis is the fact that the resultant frequency ratios (one per night run) exhibit much larger scatter than was expected. In Section 4.8 I address the possibility that this scatter might be due to analysis errors, and I discuss how we convinced ourselves that this was not the case.

4.7.1 Nearest-Neighbor and Piecewise Linear Averages

To help check the results of robust fitting we used a method of analysis which is minimally dependent on assumptions about the magnetic field drift. The basic method is to construct "nearest neighbor" ratios, in which each adjoining pair of clusters of cyclotron frequency measurements give a measurement of the frequency ratio equal to the ratio of the cluster mean values. Thus we have a set of frequency ratio measurements which we average to obtain a final result, with the uncertainty being the square root of the sample variance of these data.

In the presence of a linear field drift $B(t) = b_0 + b_1 t$ this method has the obvious failing that it results in mass ratios that are alternately too high and too low by an amount $\sim b\overline{\Delta t}/B_0$, where $\overline{\Delta t}$ is the mean time between frequency measurements. We often observe field drift rates $\sim b_1/B_0 \approx 10^{-9}/\mathrm{h}$, so for $\overline{\Delta t} \sim 10$ min this effect would contribute an extra 0.3 ppb to the uncertainty.

An extension of this nearest-neighbor method which combats this problem is the

Table 4.3: Table listing for each ratio the number of clusters N, the fit order chosen n_{chosen} and the fit order suggested by the F-test n_F. In a case where the F statistic varies successively above and below the critical value F_{crit}, two values of F are listed.

Ratio	Date	N	n_{chosen}	n_F
Cs+++/CO2	8/5	6	3	1
Cs+++/CO2	8/23	6	2	1
Cs+++/CO2	8/24	6	2	1
Cs+++/CO2	8/28	6	2	2
Cs+++/CO2	8/30	8	4	4
C5H6/Cs++	10/25	9	3	4
C5H6/Cs++	10/26	6	2	2
C5H6/Cs++	10/28	8	2	2
C5H6/Cs++	10/29	6	3	3
C3H8/87Rb++	11/7	7	2	2
C3H8/87Rb++	11/9	7	4	4
C3H7/87Rb++	11/20	7	4	3
C3H7/87Rb++	11/21	10	5	4
C3H7/87Rb++	11/22	12	3	3
C3H7/85Rb++	11/26	10	2	2
C3H7/85Rb++	11/27	12	5	2,5
C3H6/85Rb++	12/1	10	5	5
C3H6/85Rb++	12/2	8	2	1
C2/Na+	12/14	11	4	3
C2/Na+	12/15	13	5	5
C/Na++	12/17	11	4	4
C/Na++	12/18	9	4	4

Table 4.4: Table of results from robust fitting, with adjustments. The values of σ_{rob} and σ_{adj} are quoted in ppb.
(a): Original fit order (n=3) was discrepant with other orders, so we chose n=4
(b): The $n = 2$ fit was discrepant with the others, so we used a weighted average of different fit orders.
(c): We used the robust fit result but with the larger least-squares σ, to be conservative.
(d): Here we used the least-squares result and uncertainty because of the pathological behavior of the robust fit for this data set.
(e): We quote here the average of the $n = 3$ and $n = 4$ fit orders.

A/B	Date	Robust ω_c[A]/ω_c[B]	σ_{rob}	Adjusted ω_c[A]/ω_c[B]	σ_{adj}
Cs+++/CO2	8/5	0.992957581169	0.180	—	—
Cs+++/CO2	8/23	0.992957580383	0.149	—	—
Cs+++/CO2	8/24	0.992957580812	0.149	—	—
Cs+++/CO2	8/28	0.992957581063	0.122	—	—
Cs+++/CO2	8/30	0.992957581108	0.110	—	—
Cs++/C5H6	10/25	0.993893716907	0.185	0.993893717247 [a]	0.300
Cs++/C5H6	10/26	0.993893717201	0.209	—	—
Cs++/C5H6	10/28	0.993893716040	0.206	—	—
Cs++/C5H6	10/29	0.993893716149	0.294	0.993893716509 [b]	0.500
87Rb++/C3H8	11/7	1.013992022448	0.129	—	—
87Rb++/C3H8	11/9	1.013992023029	0.156	—	0.5 [c]
87Rb++/C3H7	11/20	0.990799127984	0.158	—	—
87Rb++/C3H7	11/21	0.990799127448	0.118	—	—
87Rb++/C3H7	11/22	0.990799127970	0.096	—	—
85Rb++/C3H7	11/26	1.014106122133	0.105	—	—
85Rb++/C3H7	11/27	1.014106122246	0.102	—	—
85Rb++/C3H6	12/1	0.990367650717	0.119	—	—
85Rb++/C3H6	12/2	0.990367650259	0.175	0.990367651392 [d]	0.332
Na+/C2	12/14	1.043943669539	0.102	—	—
Na+/C2	12/15	1.043943669711	0.811	—	—
Na++/C	12/17	1.043944716613	0.854	—	—
Na++/C	12/18	1.043944716768	0.110	1.043944716664 [e]	0.189

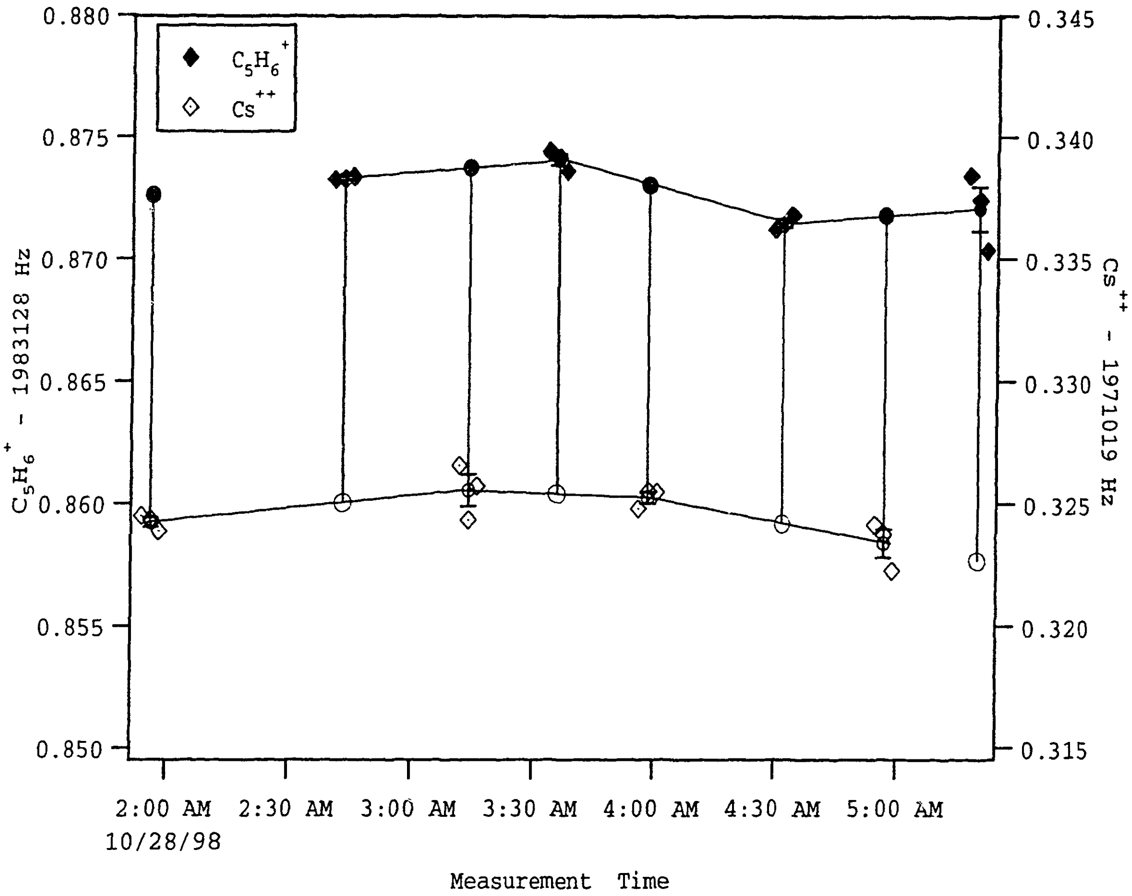

Figure 4-6: Piecewise linear fit to data. Corresponding to each vertical bar is the ratio of the frequency of an interpolated point for one ion relative to the mean frequency of a cluster for the comparison ion.

"piecewise linear" fitting technique. In this case the simplest possible assumption is made about the field drift between cyclotron frequency measurements on two different measurements of the same ion; it is assumed to be linear, and a straight line is fit between each pair of points for each ion. The frequency ratio is then calculated between interpolated frequencies from these linear fits (see Fig. 4-6).

Each vertical line in the figure corresponds to the ratio of the frequency of one ion and the interpolated frequency of the other ion. These frequency ratios are then averaged to yield a final mean ratio using a weighted average can also be performed: the weight used is $w = 1/\Delta t_1 + 1/\Delta t_2$ where Δt_1 and Δt_2 are the time separations between the interpolated point and the adjacent points. (This weighting is based on the expectation that for a random walk magnetic field the standard deviation would be $\sigma = \sqrt{\Delta}$ resulting in a weight $w = 1/\Delta t$ for a single point.) The above formula for adding weights doubles the weight of a point between two equidistant points, relative to the weight it would have with just one point alone. In general it favors interpolated points which are close to their initial points.

4.8 Run-to-Run Variations

The most striking observation regarding the results of robust fits to the alkali metal data is the large run-to-run scatter in the value of the frequency ratios r obtained for the Cs^{+++}, Cs^{++}, and Rb^{++} (except for the $^{85}Rb^{++}/C_3H_7^+$) data. See Fig. 4-7 for a representative example. For some unknown reason this scatter is much larger than the uncertainties σ_i predicted by the robust fit, which reflect the range of fit results which could reasonably accomodate the data. There are two possible causes for this:
(1) There may be a flaw in the robust analysis method; either the ratios r_i or the predicted uncertainties σ_i which it reports may be incorrect.
(2) The frequencies may shift from run to run due to some varying physical effect, such as varying coil pulling or cyclotron radii which results in variations of the measured frequency ratio r. I address this possibility in Sections 4.8.2 and 4.8.3. In this section I quantify the observed scatter in r and address the question of whether it is due to faulty analysis.

4.8.1 Quantifying the Scatter

I start by quantifying the observed scatter. Let us suppose we have a set of cyclotron frequency ratios $r_i = (\omega_{c2}/\omega_{c1})_i$ and a corresponding set of uncertainties σ_i for a particular ion pair, measured over a set of nights labelled by i. The σ_i are the *predicted* uncertainties in the measured frequency ratios r_i. We wish to assess whether they are reflective of the actual observed uncertainty in the data. We start by computing the weighted mean $\bar{r}$ [BER92], using the σ_i as relative weights:

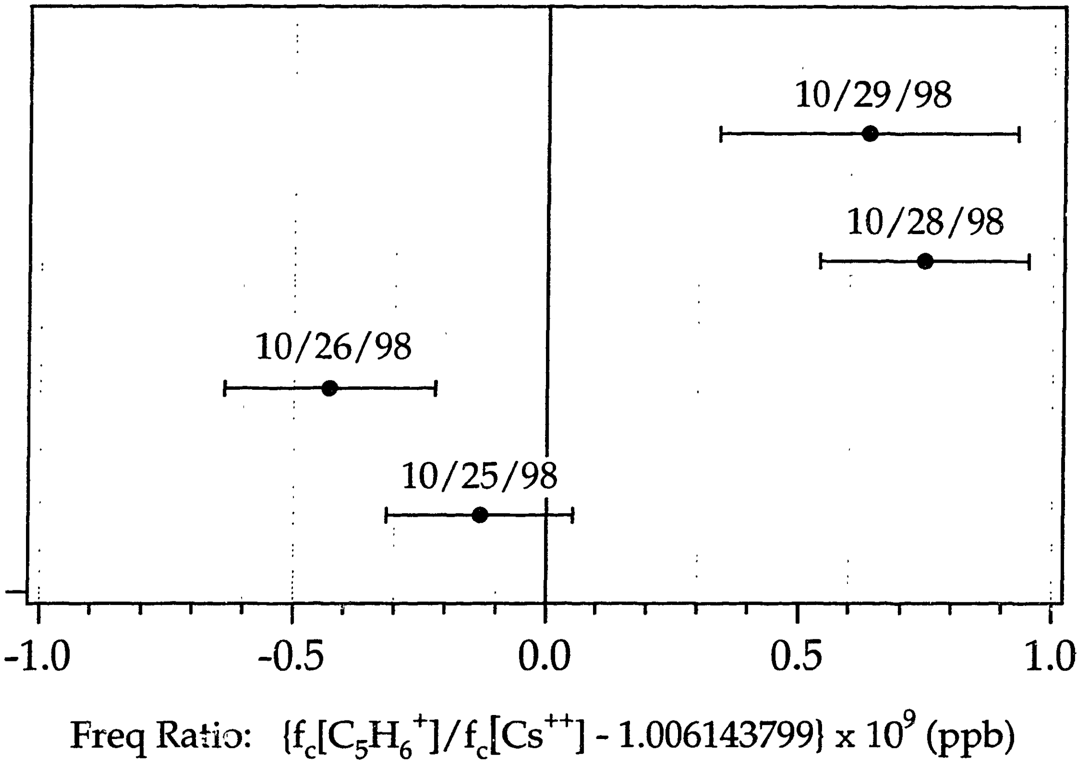

Figure 4-7: Measured values and predicted uncertainties of the frequency ratio $Cs^{++}/C_5H_6^+$, showing how the actual scatter in the measured ratios from night to night is much greater than the uncertainty predicted on a given night based on the magnetic field variation.

$$\bar{r} \equiv (\sum_i r_i/\sigma_i^2)/(\sum_i 1/\sigma_i^2) \tag{4.18}$$

To quantify the observed scatter of the ratios r_i about this weighted mean $\bar{r}$, we compute the *reduced* χ^2 statistic, χ_ν^2, a normalized measure of the inter-run variability:

$$\chi_\nu^2 \equiv \frac{\sum_i (r_i - \bar{r})^2/\sigma_i^2}{(N-1)} \tag{4.19}$$

If the predicted uncertainties σ_i are representative of the observed scatter then $\sqrt{< r_i - \bar{r} >^2} \sim \sigma_i$, and $\chi_\nu^2 \to 1$ for large N. $\chi_\nu^2 >> 1$ signals that $\sqrt{< r_i - \bar{r} >^2} >> \sigma_i$, i.e. the σ_i underestimate the observed variation. For our Cs^{+++}, Cs^{++}, and Rb^{++} data (except for $^{85}Rb^{++}/C_3H_7^+$) this turns out to be the case (Table 4.5). In such cases it is better to use the experimentally measured *weighted average variance* [BER92] of the points about the mean:

$$\sigma_{var}^2 = \frac{\sum_i w_i (r_i - \bar{r})^2}{\sum_i w_i} \times \left(\frac{N}{N-1}\right) \tag{4.20}$$

where the $w_i = 1/\sigma_i^2$ are used only as relative weights. (We can easily see that for constant weights Eq. 4.20 reduces to the usual formula for the sample variance $s^2 = \sum_i (r_i - \bar{r})^2/(N-1)$. From Eq. 4.19 and Eq. 4.20 we see that if we define an average value $\bar{\sigma}$ of the σ_i by

$$\frac{1}{\bar{\sigma}^2} \equiv (\sum_i 1/\sigma_i^2)/N \tag{4.21}$$

then we have

$$\chi_\nu^2 = \frac{\sigma_{var}^2}{\bar{\sigma}^2}. \tag{4.22}$$

Thus we have the intuitively appealing result that χ_ν^2 is the ratio of the weighted average variance σ_{var}^2 to the square of the mean predicted uncertainty $\bar{\sigma}$. If the σ_i accurately predict the observed scatter, $\bar{\sigma} \sim \sigma_{var}$ and $\chi_\nu^2 \approx 1$. If $\bar{\sigma}$ underestimates the observed scatter, $\chi_\nu^2 > 1$. If $\bar{\sigma}$ has been overestimated, then $\chi_\nu^2 < 1$. Table 4.5 tabulates σ_{var}, $\bar{\sigma}$, and χ_ν^2 for the adjusted robust fit results to the Cs, Rb, and Na

Table 4.5: Square root of the average weighted variance σ_{var}, average predicted uncertainty $\bar{\sigma}$, and reduced χ^2 (χ^2_ν) for the adjusted results of robust fitting (Table 4.4) to the Cs, Rb, and Na data. Note that the results of 8/9/98 and 8/27/98 have been excluded as described previously. The mean predicted uncertainties from the adjusted robust fits $\bar{\sigma}$ underestimate the experimentally observed scatter (σ_{var}), giving $\chi^2_\nu >> 1$ for the Cs^{+++}, Cs^{++} and Rb^{++} data, except for $^{85}Rb^{++}/C_3H_7^+$. The Na^+ and Na^{++} data have $\chi^2_\nu < 1.5$.

A/B	Runs	σ_{var} (ppb)	$\bar{\sigma}$ ppb	$\chi^2_\nu = \sigma^2_{var}/\bar{\sigma}^2$
Cs^{+++}/CO_2^+	5	0.301	0.136	4.90
$C_5H_6^+/Cs^{++}$	4	0.657	0.255	6.64
$^{87}Rb^{++}/C_3H_8^+$	2	0.358	0.155	5.33
$^{87}Rb^{++}/C_3H_7^+$	3	0.307	0.116	7.00
$^{85}Rb^{++}/C_3H_7^+$	2	0.078	0.103	0.57
$^{85}Rb^{++}/C_3H_6^+$	2	0.309	0.158	3.82
Na^+/C_2^+	2	0.109	0.090	1.47
Na^{++}/C^+	2	0.025	0.110	0.052

data. It can be seen that $\chi^2_\nu >> 1$ for all the data except $^{85}Rb^{++}/C_3H_7^+$, Na^+/C_2^+, and Na^{++}/C^+. This indicates that the predicted uncertainties from the robust fits generally underestimated the actual scatter in the Cs and Rb frequency ratios.

I used the results of the nearest-neighbor and piecewise linear fit methods to test whether the robust fit procedure might be reporting incorrect ratios r_i or uncertainties σ_i. I treated the robust fit result r_i^{rob} and the *unweighted average* of the piecewise linear and nearest neighbor results $r_i^{NN,PL} \equiv 1/2(r_i^{NN} + r_i^{PL})$ as two separate "measurements" of the frequency ratio. I computed for each run the one-run (unweighted) sample variance s_i^2:

$$s_i^2 = \frac{(r_i^{rob} - r_{avg})^2 + (r_i^{NN,PL} - r_{avg})^2}{(2-1)} \tag{4.23}$$

where $r_{avg} \equiv 1/2(r_i^{rob} + r_i^{NN,PL})$. s_i is a measure for each night of the variations in the value of r reported by the different analysis methods.

I then computed $\langle s_i^2 \rangle$ where the average is over each night for the ratio in question. $\langle s_i^2 \rangle$ is a measure of the average variation in r_i due to different fit methods. Table 4.6 gives the results. It can be seen that $\sigma^2_{var} >> \langle s_i^2 \rangle$ for all the ratios except for

Table 4.6: Variations in the frequency ratio r due to different analysis methods. The large values of $\sigma_{var}^2/\langle s_i^2\rangle$ indicate that variations in the method of fitting cannot explain the large night-to-night scatter.

A/B	Runs	σ_{var} (ppb)	$\sqrt{\langle s_i^2\rangle}$ (ppb)	$\sigma_{var}^2/\langle s_i^2\rangle$
Cs^{+++}/CO_2^+	5	0.301	0.069	19.29
$Cs^{++}/C_5H_6^+$	4	0.657	0.075	76.07
$^{87}Rb^{++}/C_3H_8^+$	2	0.358	0.059	37.30
$^{87}Rb^{++}/C_3H_7^+$	3	0.307	0.053	33.48
$^{85}Rb^{++}/C_3H_7^+$	2	0.078	0.014	29.07
$^{85}Rb^{++}/C_3H_6^+$	2	0.309	0.132	5.49
Na^+/C_2^+	2	0.109	0.032	11.67
Na^{++}/C^+	2	0.025	0.052	0.23

Na^{++}/C^+, which indicates that variations in analysis methods are not large enough to explain the observed scatter. We are implicitly assuming that the robust fit method and the nearest-neighbor/piecewise linear analysis methods are not both affected by the same "systematic" shifts from run to run, an assumption which we believe is warranted by the significant differences between the methods.

The above investigations demonstrated that the excess scatter in the measured frequency ratios could not be ascribed to analysis errors, so next we considered the possible physical sources of the scatter. In Chapter 2 I discussed a number of trap imperfections and physical effects which can lead to frequency errors. In the following sections I address the possibility of whether these could be the origins of the unexpectedly large scatter in the frequency ratios.

For the Cs, Rb, and Na data the largest-magnitude shifts were due to frequency pulling (Section 4.8.2) and radius dependent shifts (Section 4.8.3). I address each of these in turn, followed by a host of smaller effects.

4.8.2 Possible Cause: Frequency Pulling

In Section 4.8.2 I showed, following Weisskoff [WEI88] that for ions nearly in resonance with the detector (i.e. $\omega_z - \omega_0 << \gamma_0$) the axial frequency ω_z is "pulled" by its coupling to the detector by an amount:

$$\Delta\omega_z = \omega_z^{meas} - \omega_z^0 \approx (\gamma_z/\gamma_0)(\omega_z - \omega_0) \tag{4.24}$$

where ω_z^{meas} and ω_z^0 are the ion axial frequencies with and without the influence of pulling, and ω_0 and $\gamma_0/2\pi = 3$ Hz are the detector resonance frequency and FWHM. Because the normalized damped ion linewidth $\gamma_z/\gamma_0 \propto q^2Q^2/m$ the effect of pulling is especially significant for the multiply charged ions and high Q detector used for these experiments. As described in Section 4.6, we attempted to minimize the effect of the frequency pulling by adjusting the trap voltage to set $(\omega_z - \omega_0)$ as close to zero as possible before running a PNP sequence.

The ion-detector alignment procedure was not perfect; as a result we observed non-zero $|\omega_z - \omega_0|$ (typically < 100 mHz). The pulling shift due to such detunings is significant, so we used the measured values of $\overline{\omega_z}$ and ω_0 to compute the pulling shift and correct the measured values of ω_c for the effect. In a few instances the corrections to ω_c due to the pulling were as large as 5×10^{-10} for individual clusters. However the process of re-adjusting $(\omega_z - \omega_0)$ before each alkali cluster measurement tended to randomize the effect. Because the effect of the pulling shift on an individual run's frequency ratio r was in a few cases as large as a few parts in 10^{-10}, we initially suspected that it might be the cause of our night-to-night scatter. The largest shift in a final ratio due to pulling was 0.24 ppb for the $\mathrm{Cs}^{+++}/\mathrm{CO}_2^+$ data of 8/24/98.

Table 4.7 summarizes the effect of pulling on the measurements by giving the rms difference in r for each ratio computed before and after applying the pulling correction. We estimate that our measurements of $(\omega_z - \omega_0)$ were accurate to ≈ 30 mHz, so the pulling corrections are accurate to roughly 30 mHz/100 mHz $\sim 30\%$, which implies that the largest frequency pulling correction (for $\mathrm{Cs}^{+++}/\mathrm{CO}_2^+$) contributed an error of 0.3×0.120 ppb $= 0.036$ ppb. Thus the uncertainty in the frequency pulling is not large enough to explain the large σ_{var} in Table 4.5, and so it was not the source of the excess night-to-night scatter for these data.

Table 4.7: The rms shift and uncertainty in the frequency pulling for the Cs, Rb, and Na data.

A/B	$(\Delta r)_{rms}/r$ (ppb)	Uncertainty (ppb)
Cs^{+++}/CO_2^+	0.120	0.036
$Cs^{++}/C_5H_6^+$	0.064	0.019
$Rb^{++}/C_3H_x^+$	0.062	0.019
Na^+/C_2^+	0.011	0.003
Na^{++}/C^+	0.029	0.009

4.8.3 Possible Cause: Variable Cyclotron Radius

The PNP measurement technique requires that we accumulate cyclotron phase at a finite non-zero cyclotron radius ρ so that we have sufficient signal-to-noise to accurately determine the frequency and the phase ϕ_c' of the axial signal after a π-pulse (Section 2.2.5). A consequence of this is that the cyclotron frequency can be shifted significantly because of the relativistic and trap imperfection frequency shifts discussed in Section 2.3.

We attempted to drive the ions in a pair being measured to nearly equal amplitudes in order to have the radius-dependent frequency shifts nearly cancel. Table 4.8 gives the mode radii used in the alkali metal measurements. These radii were obtained from the calibration of our cyclotron amplitude which is based on the measured B_2 axial "bottle" shift and relativistic cyclotron shift for a single $^{12}C^+$ ion (see Chapter 2, Section 2.5).

Because of the potentially large magnitude of the radius-dependent frequency shifts we investigated whether the run-to-run variations in the measured cyclotron frequency ratio r might be due to variations in the radii. We were able to obtain the the cyclotron radius ρ used for phase evolution from the measured axial amplitude after the π-pulse by exploiting the action-preserving property of the π-pulse:

$$\oint_{cyc} \vec{p} \cdot d\vec{q} = \oint_{z} \vec{p} \cdot d\vec{q} \to m\omega_c\rho^2 = m\omega_z a_z^2 \to \rho = \sqrt{\frac{\omega_z}{\omega_c}} a_z \tag{4.25}$$

where ρ and a_z are the cyclotron radius and axial amplitudes before and after the π

Table 4.8: Mean radii $\langle\rho\rangle$ and radius ratios for the alkali metal cyclotron frequency measurements.

A/B	$\langle\rho\rangle$ (μm)	ρ_A/ρ_B
Cs^{+++}/CO_2^+	165	0.991
$Cs^{++}/C_5H_6^+$	210	0.991
$^{87}Rb^{++}/C_3H_8^+$	251	1.017
$^{87}Rb^{++}/C_3H_7^+$	254	0.989
$^{85}Rb^{++}/C_3H_7^+$	258	1.017
$^{85}Rb^{++}/C_3H_6^+$	262	0.989
Na^+/C_2^+	153	0.947
Na^{++}/C^+	234	0.932

pulse, respectively. Thus we obtain cyclotron radii from the measured axial amplitudes, and we examined the variations of the ratios of these radii. Taking the ratios of the measured radii enabled us to normalize out any fluctuations due to the variation of the overall gain of the SQUID detector system, which is variable.

Fig. 4-8 shows the cyclotron radii ratios obtained from the axial amplitudes after the π-pulses for the Cs^{+++}/CO_2^+ runs. This is a representative example. We made the two observations that the ratio of the mean measured radii differs from the value predicted on the basis of the calibrations discussed in Chapter 2, and there is large variation in the ratio from night-to-night.

We do not understand the origin of this variation and systematic offset. It may be purely a detection problem, or it may be reflective of the actual cyclotron amplitudes, or most likely a combination of the two. It remains a significant mystery to be solved.

To check whether this variation in cyclotron amplitudes correlated with the variation in the measured mass ratio we computed the relative cyclotron frequency ratio shifts which we would predict by taking the measured cyclotron frequency ratios from the axial data, using the mean radii predicted from the transfer function, and computing the expected frequency shifts. I plot these results in Fig. 4-9, a plot of the actual observed shift in the frequency ratio versus the shift which would be predicted based on the variations of the radii. It can be seen, there is no correlation between the observed and predicted shifts under this mechanism, and in fact the observed

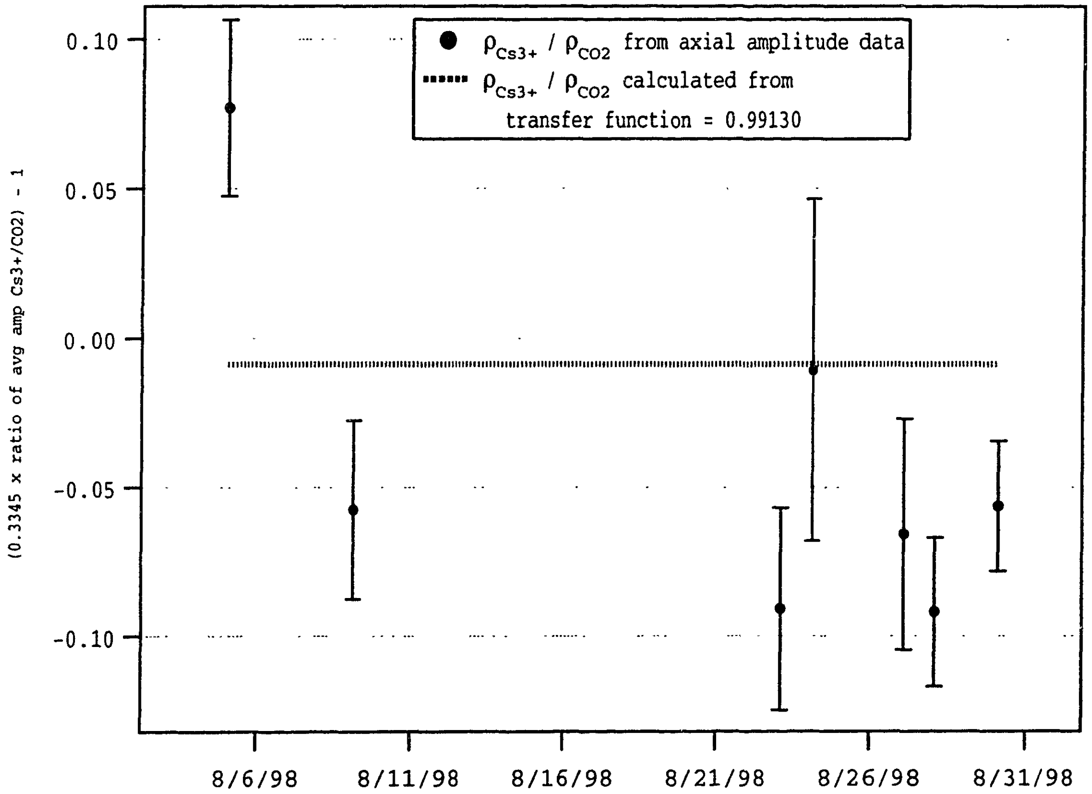

Figure 4-8: Mean cyclotron radii ratios for Cs^{+++}/CO_2^+ data

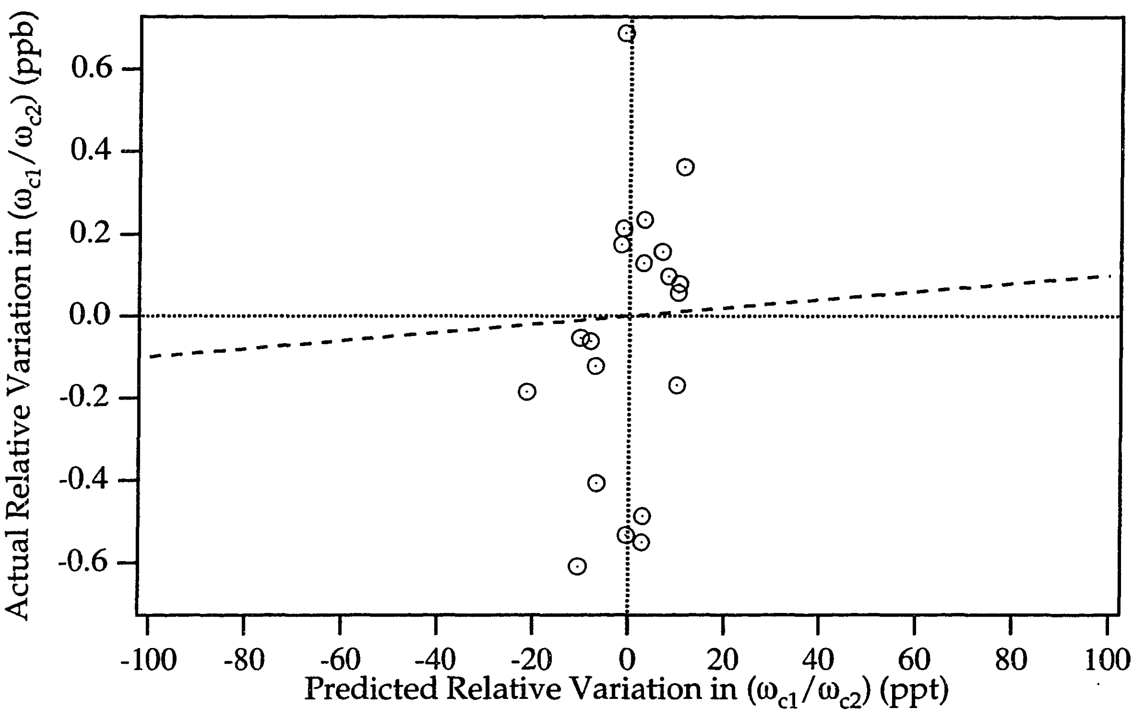

Figure 4-9: Search for correlation between actual observed mass ratio fluctuations and values predicted from observed amplitude variations. It is obvious from the plot that there is no correlation between the real and predicted variations, and also that the actual variations are much much greater than the predicted variations.

shifts are much too large to be explained by the predicted data. It is very interesting to note that the predicted shifts are the greatest for the Na measurements, because of their large relativistic shifts, but that the actual variations of the ratio are smallest for Na. Thus we are led to discount the possibility of radius dependent frequency shifts as a source of our unexplained variations, although the reason for the variation in radii remains an unresolved mystery.

4.8.4 Summary of Other Possible Causes

We considered the magnitude of the effect of varying charge patches causing ion displacements, variable trap tilts, and the effect of possible higher order electrostatic terms in combination with the varying cyclotron radii. None of these effects contributed significantly above 0.01 ppb of uncertainty, and hence none were the cause of the excess scatter.

4.8.5 Adjustment of χ^2

Despite our search for explanations, none of the effects considered above was able to explain the observed night-to-night scatter. Our multiple data runs convinced us of the random character of the scatter, so we wished to quote an uncertainty which reflected this scatter. Following Bevington and Robinson, we adopted the approach of rescaling the predicted uncertainties on the ratios (σ_i) by the factor χ_ν so that when χ_ν^2 is recalculated with these new uncertainties:

$$\sigma_i'^2 = \chi_\nu^2 \sigma_i^2 \tag{4.26}$$

we obtain $(\chi_\nu^2)' = 1$. Thus adjusting the uncertainties by the factor χ_ν brings the predicted uncertainties into agreement with the observed scatter. We then have

$$\bar{\sigma}'^2 \equiv \left(\frac{N}{\sum_i 1/(\chi_\nu^2 \sigma_i^2)}\right) = \frac{\sum_i (r_i - \bar{r})^2/\sigma_i^2}{(N-1)} \left(\frac{N}{\sum_i 1/\sigma^2}\right) = \sigma_{var}^2 \tag{4.27}$$

so that this rescaling is equivalent to taking σ_{var} as our measure of scatter.

We used this method to rescale the uncertainties for the Cs^{+++}/CO_2^+ and $Cs^{++}/C_5H_6^+$ measurements separately. For the ^{85,87}Rb measurements we assumed that all the measurements had the same distribution of uncertainties. Thus we computed for all the ^{85,87}Rb measurements a single common value of χ_ν^2. We did not adjust the uncertainties for the Na measurements because they did not exhibit night-to-night scatter in excess of the fit uncertainties. Table 4.12 in Section 4.9 gives the final values for the measured mass ratios and their uncertainties.

4.9 Measured Values for Alkali Frequency Ratios

This section details the averaging process used to extract final data values from the measured cyclotron frequency ratios for the alkali metal data. It expands upon the discussion of this given in the Physical Review Letter reprinted at the end of this chapter.

The final value for the alkali metal cyclotron frequency ratios were arrived at in the

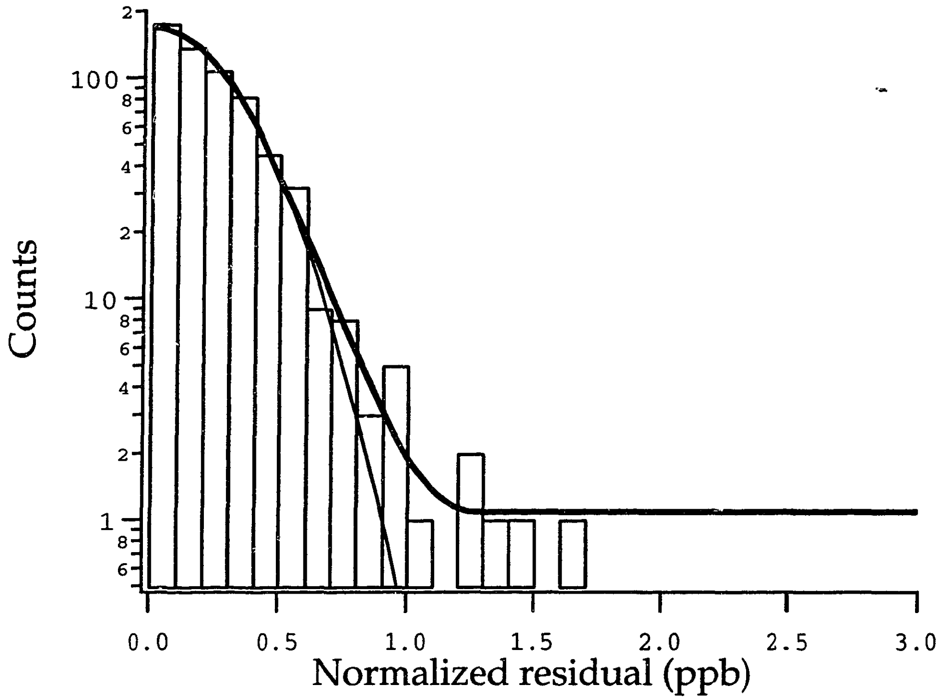

Figure 4-10: Histogram of deviations from least squares fits to all the alkali data excluding the $Cs^{++}/C_5H_6^+$ data (this data is excluded because of its larger standard deviation due to the low value of ω_z. See Fig. 4-11). The gaussian standard deviation is $\sigma = 2.82 \times 10^{-10}$ and the Hampel estimator parameters are $(a, b, c) = (1.7, 3.11, 4.53)$. Only 0.5 % of the points are completely deweighted.

following way. First we robust analyzed the data using the robust estimators shown in Fig. 4-10 and Fig. 4-11. In a few instances we adjusted the results of the robust fits to obtain final values. The results of the robust fits, the adjustments and the reasons for them, and the final values used are all given in Table ??. Next we computed the weighted average of the robust results $\bar{r}_{poly}$ and the uncertainty $\tilde{\sigma}_{poly}$ based on the average weighted variance. (The subscript *poly* is intended to indicate "polynomial", the type of function fit to using the robust fits). Similarly, we computed weighted averages of the frequency ratios obtained from nearest-neighbor (r_{nn}) and piecewise linear (r_{pl}) analyses of the data.

Finally, we assigned a final value to the ratio of $\bar{r} = 1/2[\bar{r}_{poly} + 1/2\bar{r}']$ (where $\bar{r}'_{pl} \equiv 1/2(\bar{r}_{pl} + \bar{r}_{NN})$) and a final error $\tilde{\sigma} = [\tilde{\sigma}_{poly} + ((\bar{r}_{poly} - \bar{r}_{pl})/2)^2]^{1/2}$. $\bar{r}$ and $\tilde{\sigma}$ are the final values before systematic corrections are applied.

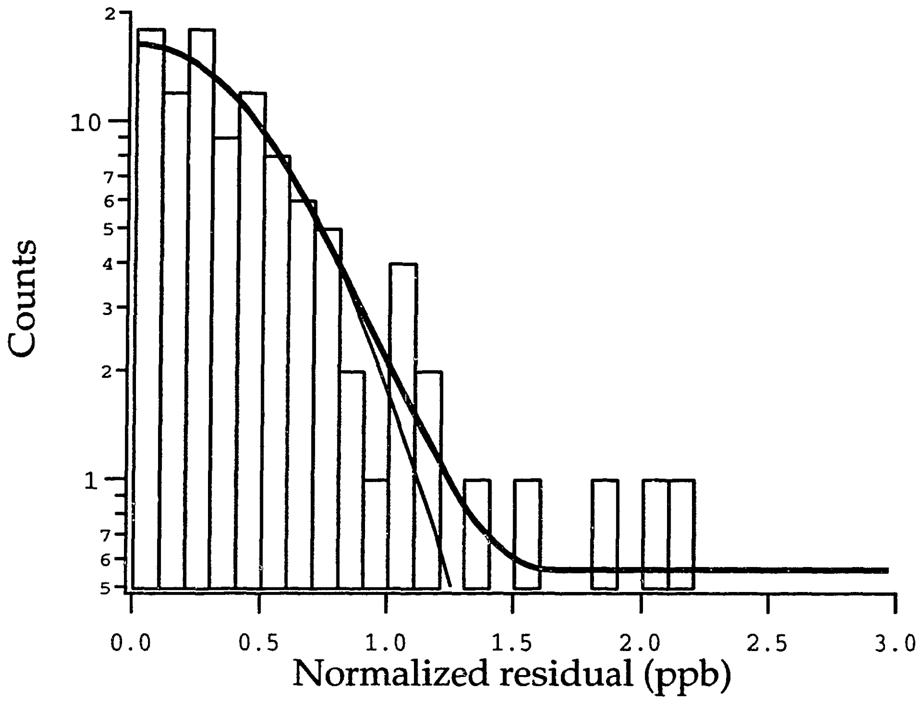

Figure 4-11: Histogram of deviations from least squares fits for the Cs^{++}/C$_5$H$_6^+$ data only. This data has a larger gaussian standard deviation than the rest of the alkali data because the axial frequency fluctuations have greater influence due to the low cyclotron frequency. The gaussian standard deviation is $\sigma = 4.7 \times 10^{-10}$ and the Hampel estimator parameters are $(a, b, c) = (1.5, 2.5, 3.5)$. Only 3 % of the points are completely deweighted.

Table 4.9: Table of final adjusted robust fit results, averaged over all nights for each mass ratio, with an adjusted uncertainty to accurately reflect the anomalously high scatter. We obtain the adjusted uncertainty σ_{poly} using the formula $\tilde{\sigma}_{poly} = \sqrt{\chi^2_\nu} \times \bar{\sigma}/\sqrt{N}$. Note that we used the joint value of χ^2_ν for the Rb data adjustments, and that we did not adjust the uncertainties for the Na data.

Freq. Ratio	$\bar{r}$ offset	$\bar{r}_{poly}$	N	$\bar{\sigma}$	χ^2_ν	$\tilde{\sigma}_{poly}$
Cs+++/CO2	0.992957580	0.934	5	0.136	4.90	0.135
Cs++/C5H6	1.006143799	0.058	4	0.255	6.64	0.329
Rb87++/C3H8	1.013992022	0.609	2	0.155	4.75	0.239
Rb87++/C3H7	0.990799127	0.803	3	0.116	4.75	0.146
Rb85++/C3H7	1.014106122	0.192	2	0.103	4.75	0.158
Rb85++/C3H6	0.990367650	0.794	2	0.158	4.75	0.243
Na+/C2	1.043943669	0.644	2	0.090	1.47	0.064
Na++/C	1.043944716	0.622	2	0.110	0.052	0.078

Table 4.10: Table of final averaged robust fit and piecewise linear results averaged over all nights for each mass ratio.

Freq. Ratio	$\bar{r}$ offset	$\bar{r}_{poly}$	$\tilde{\sigma}_{poly}$	$\bar{r}_{pl}$	$\bar{r}$	$\tilde{\sigma}$
Cs+++/CO2	0.992957580	0.934	0.135	0.912	0.923	0.135
Cs++/C5H6	1.006143799	0.058	0.329	0.621	0.340	0.433
Rb87++/C3H8	1.013992022	0.609	0.253	0.503	0.557	0.258
Rb87++/C3H7	0.990799127	0.803	0.177	0.790	0.797	0.177
Rb85++/C3H7	1.014106122	0.192	0.159	0.200	0.196	0.159
Rb85++/C3H6	0.990367650	0.794	0.243	1.104	0.949	0.291
Na+/C2	1.043943669	0.644	0.064	0.693	0.669	0.068
Na++/C	1.043944716	0.622	0.078	0.580	0.601	0.080

Table 4.11: Table detailing the application of image charge shift, trap equilibrium position shift, and radius-dependent systematic corrections to the data. All shifts are in ppb

A/B	Offset	Uncorr. $\bar{r}_{poly}$	$\tilde{\sigma}_{poly}$	Image	LEC	Final $\bar{r}$	σ
Cs+++/CO2	0.992957580	0.923	0.135	0.0622	-0.0017	0.983	0.135
Cs2+/C5H6	1.006143799	0.340	0.433	-0.0473	0.0012	0.293	0.433
Rb87++/C3H8	1.013992022	0.557	0.258	0.0306	0.0027	0.590	0.258
Rb87++/C3H7	0.990799127	0.797	0.177	0.0310	-0.0028	0.825	0.177
Rb85++/C3H7	1.014106122	0.196	0.159	0.0299	0.0028	0.2287	0.159
Rb85++/C3H6	0.990367650	0.949	0.291	0.0303	-0.0029	0.976	0.291
Na+/C2	1.043943669	0.669	0.068	0.000	0.0188	0.688	0.070
Na++/C	1.043944716	0.601	0.080	0.0080	0.0376	0.647	0.090

4.10 Systematic Corrections

Table 4.11 details the corrections for the image-charge shift, trap equilibrium position shift, and cyclotron radius dependent shifts discussed in Chapter 2.

Table 4.12: Final values of the measured ion cyclotron frequency ratios. For the Cs and Rb measurements the uncertainties were increased to reflect the unexplained night-to-night scatter.

ion A / ion B	ω_c[A] / ω_c[B]
^{133}Cs^{+++}/CO$_2^+$	0.992 957 580 983 (135)
^{133}Cs^{++}/C$_5$H$_6^+$	0.993 893 716 487 (427)
^{87}Rb^{++}/C$_3$H$_8^+$	1.013 992 022 591 (266)
^{87}Rb^{++}/C$_3$H$_7^+$	0.990 799 127 824 (174)
^{85}Rb^{++}/C$_3$H$_7^+$	1.014 106 122 230 (164)
^{85}Rb^{++}/C$_3$H$_6^+$	0.990 367 650 976 (285)
^{23}Na$^+$/C$_2^+$	1.043 943 669 690 (076)
^{23}Na^{++}/C$^+$	1.043 944 716 614 (098)

4.11 From frequency ratios to neutral mass differences

To convert from ion frequency ratios r to neutral mass ratios we account for the mass of the missing electrons [AUW93] as well as the ionization and chemical binding energies for the species involved. The details of this procedure are given in Chapter 5, Section 5.4.1. I summarize them briefly here, with particular attention to mass comparisons involving multiply charged ions.

We have the result for a neutral mass difference:

$$m_1^{neut} - m_2^{neut} = \left(\frac{q_1}{q_2}\right)(r_{12}-1)m_2^{neut} - q_1(r_{12}-1)m_e - \left(\frac{q_1}{q_2}\right) r_{12}\Delta E_2 - \Delta E_1 \tag{4.28}$$

where the ion and neutral masses are related by

$$m_i^{ion} = m_i^{neut} - q_i m_e + \Delta E_i \tag{4.29}$$

and the quantity ΔE_i is given by the difference between the heat of formation of the ion minus the heat of formation of its constituents. Table 4.13 gives the alkali metal ionization energies, and Table 4.14 the heats of formation used to compute the values of ΔE in Table 4.15.

It is worthwhile to briefly consider at what level uncertainties in the chemical binding energies contribute to the uncertainty on the final values of the neutral atomic masses. We will see that these uncertainties do not contribute more than $\sim 1 \times 10^{-11}$ to the uncertainty on the final mass.

The process of ionization by our $\approx$ 500 eV electron beam is likely to result in a complex molecular ion like $C_5H_6^+$ having significant vibrational and rotational energy. Vibrational energies are ≈ 1500 cm^{-1} $= 0.2\ eV$ for C-C bonds and ≈ 3000 cm^{-1} $=$ 0.4 eV for C-H bonds, so excited vibrational modes may contribute several parts in 10^{-11} to the mass of a $\sim$ 40 u molecule. These mass shifts will not affect our mass measurements because in most cases vibrational energy radiates on msec timescales (Homonuclear ions like C_2^+ are an exception, having radiative lifetimes $\sim$ 1 minute.)

We must also consider rotational energy levels. Molecular rotational energy level spacings are of the order of 1 cm^{-1}, so many are populated at 300 K. The change in going from 300K to 4 K is therefore $\sim 0.025eV$, which is $\Delta m/m \sim 1 \times 10^{-12}$ for H_2. Because rotational levels have very slow radiative decay rates we cannot necessarily expect the rotational energy to equilibrate to 4 K over our experimental timescale. However, we may ignore the $\sim 10^{-12}$ relative mass shift caused by residual rotational excitation.

Finally, it is worth noting that the different conformations of a complex molecule like C_5H_6 can differ in energy by as much as 1 eV (Fig. 4-12), resulting in relative mass variations $\sim 1 \times 10^{-11}$.

4.12 From mass differences to neutral masses: matrix inversion

After correcting the ion mass ratios for the image charge shift and chemical binding energies we have a set of neutral mass difference equations.

Table 4.13: Alkali ionization energies. The conversion factor to u is 1 eV = 1.073 543 9 × 10^{-9} u. The largest contribution to the uncertainty on a final mass is 8 × 10^{-12} from the Cs^{+++} value.

Ionization	eV	$\times 10^{-9}$ u
$Cs \rightarrow Cs^{+} + e^{-}$	3.893	4.179
$Cs^{+} \rightarrow Cs^{++} + e^{-}$	25.1	26.946
$Cs^{++} \rightarrow Cs^{+++} + e^{-}$	35	37.574
$Rb \rightarrow Rb^{+} + e^{-}$	4.177	4.484
$Rb^{+} \rightarrow Rb^{++} + e^{-}$	27.5	29.522
$Na \rightarrow Na^{+} + e^{-}$	5.139	5.517
$Na^{+} \rightarrow Na^{++} + e^{-}$	47.29	50.768

Table 4.14: Heats of formation. The conversion factors are 1 kJ/mol = 1.112 65 × 10^{-11} u and 1 eV/atom = 96.485 3 kJ/mol.

Species	$\Delta_f H^0$ (kJ/mol)	$\Delta_f H^0$ ($\times 10^{-9}$ u)
H	217.999	2.426
CO_2^+	935.756	10.412
O	249.173	2.772
C	716.669	797.402
C^+	1809.438	20.133
C_2^+	1937.670	21.559
$C_5H_6^+$	1115.241	12.409
$C_3H_8^+$	950.850	10.580
$C_3H_7^+$	840.883	9.356
$C_3H_6^+$	978.429	10.886
Cs	76.500	0.851
Cs^+	458.403	5.100
Cs^{++}	2880.184	32.046
Cs^{+++}	6257.170	69.620
Rb	80.900	0.900
Rb^+	490.131	5.453
Rb^{++}	3143.476	34.976
Na	107.300	1.194
Na^+	609.345	6.780
Na^{++}	5172.135	57.548

Table 4.15: Table of Values of ΔE for alkali metal measurements. The conversion factor is 1 kJ/mol = 1.112 65 × 10^{-11} u.

Species	ΔE (kJ/mol)	ΔE ($\times 10^{-9}$ u)
Cs^{+++}	6180.67	68.769
CO_2^+	-216.912	-2.413
Cs^{++}	2803.68	31.195
$C_5H_6^+$	-3776.1	-42.015
Rb^{++}	3062.58	34.076
$C_3H_8^+$	-2943.15	-32.747
$C_3H_7^+$	-2835.12	-31.545
$C_3H_6^+$	-2479.57	-27.589
Na^+	502.045	5.586
Na^{++}	5064.84	56.354
Cs^+	1092.77	12.159
C_2^+	-63.338	-0.705

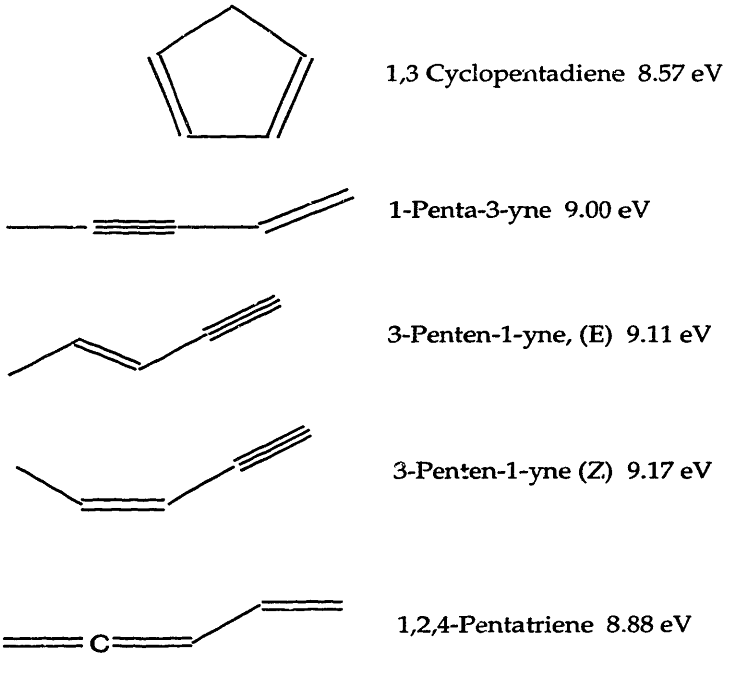

Figure 4-12: Ionization energies of C_5H_6 conformations.

$$\sum x_{ij} m_j = y_i \pm \sigma_i \tag{4.30}$$

where x_{ij} are the integer coefficients of the mass difference equations, and the m_j are the individual masses, and the y_i are the experimentally measured values of the mass differences (obtained from Eq. 4.28, and the σ_i are the uncertainties. Because of our use of two distinct routes to each mass, this set of equations is overdetermined. Our standard procedure for solving this overdetermined set of mass difference equations is detailed in Chapter 5, Section 5.4.2.

For each alkali metal isotope we measured two distinct frequency ratios. The use of two distinct reference ions provided a powerful check on systematics by allowing the computation of two independent values for each neutral mass. These values are listed in Table 4.16. Because of the larger final uncertainty on the value obtained from M[Cs] from the $\mathrm{Cs^{++}C_5H_6^+}$ measurement we quote a final uncertainty of 0.2 ppb on the neutral mass of Cs, an uncertainty which is somewhat larger than the 0.16 ppb obtained by solving the complete system of mass difference equations. The uncertainties assigned to $M[^{87,85}\mathrm{Rb}]$ are simply the predicted statistical uncertainties from the solution of the set of mass difference equations. We assigned the final value for $M[^{23}\mathrm{Na}]$ an uncertainty of 0.12 ppb so that the final error bar would span both independent measurements.

The overall value of χ^2_ν for the solution of the overdetermined set of mass difference equations was $\chi^2_\nu = 0.83$. (Recall that the mass differences used in this calculation were obtained from the set of measured mass ratios *after* the uncertainties on the Cs and Rb mass ratios were adjusted as described in Section 4.8.5.)

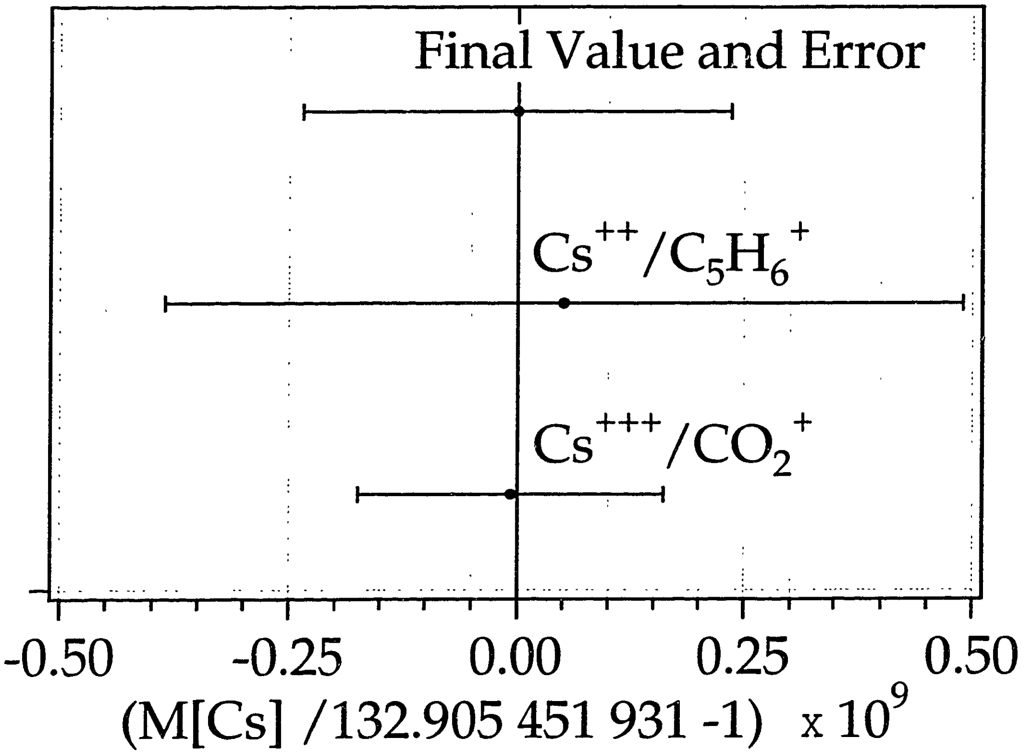

Figure 4-13: Final values of $M[^{133}\mathrm{Cs}]$. We quote a final uncertainty of 0.2 ppb on the neutral mass of Cs, (a value larger than the 0.16 ppb obtained by solving the complete set of mass difference equations) because of the relatively large uncertainty on the $Cs^{++}/C_5H_6^+$ ratio measurement.

Table 4.16: Alkali metal masses measured via different routes.

Species	Ref. ion	Mass (u)	σ_M/M (ppb)	χ^2_ν
^{133}Cs	CO_2^+	132.905 451 931 (22)	0.17	0.003
^{133}Cs	$C_5H_6^+$	132.905 451 934 (57)	0.43	0.003
^{87}Rb	$C_3H_8^+$	86.909 180 540 (24)	0.28	0.92
^{87}Rb	$C_3H_7^+$	86.909 180 511 (17)	0.19	0.92
^{85}Rb	$C_3H_7^+$	84.911 789 737 (15)	0.18	0.45
^{85}Rb	$C_3H_6^+$	84.911 789 717 (25)	0.30	0.45
^{23}Na	C_2^+	22.989 769 278 9(17)	0.07	2.97
^{23}Na	C^+	22.989 769 283 7 (22)	0.09	2.97

Table 4.17: The atomic masses of the alkali metal atoms ^{133}Cs, ^{87,85}Rb, and ^{23}Na as measured at MIT, and the previous most accurate values [AUW93]. The uncertainties on the mass values in the second column are given in parentheses. The "Error" column gives the relative uncertainty in parts per billion. The final column gives the difference between the MIT value and the previous value, expressed in ppb.

Species	Mass (u)	Error (ppb)	(MIT - prev) (ppb)
^{133}Cs [MIT]	132.905 451 931 (27)	0.2	1.64
^{133}Cs [prev]	132.905 447 000 (3000)	23.0	–
^{87}Rb [MIT]	86.909 180 520 (15)	0.17	-1.89
^{87}Rb [prev]	86.909 185 800 (2800)	32.0	–
^{85}Rb [MIT]	84.911 789 732 (14)	0.17	-0.99
^{85}Rb [prev]	84.911 792 400 (2700)	32.0	–
^{23}Na [MIT]	22.989 769 280 7 (28)	0.12	-1.46
^{23}Na [prev]	22.989 769 660 0 (2600)	11.0	–

Table 4.18: Three different measurements of the atomic mass of ^{133}Cs. We calculated the SMILETRAP value of $M[^{133}\text{Cs}]$ using their value for $M[^{133}\text{Cs}]/M[p] =$ 131.945 355 91 (24)(15) [CFB99], and our value for $M[p] = 1.007\ 276\ 466\ 3\ (5)$ u [DNB94]. The first number in parentheses following the SMILETRAP value is the statistical uncertainty; the second is an estimate of the total systematic uncertainty.

Measurement	Mass (u)	Error (ppb)
MIT	132.905 451 931 (27)	0.2
SMILETRAP	132.905 451 846 (248)(166)	1.9 (random)
Previous [AUW93]	132.905 447 000 (3000)	0.2

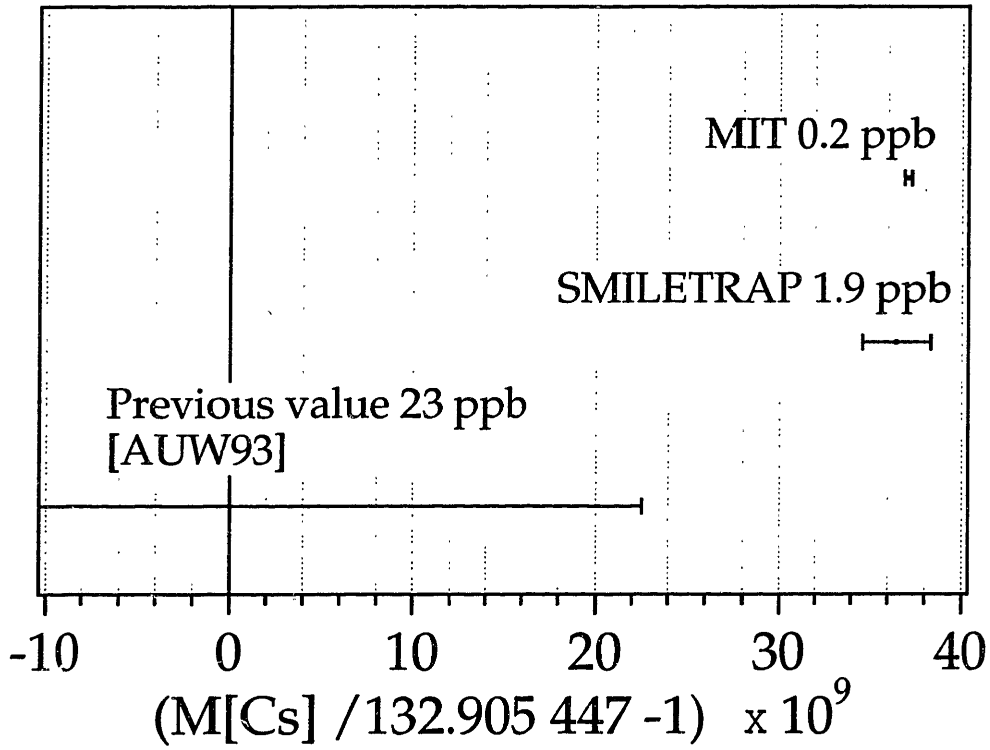

Figure 4-14: Plotted is our final value for $M[^{133}\text{Cs}]$, along with the previous 23 ppb value [AUW93] and the measurement of the SMILETRAP group [CFB99].

4.13 Final value of α

4.13.1 Calculation of M[Cs]/M[p]

We first must calculate M[p]. We have

$$\mathrm{M[p]} = \mathrm{M[H]} - \mathrm{M[e]} + \frac{\Delta E}{c^2} \tag{4.31}$$

and thus

$$\mathrm{M[p]} = \left[\mathrm{M[H]} + \frac{\Delta E}{c^2}\right] / \left[1 + \frac{\mathrm{M[p]}}{\mathrm{M[e]}}\right] \tag{4.32}$$

Table 4.19 lists the values needed to calculate M[p].

The contribution to the uncertainty in M[p] from $\Delta E/c^2$ and M[p]/M[e] are much smaller than the contribution from M[H] and can be ignored. Using these numbers we get

$$\mathrm{M[p]} = 1.007\,276\,466\,3\,(5)u \tag{4.33}$$

which we can compare with the latest result from the group of van Dyck et al.

$$M[p] = 1.007\,276\,466\,89\,(14)u \tag{4.34}$$

The two values agree within uncertainties. Now we can use this result to compute M[Cs]/M[p]. For completeness we take account of the experimental covariance between our measured values of M[Cs] and M[H], using the standard result for the error in a ratio $x = u/v$ including the covariance σ_{uv}^2:

$$(\frac{\sigma_x}{x})^2 = (\frac{\sigma_u}{u})^2 + (\frac{\sigma_v}{v})^2 - 2\frac{\sigma_{uv}^2}{uv} \tag{4.35}$$

and the covariance of our measurements of Cs and H $\sigma_{Cs-H} = 5.34 \times 10^{-18}$ u^2 we get

Table 4.19: Quantities for calculating M[Cs]/M[p]. Note that we convert the binding energy from eV to u using the conversion factor 1 eV = 1.073 544 38 (8) $\times 10^{-9}$ u

Quantity	Value	Reference
M[H]	1.007 825 031 6 (5) u	[DNB94]
$\Delta E/c^2$	13.595 eV	[CRC handbook]
M[p]/M[e]	1836.152 666 5 (40)	[FVS95]

$$\frac{\mathrm{M[Cs]}}{\mathrm{M[p]}} = 131.945\,355\,994\,(60) \tag{4.36}$$

This agrees within experimental uncertainties with the value measured by the SMILETRAP collaboration:

$$\frac{\mathrm{M[Cs]}}{\mathrm{M[p]}} = 131.945\,355\,91\,(24)(16) \tag{4.37}$$

4.13.2 Calculation of α

Using our measured value of $M(^{133}Cs)$ we are able to extract a final value for α by combining h/m_{Cs} from Chu's group with our value.

$$\alpha^2 = \frac{2R_\infty}{c}\frac{h}{m_e} \tag{4.38}$$

leading to

$$\alpha^2 = \frac{2R_\infty}{c}\frac{h}{m_{Cs}}\frac{m_{Cs}}{m_p}\frac{m_p}{m_e} \tag{4.39}$$

and finally

$$\alpha^2 = cR_\infty\frac{m_p}{m_e}\frac{m_{Cs}}{m_p}\frac{\Delta f_{rec}}{\nu^2} \tag{4.40}$$

Using the values from Table 4.20 we get

$$\alpha^{-1} = 137.035\,992\,2\,(40) \tag{4.41}$$

Table 4.20: Calculation of α.

Quantity	Value	Ref.
c	299 752 458 m/sec	exact
R_∞	10 973 731.568 516 (84) m^{-1}	[SJD99]
(m_p/m_e)	1836.152 666 5 (40)	[FVS95]
(m_{Cs})	132.905 451 931 (27)	[BPR99]
(m_p)	1.007 276 466 292 (500)	[DNB94]
Δf_{rec}	30 012.557 3 (16) (7) Hz	[YOU97]
ν	2× 335 115 966 522 (30) kHz	[URH99]

4.14 Conclusions

In this chapter I have discussed at length our measurements of mass ratios leading to neutral atomic mass values for ^{133}Cs, ^{87,85}Rb, and ^{23}Na. Here I summarize the results.

- Using the new spectrometer described in Chapter 3 (which incorporated a DC SQUID for the first time) we measured the masses of the alkali metal atoms ^{133}Cs, ^{87,85}Rb, and ^{23}Na.
- The measurement of $M[^{133}\mathrm{Cs}]$ extended our mass range by a factor of ~ 3, since previously the heaviest species we had measured was ^{40}Ar.
- The measurements reduced the uncertainty on $M[^{133}\mathrm{Cs}]$ by a factor of 115, on $M[^{87,85}\mathrm{Rb}]$ by a factor of 160, and on $M[^{23}\mathrm{Na}]$ by a factor of 90, nearly 2 orders of magnitude in each case.
- The value of $M[^{133}\mathrm{Cs}]$ is 38 ppb heavier than the previous best measured value. It agrees within 0.6 ppb with the recent measurement by the SMILETRAP group.
- The measurement of $M[^{133}\mathrm{Cs}]$ removes the uncertainty on $M[^{133}\mathrm{Cs}]$ as an obstacle to the attainment of a ppb-level value of α by the photon-recoil/mass spectrometry route.

4.15 Paper: Penning Trap Measurements of the Masses of ^{133}Cs, ^{87,85}Rb, and ^{23}Na with Uncertainties ≤ 0.2 ppb

VOLUME 83, NUMBER 22 PHYSICAL REVIEW LETTERS 29 NOVEMBER 1999

Penning Trap Measurements of the Masses of ^{133}Cs, ^{87,85}Rb, and ^{23}Na with Uncertainties $\leq$0.2 ppb

Michael P. Bradley, James V. Porto,* Simon Rainville, James K. Thompson, and David E. Pritchard

Department of Physics and Research Laboratory of Electronics, Massachusetts Institute of Technology, Cambridge, Massachusetts 02139

(Received 19 April 1999)

We report new values from Penning trap single ion mass spectrometry for the atomic masses of ^{133}Cs, ^{87}Rb, ^{85}Rb, and ^{23}Na with uncertainties $\leq$0.2 ppb, a factor of 100 improvement over the accuracy of previously measured values. We have found $M(^{133}\mathrm{Cs}) = 132.905\,451\,931(27)u$, $M(^{87}\mathrm{Rb}) = 86.909\,180\,520(15)u$, $M(^{85}\mathrm{Rb}) = 84.911\,789\,732(14)u$, and $M(^{23}\mathrm{Na}) = 22.989\,769\,280\,7(28)u$. These values are important for new ppb-level determinations of the molar Planck constant $N_A h$ and the fine-structure constant α. With the measurement of ^{133}Cs we have increased the mass range for sub-ppb measurements by a factor of 3. From $M(^{133}\mathrm{Cs})$ and other values we derive $\alpha^{-1} = 137.035\,992\,2(40)$.

PACS numbers: 32.10.Bi, 06.20.Jr, 07.75.+h

The fine-structure constant α is one of the most fundamental and best-measured quantities in physics, but the discrepancies between different precision measurements of α are noteworthy [1]. The most precise value α_{g-2} (uncertainty $=$3.8 ppb $\equiv$ 3.8 parts in 10^9) has been obtained from the measured values of $(g - 2)$ for the electron and positron and complex QED calculations [2,3]. Unfortunately, the next most precise measurements of α (24 ppb using the quantum Hall effect [4,5] and 37 ppb via neutron interferometry [6]) disagree with the $(g - 2)$ value. Thus to test the unity of physics and QED there is a need for new ppb-level measurements to compare with α_{g-2}.

A high-precision route to α founded on simple physics with no complex calculations is based on the relationship between α and the molar Planck constant $N_A h$ [7],

$$\alpha^2 = \frac{2R_\infty}{c} \frac{10^3}{M_p} \frac{m_p}{m_e} (N_A h)\,. \tag{1}$$

All the quantities linking α and $N_A h$ in Eq. (1) are accurately known: R_∞ to 0.008 ppb [8,9], m_p/m_e to 2 ppb [10], and M_p (the proton mass in atomic units u) measured by our group to 0.5 ppb [11] (Van Dyck *et al.* have recently reported a value of M_p accurate to 0.14 ppb [12]). Thus an independent measurement of $N_A h$ to 2 ppb would determine α to 1.4 ppb, a precision sufficient to test α_{g-2}. The most complicated calculations for this method are the computations of the $2P_{1/2}$, $2P_{3/2}$, and $8D$ Lamb shifts to allow R_∞ to be obtained from measurements of the $1S$-$2S$ and $2S$-$8D$ transitions in hydrogen [9]. The largest calculational uncertainty contribution to R_∞ is 0.000 26 ppb due to the $8D$ Lamb shift.

$N_A h$ can be determined by measuring the velocity v and de Broglie wavelength $\lambda_{dB} \equiv h/mv$ of a particle, since $\lambda_{dB} v = h/m = 10^3 N_A h/M$, where m is the mass of the particle in SI units. Kruger *et al.* exploited this method using neutron interferometry to measure h/m_n with 73 ppb precision [6]. Combining this with a precise measurement of M_n (from Penning trap measurements of $M[^2\mathrm{H}]$, $M[^1\mathrm{H}]$ and γ-ray measurements of the nuclear binding energy of ^{2}H [11,13,14]) gave a value of α with a precision of 37 ppb, again not sufficient to stringently test α_{g-2}.

It appears that measurements of $N_A h$ of much higher precision can be made by combining accurate atom interferometry measurements of h/m for alkalis with the ~0.1 ppb measurements of M possible using Penning traps. At Stanford atom interferometry is used to measure h/m_{Cs} via photon recoil [15] in terms of λ_{D1} (recently measured to 0.12 ppb at Max-Planck-Institut Garching [16]). Although systematic effects in the photon recoil measurement currently limit the accuracy to 55 ppb, the high precision achieved (22 ppb in 4 h) [17] shows much promise. Moreover, advances in alkali Bose-Einstein condensation technology hold great promise for similar atom interferometry measurements on Na and Rb. With measurements of h/m_{alkali} in mind, we have measured the atomic masses of the stable alkali metal isotopes ^{133}Cs, ^{87,85}Rb, and ^{23}Na. The previous mass accuracies [18] (see Table IV) would have limited the accuracy of $N_A h$ to several tens of ppb.

There are additional motivations for our measurements. New values of $N_A h$ at the few-ppb level in combination with measurements of h (such as a recent 87 ppb measurement, expected to be improved by a factor of 10 [19]) can yield values of N_A with ppb-level accuracy. Since N_A links the atomic and SI units of mass this is of great interest [7]. Furthermore, Cs and Rb are used as reference masses for measurements of heavy radioactive nuclei which are important for modeling astrophysical heavy element formation [20,21].

We obtain absolute atomic masses M from mass ratios relating the unknown mass to the atomic mass standard ^{12}C. Ion mass ratios are obtained from ratios of measured cyclotron frequencies $\omega_c = qB/mc$, where m and q are, respectively, the ion mass and charge. We make precise cyclotron frequency measurements on a single ion confined in an orthogonally compensated Penning trap [22] of characteristic size $d = 0.55$ cm placed in the $B = 8.5$ T field of a superconducting magnet. Use of a trapped single ion takes advantage of long observation times in the absence of perturbations from ion-ion interactions and allows sub-ppb precision.

An ion in our Penning trap has three normal modes of motion: trap cyclotron, axial, and magnetron, with frequencies $\omega_c' \gg \omega_z \approx 2\pi \times 160$ kHz $\gg \omega_m$, respectively. The free-space cyclotron frequency ω_c is obtained from the following expression (invariant with respect to trap tilts and ellipticity) [22]:

$$\omega_c = qB/mc = \sqrt{(\omega_c')^2 + (\omega_z)^2 + (\omega_m)^2}. \qquad (2)$$

We detect axial motion by coupling to a dc SQUID via a $Q = 5 \times 10^4$ superconducting resonant transformer. Detection damps the axial motion at a rate $\gamma_z \sim 1$ s^{-1} and cools it to 4 K. The amplitude and phase of the undamped trap cyclotron mode are measured via coupling to the axial mode established by an rf quadrupole field at frequency $\omega_\pi = \omega_c' - \omega_z$ [23]. (This coupling is also used to cool the radial modes.) We obtain ω_c' from the phase accumulated in the cyclotron mode in a given time. Using the measured values of ω_c' and ω_z we calculate $\omega_m \approx (\omega_z^2/2\omega_c')(1 + 9/4\sin^2\theta_m)$, where $\theta_m = 0.16°$ is the measured angle between the B field and trap axes (the effect of θ_m on a mass ratio is at most 0.002 ppb).

We measured the free-space cyclotron frequency ratios $r \equiv \omega_{c2}/\omega_{c1}$ listed in Table I. A cyclotron frequency ratio r was determined by a run of alternately measured clusters of ω_c of each of the two ions during the period from 1:30–5:30 A.M. when the nearby electrically powered subway was not running (Fig. 1). The measured free-space cyclotron frequencies exhibited a common slow drift. We fit a common polynomial $\Omega(t)$ plus a frequency difference to the data. From this we obtained the frequency ratio r_n and the uncertainty σ_n for a single night. The average order of $\Omega(t)$ was 3 and was chosen using the F-test criterion [24] as a guide.

Excluding the Cs^{++}/C$_5$H$_6{}^+$ data, the distribution of residuals from the polynomial fits had a Gaussian center with a standard deviation $\sigma_{\text{resid}} = 0.28$ ppb and a background ($\approx$2% of the points) of non-Gaussian outliers, as in our earlier measurements [11]. As in [11] we chose to handle the non-Gaussian outliers using a robust statistical method to smoothly deweight them [25]. The observed random fluctuations of the measured free-space cyclotron frequency should limit the precision of a one-night (4 h) measurement of r_n to ~0.1 ppb. These fluctuations are due primarily to variations of the magnetic field; however, for heavy ions with low ω_c uncertainty in ω_z can contribute significantly to uncertainty in ω_c. Thus stability of the trapping voltage is important. Our trap voltage exhibits long-term rms fluctuations of only 100 ppb and so contributes below 0.1 ppb uncertainty to a night's measurement. Observed variations in the axial frequency ~20 mHz are dominated by measurement error and contribute at most ~0.25 ppb to a single cluster for Cs^{++}/C$_5$H$_6{}^+$ (the residuals for Cs^{++}/C$_5$H$_6{}^+$ had $\sigma_{\text{resid}} = 0.44$ ppb mainly because of this).

TABLE I. Measured ion cyclotron frequency ratios, corrected for systematics.

A/B	$\frac{\overline{\omega}_c}{2\pi}$ (MHz)	Nights	$\omega_c[A]/\omega_c[B]$
^{133}Cs^{+++}/CO$_2{}^+$	2.968	5	0.992 957 580 983(135)
^{133}Cs^{++}/C$_5$H$_6{}^+$	1.977	4	0.993 893 716 487(427)
^{87}Rb^{++}/C$_3$H$_8{}^+$	2.994	2	1.013 992 022 591(266)
^{87}Rb^{++}/C$_3$H$_7{}^+$	3.028	3	0.990 799 127 824(174)
^{85}Rb^{++}/C$_3$H$_7{}^+$	3.064	2	1.014 106 122 230(164)
^{85}Rb^{++}/C$_3$H$_6{}^+$	3.100	2	0.990 367 650 976(285)
^{23}Na$^+$/C$_2{}^+$	5.578	2	1.043 943 669 690(076)
^{23}Na^{++}/C$^+$	11.155	2	1.043 944 716 614(098)

As shown in Table I we measured each frequency ratio on more than a single night. For ratios involving Cs and Rb the measured r_n were distributed with scatter $>\sigma_n$ ($\chi_\nu^2 \approx 5$). By contrast $\chi_\nu^2 \approx 0.8$ for ratios involving Na. All earlier data taken using this apparatus [11] did not exhibit these excess night-to-night variations. Possible sources of this excess scatter are presented in Table II and discussed below.

The axial frequency ω_z is "pulled" by its coupling to the detector by an amount $\Delta\omega_z = (\gamma_z/\gamma_0)(\omega_z - \omega_0)$, where ω_0 and $\gamma_0/2\pi = 3$ Hz are the detector resonance frequency and FWHM. We adjusted ω_z to be equal to the slowly drifting ω_0 (~50 mHz/h), measured before each alkali ion cluster. We then used the measured values of ω_z and ω_0 ($|\omega_z - \omega_0|$ typically <100 mHz) to correct the measured ω_z for the remaining pulling shift. Table II gives the rms difference in r_n for each night computed before and after applying this correction. The ~30% accuracy of our corrections implies that frequency pulling represents an error in our final ratios below 0.03 ppb and was not the source of the excess night-to-night fluctuations of r_n.

Relativistic mass variation and spatial imperfections $\Delta\vec{B} = -(B_2/2)\rho^2\hat{z}$ and $\Delta V/V_{\text{trap}} = -(3/16)(C_4/d^4)\rho^4$ [22] of the trap fields lead to radius-dependent shifts of the cyclotron frequency

$$\frac{\Delta\omega_c}{\omega_c} = \left(-\frac{\omega_c'^2}{2c^2} - \frac{B_2}{2B_0} + \frac{3\omega_m C_4}{2\omega_c d^2}\right)\rho^2. \qquad (3)$$

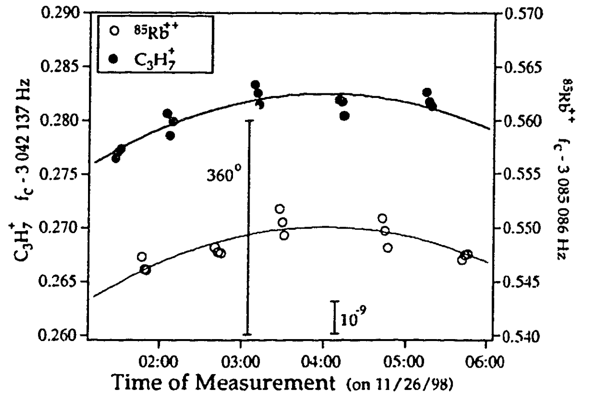

FIG. 1. Typical night of data. The solid line is a second order polynomial fit to the data. The 360° bar shows the magnitude in Hz of a 360° error in phase unwrapping.

TABLE II. Random uncertainties (σ) and systematic shifts (Δ) for frequency ratios r in ppt (parts per 10^{12}).

	$\frac{\mathrm{Cs}^{+++}}{\mathrm{CO_2}^+}$	$\frac{\mathrm{Cs}^{++}}{\mathrm{C_5H_6}^+}$	$\frac{\mathrm{Rb}^{++}}{\mathrm{C_3H}_x{}^+}$	$\frac{\mathrm{Na}^{+}}{\mathrm{C_2}^+}$	$\frac{\mathrm{Na}^{++}}{\mathrm{C}^+}$
$\sigma(r_n)/r$ axial frequency pulling	128	64	62	11	29
$\Delta r/r$ relativity[a]	2	1	7	4	79
$\Delta r/r$ B_2[a]	−2	−4	9	−13	−38
$\Delta r/r$ C_4[a]	−1	−4	2	−9	−6
$\Delta r/r$ different positions[b]	2	1	3	−19	−38

[a] These shifts in the ratio are due to systematic differences in the cyclotron radii ($\Delta\rho/\rho \approx 1\%$ to 7% with $\langle\rho\rangle = 230\ \mu\mathrm{m}$). $B_2/B_0 = -1 \times 10^{-6}/\mathrm{cm}^2$ and $|C_4| < 10^{-4}$.

[b] Shifts due to differential axial displacement (the largest being $\Delta z \approx 0.24\ \mu\mathrm{m}$ for $\mathrm{Na}^{++}/\mathrm{C}^+$) combined with the measured $B_1/B_0 = -1.6 \times 10^{-6}\ \mathrm{cm}^{-1}$.

For our trap $B_2/B_0 = 10^{-6}\ \mathrm{cm}^{-2}$ and $|C_4| < 10^{-4}$. Systematic differences in cyclotron orbit radii gave negligible systematic shifts in r except for $\mathrm{Na}^{++}/\mathrm{C}^+$ ($\Delta r/r = 0.035$ ppb). We adjusted the final ratio for this shift. To reflect uncertainty in the absolute radius ρ we assigned the adjustment a 50% uncertainty added in quadrature with the other uncertainties.

Table II gives the systematic shifts in r for differential displacements of ions from the geometric center of the trap (due to the electric field from fixed charge patches) in combination with B-field inhomogeneities. The z component of the patch electric field was measured with <10% uncertainty by applying offset potentials and measuring the quadratic shifts in ω_z, as described in [26]. $\mathrm{Na}^{++}/\mathrm{C}^+$ experienced the largest systematic shift $\Delta r/r = 0.08$ ppb. We adjusted all ratios for this systematic shift and assigned the adjustment a 100% uncertainty added in quadrature with the statistical uncertainty to reflect uncertainty concerning the radial component of the charge patch electric field.

The systematic shifts in Table II are constant from night to night and also are much too small to explain the observed night-to-night scatter.

To test the hypothesis that the excess night-to-night fluctuations were due to improper choice of fit order for $\Omega(t)$ we computed r_n by a completely different method. A value of r was calculated for each cluster in a night by taking the ratio of its frequency to the frequency obtained by linear interpolation between the two neighboring clusters of the other ion type. The values of r for each cluster were averaged to yield a single value of r_n for each night. This "piecewise linear" method and the polynomial fits gave similar night-to-night variations in r_n, suggesting that the variations were not polynomial fitting artifacts.

We calculated the weighted average, for the polynomial fit and piecewise linear methods separately, of the values of r_n. There was no statistically significant difference between these averages $\bar{r}_{\mathrm{poly}}$ and $\bar{r}_{\mathrm{pl}}$ except for $\mathrm{Cs}^{++}/\mathrm{C_5H_6}^+$ (0.57 ppb disagreement) due to one night with anomalously constant magnetic field, which gave a small uncertainty and hence significantly higher weight to that night's r_n computed with the piecewise linear method. To account for any such discrepancies we quote the average $\bar{r} = (1/2)(\bar{r}_{\mathrm{poly}} + \bar{r}_{\mathrm{pl}})$ and a final uncertainty $\bar{\sigma}^2 = \bar{\sigma}^2_{\mathrm{poly}} + [(\bar{r}_{\mathrm{poly}} - \bar{r}_{\mathrm{pl}})/2]^2$, where $\bar{\sigma}_{\mathrm{poly}}$ is the uncertainty in $\bar{r}_{\mathrm{poly}}$ after the rescaling described below.

Ultimately we did not discover the origin of the night-to-night fluctuations of r_n for Cs and Rb. We therefore increased the quoted statistical uncertainties to ensure that they reflect the observed night-to-night scatter. For $\mathrm{Cs}^{++}/\mathrm{C_5H_6}^+$ and $\mathrm{Cs}^{+++}/\mathrm{CO_2}^+$, we increased each night's statistical uncertainty until $\chi^2_\nu = 1$ (from 6.6 and 4.9, respectively) for each ratio separately. For the $^{87,85}\mathrm{Rb}$ ratios we assumed that the night-to-night fluctuations were drawn from a common statistical distribution since the Rb measurements all had similar m/q. Therefore, we increased the statistical uncertainty on all the Rb r_n by a common factor to reduce the overall Rb χ^2_ν from 4.7 to 1. The resulting increased statistical uncertainties for $\bar{r}_{\mathrm{poly}}$ are the $\bar{\sigma}_{\mathrm{poly}}$ used above. The Na ratios had no significant night-to-night fluctuations and required no adjustment of their uncertainties.

TABLE III. Measured alkali masses from different routes.

Species	Ref. ion	Mass (u)	σ_M/M (ppb)	χ^2_ν
$^{133}\mathrm{Cs}$	$\mathrm{CO_2}^+$	132.905 451 931(22)	0.17	0.003
	$\mathrm{C_5H_6}^+$	132.905 451 934(57)	0.43	
$^{87}\mathrm{Rb}$	$\mathrm{C_3H_8}^+$	86.909 180 540(24)	0.28	0.92
	$\mathrm{C_3H_7}^+$	86.909 180 511(17)	0.19	
$^{85}\mathrm{Rb}$	$\mathrm{C_3H_7}^+$	84.911 789 737(15)	0.18	0.45
	$\mathrm{C_3H_6}^+$	84.911 789 717(25)	0.30	
$^{23}\mathrm{Na}$	$\mathrm{C_2}^+$	22.989 769 278 9(17)	0.07	2.97
	C^+	22.989 769 283 7(22)	0.09	

TABLE IV. Measured neutral alkali masses.

Species	MIT Mass (u)	1993 Mass (u) [18]
^{133}Cs	132.905 451 931(27)	132.905 447 000(3000)
^{87}Rb	86.909 180 520(15)	86.909 185 800(2800)
^{85}Rb	84.911 789 732(14)	84.911 792 400(2700)
^{23}Na	22.989 769 280 7(28)	22.989 769 660 0(2600)

After correcting for a 93(1) μHz$/e$ image-charge shift, we convert ion frequency ratios r to neutral mass ratios by accounting for missing electrons [18] and ionization and chemical binding energies [27]. These adjustments contribute ≤ 0.03 ppb uncertainty to the final neutral mass ratios. We neglect vibrational/rotational excitation due to ionization. Vibrational energy decays in msec (except for homonuclear species like $C_2{}^+$, where the decay time ~ 1 min). Rotational energies ($\sim$meV) can be ignored.

From the neutral mass ratios we obtained a set of neutral mass difference equations. We added to this the mass difference equations used to determine the atomic masses in [11]. Solution of this overdetermined set of linear equations gave the neutral masses of the alkali metals (see Table IV) with uncertainties σ_{od} as well as the previously published neutral masses with $\chi_\nu^2 = 0.83$. The previously published masses were essentially unchanged and so are not reported. Uncertainties in $M[^{16}\mathrm{O}]$ and $M[\mathrm{H}]$ contributed <0.1 ppb uncertainty to the alkali masses.

The use of two distinct reference ions gave a check on systematics by providing two independent values for each neutral mass (Table III). For Rb and Cs χ_ν^2 is less than 1. However, because of the larger uncertainty on $M[\mathrm{Cs}]$ from $\mathrm{Cs}^{++}/\mathrm{C}_5\mathrm{H}_6{}^+$ we quote a final uncertainty of 0.20 ppb $> [\sigma_{\mathrm{od}}(\mathrm{Cs}) = 0.16$ ppb]. For ^{87,85}Rb we quote $\sigma_{\mathrm{od}}(^{87,85}\mathrm{Rb})$ as the final uncertainties. For the neutral masses from $\mathrm{Na}^{++}/\mathrm{C}^+$ and $\mathrm{Na}^+/\mathrm{C}_2{}^+$, the statistical uncertainties are 0.09 and 0.07 ppb, respectively. The 0.2 ppb disagreement of the two values may be evidence for a systematic at the 0.1 ppb level. To reflect this we assigned $M[^{23}\mathrm{Na}]$ a 0.12 ppb uncertainty $>[\sigma_{\mathrm{od}}(\mathrm{Na}) = 0.06$ ppb] which spans both independent measurements.

Table IV gives final values for $M[^{133}\mathrm{Cs}]$, $M[^{87}\mathrm{Rb}]$, $M[^{85}\mathrm{Rb}]$, and $M[^{23}\mathrm{Na}]$ obtained from the solution of the mass difference equations with uncertainties from the above discussion. Also included in Table IV are alkali masses from the 1993 mass evaluation [18]. Our values differ from the 1993 values by $\sim 1.5\sigma_{1993}$. Our value for $M(^{133}\mathrm{Cs})$ lies within the uncertainty of the recent measurement of $M(^{133}\mathrm{Cs})$ reported by the SMILETRAP Collaboration [28]. Using R_∞ [8], m_p/m_e [10], the preliminary value of the photon recoil shift [17], f_{D1} for the photon recoil transition [29], and our values for $M(^{133}\mathrm{Cs})$ and M_p we obtain $\alpha^{-1} = 137.035\,992\,2(40)$.

We are grateful to Roland Nguyen for winding our $Q \approx 5 \times 10^4$ detector coil. This work was supported by the National Science Foundation (Grant No. PHY-9514795), a NIST Precision Measurements Grant (Grant No. 60NANB8D0063), and the Joint Services Electronics Program (Grant No. DAAH04-95-1-0038).

---

*Currently at NIST, Gaithersburg, MD 20899-8421.

[1] T. Kinoshita, Rep. Prog. Phys. **59**, 1459 (1996).
[2] T. Kinoshita, IEEE Trans. Instrum. Meas. **46**, 108 (1997); Phys. Rev. Lett. **75**, 4728 (1995).
[3] R. S. Van Dyck, Jr., P. B. Schwinberg, and H. G. Dehmelt, Phys. Rev. Lett. **59**, 26 (1987).
[4] M. E. Cage *et al.*, IEEE Trans. Instrum. Meas. **38**, 284 (1989).
[5] A. Jeffery *et al.*, IEEE Trans. Instrum. Meas. **46**, 264 (1997).
[6] E. Kruger, W. Nistler, and W. Weirauch, Metrologia **35**, 203 (1998).
[7] B. N. Taylor, Metrologia **31**, 181 (1994).
[8] C. Schwob *et al.*, Phys. Rev. Lett. **82**, 4960 (1999).
[9] Th. Udem *et al.*, Phys. Rev. Lett. **79**, 2646 (1997).
[10] D. L. Farnham, R. S. Van Dyck, Jr., and P. B. Schwinberg, Phys. Rev. Lett. **75**, 3598 (1995).
[11] F. DiFilippo, V. Natarajan, K. R. Boyce, and D. E. Pritchard, Phys. Rev. Lett. **73**, 1481 (1994).
[12] R. S. Van Dyck, Jr., D. L. Farnham, S. Zafonte, and P. B. Schwinberg, *ICAP XVI Abstracts, Windsor, 1998* (University of Windsor, Windsor, 1998), pp. 294–295.
[13] R. S. Van Dyck, Jr., D. L. Farnham, and P. B. Schwinberg, *Abstracts of the American Physical Society, 1993* (American Physical Society, Ridge, NY, 1993).
[14] G. L. Greene, E. G. Kessler, Jr., R. D. Deslattes, and H. Börner, Phys. Rev. Lett. **56**, 819 (1986).
[15] D. Weiss, B. Young, and S. Chu, Phys. Rev. Lett. **70**, 2706 (1993); Appl. Phys. B **59**, 217 (1994).
[16] Th. Udem, J. Reichert, R. Holzwarth, and T. W. Hänsch, Phys. Rev. Lett. **82**, 3568 (1999).
[17] B. C. Young, Ph.D. thesis, Stanford, 1997.
[18] G. Audi and A. G. Wapstra, Nucl. Phys. **A565**, 1 (1993).
[19] E. R. Williams, R. L. Steiner, D. B. Newell, and P. T. Olsen, Phys. Rev. Lett. **81**, 2404 (1998).
[20] H. Stolzenberg *et al.*, Phys. Rev. Lett. **65**, 3104 (1990).
[21] B. Fogelberg *et al.*, Phys. Rev. Lett. **82**, 1823 (1999).
[22] L. S. Brown and G. Gabrielse, Rev. Mod. Phys. **58**, 233 (1986).
[23] E. A. Cornell, R. M. Weisskoff, K. R. Boyce, and D. E. Pritchard, Phys. Rev. A **41**, 312 (1990).
[24] P. R. Bevington and D. K. Robinson, *Data Reduction and Error Analysis for the Physical Sciences* (McGraw-Hill, Boston, 1992), 2nd ed.
[25] P. J. Huber, *Robust Statistics* (Wiley, New York, 1981).
[26] V. Natarajan, K. R. Boyce, F. DiFilippo, and D. E. Pritchard, Phys. Rev. Lett. **71**, 1998 (1993).
[27] S. G. Lias *et al.*, in *NIST Chemistry WebBook*, NIST Standard Reference Database No. 69, edited by W. G. Mallard and P. J. Linstrom (NIST, Gaithersburg, MD, 1998) (http://webbook.nist.gov).
[28] C. Carlberg, T. Fritioff, and I. Bergstrom, preceding Letter, Phys. Rev. Lett. **83**, 4506 (1999).
[29] Thomas Udem (private communication).

Chapter 5

The MIT Mass Table: A Preliminary Reanalysis

This bulk of this chapter consists of a preliminary draft of a paper entitled *Single-Ion Cyclotron Resonance Mass Spectrometry at MIT*, which is intended for submission to the journal *Reviews of Modern Physics.* This paper is intended to constitute a comprehensive re-analysis of all our old mass spectrometric data using a variety of analysis techniques developed primarily by V. Natarajan, F. DiFilippo, and F. Palmer, as well as a general survey of the instrumentation and techniques used by the MIT ICR lab. This paper includes a discussion of the alkali metal mass measurements presented in our recent Physical Review Letter [BPR99], and discussed in detail in Chapter 4 of this thesis. This preliminary draft is included in this thesis for completeness. The work in this paper consists of significant measurements, analysis, and written contributions from V. Natarajan, F. DiFilippo, and F. Palmer. Starting from a material written by V. Natarajan, F. DiFilippo, and F. Palmer, this paper has been rewritten by myself in collaboration with Prof. David E. Pritchard. Before submission we will send out the paper for review by the authors in the preliminary author's list. As stated above, we have included this paper in this thesis primarily for the sake of completeness.

Paper: Single-Ion Cyclotron Resonance Mass Spectrometry at MIT

Preliminary Authors List:

Michael P. Bradley, Frank DiFilippo [1], Vasant Natarajan [2], Fred L. Palmer [3], James V. Porto [4], Simon Rainville, James Thompson, David E. Pritchard

Massachusetts Institute of Technology,
Cambridge, Massachusetts, 02139

Abstract

Single ion Penning trap mass spectrometry has revolutionized atomic mass measurement science by making possible measurements with relative accuracy $< 10^{-9}$. This has opened the doors to a wide array of new applications. The MIT group is one of the leaders in this field. In this paper we briefly summarize the history and state-of-the-art, and then present the results obtained with the MIT spectrometer. In the MIT spectrometer, a set of measured cyclotron frequencies are fit with a polynomial to model long-term field drift. Robust statistics is used to ensure self-consistent treatment of magnetic field fluctuations. Alternative analysis methods have also been used to verify the correctness of the robust fitting. The atomic mass ratios measured at MIT form an overdetermined set, such that each atomic mass can be derived from at least two independent groups of ion mass comparisons. The mass ratios measured at MIT have contributed to a variety of applications in fundamental constants and metrology, including new determinations of the fine-structure and Molar Planck constants, re-calibration of X-ray energies, and a plan for a new atomic-based kilogram standard.

5.1 Introduction

In the last decade the Penning trap has replaced the magnetic mass spectrometer as the most accurate instrument for determining the mass of atomic particles. This has

---

[1] Present Address: Picker Int'l

[2] Present Address: Indian Institute of Science

[3] Present Address: Osram Sylvania, Beverly, MA

[4] Present Address: Nat'l Inst. of Standards and Technology, Gaithersburg, MD, 20899-8421

led to a revolution which has seen fractional accuracies increase by nearly three orders of magnitude - from a few parts in 10^8 to better than one part in 10^{10}. Since the general level of accuracy in measurements of the fundamental constants is around 10^{-8}, this advance was necessary to remove the limitations imposed in deducing fundamental constants from many precise energy/frequency measurements. (The dimensions of energy are ml^2t^{-2}.). This increase in accuracy also has important metrological applications.

This atomic mass measurement revolution is built on four pillars: determination of mass from a frequency measurement (presently the most accurately measurable physical quantity), trapping the ion to allow a long time for making this measurement, measuring only a single ion in order to remove perturbations, and confining the ion to a small spatial region with well characterized fields. The Penning trap, invented by Penning in 1936, was developed into a high precision device to measure the properties of single stable particles at the University of Washington by Hans Dehmelt and his collaborators [DEH95]. The extension of this approach to the heavy atoms and molecules needed to measure a wide variety of atomic masses required the development of detectors able to detect the image current ($\sim 10^{-14}$ A) induced by the ion and more precise ion manipulation techniques; these have been pioneered primarily by van Dyck at UW and our group at MIT.

The Penning trap consists of a strong uniform magnetic field $\vec{B}$ and a weak quadrupole electric field $\vec{E}(\rho, z)$ which provides confinement along the field lines [BRG86]. Measurement of the three normal mode frequencies of the trapped ion allows determination of the free space cyclotron frequency of the ion

$$\omega_c = \frac{qB}{m} \tag{5.1}$$

which leads directly to mass comparisons with accuracy limited by the constancy of B, since q is quantized. We describe the Penning trap and the "pulse and phase" and the "separated oscillatory fields" methods developed to determine ions' cyclotron frequencies in the next section.

In contrast to many precision experiments where the final result is determined from a single careful measurement, Penning trap mass spectrometry is intrinsically redundant. For example, the mass doublet ratios O^+/CH_4^+, $CO^+/C_2H_4^+$, and $CO_2^+/C_3H_8^+$ all determine the mass difference (C+4H−O), but using species of widely different total mass in the trap. Any particular atomic isotope may be compared in different molecules with many different other molecules, eventually tying it to the atomic mass standard, ^{12}C, by several independent routes. In our measurements, we have made approximately 1750 cyclotron frequency measurements, on 28 different mass ratios, finally extracting 14 different isotopic masses. The robust statistical analysis, comparison of several ways to extract mass differences, many systematic checks and systematic errors relating to our final table of atomic mass differences are discussed in Section 5.3. Our final table of atomic masses is presented in Section 5.4

The new level of accuracy is an order of magnitude beyond that with which macroscopic kilogram masses can be compared, a limit imposed primarily by adsorbed gas. Besides accuracy, the possibility that the kilogram artifact could be damaged or suffer long term drift underlines the necessity to replace the kilogram artifact with an atomic mass standard. Another metrological application opened by the atomic mass revolution is the possibility of determining the energy released (e.g. as gamma rays) in nuclear reactions with metrologically useful precision. The new level of accuracy in mass comparison also has implications for determining fundamental constants. In particular it offers a new way to determine the fine structure constant. This approach is built on relatively simple physics, and could well provide the best check of QED of any experiment. These new applications of atomic mass measurement to metrological and fundamental physics are discussed in Section 5.5.

5.1.1 Historical route to single-ion mass spectrometry

The history of mass spectrometry dates to the 1897 measurement by J.J. Thomson of m/e for the electron. Thomson's method for finding m/e by measuring the radius of curvature of an electron beam of known velocity in a known magnetic field was the basis for a major class of mass spectrometers used throughout this century [NIR51].

These devices found wide application, leading to the discovery of many isotopes and allowing chemical analysis of unknown compunds.

Despite the many advances in ion-beam mass spectrometry over the years, only with the advent of single ion Penning trap cyclotron resonance mass spectrometry did atomic mass measurements of with relative uncertainty $< 1 \times 10^{-9}$ become possible. This has created a host of new applications in fundamental metrology and physics.

The key to the ultrahigh relative accuracy of 10^{-10} achieved using single trapped ion mass spectrometers is *long observation time* measurements of the cyclotron frequencies of *single* ions. Direct measurement of the cyclotron frequency allows all the powerful methods of RF frequency measurement technology to be employed. The long observation times needed to make high-precision frequency measurements are achieved by spatially confining the ions in the well-controlled magnetic and electric fields of a Penning trap. Finally, the use of single ions eliminates frequency shifts due to ion-ion Coulomb interactions which otherwise would limit the frequency measurements to relative accuracies of 1×10^{-9}.

Historically the drive toward cyclotron resonance on single trapped ions was advanced on two fronts, with chemists making cyclotron frequency measurements on clouds of relatively heavy molecular ion fragments, while physicists developed methods for trapping and isolating single-charged particles for a variety of precision measurement applications.

In commercially available chemical analysis ICR mass spectrometers an unknown sample is ionized using laser desorption or electrospray techniques, resulting in a cloud of ionized fragments. Fourier transforming the time-domain response of the ion cloud to a broadband RF excitation pulse allows the mass spectrum of the ionized fragments in the cloud to be rapidly determined. From this mass spectrum the chemical composition of the original compound can be deduced. The design of chemical mass spectrometers has focused more on the use of multiple cells for transporting and storing reaction products, and less on achieving high precision. Because space-charge effects due to the use of ion clouds limits relative accuracies to $> 10^{-9}$, the use of non-quadrupolar traps with large spatial inhomogeneities is sufficient. Despite these limitations, some impressively high precision results have been achieved [GOR93].

Hans Dehmelt, a physicist at the University of Washington, pioneered measurments with charged particles in the well-controlled magnetic and electric fields of a Penning trap. Beginning in the 1960s with hyperfine spectroscopy of trapped ions and moving to the trapping of single electrons, followed by a series of ever more precise measurements, Dehmelt's group continuously advanced the frontier of charged particle trapping for precision measurements.

These two lines of approach met in the development of single-ion Penning trap mass spectrometers. The first significant mass spectrometry measurement in a true hyperbolic Penning trap was a measurement of the m_p/m_e mass ratio using clouds of $\sim$ 500 protons and $\sim$ 10 electrons. The first mass spectrometry on single ions in Penning traps was done by Van Dyck *et al.* (1981).

5.2 Basic Physics of Penning Trap Mass Measurement

5.2.1 Penning Traps for Mass Spectrometry

The essential advantage of Penning trap mass spectrometers over Nier-type sector magnet mass spectrometers is that the ion's cyclotron resonance frequency can be determined more precisely than the radius of curvature of an ion beam in a magnetic field $\vec{B}$.

$$\omega_c = \frac{qB}{m} \quad \text{(SI units)} \tag{5.2}$$

where q and m are the ion's mass and charge.

Unfortunaately, one can't measure ω_c accurately using an ion in a uniform $\vec{B}$-field because the ion's freedom to move parallel to the magnetic field lines restricts the measurement time to milliseconds, with correspondigly large frequency error. In addition, the large extent of the ion's motion in the field would mandate high field uniformity over an unachievably large area.

These problems are solved in a Penning trap (Fig. 5-1) which consists of a uniform axial magnetic field $\vec{B} = B_0\hat{z}$ and a weaker quadrupole electric potential to confine the axial motion of the ion

$$\Phi(\vec{r}) = \frac{V}{2}\left(\frac{z^2 - \frac{1}{2}\rho^2}{d^2}\right) \tag{5.3}$$

where d (defined in Fig. 5-1) is the characteristic size of the trap [PEN36], [BRG86]. This electric field is generated by biasing the central ring electrode of the trap to a voltage $-V$ ($V > 0$) with respect to the two (grounded) endcap electrodes. A Penning trap is only a virtual trap, as the electric field points radially outward at the midplane. The radial motion is dynamically stabilized by the magnetron motion of the ion around the line $\rho = 0$.

5.2.2 Penning trap dynamics

The physics of a single ion in a Penning trap is well understood and has been described in detail in the literature [BRG86]. The motion is a superposition of three normal modes of oscillation: the "axial" mode, the "trap cyclotron" mode, and the "magnetron" mode, with angular frequencies ω_z, ω_c', and ω_m, respectively. The axial mode is a harmonic oscillation along the magnetic field lines at a frequency $\omega_z = \sqrt{qV/md^2}$. The presence of the radial de-confining electric field causes a lowering of the cyclotron frequency to give a "trap" cyclotron mode at frequency ω_c':

$$\omega_c' = \frac{1}{2}\omega_c + \frac{1}{2}\sqrt{\omega_c^2 - 2\omega_z^2} \tag{5.4}$$

and a magnetron mode at frequency ω_m:

$$\omega_m = \frac{1}{2}\omega_c - \frac{1}{2}\sqrt{\omega_c^2 - 2\omega_z^2} \tag{5.5}$$

such that $\omega_c' + \omega_m = \omega_c$, the "free-space" cyclotron frequency for an ideal trap. In practice ω_c is obtained by adding the three mode frequencies in quadrature,

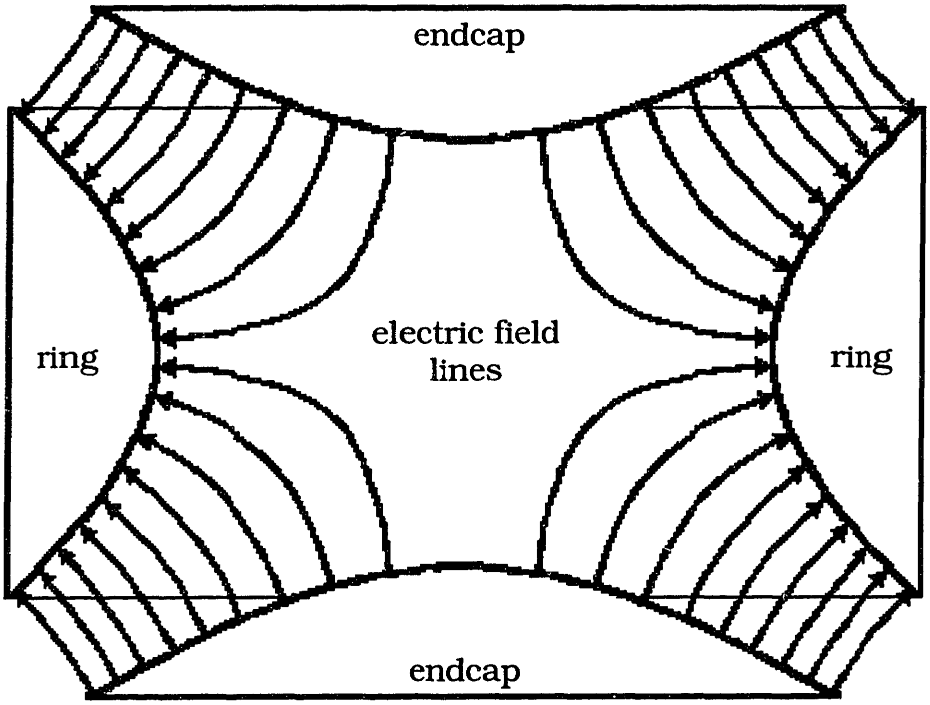

Figure 5-1: Cross-sectional view of the basic Penning trap electrode geometry. To confine ions the endcaps are grounded and the ring is made negative. The electrodes are machined to be hyperbolas of revolution, which are the equipotentials of Laplace's equation for a quadratic potential.

$$\omega_c = \frac{qB}{mc} = \sqrt{(\omega_c')^2 + (\omega_z)^2 + (\omega_m)^2}. \tag{5.6}$$

a prescription insensitive to both tilts of the trap axis with respect to the magnetic field and azimuthal ellipticity of the trap electrodes [BRG86]. In the MIT trap, $B = 85000$ G, and for a $^{14}\mathrm{N}_2^+$ ion, the mode frequencies are $\omega_c'/2\pi$ = 4.6 MHz, $\omega_z/2\pi$ = 160 kHz, and $\omega_m/2\pi$ = 2.8 kHz.

It is worth noting that the ratio of the electric force to the magnetic force acting on a trapped ion is ω_z^2/ω_c^2, which is the expansion parameter for most trap perturbations, as well as for propagation of errors in ω_z [BRG86]. Thus it is advantageous to operate with small values of ω_z^2/ω_c^2.

5.2.3 Detecting the Modes

There are several possibilities for ion detection in a Penning trap. It is possible to directly measure the cyclotron frequency by detecting the currents induced in the ring electrode (Van Dyck, Schwinberg, and Bailey, 1980, and Gabrielse et al., 1999) This has the disadvantage that the trap can be used for only a single m/q ratio, because broadband detectors with the sensitivity to detect a single ion cannot be made.

An advantage of the Penning trap is that the trap voltage V can easily be adjusted to keep ω_z constant when m/q changes. Thus narrowband detection with S/N sufficient to detect a single ion can be performed for arbitrary m/q. This approach has been adopted by the UW, MIT, and JILA groups, all of which directly detect only the axial motion at frequencies $\omega_z/2\pi$ between 0.15 and 4 MHz. A coupling between the axial and cyclotron modes is then required to detect the cyclotron mode. A radially varying magnetic field (a "magnetic bottle") is widely used to couple the cyclotron and axial modes. (Van Dyck, Dunn, Gabrielse) for cyclotron detection, though it has the disadvantage that the non-uniform B field results in radius-dependent cyclotron frequency shifts. The MIT group is the only group to use an RF field to phase-coherently couple the cyclotron and the axial modes for detection.

It is also possible to entirely forgo detection in the trap, and instead measure cyclotron excitation by measuring time-of-flight in an inhomogeneous B field after the ions are ejected from the trap. (Stockholm and Mainz/GSI groups)

From this point on we will restrict the discussion to the detection methods used at MIT. The ion's axial motion is detected and also damped via the current which it induces in the endcaps of the trap. This current results from variation of the image charge which the ion induces on the upper and lower endcaps [WEI88]:

$$q_{image} = qC_1 \left(\frac{z}{2z_0} \right) \tag{5.7}$$

where z is the ion's axial displacement from the center of the trap and $C_1 \approx 0.8$ (Gabrielse, 1984) is a factor which expresses the extent to which the trap endcap electrodes deviate from a parallel plate capacitor. The image current induced in the endcaps of the trap by an ion's axial motion of amplitude $a_z \approx 0.1z_0$ is $i_{image} \approx qC_1(\omega_z a_z/2z_0) \sim 10^{-14}$ A. We have developed detectors consisting of a high-Q ($Q \sim 3-5 \times 10^4$) tuned circuit and a SQUID (initially an RF SQUID, now a DC SQUID) to attain a sufficient signal-to-noise ratio to detect the axial motion of single ions [WLB88].

For maximum precision, the frequency, phase and amplitude of the ion's axial motion must be accurately extracted from the smallest possible signal, corresponding to as small an axial amplitude as possible. The axial signal is a sinusoid that decays at a rate $\gamma_z \sim 1$ sec^{-1} as the ion is damped by its interaction with the detector. The simplest method of analysis is to perform a digital Fourier transform on the data and to use the spectral parameters of the peak bin. However, such an analysis gives biased estimates since it fails to account for the damping [KUT82]. A better procedure is to perform an analog of the Laplace transform with a complex frequency, where the imaginary part is the damping constant. This is implemented simply by pre-multiplying the data with $e^{-t/\tau}$, where t is the amplitude decay time, and then taking a Fourier transform. The ion's parameters are obtained by finding the peak of the transform. This procedure works better because it weights the data progressively less at later times (as the signal damps). We have shown that this procedure gives unbiased estimates and errors that are close to theoretical minimum bounds for the observed signal-to-noise ratio [NAT93].

In our apparatus only the axial motion of the ions is detected and damped. Radiative decay times are very long ($> 10^5$ years) for the cyclotron and magnetron motions of trapped ions. This has the benefit that the trap cyclotron mode has effectively zero linewidth and is not subject to frequency pulling due to continuous coupling to the detector. Not observing the cyclotron motion directly with the detector means that an indirect method must be employed. To access the radial magnetron and trap cyclotron modes, we couple them to the axial mode using an RF quadrupole field tilted with respect to the main trap field. This coupling scheme is reminiscent of sideband cooling except that it is completely deterministic in that it does not involve spontaneous decay. It is based on the classical coupling of two oscillators by a coupling force oscillating at nearly their difference frequency.

In the presence of the coupling field the trap cyclotron and axial mode amplitudes are governed by the same equations of motion as those obtained from the Schrodinger equation for the coupling of two quantum states by an oscillating field. For $\omega_{cpl} = \omega_c' - \omega_z$, the solution of this problem is a complete oscillation of the scaled mode amplitudes [RAM57] at the Rabi frequency $|\Omega|$. We use this Rabi oscillation to "read out" the amplitude and phase of the otherwise undetected trap cyclotron mode. By using a "π" pulse with duration $\Delta t = (\pi/\Omega)$ we completely and *phase-coherently* transfer the trap cyclotron mode amplitude (scaled by $\sqrt{\omega_c'/\omega_z}$) and phase to the axial mode where we detect it. A related mode-coupling technique is used to cool the magnetron motion so that the ion is located at the center of the trap before measuring ω_c'.

5.2.4 Measuring Trap Cyclotron Frequency: PNP and SOF methods

We have developed two indirect methods to measure ω_c' using mode coupling pulses: the "pulse and phase" (PNP) method and the "separated oscillatory fields" (SOF) method. In the PNP method, the trap cyclotron frequency is measured by driving a previously cooled ion to a trap cyclotron orbit radius ρ_c, allowing the ion to evolve "in the dark" for a time T, and applying a π-pulse to switch the cyclotron action into the axial motion, allowing us to measure the accumulated trap cyclotron phase [CWP90]. A series of measurements of accumulated phase versus T allows the phase to be progressively "unwrapped" and yields a measurement of ω_c' with *precision* limited only by the phase detection error and the phase accumulation time T.

In the SOF method, the ion is driven by a pair of RF pulses at frequency $\omega_D \approx \omega_c'$. The pulses are separated by a time T. Depending on the relative phase between the ion and the drive at time T, these two pulses interfere; i.e. add constructively or destructively. Therefore the final trap cyclotron orbit radius varies sinusoidaly with the phase $(\omega_D - \omega_c')T$ accumulated between the pulses. This radius is then measured by using a π-pulse to swap it into the axial mode. Measurement of the beat frequency $(\omega_D - \omega_c')$ yields ω_c'. Because we cannot tell the sign of the resultant cyclotron amplitude, the SOF method is a factor of 2 less precise than the PNP method for a given T, but it has the advantage that information about the cyclotron phase evolution is encoded in the cyclotron amplitude, which is insensitive to subsequent changes in the trap voltage. The SOF method is particularly useful for measuring ions of very different m/q because changing V to bring ions into resonance with the detector does not change the stray electric field due to charge patches, and thus the equilibrium position of the ions in the trap depends on the trap voltage V. For ions of very different m/q this can result in significantly different axial positions and systematic errors in the measured frequencies. With SOF phase can be accumulated with the same trap voltage V (i.e. identical trap conditions) for ions of arbitrarily different m and q, with the voltage being changed after the second pulse to allow axial readout of the cyclotron amplitude information. With both methods, ω_c' can be measured to 10^{-10} precision with a series of measurements, the longest having a delay time of ~ 1 minute.

5.2.5 Effect of Field Inhomogeneities

All real Penning traps deviate from the ideal trap considered so far. The magnetic field will never be perfectly homogeneous, and its deviation from homogeneity may be described by a power series expansion:

$$\vec{B}(\rho, z) = B_0\hat{z} + B_1(z\hat{z} - \rho\hat{\rho}) + B_2[(\rho^2 - \frac{1}{2}z^2)\hat{z} - z\rho\hat{\rho}] + \ldots \tag{5.8}$$

Similarly, truncation of the electrodes and fixed charge patches result in electrostatic imperfections which may be described by the following expansion in Legendre polynomials:

$$\Phi(\vec{r}) = -\frac{V}{2}\sum_{l=0,2,4\ldots}^{\infty} C_l r^l P_l(\cos\theta) + K \tag{5.9}$$

Both types of field variation result in radius-dependent cyclotron frequency shifts. In addition, even in a perfect trap, the relativistic mass increase of an ion causes a fundamental radius-dependent cyclotron frequency variation. The overall effect of these variations on ω_c is given by [BRG86]:

$$\frac{\Delta\omega_c}{\omega_c} = \left(-\frac{\omega_c'^2}{2c^2} - \frac{B_2}{2B_0} + \frac{3\omega_m C_4}{2\omega_c d^2}\right)\rho_c^2 \tag{5.10}$$

By measuring these radius-dependent shifts we can shim the $\vec{B}$ field and "tune" C_4 such that $B_1/B_0 < 10^{-6}$ cm^{-1}, $B_2/B_0 < 10^{-6}$ cm^{-2}, and $C_4 < 10^{-4}$.

5.2.6 Measuring Atomic Masses

The unified atomic mass unit u is defined by the statement that a single atom of ^{12}C at rest in the ground state has a mass of exactly 12.000... u. Atomic mass measurements are therefore measurements of mass relative to ^{12}C. Ion cyclotron resonance mass spectrometry exploits the fact that the ratio of the cyclotron frequencies of two ions

$$\frac{\omega_{c2}}{\omega_{c1}} = \left(\frac{q_2 B}{m_2 c}\right)\left(\frac{m_1 c}{q_1 B}\right) \tag{5.11}$$

is the ratio of the charge/mass ratios of the two ions. Thus measurement of the ratio of the cyclotron frequencies of two ions permits a measurement of the ratio of their masses, since the ion charges are quantized.

We make cyclotron frequency ratio measurements by alternately loading ions of two different species into our trap and measuring their cyclotron frequencies (Fig. 5-2). We take data between the hours of 1 a.m. and 5:30 a.m. when the nearby electrically-powered subway is not running. Each PNP or SOF sequence gives a "cluster" of 2-6 measurements of trap cyclotron frequency, as well as a set of measurements of the axial frequency ω_z. We average the value of ω_z to obtain a mean value which we then use in Eq. 5.6 to obtain a value of ω_c corresponding to each ω_c'.

From the set of measured cyclotron frequencies ω_c we extract a frequency ratio and hence a mass ratio. By making a series of mass ratio measurements which are direct and indirect comparisons to ^{12}C, we extract absolute atomic masses. Usually the most accurate mass ratio measurements are made on so-called "mass doublets"-ions with nearly identical m/q (e.g. N_2^+/CO^+, with $m/q = 28$ u/e). The advantage of using mass doublets is that the trap conditions and frequencies are nearly identical for the two ions involved. Also it is easy to show (Section 5.4.1) that a mass doublet $A_nB_k^+/C_pD_q^+$ determines the mass difference $pM[C]+qM[D]-nM[A]-kM[B]$. Mass differences are traditionally the way mass spectrometry measurements are reported. However, mass doublet measurements alone make it difficult to determine the masses of H and D [NBD93], which are important constituents of the hydrocarbon molecules often used as reference masses in a doublet (e.g. comparison of ^{14}N with CH_2 or CD would determine the atomic weight of ^{14}N if H and D are known.) Thus direct mass comparisons to ^{12}C (which typically require non-doublet measurements) can be very useful.

5.3 Mass Ratios and Uncertainties

5.3.1 Extracting mass ratios from cyclotron frequencies

Magnetic field variations

The result of one night's data-taking is a series of cyclotron frequency measurements on two different ion species (e.g. Fig. 5-2). Each time an ion is made its cyclotron frequency is measured several times, giving "clusters" of frequency measurements. The number of measurements in a cluster varies from 2 to 6 (more for ions that are difficult to make). The central analysis problem in our experiment is to extract a frequency ratio from such a set of clusters of measured cyclotron frequencies. If the magnetic field $B(t)$ were constant, the ratio of free-space cyclotron frequencies for two ions measured at times t_1 and t_2 would determine the mass ratio

$$\frac{m_1}{m_2} = \frac{q_1}{q_2}\frac{B(t_1)}{B(t_2)}\frac{\omega_{c2}(t_2)}{\omega_{c1}(t_1)} \tag{5.12}$$

to high precision since the ratio q_1/q_2 is a known rational number. However we find that the cyclotron frequencies exhibit correlated slow drift with time which we attribute to dimensional changes of the magnet coils, externally imposed field variations, and possibly motion of the trap in any field gradients which may be present. Although other sources of random error (such as thermal noise) contribute to temporal variations in repeated measurements of the cyclotron frequency, magnetic field fluctuations dominate (see Section 5.3.2 and Table 5.2), and limit the accuracy of our cyclotron frequency ratio measurements to $\sim 10^{-10}$ for one night of measurement, roughly the precision of a single cyclotron frequency for a 1 minute PNP or SOF measurement.

Obtaining a Mass Ratio

a. Least-Squares Fits, Non-Gaussian Fluctuations, and Robust Statistics. Our standard method for determining frequency ratios $r = \omega_{c1}/\omega_{c2}$ from measured cyclotron frequencies is based on robust fits to the magnetic field variation. Robust fitting may

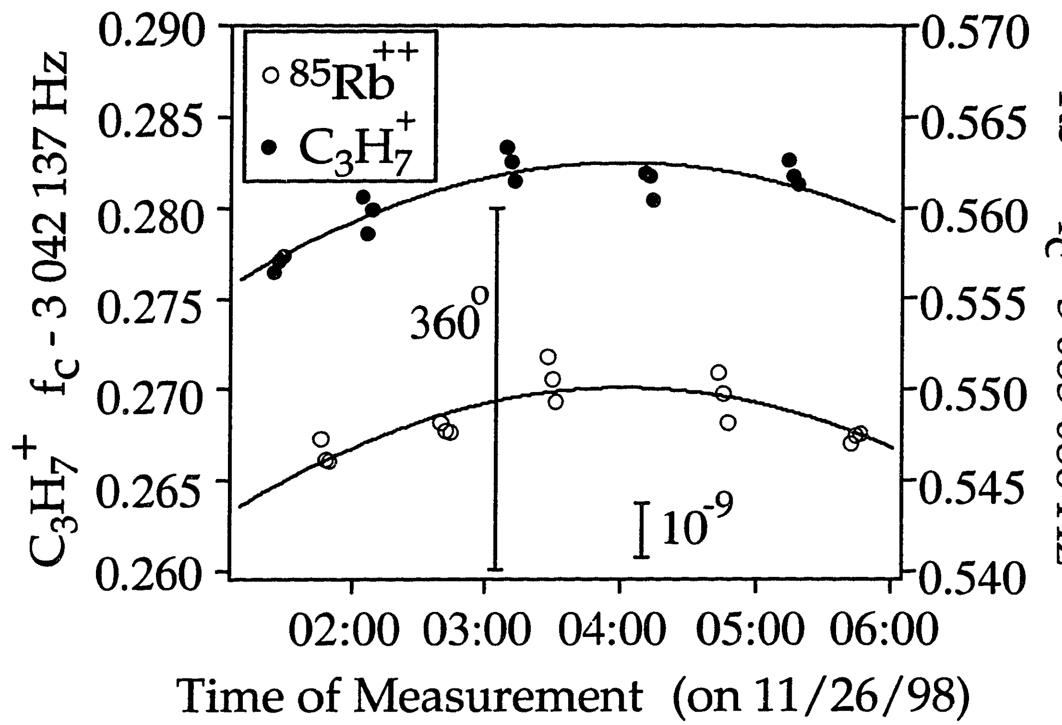

Figure 5-2: Typical night of data. The solid line is a second order polynomial fit to the data. The 360° bar shows the magnitude in Hz of a 360° error in phase unwrapping.

be regarded as an extension of the least-squares method, which we now describe. To extract the cyclotron frequency ratio

$$r \equiv \frac{\omega_{c1}}{\omega_{c2}}, \tag{5.13}$$

we fit the cyclotron frequency data by representing the field variation as a sum of slow drifts $B(0)f(t)$ plus uncorrelated short-term variations $\delta B(t)$:

$$B(t) = B(0)[1 + f(t)] + \delta B(t) \tag{5.14}$$

We choose an n^{th} order polynomial to represent $f(t)$. The frequency ratio r and field drift $f(t)$ are obtained by jointly fitting the set of measured free-space cyclotron frequencies $\omega_{c1}(t_1), \omega_{c2}(t_2), \omega_{c1}(t_3), \omega_{c2}(t_4)\ldots$ We first multiply the $\omega_{c2}(t_i)$ by r_0, the best value of r based on available mass data to make ω_{c1} and ω_{c2} comparable for ease in fitting. We fit by the least squares method, minimizing the quantity χ^2:

$$\chi^2 = \Sigma_j[\omega_{c1}(t_j) - q_1 B_0 f(t_j)/m_1]^2/\sigma_j^2(\omega_c) + \Sigma_k[r_0\omega_{c2}(t_k) - q_2 B_0 f(t_k)/m_2 + \Delta\omega_c]^2/\sigma_k^2(\omega_c) \tag{5.15}$$

with respect to $f(t)$ and the frequency offset between the two curves $\Delta\omega_c$. The indices j and k label individual measurements for the two ions, and $\sigma_{j,k}(\omega_c)$ are the measurement uncertainties. From the best fit value for the frequency offset, $\Delta\omega_c = \omega_{c1}(0) - r_0\omega_{c2}(0)$, we compute the final frequency ratio r,

$$r = \frac{\omega_{c1}}{\omega_{c2}} = r_0 + \frac{\Delta\omega_c}{\omega_{c2}(0)} \tag{5.16}$$

The uncertainty in r and σ is obtained in the standard way [BER92] from the second derivative of the χ^2 function. χ^2 is minimized by adjusting the parameters of $f(t)$. The order, n, of $f(t)$ is critical: if n is too low $f(t)$ cannot track the field drift correctly; if n is too high, $f(t)$ will exaggerate short-term fluctuations.

Our choice of fit order n is guided by a statistical test (the F-test) which assesses whether the relative change in χ^2 quantified by the F-statistic

$$F_{\chi,n} = \frac{\chi^2(n-1) - \chi^2(n)}{\chi^2(n)/\nu} \tag{5.17}$$

is significant, under the assumption of gaussian fluctuations [BER92]. We are guided by the principle that the optimal fit order is the lowest order such that the probability P that random data will give an F_χ exceeding our measured value is $P \sim 0.5$.

Underlying the use of least-squares fits to slow drifts and the F-test is the assumption that the field variations consist of long term drifts and short term gaussian-distributed random noise fluctuations. The distribution of fit residuals (Figs. 5-4, 5-5) for our data shows that that there is a substantial excess of outliers beyond 2σ of the gaussian which closely fits the center of the distribution. In fact excess outliers are usual in most experiments. Excess outliers have adverse effects on data analysis when the least squares method is used because outliers disproportionately influence the average. Data rejection methods exist which attempt to identify and eliminate

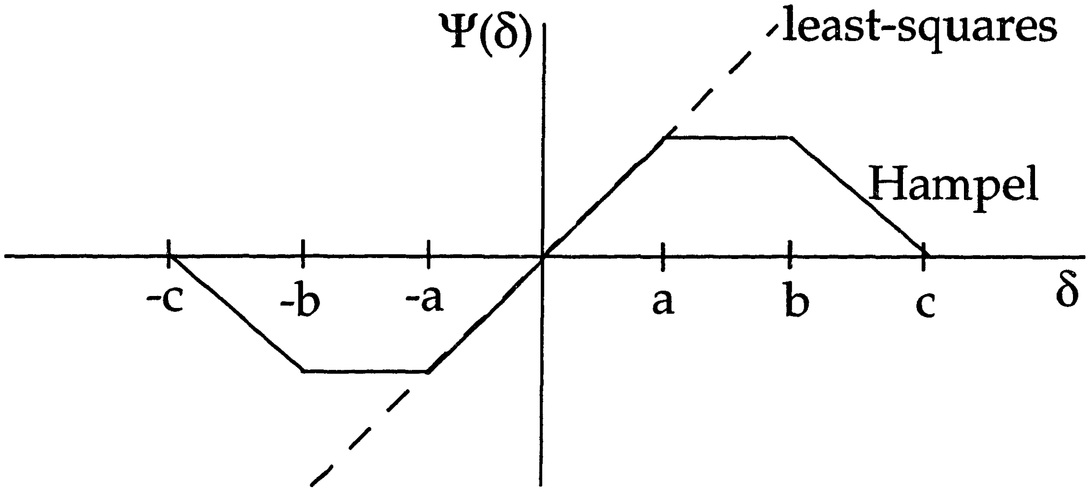

Figure 5-3: General form of Hampel Estimator. The dashed line shows the linear behavior of the estimator $\psi(\delta)$ for a gaussian (least-squares) fit.

non-gaussian outliers, but these methods have been shown to be biased for varying degrees of noise contamination [HUB81]. We use *robust statistics* to consistently deweight outliers.

The central idea of robust statistics is that additional outliers arise from occasional high-variance events, hence all outliers should be deweighted according to their excess. To do this the actual observed noise distribution $P(\delta)$ (with the excess outliers as shown in Figs. 5-4, 5-5) is fit to a model function with a gaussian center and non-gaussian tails. It is convenient to express $P(\delta)$ in terms of its logarithmic derivative, $\psi(\delta)$:

$$P(\delta) = exp(-\int \psi(\delta) d\delta) \tag{5.18}$$

where $\delta = (\omega_c - \overline{\omega_c})/\sigma_c$ is the normalized value of the residual deviation for a measurement. To find the most probable value of the fit $\overline{\omega_c}$ one maximizes the joint probability $\Pi_i P(\delta_i)$ of all the deviations; this is equivalent to setting the sum $\sum_i \psi(\delta_i) = 0$. If $P(\delta_i)$ is a Gaussian then $\psi(\delta) = \delta$, so that points with larger δ contribute more to $\bar{\omega}_c$.

We fit our noise distributions using a form for $\psi(\delta)$ considered by many statisticians to be representative of actual physical data, the three-part descending Hampel estimator (Fig. 5-3) [AND72].

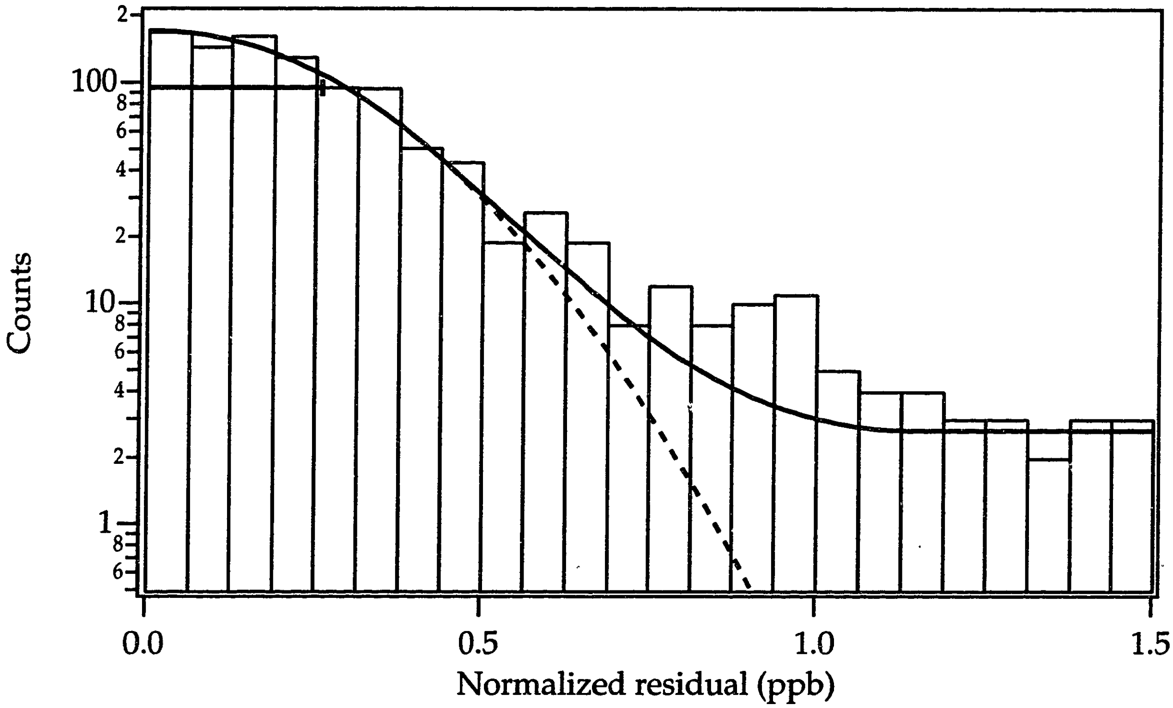

Figure 5-4: Distribution of Residuals and Hampel Estimator for 1992-1993 data. Each data set was analyzed separately, and it was found that both were well described by a Hampel estimator (solid curve) with parameters $(a, b, c) = (1.6, 2.5, 4.3)$ and $\sigma = 2.6 \times 10^{-10}$ (plotted as a horizontal bar). The dashed curve is a gaussian distribution with standard deviation $= \sigma$. Of the 1060 data points, only 9 were completely thrown away.

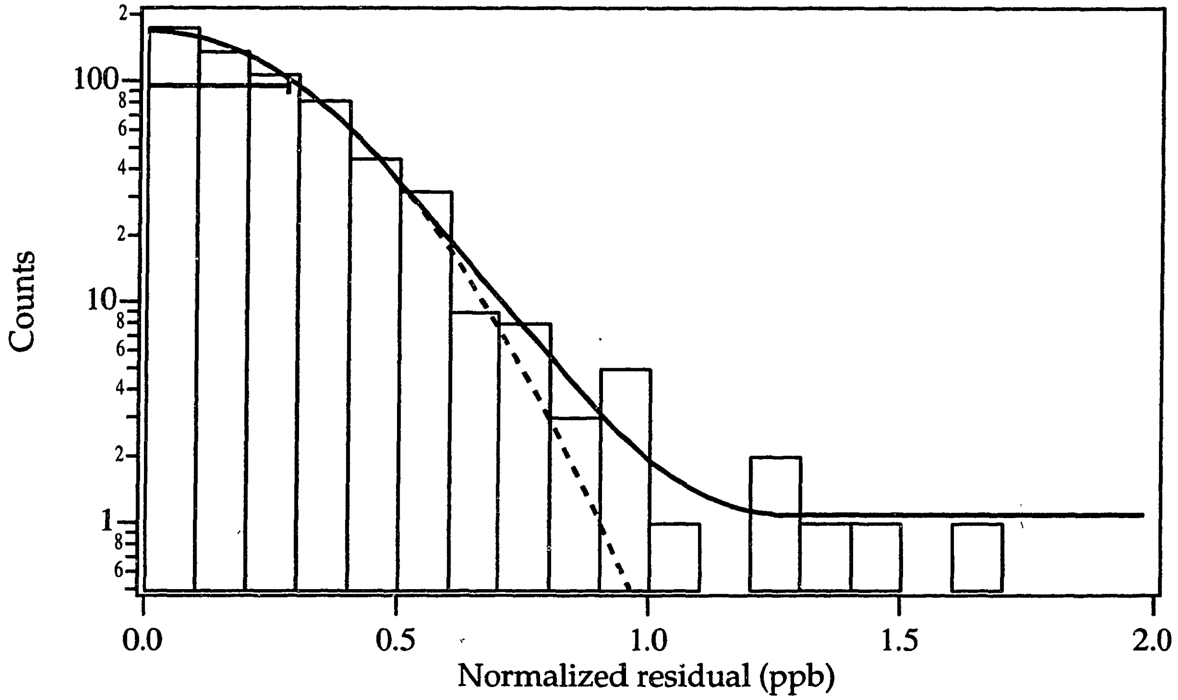

Figure 5-5: Distribution of Residuals and Hampel Estimator for Alkali Data, excluding the Cs^{++} data (see text for explanation). This data is described well by a Hampel estimator (solid curve) with parameters $(a, b, c) = (1.7, 3.11, 4.53)$ and $\sigma = 2.82 \times 10^{-10}$ (plotted as a horizontal bar). The dashed curve is a gaussian distribution with standard deviation $= \sigma$. Of the 611 data points, only 3 were completely deweighted.

Robust fitting can be conveniently implemented by using an iterated version of conventional weighted least squares fitting [HUB81]. Each measurement is weighted by a factor of $w = \psi(\delta)/\delta$. Hence ψ is usually called an *estimator.* Points with small δ receive full consideration by the fit ($w = 1$), and points with large δ receive reduced consideration ($w < 1$). Least squares fitting is done iteratively (since ω_c changes after each attempt) until the fit parameters converge.

We stress that in our experiment 85% of the points are treated with weight 1, and robust statistics differs from conventional least-squares analysis only at the margins: 6.7% of the points we deweighted by more than 30% and only 0.09% of the data points were discarded completely.

b. Cluster-based analyses As a "sensibility check" on our standard robust fit/F-test analysis we have developed 2 complimentary methods for extracting frequency ratios r from our data. They have the common feature that both treat the cluster of cyclotron frequency measurements as the basic unit of data. The cluster-weighted analysis method is motivated by the fact that relies on the idea that there are a number of plausible mechanisms which could adversely affect an entire cluster of cyclotron measurements on one ion: a contaminant ion accidentally surviving the purification stage, a charge patch on the electrodes from the e-beam ionization pulse, or a temporarily localized fluctuation in the external B-field or the dimensions of the apparatus itself. A reasonable hypothesis is that clusters for which these effects are most severe will exhibit the greatest intra-cluster scatter. Fig. 5-6 shows that this idea is borne out by our data. A fit to the binned data provides an analytic function expressing the discrepancy vs. the intra-cluster scatter. We use this function to assign an error to the average cyclotron frequency of each cluster. The data from the alternating clusters can then be analyzed according to the method of robust statistics.

Our second alternative analysis method uses a much simpler model of the field fluctuations. While the simplest way to analyze the cyclotron frequency data would be to treat each pair of adjacent cyclotron frequency clusters as an independent measurement of the frequency ratio, it suffers from the obvious flaw that a simple linear field drift would result in a bimodal distribution of ratios and a consequent overestimate

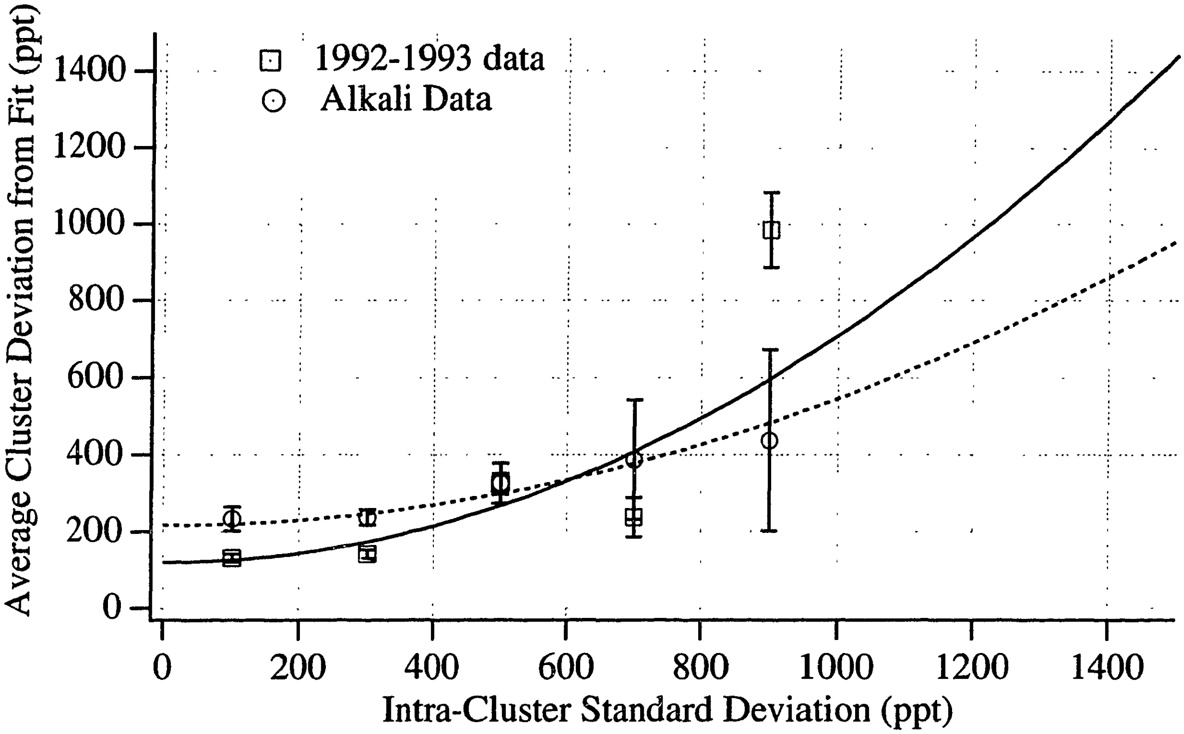

Figure 5-6: Correlation of fit deviation with intra-cluster scatter- binned data.

of the uncertainty on the measured ratio. Thus we used the method of "piecewise-linear" fits, finding a ratio for each cyclotron frequency cluster by comparing it with a straight line drawn between the adjacent clusters of cyclotron frequencies of the other ion type. An entire night of data then gives a set of mass ratios which are averaged.

Summary of analysis results

The mass data collected by the ICR lab was taken in three distinct periods: Sept. 1992 - Feb. 1993, July 1993 - Oct. 1993, and Aug. 1998 - Dec. 1998. The first two data-taking periods were interupted by the accidental quenching of our superconducting magnet, and the last data set was taken after completely rebuilding the apparatus and using a detector based on a dc rather than an rf SQUID [WLB88]. Results based on the 1992-93 data have been previously reported in [NBD93], [DNB94], [NAT93], [DIF94]. The results of the 1998 data on alkali metals have been reported recently in [BPR99].

We have analyzed or reanalyzed these data using robust statistics as our standard initial data analysis method. For each data set we compute a separate Hampel estimator, reasoning that the changes to the apparatus between each data set could have changed the sources of background noise. In addition, we used a separate robust estimator for the $Cs^{++}/C_5H_6^+$ data alone, because for these heavy ions the axial frequency uncertainty signficantly increased the observed scatter than in any other case. Except for the $Cs^{++}/C_5H_6^+$ data, we discovered that the non-gaussian distribution was essentially identical for each of the data sets. Except for the special cases noted below, all the 1992-93 results quoted in Table 5.1 were obtained using robust fitting. All the 1998 data quoted is an average of robust fit and nearest-neighbor/piecewise linear fit results as described below.

The previously reported values [DNB94] of the Sept. 1992-Feb. 1993 results were obtained by conventional least-squares fitting of the field drift with a polynomial order chosen using our best judgement, rather than using robust statistics and the F-test. In contrast, the July 1993 - Oct. 1993 data were fit using robust fitting, with the polynomial order being chosen via the F-test [DNB94].

For the alkali metal data of 1998 robust statistics and the F-test again provided the basis for the analysis. In certain cases we were not satisified with the results of the F-test/robust-fit results. For the $Cs^{++}/C_5H_6^+$ data runs of 10/25 and 10/29 and the Na^{++}/C^+ data of 12/18 the results varied significantly with fit order, so we quoted an average value with an expanded uncertainty to encompass them. For the 11/9 $C_3H_8^+/^{87}Rb^{++}$ result we used the least-squares uncertainty because the robust fit uncertainty seemed unreasonably low. For the 12/2 $C_3H_6^+/^{85}Rb^{++}$ result we used the least-squares result because the robust fit clearly had the wrong curvature to fit the field drift.

A striking result for the Cs and Rb data, not seen in the previous data or in the Na data, was variability of the frequency ratio r from run to run at a level well above the uncertainties predicted by the robust fits. By computing piecewise linear and nearest neighbor values for the frequency ratio r we confirmed that this excess scatter was not an artifact of the robust fitting procedure. In order to correctly reflect this excess scatter in our quoted error, we quoted a value for the final error $\tilde{\sigma}_{poly}$ in the robust frequency ratio equal to the square root of the average weighted variance of the data. In Table 5.1 we quote final average values for the alkali metal frequency ratios $\bar{r} = 1/2[r_{poly} + 1/2(\overline{r}_{pl})]$ where r_{poly} is the value of the frequency ratio from the adjusted robust analysis and $\overline{r}_{pl} = 1/2(r_{pl} + r_{nn}$ is the average of the results from piecewise linear and nearest-neighbor fits, respectively. We quote an uncertainty on the alkali metal frequency ratios of $\bar{\sigma}^2 = \tilde{\sigma}^2_{poly} + [(\bar{r}_{poly} - \bar{r}_{pl})/2]^2$.

5.3.2 Sources of Error

The magnetic field fluctuations described above limit the accuracy of a 1-night measurement to 0.1 ppb. Below we consider other sources of random and systematic error, and show that they are insignificant in most cases.

Summary of Errors

Table 5.2 summarizes the uncertainties in the experiment for measurements on an $m/q = 30$ u/e ion. The uncertainties in the mass ratio and in the individual measurements of the cyclotron frequency are listed along with how the error scales with mass and charge. The $\sim$ 0.1 ppb random error in the mass ratio from the magnetic field noise is the dominant uncertainty in our experiment. There are other random errors from axial frequency uncertainty and the effect of thermal noise on the cyclotron radius.

In the few cases where the systematic shift is comparable to the statistical uncertainty we adjust the measured ratio to account for the systematic shift. When the systematic is much smaller we do not adjust for it, and it contributes insignificantly to the final error.

Random errors

a. Magnetic field variations. As discussed at length above, the variations of the magnetic field are the dominant source of error in our experiment. The observed random fluctuations of the measured free-space cyclotron frequency limit the precision

Table 5.1: Measured ion cyclotron frequency ratios and corresponding mass differences used to compute the masses in Table 5.5. For all the non-alkali-metal data doublet measurements (taken in 1992-1993) the final frequency ratios quoted are the results of robust fitting, except in case b. There were too few non-doublet runs to obtain a robust estimator for the non-doublet runs. The final frequency ratios quoted for the 1998 alkali metal data are unweighted averages of the adjusted results (notes c, d, e) of robust and piecewise linear fits.

A/B	$\omega_c[\mathrm{A}]/\omega_c[\mathrm{B}]$	Mass Difference	Value
N_2^+/CO^+	0.999 598 887 572 (77)	2N - C - O	0.011 233 390 9 (22)
$C_2H_4^+/N_2^+$	0.999 102 696 201 (55)	C + 2H - N	0.012 576 059 8 (8)
$C_2D_2H_2^+/{}^{15}N_2^+$	0.998 547 569 780 (50)	C + D + H - 15N	0.021 817 911 9 (8)
$C_2H_4^+/CO^+$	0.998 701 943 805 (66)	C + 4H - O	0.036 385 507 3 (19)
$C_2D_2H_2^+/{}^{13}C_2H_4^+$	0.999 805 486 870 (77)	C + D - 13C - H	0.002 921 908 6 (12)
Ne^+/Ar^{++}	0.999 437 341 275 (106)	2Ne - Ar	0.022 497 224 5 (42)
$C_3H_4^+/Ar^+$	0.998 278 399 350 (88)	3C + 4H - Ar	0.068 917 005 3 (35)
$CD_2H_2^+/CD_3^+$	0.999 914 190 78 (10)	2H - D	0.001 548 283 6 (18)
CD_4^+/Ne^+	0.996 810 562 61 (13)	C + 4D - Ne	0.063 966 932 9 (26)
CD_4^+/Ar^{++}	0.996 249 698 36 (9)	2C + 8D - Ar	0.150 431 109 4 (36)
C^+/CD_4^+	1.671 397 950 39 (31)	D	2.014 101 778 5 (9)
C^+/CD_3^+	1.503 548 462 35 (20)	D	2.014 101 777 6 (6)
Ne^+/Ar^+	1.998 902 121 05 (30)	Ar - Ne	19.969 942 947 9 (60)
CH_4^+/O^+	0.997 730 269 42 (8)	C + 4H - O	0.036 385 506 2 (13)
$C_2H_2^+/SiH_2^+$	0.998 293 230 20 (8)	2C + 2D - Si	0.051 277 022 4 (24)
C^+/CH_4^+	1.335 957 033 78 (23)	H	1.007 825 031 7 (7)
${}^{15}N_2^+/SiH_2^+$	0.999 745 290 40 (8)	2^{15}N - Si - 2H	0.007 641 200 7 (24)
$CH_3^+/{}^{15}N^+$	0.998 444 631 99 (11)	C + 3H - 15N	0.023 366 197 9 (17)
$C_3H_8^+/CO_2^+$	0.998 348 443 16 (10)	H	0.036 385 506 0 (22)
$CDH_3^+/{}^{13}CH_4^+$	0.999 828 496 65 (9)	C+D-^{13}C - H	0.002 921 907 4 (15)
${}^{133}Cs^{+++}/CO_2^+$	0.992 957 580 983 (135)	3C +60 - Cs	-0.935 964 211 (18)
${}^{133}Cs^{++}/C_5H_6^+$	0.993 893 716 487 (427)	12H + 10C -Cs	-0.811 551 556 (58)
${}^{87}Rb^{++}/C_3H_8^+$	1.013 992 022 591 (266)	16H + 6C - 87Rb	1.216 019 965 (23)
${}^{87}Rb^{++}/C_3H_7^+$	0.990 799 127 824 (174)	14H + 6C - 87Rb	-0.799 630 068 (15)
${}^{85}Rb^{++}/C_3H_7^+$	1.014 106 122 230 (164)	14H + 6C - 85Rb	1.197 760 706 (14)
${}^{85}Rb^{++}/C_3H_6^+$	0.990 367 650 976 (285)	12H + 6C - 85Rb	-0.817 889 340 (23)
${}^{23}Na^+/C_2^+$	1.043 943 669 690 (076)	2C - Na	1.010 230 721 0 (17)
${}^{23}Na^{++}/C^+$	1.043 944 716 614 (098)	2C - Na	1.010 230 716 4 (21)

Table 5.2: Summary of Random [R] uncertainties and systematic [S] shifts for doublet (d) and non-doublet (n) comparisons for m/q = 30 u/e ions.

Source of uncertainty	Error in ω_c (ppt)	Error in ratio (ppt)	Scaling
Magnetic Field Fluctuations	270 [R]	100 [R]	
Axial Frequency Uncertainty	60 [R]	20 [R]	$(m/30)^2$
Thermal Noise in ρ_c	40 [R]	20 [R]	
Tuned circuit pulling	< 20 [S]	< 30 [R]	-
ρ_c imbalance (relativity)	10(d), 20(n) [S]	10(d), 20(n) [S]	$(30/m)$
ρ_c imbalance (magnetic)	10(d), 30(n) [S]	10(d), 30(n) [S]	$(30/m)$
ρ_c imbalance (electric)	8(d), 30(n) [S]	8(d), 30(n) [R]	$(m/30)^2$
Surface patch charges	4(d), 0(n) [S]	4(d), 0(n) [S]	(30/m)
Image charge	0.015 [S]	0.015 [S]	(m/30)

of a one-night (4 h) measurement of r_n to ~ 0.1 ppb.

b. Axial Frequency Measurement Error. After the random magnetic field fluctuations, the dominant source of random error is the measurement uncertainty $\sigma(\omega_z)$ in the axial frequency ω_z due to the 4 K thermal noise against which the ion axial motion must be detected. Eq. 5.6 implies that fluctuations in the measured value of ω_z will contribute a relative cyclotron frequency measurement uncertainty given by:

$$\frac{\sigma(\omega_c)}{\omega_c} = \left(\frac{\omega_z}{\omega_c}\right)^2 \frac{\sigma(\omega_z)}{\omega_z}. \tag{5.19}$$

Hence the ≈ 7 mHz uncertainty on the mean value of ω_z for one cluster corresponds to a 0.06 ppb uncertainty per cluster and a 0.02 ppb random error in the mass ratio, for a $m/q = 30$ u/e ion. For the heaviest ions measured, C_5H_6 and Cs^{++} ($m/q = 66$ u/e), we observed significant excess variation in the free-space cyclotron frequency ω_c due to measurement error in ω_z. The stability of our trap voltage is a secondary source of random uncertainty in ω_z. Our trap voltage exhibits long-term RMS fluctuations of only 100 ppb, and so contributes well below 0.1 ppb to a night's measurement.

c. Tuned circuit pulling. The interaction of the ion's axial oscillation with the detector tuned circuit "pulls" the ion's axial frequency ω_z by an amount $\Delta\omega_z = (\gamma_z/\gamma_0)(\omega_z - \omega_0)$ where ω_0 and $\gamma_0/2\pi$ are the detector circuit resonance frequency and

FWHM. This shift means that the measured axial frequency has the incorrect value for use in Eq. 5.6. Since $\gamma_z/\gamma_0 \propto Qq^2/m$ this is a significant problem for multiply charged ions when using a high-Q detector. For the predominantly singly-charged ions and the coil $Q \approx 30000$ used in 1992-93 the effect of frequency pulling is negligible. ($\gamma_z/\gamma_0 = 0.02$ for $m = 30$ and $q = 1$, resulting in $\Delta\omega_c/\omega_c = 0.008$ ppb for a 50 mHz axial detuning from the coil.)

For the heavy multiply-charged ions Cs^{++}, Cs^{+++} and Rb^{++} and the coil $Q \approx 50000$ used in 1998-99 the axial frequency shift due to pulling is significantly larger ($\gamma_z/\gamma_0 = 0.12$ for Cs^{+++}) and it caused a larger relative shift in the lower cyclotron frequencies. We minimized the frequency pulling in our alkali measurements by adjusting ω_z to be equal to the slowly drifting ω_0 (typically $\sim$ 50 mHz/hour) which was measured before each alkali ion cluster. We then used the measured values of ω_z and ω_0 ($|\omega_z - \omega_0|$ typically $<$ 100 mHz) to correct the measured values of ω_z for the pulling shift. Our measured frequency ratios for $\mathrm{Cs}^{+++}/\mathrm{CO}_2^+$ had the largest rms adjustment (0.12 ppb) for pulling. The $\sim$ 30% accuracy of our corrections implies that frequency pulling represents an error in our final ratios of at most 0.03 ppb and was not the source of the observed excess night-to-night fluctuations of the frequency ratio for Cs and Rb.

d. Thermal noise in cyclotron radius. Thermal noise in the cyclotron radius ρ_c also causes random error. Since the ion is cooled by a resistive detector, there is thermal uncertainty in the ion's initial location in phase space. The axial temperature T_z is $\approx$ 4 K due the the coupling of the ion's axial motion to the 4 K tuned circuit. The cyclotron mode is cooled via π-pulsing the cooled axial motion into the cyclotron mode [?], resulting in a cyclotron temperature T_c equal to $T_z(\omega_c'/\omega_z)$, which is 110 K for an ion with $m/q = 30$ u/e. This corresponds to a thermal rms cyclotron radius $\sqrt{<\rho_c^2>_{th}} = 9\ \mu\mathrm{m}$. These fluctuations in ρ_c lead to fluctuations in the observed cyclotron frequency because of the relativistic mass shift and trap field imperfections of Eq. 5.10. Coupled with thermal noise, these anharmonicities cause a random error of $\sim 40 \times 10^{-12}$ per cyclotron frequency measurement. Although this error is insignificant now, it may be dominant in two-ion mass spectrometry [COR92] in which both magnetic and electric field fluctuations cancel. We have investigated classical squeezing methods to reduce the effects of thermal noise by about a factor of 5 and we have demonstrated the ability to make sub-thermal measurements by parametric amplification at $2\omega_z$ [DNB92].

e. Radius-dependent systematic shifts Since ω_c is measured at nonzero cyclotron amplitude ($\rho_c \sim 250$ μm), the terms in Eq. 5.10 cause a frequency shift approaching 10^{-9}, we take care to assure that ρ_c is the same for both ions to avoid systematic errors in the frequency ratio. For "mass doublets" (ions with nearly equal m/q), this shift cancels to lowest order since the ions are driven to nominally the same radius ρ_c. However, systematic imbalances in ρ_c can arise due to unknown frequency dependence of the transfer function of the cyclotron drive electronics. The frequency dependence of the transfer function was determined from π-pulse data [DIF94],[BPR99], allowing us to maintain $\Delta\rho/\rho < 2\%$, leading to an upper bound on systematic error of 0.01 ppb for most doublets from both relativity and the magnetic bottle B_2 [DNB94]. The only exception is for the PNP measurements of Na^{++}/C, where the relatively large difference in m/q and light masses led to $\Delta\rho/\rho \approx 7\%$ and a large relativistic shift for which the data were corrected [BPR99]. The error from the higher-order electric field C_4 is also below 10^{-11}; although the error is systematic over the course of one run, it is random between ratio measurements because trap is retuned (changing C_4) before each run.

For non-doublets, these anharmonic shifts do not cancel to lowest order. Instead, the cyclotron amplitudes are controlled so that the relativistic shifts cancel, and corrections are made for the B_2 and C_4 shifts [NAT93]. The resultant systematic errors are calculted to be $\sim$ 0.03 ppb, insignificant compared to the errors from magnetic field fluctuations.

f. PNP Equilibrium Position Shift In PNP measurements different ions are differentially displaced from the trap center by the electric field from fixed charge patches. The electric field from fixed charge patches on the trap electrodes displaces ions from the trap center, and leads to differential displacements as the trap voltage is changed to bring ions into resonance with the detector in PNP measurements. (We measure the z component of the electric field due to charge patches with $< 10\%$ uncertainty by applying an offset potential and measuring the quadratic shift in ω_z, as described in [?]. Because of B-field inhomogenities, different equilibrium positions result in a differential systematic cyclotron frequency shift. For the doublets measured in 1992-1993 and most of the alkali metal measurements this systematic error was below 0.004 ppb. For Na^+/C_2^+ and Na^{++}/C^2 the shift was larger (0.019 ppb and 0.038 ppb respectively) because of the large $\Delta m/m$ and light masses involved. We corrected the Na measurements for these shifts (we assigned a 100% error to the correction because of our lack of knowledge of the radial component of the patch electric field due). The SOF measurements are made using the same trap voltage for both ions to eliminate such differential shifts.

g. Image Charge Shift The electric field due to the ion's image charge (ref. Van Dyck) causes radial frequency shifts $\Delta\omega_c' = -\Delta\omega_m = 93(1)\ \mu\text{Hz}/e$ (calculated using a finite difference solution of Laplace's equation for our hyperboloidal trap geometry). We correct our measured ω_c' frequencies for this effect before using them in Eq. 5.6 to obtain ω_c.

h. Magnetron Angle Normally we obtain ω_m from the measured ω_c' and ω_z using $\omega_m \approx (\omega_z^2/2\omega_c')(1 + 9/4\sin^2\theta_m)$ where $\theta_m = 0.16°$ is the measured angle between the B-field and trap axes. The effect of θ_m on a cyclotron frequency ratio is at most 0.002 ppb.

In summary, the magnetic field noise limits the accuracy of one night measurements to $\sim 10^{-10}$, and other sources of random and systematic errors are calculated to be about an order of magnitude smaller. We now show that the quoted accuracies are verified by a series of checks from redundancies in mass ratios.

5.3.3 Consistency Checks

We can exploit the redundancies in our overdetermined set of measurements to check for a variety of systematic effects. These checks allow greater confidence in our results than statistics alone can provide.

Table 5.3: Summary of Consistency Checks. The number of excess independent measurements ν and the reduced chi-square χ^2_ν are listed. The last column lists the statistical probability of exceeding the observed value of χ^2_ν for each check.

Check	ν	χ^2_ν	P
Closed loops	3	1.53	20 %
Magnet Rebuild	3	0.26	85 %
Redundant Ratios	4	0.39	82 %
Doublet/non-doublet	3	0.16	92 %
Overall	24	0.74	81 %

Repeated Measurements

Repeating measurements on the same pair of ions over several night runs with different field fluctuations tests the correctness of the uncertainties obtained from field fitting. For the 1992-93 data 7 ratios were measured more than once (for a total of 13 excess repetitions) with a reduced chi-square of $\chi^2_\nu = 0.75$. For the alkali metal data of 1998-99 the results of such measurements were satisfactory only for Na^+ and Na^{++} ($\chi^2_\nu = 0.8$). For ratios involving Cs^{++}, Cs^{+++} and Rb^{++} the repeated measurements were distributed with scatter larger than the uncertainty reported by field fitting, and had $\chi^2_\nu \approx 5$.

None of the sources of error in section II.B is large enough to explain the large night-to-night variation in the Cs^{++}, Cs^{+++}, and Rb^{++} ratios. We obtained similar variations when using the piecewise linear analysis method, proving that the variation was not an artifact of the field fitting process (e.g. due to an incorrect choice of fit order). This is discussed in more detail in our recent a paper [BPR99].

Our final uncertainties on these measured ratios accurately reflect this night-to-night scatter. For $Cs^{++}/C_5H_6^+$ and Cs^{+++}/CO_2^+, we increased each night's statistical uncertainty until $\chi^2_\nu = 1$ (from 6.6 and 4.9 respectively) for each ratio separately. For the ratios involving Rb we assumed that the night-to-night fluctuations were drawn from a common statistical distribution since each of the measurements was performed at very similar m/q ratios. Therefore, we increased the statistical uncertainty on all of the Rb frequency ratios by a common factor to reduce the overall Rb χ_ν^2 from 4.7 to 1. The Na ratios exhibited no significant night-to-night fluctuations and required no adjustment of their uncertainties.

Closed Loops

Another check on the 1992-93 data involves "closed loops" of ratios. Given three ions A^+, B^+, and C^+ of nominally the same mass, there are three possible doublets that can be measured: A^+/B^+, B^+/C^+ C^+/A^+. If the ratios are multiplied together, the product should be equal to one, within experimental error. This provides an independent check on the error assigned to the ratios (Except for errors proportional to the small mass differences). Closed loops are also sensitive to systematic errors which are nonlinear with respect to the difference in mass. This type of error could arise from surface potentials on the trap electrodes and higher order electric field inhomogeneities. There are three such closed loops having a reduced chi-square of $\chi_\nu^2 = 1.53$. (Statistically, a reduced chi-square of this value or higher should arise in 20% of the cases, so having $\chi_\nu^2 = 1.53$ is not anomalously high.)

Experimental Reassembly

In the midst of the 1992-93 measurements, our superconducting magnet accidentally quenched. The magnet dewar and shield was reassembled, reenergized, and reshimmed, changing the higher-order inhomogeneities in the magnetic field. In doing so, the trap was thermally cycled between 300 K and 4 K, changing the surface patch charges on the trap electrodes which contribute to higher-order terms in the electric field. Measurements done both before and after the magnet rebuild therefore check systematic errors resulting from field imperfections. There were three such measurements, having a reduced chi-square of $\chi_\nu^2 = 0.26$.

Redundant Ratios

It is easy to show that a mass ratio ≈ 1 determines a mass difference.

Some doublet ratios are redundant, determining the same mass difference using different molecular ions. For example, the mass doublet ratios O^+/CH_4^+, $CO^+/C_2H_4^+$, and $CO_2^+/C_3H_8^+$ all determine the mass difference (C+4H−O), but at mass 16, 28, and 44 u, respectively. Such redundant ratios check for virtually all systematic errors, since these ratios are measured at the low medium, and highest of our m/q ratios (excepting the alkali measurements). The different trap voltages are differentially sensitive to surface patch charge effects, and the different cyclotron frequencies test for errors in the phase-coherent cyclotron mode coupling techniques and the host of errors that scale as $(\omega_z/\omega_c)^2$. Also, errors which depend on the frequency ratio would be checked. The 1992-1993 measurements contain a total of four redundancies with $\chi_\nu^2 = 0.39$.

Nondoublet/doublet tests

Non-doublet ratios could also be determined solely from doublet ratios, providing a test of possible systematic errors arising from differences in the measurement techniques. Anharmonic frequency shifts which cancel to lowest order for doublets do not naturally cancel for non-doublets. The cyclotron modes are intentionally driven to different amplitudes in order to cancel the relativistic shift, but a magnetic bottle shift remains. Three doublet / non-doublet redundancies resulted in $\chi_\nu^2 = 0.16$, indicating that such systematic errors are insignificant at the 10^{-10} level of precision.

5.4 Atomic Masses

5.4.1 Cyclotron frequency ratios and neutral mass differences

Mass ratios were measured for a wide variety of molecular ions, and the results are listed in Table 2. Many ratios were measured multiple times to reduce statistical error. As will be discussed in the next two sections, the ion species were selected to allow several self-consistent checks for systematic error and to provide accurate neutron separation energies for determining fundamental constants. Enough ratios were measured so that each atomic mass reported was determined by at least two independent routes.

The first step in converting ion mass ratios into atomic masses is to account for chemical binding energies and ionization energies:

$$A_nB_k^+ \rightarrow nA_{(g)} + kB_{(g)} - e^- + \Delta E \tag{5.20}$$

The energy ΔE required to form a molecular ion from the elements is calculated from the standard heats of formation in the gaseous state at 0 K [LIA88]. Afterwards, the mass ratio r can be expressed in terms of the individual atomic masses, as in this example:

$$r = \frac{m[A_nB_k^+]}{m[C_pD_q^+]} = \frac{nA + kB - e^- + \Delta E_1}{pC + qD - e^- + \Delta E_2} \tag{5.21}$$

which, after rearranging, yields a mass differences:

$$pC + qD - nA - kB = (1-r)(pC + qD - e^-) + \Delta E' \tag{5.22}$$

Although C and D also appear on the right side of the equation, they are multiplied by the small factor $(1-r)$ and do not need to be known a priori to high precision. In addition, species which appear in both the numerator and the denominator cancel to first order in the mass difference, for example, the ratio m[CD_3^+]/m[$\mathrm{CD}_2H_2^+$] determines the mass difference 2H$-$D.

Table 2 also lists the mass differences and their uncertainties obtained from the measured values of the mass ratios. This table of mass differences can be expressed in matrix form:

$$XM = Y \pm \sigma \tag{5.23}$$

where X is a $P \times Q$ matrix of the coefficients, M is a column vector of the Q atomic masses, and $Y \pm \sigma$ is a column vector of the P mass differences and uncertainties. (The reference atom ^{12}C, which is defined to have a mass of exactly 12 u, is included on the right side of the equation.)

5.4.2 Global fit to overdetermined set

The best values of the atomic masses are obtained from a global least squares fit:

$$M = X^{-1}Y \tag{5.24}$$

where

$$X_{jk} = \sum_{i=1}^{P} \frac{x_{ij}x_{ik}}{\Sigma_i^2}, Y_j = \sum_{i=1}^{P} \frac{x_{ij}y_i}{\Sigma_i^2} \tag{5.25}$$

The inverted matrix X^{-1} is the covariance matrix, which directly yields the uncertainties in the atomic masses. The ability to invert the X matrix depends on whether each individual species can be directly related to ^{12}C. This is rather difficult to accomplish solely with doublets in the mass range where we operate (10-50 u). For example, the three ratios N^+/CH_2^+, O^+/CH_4^+, and CO^+/N_2^+ may not seem to be redundant, but they actually are. We have found one set of doublets ($Ar^+/C_3H_4^+$, Ar_{++}/CD_4^+, and $CD_3^+/CD_2H_2^+$) which breaks the singularity in the matrix by determining H directly in terms of C. Non-doublet measurements [NBD93], such as CH_4^+/C^+, have been very useful for providing links to invert the matrix. An atomic mass table (Table 3) of thirteen isotopes and the neutron is obtained by fitting to the entire set of our mass ratio measurements. For comparison, the best values from conventional mass spectrometry are also listed, showing an improvement in precision of a factor of 10-1000 using Penning traps. The 1993 atomic mass evaluation [AUW93] contains some data from Penning trap experiments, including preliminary value [NBD93] of some results reported here. Table 3 also lists measurements from other Penning trap experiments. The U. Washington group has measured the masses of several light isotopes, most notably ^{3}He and ^{3}H with uncertainties generally around a factor of 2 larger than our

Table 5.4: Summary of Consistency Checks. The number of excess independent measurements ν and the reduced chi-square χ^2_ν are listed. The last column lists the statistical probability of exceeding the observed value of χ^2_ν for each check.

Check	ν	χ^2_ν	P
Closed loops	3	1.53	20 %
Magnet Rebuild	3	0.26	85 %
Redundant Ratios	4	0.39	82 %
Doublet/non-doublet	3	0.16	92 %
Overall	24	0.74	81 %

experiment [VFS93b], [VFS93c], and they have recently reported a value of M_p accurate to 0.14 ppb [VFZ98]. The Stockholm-Mainz group has measured the mass of ^{28}Si in a Penning trap by the time-of-flight method and has achieved 10^{-8} precision [JER93]. Recently the SMILETRAP collaboration has measured the mass of ^{133}Cs with uncertainty 1.8×10^{-9} [CFB99]. The group at Ohio State has determined several mass differences by FT-ICR spectrometry on ion clouds with uncertainties about 20 times larger than our corresponding values [GOR93]. With the exceptions of ^{16}O and ^{20}Ne, our measurements are in good agreement with these other Penning trap values.

5.5 Applications to Metrology and Fundamental Physics

With accuracies $\sim$ 0.1 ppb, atomic mass measurements have important new implications for metrology and fundamental physics. [DNB94] In this section we discuss the contributions of our measurements to defining an atom-based mass standard, calibrating γ-ray wavelengths, and determining the fundamental constants α and $N_A h$ (the Molar Planck constant).

Table 5.5: Atomic Mass Table. Listed are the masses (in u) of thirteen isotopes and the neutron determined from the MIT values in Table 5.1, the 1993 atomic mass evaluation, and other Penning trap experiments. The numbers in parentheses indicate the errors in the rightmost figures. for the purpose of comparison, zeros have been added so the numbers of digits are equal. The uncertainty of the neutron mass from this experiment is limited by the error in the deuteron binding energy.

Atom	MIT Mass (u)	Non-P T values (u) [AUW88]	Other P T values (u)
^{1}H	1.007 825 031 6 (5)	1.007 825 035 0 (120)	1.007 825 032 21 (14)
n	1.008 664 923 5 (23)	1.008 664 919 0 (140)	1.008 664 918 7 (26)
^{2}H	2.014 101 777 5 (5)	2.014 101 779 0 (240)	2.014 101 776 9 (11)
^{13}C	13.003 354 838 1 (10)	13.003 354 826 0 (170)	13.003 354 840 4 (41)
^{14}N	14.003 074 004 0 (12)	14.003 074 002 0 (260)	14.003 074 005 6 (18)
^{15}N	15.000 108 897 7 (11)	15.000 108 970 0 (400)	
^{16}O	15.994 914 619 5 (21)	15.994 914 630 0 (500)	15.994 914 626 3 (30)
^{20}Ne	19.992 440 175 4 (23)	19.992 435 600 0 (22000)	
^{28}Si	27.976 926 532 4 (20)	27.976 927 100 0 (7000)	27.976 926 575 0 (380)
^{40}Ar	39.962 383 124 0 (33)	39.962 383 700 0 (14000)	
^{133}Cs	132.905 451 931 (27)	132.905 447 000 (3000)	132.905 451 844 (270)
^{87}Rb	86.909 180 520 (15)	86.909 185 800 (2800)	
^{85}Rb	84.911 789 732 (14)	84.911 792 400 (2700)	
^{23}Na	22.989 769 280 7 (28)	22.989 769 660 0 (2600)	

5.5.1 Kilogram Standard

Our demonstrated ability to compare atomic masses at the 10^{-10} level establishes comparison of atomic masses as a more precise operation than comparison of macroscopic masses, which is limited to a relative precision of $\sim 10^{-9}$ (especially for masses of different density) [QUI91]. This makes attractive an atomic definition of mass, which could be achieved by defining the Avogadro constant, N_A (this would be analogous to the way in which defining the speed of light c has defined length in terms of the time standard). Accurately realizing an atomic mass standard would enable replacement of the last SI artifact standard, namely the kilogram.

The S.I. unit of mass, the kilogram, is defined to be the mass of the prototype platinum-iridium cylinder at the Bureau International des Poids et Mesures. Reliance on a unique artifact standard has the disadvantage that it may drift or be damaged during handling. [QUI91] (To guard against mishandling, the prototype kilogram has been compared to secondary standards only 3 times this century.) The old artifact standards for time, distance, voltage and resistance have been replaced by operational standards based on fundamental physical principles: the second is defined as a definite number of periods of the hyperfine resonance frequency of the ground state of Cs, the metre is defined as the distance light travels in 1/c seconds, where c is a defined constant, the standard Volt is defined in terms of the Josephson effect, and the standard Ohm is defined in terms of the quantum Hall effect. Similarly it would be desirable to develop a mass standard based on fundamental quantities, like the mass of an atom. Falling-coil experiments provide an indirect way to link macroscopic masses to the standard Volt and Ohm, but a practically realizable mass standard defined in terms of an atomic mass would be ideal.

A promising method for realizing an atomic kilogram is to accurately measure the lattice constant d and mass density ρ of a crystalline material of atomic mass M; this is the *XRCD* (*X-Ray Crystal Density*) method. With the current mass standard such measurements determine the Avogadro constant N_A via $N_A = M/10^3\rho(V/n)$ where V is the volume of a unit cell containing n atoms; with an atomic mass standard based on a defined value of N_A, the crystal would be a mass density standard leading to a macroscopic realization of the kilogram. Although ^{12}C is the standard for atomic masses neither crystalline form of ^{12}C is suitable for macroscopic mass standards; graphite is too soft, and diamond is too difficult to produce in quantity. Hence ^{28}Si is the preferred material. Although the XRCD method on Si currently yields measurements of N_A with precisions $\sim 10^{-6}$ and which disagree by $\sim 3 \times 10^{-6}$ [MAR99], the Si d_{220} lattice spacing has been measured with relative uncertainty 3×10^{-8} [BAS95], opening the door to kilogram standards at the 10^{-8} level. Realizing the kilogram with 10^{-8} accuracy would provide a valuable check on the long-term stability of the artifact standard. The previous (non-Penning-trap) value of $M(^{28}\mathrm{Si})$ was accurate to 2.5×10^{-8}, and would have been a limitation in the accuracy of N_A. The value from our experiment, accurate to 7×10^{-11} and confirmed to 10^{-9} [JER93] removes this limitation.

5.5.2 γ-ray Re-Calibration

Another application of precision mass spectrometry in the field of metrology is to "weigh" γ-rays. By Einstein's principle, $\Delta E = \Delta mc^2$, so the energy released in a nuclear process in the form of γ-rays can be measured as a difference in the mass of the initial and final nuclei. Since wavelength measurements of γ-rays whose energies exceed 1 MeV are difficult due to their small diffraction angles from crystal spectrometers (≤ 0.01 rad resulting from the short wavelengths ≤ 0.01A), neutron separation energies determined by mass spectrometry are often used to calibrate γ-ray wavelengths in the 2-13 MeV range. If a set of γ-rays with wavelengths λ'_i (corrected for recoil effects) are emitted, we can define $1/\lambda'_{eff} \equiv \sum_i 1/\lambda'_i$ and we have the energy balance equation:

$$E_\gamma = \frac{hc}{\lambda'_{eff}} = \Delta mc^2 \rightarrow \lambda'_{eff} = \frac{h}{c}\frac{1}{\Delta m} \rightarrow \lambda'_{eff} = \frac{N_A h}{c}\frac{10^3}{\Delta M} \qquad (5.26)$$

Since the γ-ray energy emitted in a typical neutron-capture is typically $\sim 10^7$ eV, and typical nuclei have masses $\sim$ 10 GeV/c^2, mass measurements with precision

10^{-10} on the nuclei involved yield measurements of Δm with accuracies $\sim 10^{-7}$. This precision is comparable to the best precision achievable for the measurement of absolute wavelengths using flat-crystal gamma-ray spectrometry [GRE94].

The neutron capture reactions $^{14}\mathrm{N}(n,\gamma)$ and $^{12}\mathrm{C}(n,\gamma)$ are two processes that are attractive for γ-ray wavelength calibration:

$$^{14}\mathrm{N} + n \rightarrow ^{15}\mathrm{N} + \gamma_1 + \gamma_2 \quad (10.8\ \mathrm{MeV}) \tag{5.27}$$

$$^{12}\mathrm{C} + n \rightarrow ^{13}\mathrm{C} + \gamma \quad (4.9\ \mathrm{MeV}) \tag{5.28}$$

When combined with $^{1}\mathrm{H}(n,\gamma)$:

$$^{1}\mathrm{H} + n \rightarrow \mathrm{D} + \gamma \quad (2.2\ \mathrm{MeV}) \tag{5.29}$$

the neutron mass cancels, yielding the energy balance equations:

$$m[^{14}\mathrm{N} + \mathrm{D} - ^{15}\mathrm{N} - ^{1}\mathrm{H}]c^2 = hc/\lambda_1^* \tag{5.30}$$

$$m[^{12}\mathrm{C} + \mathrm{D} - ^{13}\mathrm{C} - ^{1}\mathrm{H}]c^2 = hc/\lambda_2^* \tag{5.31}$$

Thus precise measurements of the mass differences $M[^{14}\mathrm{N}$ + D - $^{15}\mathrm{N}$ - $^{1}\mathrm{H}]$ and $M[^{12}\mathrm{C}$ + D - $^{13}\mathrm{C}$ - $^{1}\mathrm{H}]$ are valuable for γ-ray spectroscopy.

In 1993, the ratios $^{14}\mathrm{N}_2^+/\mathrm{C}_2\mathrm{H}_4^+$ and $^{15}\mathrm{N}_2^+/\mathrm{C}_2\mathrm{D}_2\mathrm{H}_2^+$ were measured, leading to a value of $\Delta M = ^{14}\mathrm{N} + \mathrm{D} - ^{15}\mathrm{N} - \mathrm{H} = 9\quad 241\quad 852.1(1.1)$ nu. As a redundancy check, a value of $\Delta M = 9\quad 241\quad 853.7(1.7)$ nu was obtained independently from all other ratios ($^{15}\mathrm{N}^+/\mathrm{CH}_3^+$, $\mathrm{N}_2^+/\mathrm{CO}^+$, etc.). The previously accepted value of $\Delta M$from conventional mass spectrometry [SMI75] is 9 241 780(8), so the MIT value is more precise by a factor of about 10. Smith's value and the MIT value for ΔM do not agree, differing by nine times the reported uncertainty in Smith's value. The γ-ray energy calibration [WAP90] was based on the inconsistent prior value for ΔM. Unlike our redundant Penning trap measurements, the earlier result was based on a single

Table 5.6: Atomic Mass Differences. Atomic mass differences measured by the MIT Penning trap experiment and the Ohio State FT-ICR experiment.

Mass difference	MIT Value (u)	Ohio State value (u)
CH_2^+ - N^+	0.012 576 046 4 (6)	0.012 576 039 0 (190)
H_2O^+ - DO^+	0.001 548 279 4 (9)	0.001 548 296 0 (120)
D_2O^+ - $^{20}Ne^+$	0.030 677 980 2 (25)	0.030 677 480 0 (670)

mass comparison. The improved mass difference obtained by Penning trap mass spectrometry resulted in an 8 ppm revision of this calibration.

5.5.3 Fine-Structure Constant

Accurate mass measurements will play an important role in improving the measured value of the fine-structure constant, helping to resolve current disagreements between different measurements of α [KIN96]. This application is a consequence of a high-precision route to α based on the relationship between α and the molar Planck constant $N_A h$ [TAY94],

$$\alpha^2 = \frac{2R_\infty}{c}\frac{10^3}{M_p}\frac{m_p}{m_e}(N_A h). \tag{5.32}$$

All the quantities linking α and $N_A h$ in Eq. (5.32) are known to high precision: R_∞ to 0.008 ppb [UHG97], m_p/m_e to 2 ppb [?], and M_p (the mass of the proton in atomic units u), measured by our group to 0.5 ppb [DNB94], and recently by Van Dyck *et al.* (1998) to 0.14 ppb [VFZ98]. Thus an independent measurement of $N_A h$ to 2 ppb would determine α to 1.4 ppb, and which would be the highest precision measurement of α available.

$N_A h$ can be accurately determined by measuring the velocity v and de Broglie wavelength $\lambda_{dB} \equiv h/mv$ of a particle of known atomic mass M. This follows from $\lambda_{dB} v = h/m = 10^3 N_A h/M$ where m is the mass of the particle in SI units, implying

$$N_A h = M\lambda_{dB} v \times 10^3 \tag{5.33}$$

Kruger et al. [KRU98] exploited this method using neutron interferometry to measure h/m_n with a precision of 73 ppb. Combining this with a precise measurement of M_n obtained from Penning trap measurements of $M[^2\mathrm{H}]$, $M[^1\mathrm{H}]$ [DNB94], [?] and γ-ray measurements of the nuclear binding energy of ^{2}H [GRE86] resulted in a value of α with a precision of 37 ppb.

It appears that measurements of $N_A h$ and hence α of much higher precision can be made by using atoms instead of neutrons to determine h/m. Atom interferometers appear capable of measuring recoil velocities from photon absorption, leading to values of h/m_{alkali} accurate at the 10^{-9} level. We have recently measured M for the alkali metals Cs, Rb, and Na. Chu's group at Stanford is measuring h/m for Cs in terms of λ_{D1} for Cs, which has recently been accurately measured at MPI Garching [URH99]. Although systematic effects in the photon recoil measurement currently limit the accuracy to 50 ppb (hence limiting the uncertainty on α to 25 ppb), the high precision achieved (22 ppb in 4 h) [YOU97] shows promise for much better measurements of α. Moreover, advances in alkali BEC technology also hold great promise for improving the accuracy of h/m atom interferometry measurements on Na and Rb. Our sub-ppb measurements of the masses ^{133}Cs, ^{87,85}Rb and ^{23}Na, H, and ^{2}H are a strong foundation from which to improve measurements of α to ≤ 1 ppb (where m_p/m_e becomes a limit).

5.5.4 Molar Planck Constant $N_A h$

From Eq. 5.26 we see that mass spectrometry at the 10^{-10} accuracy level (leading to measurements of neutron-capture ΔMs accurate to 10^{-7}) combined with absolute gamma-ray wavelength measurements at the 10^{-7} level would allow $N_A h$ to be determined with uncertainty 10^{-7}. Equation 5.26 connecting $N_A h$ (and hence α via Eq. 5.32) is a consequence of the formula $E = mc_m^2$, where c_m^2 is the limiting velocity of matter in special relativity. Combining it with a measurement of α from the Quantum Hall Effect (a purely electromagnetic phenomenon) will allow a test of special relativity's assumption that c_m equals the speed of electromagnetic waves c_{EM}. Although this test (relative uncertainty $\sim 10^{-5}$) is not as accurate as tests of the isotropy of space (relative uncertainties $\sim 10^{-22}$) it has the great advantage of not depending upon any assumption of a preferred frame of reference. The most promising measurement for this application would be the neutron capture reaction $^{32}\mathrm{S}+n \rightarrow {}^{33}\mathrm{S}+\gamma$. (Kessler, private communication)

5.6 Future directions

Our main goal in the future is to achieve a precision of 10^{-11} or better. At that level, chemical bonds could be weighed with reasonable accuracy. To achieve this goal, we are considering ways to shield the magnetic field fluctuations, to measure two ions simultaneously, and to "squeeze" thermal noise. In addition, we are considering improved methods of loading ions into our trap to enable a wider variety of measurements, in particular the $^3\mathrm{H} -^3 \mathrm{He}$ mass difference.

5.7 Acknowledgements

This work was supported by the National Science Foundation (Grant No. PHY-9222768), the Joint Services Electronics Program (Grant No. DAAL03-92-C-0001), and the National Institute of Standards and Technology, through a NIST Precision Measurements grant. One of us (F.D.) acknowledges additional support from an N.S.F. Graduate Fellowship. We are grateful to Roland Nguyen for winding our $Q = 50000$ coil. We also would like to thank M. Matthews for helpful discussions on fitting to the magnetic field drift

Table 5.7: Re-analyzed mass ratios from the 1992-93 data set. Listed are mass ratios for which the discrepancy between the single-point-based least squares fit result and the cluster-based robust fit result resulted in a value of $\chi^2_\nu > 0.5$. The numbers tabulated are the "mass ratios" $q[\mathrm{B}]m[\mathrm{A}]/q[\mathrm{A}]m[\mathrm{B}] = \omega_c[\mathrm{B}]/\omega_c[\mathrm{A}]$ for the corresponding ion ratio A/B. The fit methods tabulated are the least-squares and robust fit results for cyclotron frequency measurements treated as single data points, the corresponding methods for the data grouped in clusters, and the $1/\Delta t$-weighted piecewise linear fit method.

$\mathrm{Ar}^{++}/\mathrm{CD}_4^+$ 10/17/92

Method	n	Result
Least-squares, single point	4	0.996 249 698 100 (100)
Robust, single point	8	0.996 249 698 364 (092)
Least-squares, cluster	8	0.996 249 698 365 (101)
Robust, cluster	2	0.996 249 698 358 (090)
Piecewise Linear	-	0.996 249 698 390 (043)

$\mathrm{Ar}^{++}/\mathrm{Ne}^+$ 10/22/92

Method	n	Result
Least-squares, single point	5	0.999 437 341 250 (150)
Robust, single point	3	0.999 437 341 544 (139)
Least-squares, cluster	5	0.999 437 341 472 (252)
Robust, cluster	3	0.999 437 341 593 (180)
Piecewise Linear	-	0.999 437 340 474 (547)

$\mathrm{CD}_3^+/\mathrm{CD}_2\mathrm{H}_2^+$ 12/5/92

Method	n	Result
Least-squares, single point	6	0.999 914 190 600 (200)
Robust, single point	6	0.999 914 190 215 (124)
Least-squares, cluster	6	0.999 914 188 943 (738)
Robust, cluster	3	0.999 914 190 870 (170)
Piecewise Linear	-	0.999 914 189 405 (814)

$\mathrm{Ar}^+/\mathrm{C}_3\mathrm{H}_4^+$ 12/30/92

Method	n	Result
Least-squares, single point	6	0.998 278 399 400 (120)
Robust, single point	5	0.998 278 399 416 (107)
Least-squares, cluster	6	0.998 278 399 445 (114)
Robust, cluster	2	0.998 278 399 210 (150)
Piecewise Linear	-	0.998 278 399 362 (162)

Chapter 6

Shielding Magnetic Field Gradients

Michael P. Bradley, David E. Pritchard
Room 26-142, MIT, Cambridge, MA, 02139

6.1 Abstract

Time-varying magnetic field gradients can be shielded from experimental regions by using oppositely-wound solenoid pairs. We discuss the manner in which such shielding may be achieved, and present a design for a solenoid pair to shield an applied field gradient at the origin, as well as a family of designs which provide differential field cancellation at two points. The coils need not be superconducting; their conductivity will simply set a lower limit on the frequency of time-varying gradients which can be effectiviely shielded.

6.2 Introduction

Magnetic field gradients cause line broadening in nmr, errors in precision spectroscopy, and generally degrade the quality of other data in magnetic-field dependent experiments. In this paper, we propose a method of shielding external magnetic field gradients using two solenoids connected in opposition. Ours is a passive approach: the external gradient induces a current in the solenoid pair which generates a gradient in opposition to the external gradient, canceling out its pernicious effects. There are two closely related situations in which external gradients could beneficially be suppressed: the complete suppression of the gradient over as large a region around the origin as possible, and the suppression of magnetic field differentials between two regions separated by a small distance symmetrically about the origin. This latter application is important when comparing two nmr samples or the cyclotron frequencies of two trapped ions. We exhibit designs which eliminate the effects of external gradients on both net gradients at the origin and differentials between two neighboring regions.

Our work builds on earlier work on the shielding of uniform external fields (and importantly their temporal variation). Van Dyck used a double loop - crudely a flux-gathering outer loop connected to a field-generating inner loop - to eliminate the influence of the external magnetic field in a superconducting magnet used for charged particle resonance experiments [VMF86]. Tan and Gabrielse showed that a solenoid of the proper aspect ratio can completely shield a uniform external field from its center. In practice the performance of either approach is limited by the current induced in the shielding coil if it twists in the uniform field which is being stabilized, or translates in the spatial gradients of this "uniform" field. For this reason the most successful approach is to incorporate the shielding solenoid into the superconducting magnet which produces the field, in effect making a magnet whose central longitudinal field is independent of the external field in which it operates.

In order to avoid such problems when shielding gradients, we propose here that external gradients be shielded by opposing solenoids connected in series. These link no net flux, so that twisting the pair in a uniform field does not induce any net current in the solenoids. We note that separately shorting each of the solenoids would produce identical gradient shielding and in addition some shielding of uniform external fields, but at the expense of sensitivity to twisting.

Our paper is divided into three short sections. The first sets out the general solenoid configuration and outlines how to calculate the induced B-field due to an externally applied gradient. The second considers the problem of making as large a region as possible around the origin free from the applied gradient and presents an optimum design. The last section considers the suppression of differential fields between two points separated by a finite distance, and presents a family of solenoid designs for this purpose.

6.3 Counter-Connected Solenoids in Applied Field Gradients

In this paper we will consider the gradient shielding capabilities of coaxial, counter-connected identical solenoids of length l and radius r. (See Fig. 6-1) By "counter-connected" we mean that the solenoids are connected so that a flowing current sets up fields which oppose one another, creating only a gradient midway between the solenoids. We define the z-axis as the axis of the solenoids, with $z = 0$ being the midplane. The centers of the solenoids are separated by distance s. We consider single-layer solenoids with n' turns per unit length. In the limit of thin wire ($1/n' << l$), the results do not depend on n'.

We consider the response of the solenoid configuration of Fig. 6-1 to an applied field gradient $\vec{B}_{ext} = B'_{ext} z\hat{z}$. In the presence of this gradient each solenoid links a net flux $N\phi$:

$$N\phi = (n'l)B'_{ext}\frac{s}{2}A \tag{6.1}$$

where $N = n'l$ is the number of turns on each solenoid and $A = \pi r^2$ is the cross-sectional area. The current induced in response to this flux change is:

$$I_{ind} = \frac{2N\phi}{L-M} = \frac{n'lB'_{ext}sA}{L-M} \tag{6.2}$$

where L and M are the self and mutual inductances of the solenoids, calculable using the methods of [GAR63]. The axial field $\vec{B}_{ind}(z) = B_{ind}(z)\hat{z}$ due to the induced current can be obtained using the well-known result for the axial field of a solenoid [SMY55]. The net field due to the applied gradient in the presence of the gradient

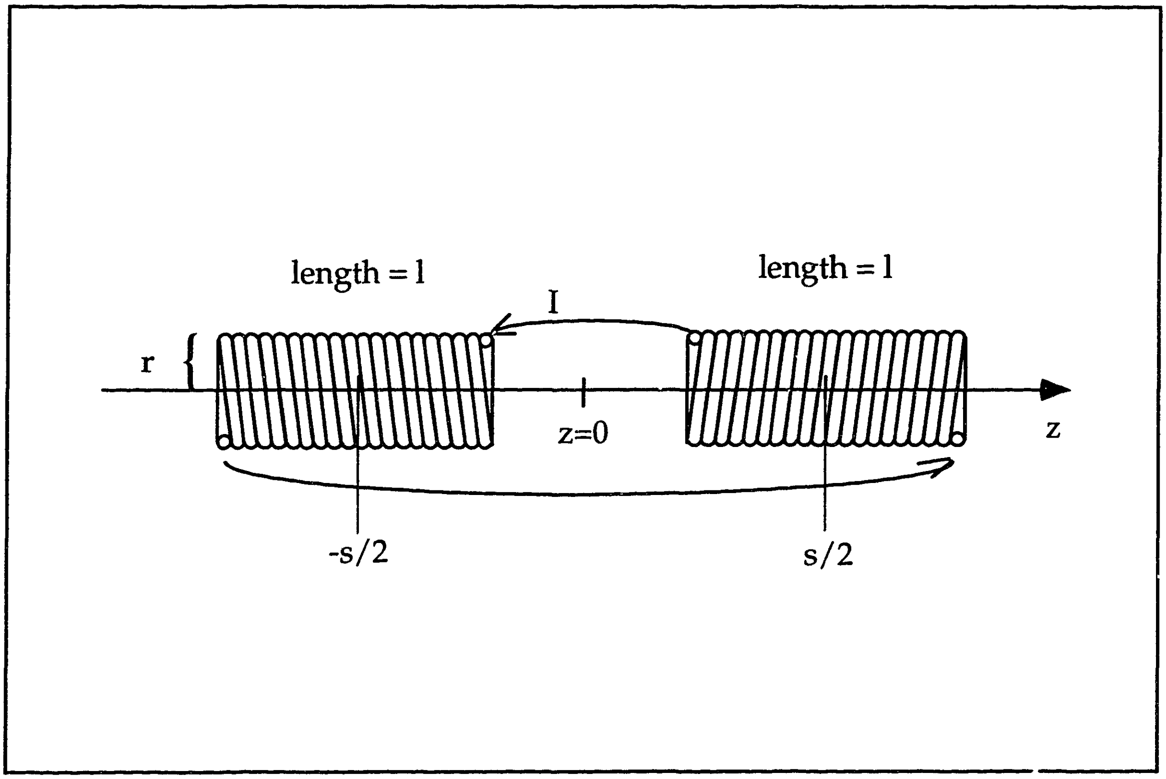

Figure 6-1: Basic solenoid geometry for gradient shielding applications. The solenoids have the same length l and radius r, the same number of turns per units length n', and their centers are separated by a distance s. They are *counter-connected* in a circuit so that a current I flowing as indicated causes the solenoids to generate opposing fields, creating only a gradient at $z = 0$. Then the solenoid pair will link net flux if placed in a field gradient, and no net flux if placed in a uniform field.

shielding coils is then

$$B_{net}(z) = B'_{ext}z + B_{ind}(z). \tag{6.3}$$

Figure 6-2 is an illustrative plot of the induced field due to an applied gradient for a scaled radius $\rho \equiv r/s = 0.3$ and three different values of the scaled length $\lambda \equiv l/s$. It can be seen that as the scaled length $\lambda = l/s$ is increased we pass from a region in which the induced gradient *undercompensates* the applied gradient into a region where it *overcompensates* the applied gradient. Between the undercompensating and overcompensating cases we can find a pair of values (ρ, λ) where there is perfect compensation at a certain point z_S along the z axis. This type of configuration allows us to shield two points at $\pm z_S$ such that $B_{tot} = 0$ and $\partial B_{tot}/\partial z = 0$. In Section 6.4 we discuss how we may shield a gradient at the origin by moving the perfectly shielded points as close to the origin as possible. In Section 6.5 we describe how such pairs of perfectly shielded points can be used to provide two-point differential shielding.

6.4 Shielding A Gradient at the Origin

As ρ and λ are increased the points of perfect shielding move towards the origin, suggesting that a region of perfect gradient cancellation may be found centered about the origin for a correctly chosen solenoid configuration. We find that the solenoid configuration with the scaled radius and length $\rho = 0.485, \lambda = 0.408$ gives $B_{net} = 0$ and $\partial B_{net}/\partial z = 0$ at the origin. (We also have $\partial^2 B_{net}/\partial z^2 = 0$ at the origin by the symmetry of the solenoid arrangement.) Our figure of merit for characterizing the gradient shielding at the origin provided by this configuration is therefore the normalized third derivative:

$$1/(B'_{ext}s)\partial^3 B_{net}/\partial(z/s)^3 = -0.6 \tag{6.4}$$

The Taylor expansion of B_{net} about the origin is

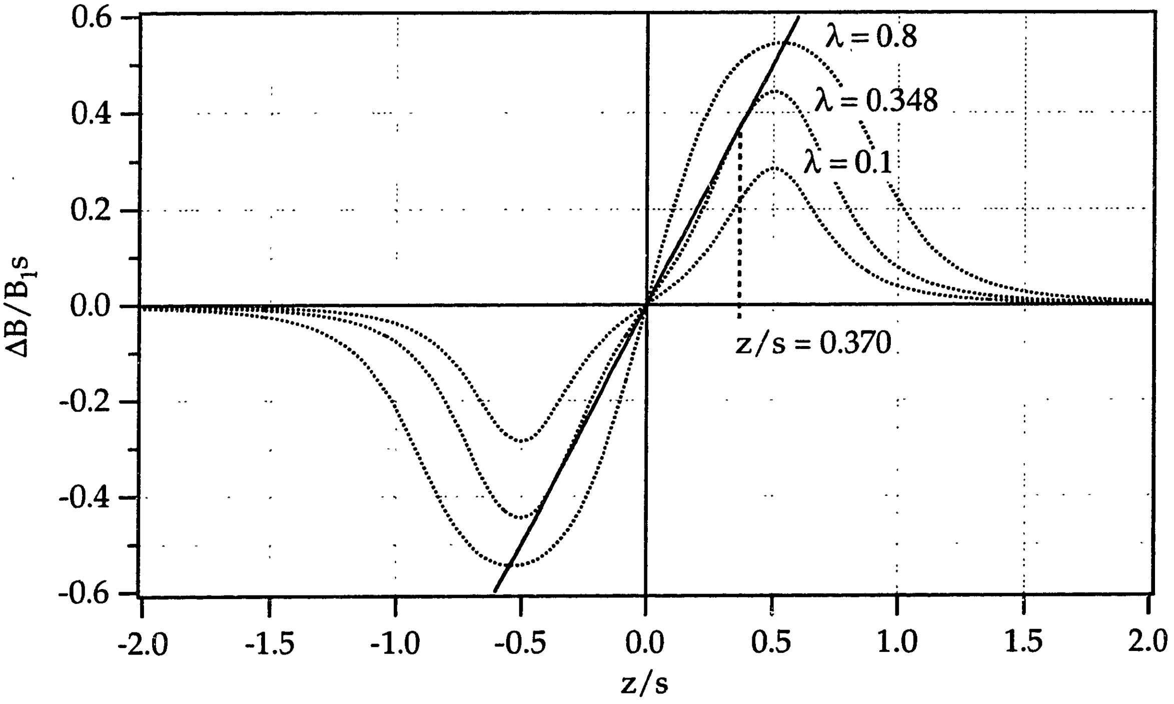

Figure 6-2: Plotted using dotted lines are induced field profiles $-B_{ind}(z)$ for a scaled radius $\rho = r/s = 0.3$ and three different values of the scaled length $\lambda \equiv l/s$. The solid line with 45° slope is the applied field gradient $B'_{ext}z$. For $\lambda = 0.1$ the induced field *undercompensates* for the applied gradient, and for $\lambda = 0.8$ the induced field *overcompensates* for the applied gradient. For $\lambda = 0.348$ the induced field perfectly compensates for the applied gradient, i.e. $B_{net} = 0$ and $\partial B_{net}/\partial z = 0$ at the two points $z_S = \pm 0.370$.

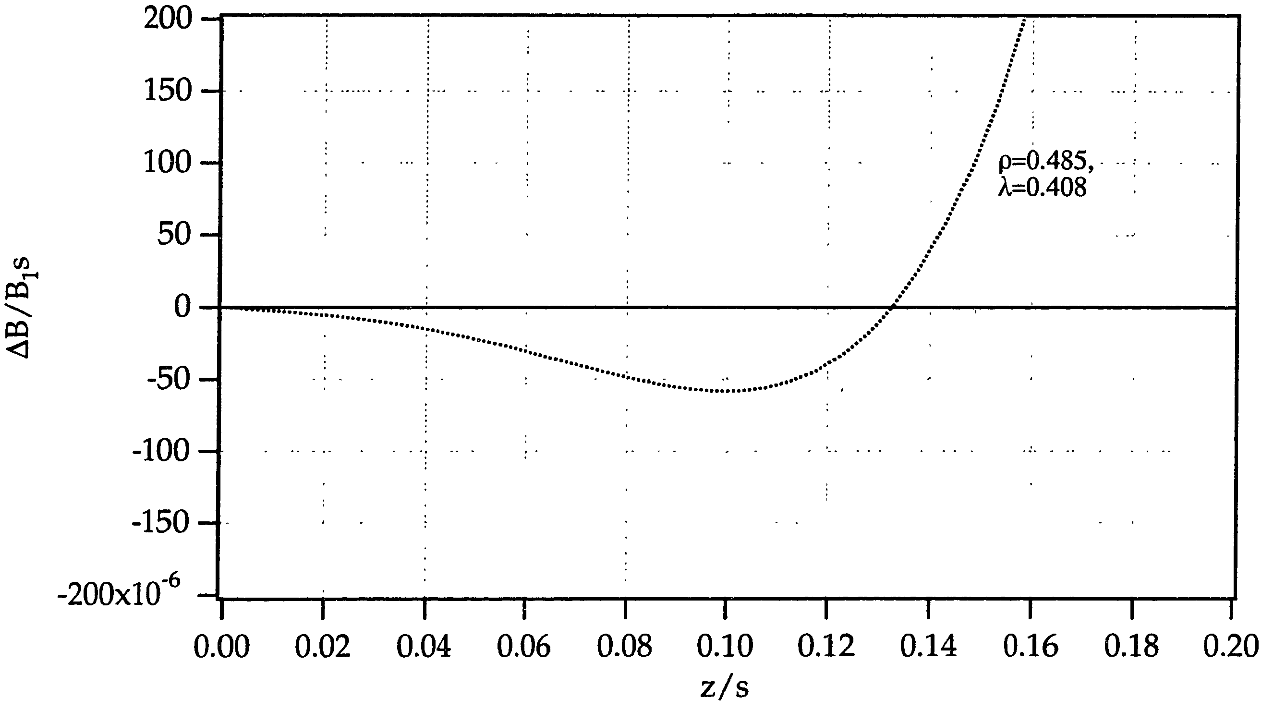

Figure 6-3: Plot of the net field $B_{net}(z)$ due to a pair of counter-connected solenoids with scaled radius and length $\rho = 0.485, \lambda = 0.408$. This configuration gives B_{net} and $\partial B_{net}/\partial z = 0$ at the origin ($\partial^2 B_{net}/\partial z^2 = 0$ at the origin by symmetry), and a minimal value of $\partial^3 B_{net}/\partial z^3$, making it the ideal configuration for shielding a gradient at the origin.

$$B_{net} = \frac{1}{6}\left(\frac{\partial^3 B_{net}}{\partial z^3}\right) z^3 \tag{6.5}$$

This results in a relative field variation at z of

$$\frac{\Delta B}{B'_{ext} z} = \frac{1}{6}\frac{1}{B'_{eff} s}\frac{\partial^3 B}{\partial (z/s)^3}\left(\frac{z}{s}\right)^3\left(\frac{s}{z}\right) = -0.1\left(\frac{z}{s}\right)^2 \tag{6.6}$$

Thus the applied gradient at the origin is cancelled to better than 1 part in 1000 over the range $-0.1s < z < 0.1s$ with this configuration.

6.5 Differential Shielding

Figure 6-4 shows that as ρ and λ are increased, the points of perfect shielding at $z = \pm z_S$ move toward the origin. In practical cases we usually start with a known

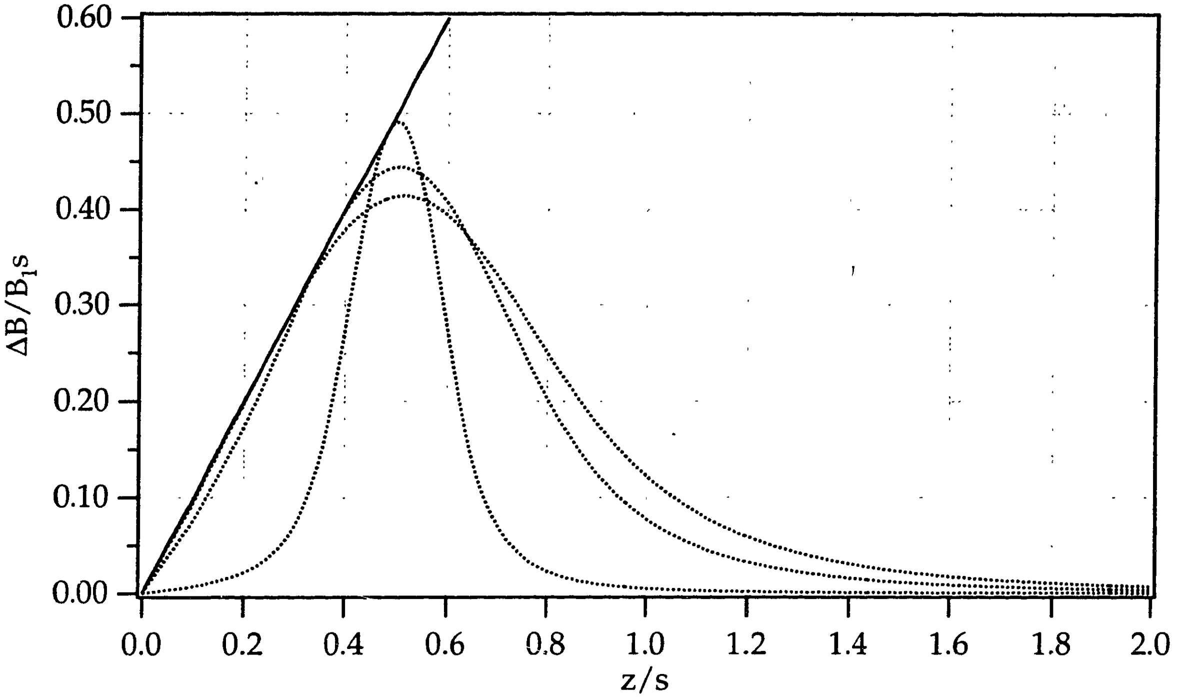

Figure 6-4: Sample differential shielding configurations. Plotted using dotted lines are induced field profiles $-B_{ind}(z)$ for pairs of values of the scaled radius ρ and length λ. Plotted are field profiles for $(\rho, \lambda) = (0.102, 0.165), (0.302, 0.348), (0.402, 0.388)$, which give perfect shielding at the points $z = \pm 0.483, \pm 0.370, \pm 0.270$ respectively. The configurations with larger ρ and λ give broader induced field profiles. The solid line with 45° slope is the applied field gradient $B'_{ext}z$.

separation between the points to be shielded, and a range of acceptable values for the solenoid radius r, and we need to choose appropriate values of l and s for the gradient shielding solenoids. Therefore it is useful to consider the new dimensionless variables $\rho' \equiv r/\Delta z_S$, $\lambda' \equiv l/\Delta z_S$, $\sigma' \equiv s/\Delta z_S$, where $\Delta z_S = 2z_S$ is the separation between the two perfectly shielded points. Figure 6-5 is a plot of λ' and σ' versus ρ'. The maximum value of ρ' is 1.61572; for ρ' above this value there are no configurations which give perfect differential shielding at two spatially separated points.

6.6 Summary and Conclusions

Time varying magnetic field gradients can limit the precision of spectroscopy on extended experimental regions. As a proposed solution, we show how oppositely-

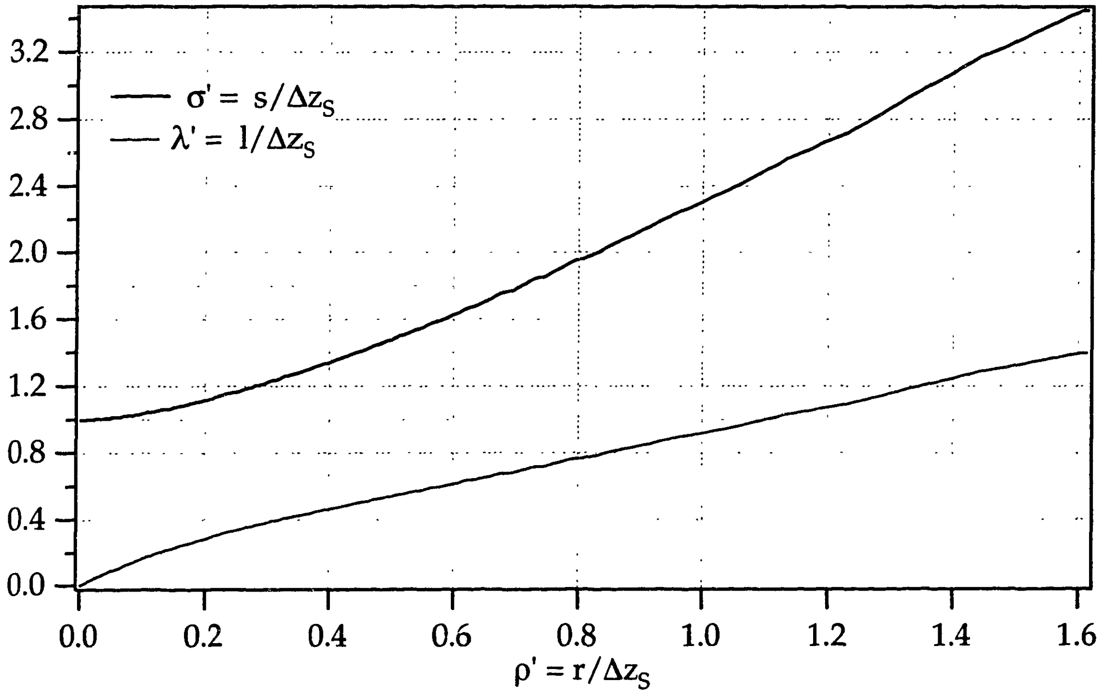

Figure 6-5: Graph showing the separation of the solenoid centers s and the solenoid length l relative to the separation between the points desired to be differentially shielded Δz_S. Note that the shielded points typically lie between the coil centers because Δz_S is usually less than s.

connected solenoid pairs can be used to shield experimental regions from applied field gradients. We give a coil configuration capable of shielding the applied gradient near the origin, and a family of configurations which provide differential shielding at points arranged symmetrically about the origin.

Bibliography

[AND72] D.F. Andrews et. al., *Robust Estimates of Location: Survey and Advances*, (Princeton University Press, Princeton, NJ, 1972).

[AUW93] Georges Audi and A. G. Wapstra, *Nuc. Phys. A565*, 1 (1993).

[BAS95] Basile, Giuseppe, Angelo Bergamin, Giovanni Cavagnero, Giovanni Mann, Ettore Vittone and Gianfranco Zosi., 1995. "The (220) Lattice Spacing of Silicon", *IEEE Trans. Inst. Meas.* **44**, 526-529.

[BER92] P. R. Bevington, D. K. Robinson, *Data Reduction and Error Analysis for the Physical Sciences*, 2nd ed., (McGraw-Hill, Boston, 1992).

[BOY92] K.R. Boyce, "Improved Single-Ion Cyclotron Resonance Mass Spectroscopy", Ph.D. Thesis, MIT (1992)

[BOR97] Borgenstrand, H. et al., "Proceedings of the 6th International Symposium on Electron Beam Ion Sources and their Applications", edited by L. Liljeby, *Physica Scripta*, **T71**, 88 (1997).

[BPR99] M. P. Bradley, J. V. Porto, S. Rainville, J. K. Thompson, and D. E. Pritchard, "Penning Trap Measurements of the Masses of ^{133}Cs, ^{87,85}Rb, and ^{23}Na with Uncertainties $\leq$0.2 ppb", *Phys. Rev. Lett.* **83**, 4510-4513.

[BRG86] Lowell S. Brown and Gerald Gabrielse, 1986, "Geonium Theory: Physics of a single electron or ion in a Penning trap.", *Rev. Mod. Phys.* **58** 233-311.

[CAG89] M. E. Cage, et al., 1989, "NBS Determination of the Fine-Structure Constant, and of the Quantized Hall Resistance and Josephson Frequency-to-Voltage Quotient in SI Units.", *IEEE Trans. Inst. Meas.* **38**, 284.

[CFB99] C. Carlberg, T. Fritioff, and I. Bergstrom, 1999, "Determination of the ^{133}Cs and Proton Mass Ratio Using Highly Charged Ions" *Phys. Rev. Lett.* **83**, 4506-4509.

[COR90] E.A. Cornell, "Mass Spectroscopy Using Single Ion Cyclotron Resonance", Ph.D. Thesis, MIT (1990).

[COR92] Cornell, E.A., K.R. Boyce, D.L.K. Fygenson, and D.E. Pritchard, 1992, "Two ions in a Penning trap: Implications for precision mass spectroscopy", *Phys. Rev. A* **45**, 3049-3059.

[COT86] E.R. Cohen, B.N. Taylor, "The 1986 Adjustment of the Fundamental Constants", *Rev. Mod. Phys.* **57**, 1121 (1987)

[CWB89] E.A. Cornell, R.M. Weisskoff, K.R. Boyce, R.W. Flanagan, Jr., G.P. Lafyatis, and D.E. Pritchard, "Single-Ion Cyclotron Resonance Measurement of $M(\mathrm{CO}^+/M(\mathrm{N}_2^+)$ *Phys. Rev. Lett.* **63** 1674 (1989).

[CWP90] E. A. Cornell, R. M. Weisskoff, K. R. Boyce, and D. E. Pritchard, *Phys. Rev. A* **41**, 312 (1990).

[DEH95] Dehmelt, H. Physica Scripta, Vol. T59, p. 87-92, (1995).

[DEP99] David E. Pritchard, private communication.

[DES79] R.D. Deslattes and E.G. Kessler, Jr., in Atomic Masses and Fundamental Constants - 6, J.A. Nolen, Jr. and W. Benenson, Eds., (Plenum Press, New York, 1979), p. 203; W.H. Johnson, in Precision Measurements and Fundamental Constants II, B.N. Taylor and W.D. Phillips, Eds., Natl. Bur. Stand. (U.S.), Spec. Publ. 617 (U.S. Government Printing Office, Washington D.C., 1984), p. 335

[DEW89] M.S. Dewey et. al., *Nucl. Instr. Meth. Phys. Res. A284*, 151 (1989).

[DIF94] DiFilippo, F. 1994, "Precise Atomic Masses for Determining Fundamental Constants", Ph.D. thesis (M.I.T., unpublished, 1994).

[DNB92] F. DiFilippo, V. Natarajan, K.R. Boyce, and D.E. Pritchard, *Phys. Rev. Lett.* **68**, 2859 (1992).

[DNB94] DiFilippo, Frank, Vasant Natarajan, Kevin R. Boyce, and David E. Pritchard, 1994, "Accurate Atomic Masses for Fundamental Metrology", *Phys. Rev. Lett.* **73**, 1481-1484.

[FLA87] R. W. Flanagan, "Trapping and Detection of Ions", Ph.D. Thesis, MIT (1987).

[FMM98] B. Fogelberg, K.A. Mezilev, H. Mach, V.I. Isakov, and J. Slivova, 1999, "Precise Atomic Mass Values near ^{132}Sn: The Resolution of a Puzzle", *Phys. Rev. Lett.* **82** 1823-1826.

[FVS95] Dean L. Farnham, Robert S. Van Dyck Jr., and Paul B. Schwinberg, "Determining the Electron's Atomic Mass and the Proton/electron Mass Ratio via Penning Trap Mass Spectroscopy", 1995, *Phys. Rev. Lett.* **75**, 3598-3601.

[GAB84] G. Gabrielse, *Phys. Rev. A* **29**, 462, (1984).

[GAR63] Garrett, M.W., "Calculation of Fields, Forces, and Mutual Inductances of Current Systems by Elliptic Integrals", Journal of Applied Physics, Vol. 34, No. 9, pp. 2567-2573 (1963).

[GAT88] Gabrielse, G. and Tan, J. "Self-shielding superconducting solenoid systems", J. Appl. Phys., 63, (10), pp. 5143-5148 (1988).

[GKH99] G. Gabrielse, A. Khabbaz, D.S. Hall, C. Heimann, H. Kalinowsky, W. Jhe, *Phys. Rev. Lett.* **82**, p.3198 (1999).

[GKT80] G. Gräff, H. Kalinowsky, and J. Trant, 1980, Z. Phys. A *297*, 35.

[GOR93] M.V. Gorshkov et. al., *Phys. Rev. A* **47**, 3433 (1993); M.V. Gorshkov et. al., *J. Am. Soc. Mass Spec.* **4**, 855 (1993); M.V. Gorshkov et. al., *Int. J. Mass Spec. Ion Proc.* **128**, 47 (1993).

Gorshkov, M.V., Marshall, A.G., and Nikolaev, E.N., 1993, "Analysis and elimination of sytematic errors originating from coulomb mutual interaction and image charge in Fourier transform ion cyclotron resonance precise mass difference measurements", J. Am. Soc. Mass Spec.

[GRE86] G. L. Greene, E. G. Kessler Jr., R. D. Deslattes and H. Börner, 1986, "New Determination of the Deuteron Binding Energy and the Neutron Mass", *Phys. Rev. Lett.* **56**, 819-822.

[GRE94] G.L. Greene and E.G. Kessler, Jr., private communications.

[HAS55] Hastings, C. "Approximations for Digital Computers", Princeton University Press, 1955.

[HFH82] D.R. Hertling, R.K. Feeney, D.W. Hughes, W.E. Sayle II, "Absolute experimental cross sections for the electron impact single, double, triple, and quadruple ionization of Cs^+ ions", J. Appl. Phys., Vol. 53, No. 8, Aug. 1982, p. 5427-5435.

[HJD99] T.P. Heavner, S.R. Jefferts, G.H. Dunn, *IEEE Trans. Inst. Meas.* , **48** p. 189 (1999)

[HUB81] P. J. Huber, *Robust Statistics* (Wiley, New York, 1981).

[JEL97] Anne-Marie Jeffery, R.E. Elmquist, Lai H. Lee, John Q. Shields, and R.f. Dziuba, "1997, "NIST Comparison of the Quantized Hall Resistance, and the Realziation of the SI OHM Through the Calculable Capacitor", 1997, *IEEE Trans. Inst. Meas.* **46**, 264-268.

[JER93] Roland Jertz *et. al.*, 1993, "Direct Determination of the Mass of ^{28}Si as a contribution to a New Definition of the Kilogram", *Physica Scripta* **48**, 399.

[JOS62] Josephson B. D. *Phys. Lett.* **1** 251 (1962).

[KAK93] M. Kaku, "Quantum Field Theory: A Modern Introduction." Oxford University Press (1993).

[KES95] E.G. Kessler Jr., private communication (1995).

[KIN95] Toichiro Kinoshita, 1995, "New Value of the α^3 Electron anomalous Magnetic Moment", *Phys. Rev. Lett.* **75**, 4728-4731.

[KIN96] T. Kinoshita, *Rep. Prog. Phys.* **59**, 1459 (1996).

[KIN97] T. Kinoshita, *IEEE Trans. Inst. Meas.* **46**, 108 (1997).

[KRU98] E. Krüger, W. Nistler, and W. Weirauch, 1998, "Determination of the fine-structure constant by a precise measurement of h/m_n: the final result.", *Metrologia* **35**, 203-209.

[KUT82] R. Kumaresan and D.W. Tufts, 1982, "", IEEE Trans. Acous. Speech, and Sig. Proc. ASSP-30, 833 (1982).

[LIA99] S. G. Lias, et al., "Ion Energetics Data" in NIST Chemistry WebBook, NIST Standard Ref. Database Number 69, Eds. W.G. Mallard and P.J. Linstrom, Nov. 1998, NIST, Gaithersburg MD, 20899 (http://webbook.nist.gov).

[LAP95] S. Laporta, *Phys. Lett. B*, **343**, 421 (1995)

[LAR96] S. Laporta and E. Remiddi,*Phys. Lett. B*, **379**, 283 (1996)

[MAR99] Jens Martin, Horst Bettin, Ulrich Kuetgens, Detlef Schiel, and Peter Becker, "About the Exisiting Discrepancy in the Determinations of the

Avogadro Constant", IEEE Trans. Inst. Meas., Vol. 48, No. 2, April 1999 (pp. 216-220).

[NAT93] V. Natarajan, 1993 "Precision Mass Spectroscopy at 0.1 ppb", Ph.D. thesis (M.I.T., unpublished).

[NBD93] Vasant Natarajan, Kevin R. Boyce, Frank DiFilippo, and David E. Pritchard, 1993, "Precision Penning Trap Comparisons of Nondoublets: Atomic Masses of H, D, and the Neutron", *Phys. Rev. Lett.* **71**, 1998-2001.

[NGU98] Nguyen, R., "Loss Mechanisms in Superconducting Niobium Coils" Undergraduate Thesis, MIT, (1998).

[NIR51] Nier, A.O. and Roberts, T.R., 1951, "The determination of atomic mass doublets by means of a mass spectrometer", Phys. Rev. *81*, 507.

[PAP62] Panofsky, W.K.H., and Phillips, M., "Classical Electricity and Magnetism", 2nd ed., Addison-Wesley, Reading, Massachusetts, 1962.

[PEN36] F.M. Penning, "Die Glimmentladung bei niedrigem druck zwischen koaxialen zylindern in einem axialen Magnetfeld", 1936, Physica *3*, 873.

[PTV92] Press, W.H., Teukolsky, S.A., Vetterling, W.T., and Flannery, B.P., "Numerical Recipes in C", 2nd ed., Cambridge University Press, Cambridge, 1992.

[QUI91] Quinn, Terry J. "The Kilogram: The Present State of Our Knowledge", 1991, *IEEE Trans. Instr. Meas.* **40**, 81.

[RAM57] N. Ramsey, Molecular Beams, 1957.

[SCH51] Schwinger, *J. Phys. Rev.* **82**, 914 and **91** 713 (1951).

[SDV81] P.B. Schwinberg, H.G. Dehmelt, and R.S. Van Dyck, Jr., *Phys. Lett.* **81A** 119 (1981).

[SEY92] P. Seyfried *et. al.*, 1992, "A Determination of the Avogadro Constant", *Z. Phys. B* **87**, 289-298.

[SJD99] C. Schwob, et al., *Phys. Rev. Lett.* **82**, 4960 (1999).

[SMI75] L.G. Smith and A.H. Wapstra, *Phys. Rev. C* **11**, 1392 (1975)

[SMY39] Smythe, W.R., "Static and Dynamic Electricity", 2nd ed., McGraw-Hill, New York, 1950.

[STO90] H. Stolzenberg, Becker, St., Bolen, G., Kern, F., Kluge, H.-J., Oto, Th., Savard, G., Schweikhard, L., Audi, G. and Moore, R.B., 1990, *Phys. Rev. Lett.* **65**, 3104-3107.

[TAY91] B.N. Taylor, *IEEE Trans. Instr. Meas.* **40**, 86 (1991).

[TAY94] Barry N. Taylor, 1994, "Determining the Avogadro Constant from Electrical Measurements", *Metrologia* **31**, 181-194.

[TAY99] Barry Taylor, private communication.

[TJL83] Tsai, J.-S., Jain, A.K., and Lukens, J.E., *Phys. Rev. Lett.* **51**, 316 (1983).

[UHG97] Th. Udem, Huber, A., Gross, B., Reichert, J., Prevedelli, M., Weitz, M., and Hänsch, T.W., 1997, "Phase-Coherent Measurement of the Hydrogen 1S-2S Transition Frequency with an Optical Frequency Interval Divider Chain", **79**, *Phys. Rev. Lett.* **79**, 2646-2649.

[URH99] Th. Udem, J. Reichert, R. Holzwarth, and T. W. Hänsch, 1999, "Absolute Optical Frequency Measurement of the Cesium D_1 Line with a Mode-Locked Laser.", *Phys. Rev. Lett.* **82**, 3568-3571.

[VFS93a] Robert S. Van Dyck, Jr., Farnham D.L., and Schwinberg, P.B., 1993, "Tritium-Helium-3 Mass Difference Using the Penning Trap Mass Spectroscopy", 1993, *Phys. Rev. Lett.* **70**, 2888.

[VFS93b] R. S. Van Dyck Jr., D. L. Farnham, and P. B. Schwinberg, Abstracts of the American Physical Society, 1993.

[VFS93c] R.S. Van Dyck, Jr., D.L. Farnham, and P.B. Schwinberg, *Bull. Am. Phys. Soc. 38* 946, 947 (1993).

[VFZ98] Robert S. Van Dyck, Jr., Dean L. Farnham, Stephen Zafonte, and Paul B. Schwinberg, 1998, "High Precision Penning Trap Mass Spectroscopy and a New Measurment of the Proton's Atomic Mass", *ICAP XVI Abstracts, Windsor*, 294-295.

[VMF86] Van Dyck, R. S. Jr., Moore, F.L., Farnham, D.L., and Schwinberg, P.B., "Variable magnetic bottle for precision geonium experiments", Rev. Sci. Instrum. 57 (4), April 1996, pp. 593-597.

[VMF89] Van Dyck, R.S. Jr., Moore, F.L., Farnham, D.L., and Schwinberg, P.B. "Number dependency in the compensated Penning trap", *Phys. Rev. A* **40** 6308 (1989).

[VSD87] R. S. Van Dyck, Jr., P. B.Schwinberg, and H. G. Dehmelt, *Phys. Rev. Lett.* **59**, 26

[WAP90] A.H. Wapstra, *Nucl. Instr. Meth. Phys. Res. A292*, **671** (1990).

[WAU85] A.H. Wapstra and G. Audi, 1993, "The 1993 Atomic Mass Evaluations (I). Atomic Mass Table", 1985, *Nucl. Phys.* **A432** 1-65.

[WED73] Wineland, D.J., P. Ekstrom, and H.G. Dehmelt, 1973, Phys. Rev. Lett., *31*, 1279.

[WEI88] R. M. Weisskoff, "Detecting Single, Trapped Ions", Ph.D. Thesis, MIT, 1988.

[WID75] Wineland, D. and Dehmelt, H. "Principles of the stored-ion calorimeter", *J. Appl. Phys.* **46**, No. 2, p. 919 (1975).

[WIN75] D.J. Wineland and H.G. Dehmelt, *Int. J. Mass Spec. Ion Proc.* **16**, 338 (1975).

[1] Williams, E.R. et al., *IEEE Trans. Instr. Meas.* **38**, 233 (1989).

[WLB88] Weisskoff, R.M., G.P. Lafyatis, K.R. Boyce, E.A. Cornell, R.W. Flanagan Jr., and D.E. Pritchard, 1988, *J. Appl. Phys.* **63**, 4599-4604.

[WSN98] E. R. Williams, R. L. Steiner, D. B. Newell, and P.T. Olsen, *Phys. Rev. Lett.* **81**, 2404 (1998).

[WYC93] David S. Weiss, Brenton C. Young, and Steven Chu, 1993, "Precision Measurement of the Photon Recoil of an Atom Using Atomic Interferometry", 1993, *Phys. Rev. Lett.* **70**, 2706-2709.

[WYC94] David S. Weiss, Brenton C. Young, and Steven Chu, 1993 *Appl. Phys. B* **59**, 217 (1994).

[YOU97] B. C. Young, Ph.D. Thesis, Stanford (1997).

Acknowledgments

I have many mentors, teachers, colleagues and friends to thank for making this work possible. Above all I have to thank my parents for encouraging my childhood curiosity about all things, especially those scientific in character. They patiently answered my many questions, and when they could not bought me books which could. They were generous to a fault in providing me with electronics and aeronautics kits, and indulging all my messy experimentation. This long-ago nuturing was without a doubt the *primum mobile* for this thesis. Thanks Mom and Dad!

My professors at UNB were instrumental in giving me the training that made it possible for me to attend MIT. I particularly want to thank Dr. Cotter and Dr. Leung for introducing me to the EE and Physics versions of electromagnetism, a subject which has been a source of continual pleasure for me. Dr. Richard Papenhausen, an MIT alumnus himself, deserves a special thanks for being the first to suggest I consider attending MIT.

Of course a huge debt of thanks goes to my graduate thesis advisor, Prof. David E. Pritchard. He is truly an exceptional physicist, and a generous man. He has directly or indirectly taught almost everything I know about experimental physics, and his unique ability to analyze almost any scientific problem in terms of its fundamentals has had a profound influence on me.

This work was supported by the National Science Foundation (NSF), the Joint Services Electronics Program (JSEP), and the National Institute of Standards and Technology (NIST) through a NIST Precision Measurements Grant. I am grateful to all these organizations for providing funding for my work at MIT. I am also grateful to MIT for providing a Forum Fellowship to fund my first semester of graduate studies.

My immediate predecessors in the lab, Dr. Frank DiFilippo and Dr. Vasant Natarajan provided me with my introduction to ion trapping and mass spectrometry, and set an inspirational standard for excellence in the lab. I only regret that we did not have more time to work together. Dr. Fred Palmer worked steadily with me through a difficult time with the apparatus, and taught me everything I know

about cryogenics, and a lot about electronics and vacuum systems. Fred is the most versatile scientist I have ever worked with- his range of abilities from advanced theory to practical circuit construction is astounding, and he is in addition a kind and patient soul. Thanks Fred!

Dr. Trey Porto was Fred's successor and proved to be a worthy heir, bring much the same range of talents to the lab. His efforts were absolutely essential to the measurements described in this thesis, plus he turned out to be a boon companion and an all-around nice guy.

I cannot omit the succession of talented undergraduates who assisted us in various ways; Abe Stroock, Szymon Rusinkiewicz, David Garrison, Mark Huang, Roland Nguyen, Baruch Feldman, Sidney Burks, and Josh Jackson. They all showed a maturity, dedication and ability well beyond their years and formal training. I particularly want to thank Roland, as he wound the $Q = 50000$ coil which was an integral part of the ion detector used for the measurements described in this thesis.

I was surprised at how much I learned from the two junior graduate students in the ICR Lab, Simon Rainville and James Thompson. Sometimes I suspect they have taught me more than I taught them! What is certain is that they were essential team members during the data-taking and analysis phases, and helped me in innumerable ways with my thesis work. Plus, they are both super-nice guys! I wish them the best of luck with the experiment, and pledge them whatever help I can provide.

The members of my thesis committee deserve special thanks. It has been a pleasure to know Prof. Wolfgang Ketterle personally as his star has risen, and I have always appreciated his interest in and insight reagrding our experiment. Prof. Aron Bernstein has also been generous with his time and suggestions, and has tolerated the ambiguity regarding the exact date of my thesis defense with good humor.

Nothing in our lab would get done without the ever helpful Carol Costa. I have gotten to know Carol quite well over the years; her encouragement has been continual, and her advice has always been on the mark.

Peggy Berkowitz, Pat Solakoff, Alicia Duarte, Nancy Savioli, and Claudia Labolita-James in the physics headquarters deserve a big thank you from all physics graduate students for making our lives as administratively un-complicated as possible. Tran in the reading room was a good friend over the years. Marc Davey and the night custodial crew were cheerful and accomodating when we had to shut down the elevator during a data run. Gerry Power was a frequent friendly visitor, and an amazingly helpful person. Peter Morley and Steve the welder in the LNS shop provided essential skills for building the new apparatus.

Finally, I must thank my dear wife, Rachel, her parents Bob and Sophie, and all her family for their support. Rachel was a rock; when unresolve reared its head, she steadied me; when doubt entered my mind she banished it; when despond crept in she cheered me. She more than any other has borne the daily ups and downs of this thesis work, and I thank her.

THESIS PROCESSING SLIP

FIXED FIELD: ill. ______ name ______

index ______ biblio ______

► **COPIES:** [✓ Archives] Aero Dewey Eng Hum

Lindgren Music Rotch [✓ Science]

TITLE VARIES: ►☐ 133 Cs
instead of the word
Cesium (See [illegible]

NAME VARIES: ►☐ ______

IMPRINT: (COPYRIGHT) ______

► **COLLATION:** 197 P

► **ADD: DEGREE:** ______ ► **DEPT.:** ______

SUPERVISORS: ______

NOTES:

cat'r: date:

page:

► F63

► **DEPT:** Phy

► **YEAR:** 2000 ► **DEGREE:** Ph. D.

► **NAME:** BRADLEY, Michael
Patrick